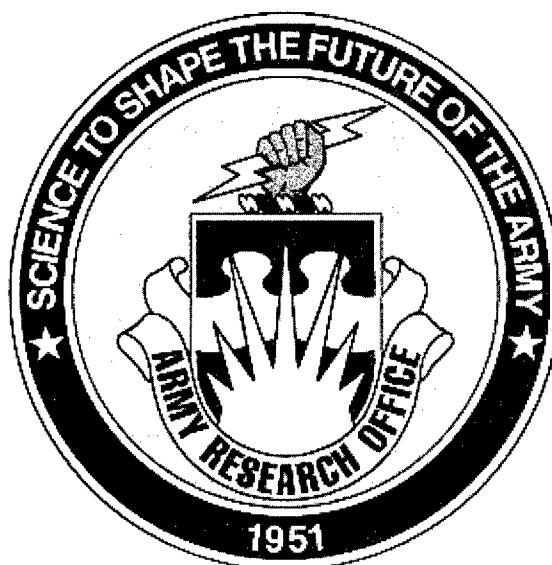


Army Research Office And Air Force Office of Scientific Research



DISTRIBUTION STATEMENT A
Approved for Public Release
Distribution Unlimited

2004 Contractors' Meeting In Chemical Propulsion

20040706 063

REPORT DOCUMENTATION PAGE

Public reporting burden for this collection of information is estimated to average 1 hour per response, including the time for reviewing instructions, data needed, and completing and reviewing this collection of information. Send comments regarding this burden estimate or any other aspect of this burden to Department of Defense, Washington Headquarters Services, Directorate for Information Operations and Reports (0704-0188), 1215 Jefferson Davis Highway, Suite 1204, Arlington, VA 22202-4302. Respondents should be aware that notwithstanding any other provision of law, no person shall be subject to any penalty for failing to comply with a collection of information if it does not display a currently valid OMB control number. PLEASE DO NOT RETURN YOUR FORM TO THE ABOVE ADDRESS.

0330

1. REPORT DATE (DD-MM-YYYY) 17-06-2004		2. REPORT TYPE Technical		3. DATES COVERED (From - To) 01-06-2003 - 31-05-2004	
4. TITLE AND SUBTITLE (U) Army Research Office and Air Force Office of Scientific Research 2004 Contractors Meeting in Chemical Propulsion				5a. CONTRACT NUMBER	
				5b. GRANT NUMBER	
				5c. PROGRAM ELEMENT NUMBER 61102A, 61102F	
				5d. PROJECT NUMBER	
6. AUTHOR(S) David M. Mann and Julian M. Tishkoff				5e. TASK NUMBER	
				5f. WORK UNIT NUMBER	
				8. PERFORMING ORGANIZATION REPORT NUMBER	
7. PERFORMING ORGANIZATION NAME(S) AND ADDRESS(ES) Army Research Office Air Force Office of Scientific Research Triangle Park NC Research 27709-2211 Arlington VA 22203-1954				10. SPONSOR/MONITOR'S ACRONYM(S)	
9. SPONSORING / MONITORING AGENCY NAME(S) AND ADDRESS(ES) AFOSR/NA 4015 Wilson Boulevard Room 713 Arlington VA 22203-1954				11. SPONSOR/MONITOR'S REPORT NUMBER(S)	
12. DISTRIBUTION / AVAILABILITY STATEMENT Approved for public release; distribution is unlimited					
13. SUPPLEMENTARY NOTES					
14. ABSTRACT Abstracts are given for 6.1 basic research in chemical propulsion sponsored by the Army Research Office and the Air Force Office of Scientific Research.					
15. SUBJECT TERMS Flames, Propulsion, Gas Turbines, Diesel Engines, Scramjets, Pulse Detonation Engines, Hydrocarbon Fuels, Diagnostics, Spray, Droplet, Supercritical Fluids, Turbulence, Combustion					
16. SECURITY CLASSIFICATION OF:			17. LIMITATION OF ABSTRACT UL	18. NUMBER OF PAGES 185	19a. NAME OF RESPONSIBLE PERSON Julian M. Tishkoff
a. REPORT Unclassified	b. ABSTRACT Unclassified	c. THIS PAGE Unclassified			19b. TELEPHONE NUMBER (include area code) (703) 696-8478

ARO/AFOSR Contractors' Meeting in Chemical Propulsion

TABLE OF CONTENTS

Agenda	1
The Army Research Office Program in Propulsion and Energetics <i>D.M. Mann, ARO/Mechanical & Environmental Sciences Division</i>	5
AFOSR Sponsored Research in Combustion and Diagnostics <i>J.M. Tishkoff, AFOSR/NA</i>	9
Chemical Kinetics and Aerodynamics of Ignition <i>C.K. Law, Princeton University</i>	11
Physical and Chemical Processes in Flames <i>C.K. Law, Princeton University</i>	15
Development of a Comprehensive and Predictive Reaction Mechanism of Liquid Hydrocarbon Fuel Combustion <i>H. Wang, University of Delaware</i>	19
Experimental and Detailed Numerical Studies of Fundamental Flame Properties of Gaseous And Liquid Fuels <i>F.N. Egolfopoulos, University of Southern California</i>	23
The Low Temperature Oxidation Chemistry of JP-8 and its Surrogates at High Pressure <i>N.P. Cemasky and D.L. Miller, Drexel University</i>	27
Autoignition and Combustion of Diesel and JP-8 <i>K. Seshradi, University of California, San Diego</i>	31
Experimental and Computational Characterization of Combustion Phenomena <i>J.R. Gord, AFRL/PRTC</i>	35
Advanced Diagnostics for Reacting Flows <i>R.K. Hanson, Stanford University</i>	39
Ramjet Research <i>C.D. Carter and M.R. Gruber, AFRL/PRA</i>	43
Advanced Imaging of Premixed Turbulent Combustion Processes <i>F.C. Gouldin, Cornell University</i>	47
Advanced Stimulated Scattering Measurements in Supercritical Fluids <i>G. Faris, SRI International</i>	51
Shock Tube Measurements of Ignition Processes in Diesel-Related Fuels <i>R.K. Hanson, Stanford University</i>	55
Stabilization and Blowout of Gaseous and Spray Jet Flames <i>K.M. Lyons, North Carolina State University</i>	59
Drop/Gas Interactions of Dense Sprays <i>G.M. Faeth, University of Michigan</i>	63

LES of Sooting Flames <i>S. Menon, Georgia Institute of Technology</i>	67
Advanced Supercritical Fuels <i>T. Edwards, C. Bunker and T. Jackson, AFRL/PRTG</i>	71
Supercritical Fuel Pyrolysis <i>M.J. Wornat, Louisiana State University</i>	75
Burning Speed Measurements of JP-8 Air Mixtures at High Pressure and Temperature <i>H. Metghalchi, Northeastern University</i>	79
Time Resolved Measurements and Reactive Pathways for Hypergolic Bipropellant Combustion <i>J.E. Smith, University of Alabama, Huntsville</i>	83
Plasma-Propellant Interaction Studies <i>S.T. Thynell and T.A. Litzinger, Pennsylvania State University</i>	87
Abstracts of Work Units Not Presented at the Meeting	
Porous Media Combustion Concepts for Propulsion Gas Turbines <i>A.K. Agrawal and S.R. Gollahalli, University of Oklahoma</i>	95
Turbulent Mixing and Combustion for High-Speed, Air-Breathing Propulsion Applications <i>P.E. Dimotakis, California Institute of Technology</i>	99
A New Class of Hybrid Schemes Based on Large-Eddy Simulation and Low-Dimensional Stochastic Models <i>T. Echekki, North Carolina State University</i>	103
Particulate Size and Composition <i>D. Foster, University of Wisconsin, Madison</i>	107
Plasma Research for Aerospace Applications <i>B. Ganguly, AFRL/PRPE</i>	111
Filtered Mass Density Function for Subgrid Scale Modeling of Turbulent Diffusion Flames <i>P. Givi, University of Pittsburgh</i>	115
Computer-Based Adaptation Tool for Advanced Diesel Engines Used in Military Applications <i>N.A. Henein, D. Taraza and N. Chalhoub, Wayne State University</i>	119
Statistical Interpretation of Scalar Time-Series Measurements in Turbulent Partially Premixed Flames <i>N.M. Laurendeau, G.B. King and M.W. Renfro, Purdue University</i>	123
Acoustic Sensing and Actuation in Gaseous Flows <i>T. Lieuwen, Georgia Institute of Technology</i>	127
Ballistic Imaging in the Primary Breakup Region of Diesel Injector Sprays <i>M. Linne and T. Parker, Colorado School of Mines</i>	131
Large-Eddy Simulation of Turbulent Combustion <i>H. Pitsch, Stanford University</i>	135
PDF Modeling of Turbulent Combustion <i>S.B. Pope, Cornell University</i>	139

Model Development for IC Engines R.D. Reitz and C.R. Rutland, University of Wisconsin, Madison	143
Study of In-Cylinder Reactions of High Power-Density Direct Injections Diesel Engines <i>K.T. Rhee, Rutgers, The State University of New Jersey</i>	147
Pulse Detonation Physiochemical and Exhaust Relaxation Processes <i>F. Schauer, AFRL/PRTC</i>	151
Experimental Study of Velocity, Scalar, and Scalar-Dissipation Filtered Joint Density Function <i>C. Tong, Clemson University</i>	155
Experimental Investigation of the Interaction of Electrothermal Plasmas with Solid Propellants <i>P.L. Varghese and N.T. Clemens, The University of Texas at Austin</i>	159
Concurrent Research on High Gravity (g) Combustion with Enabling Materials <i>J. Zelina, AFRL/PRTC</i>	163
List of Invitees	167

ARO/AFOSR CONTRACTORS MEETING

IN

CHEMICAL PROPULSION

Westward Look Resort

Tucson AZ

7-9 June 2004

MONDAY, 7 JUNE

- 1:00 - 1:15 Army Research Office Overview - David Mann
- 1:15 - 1:30 AFOSR Combustion and Diagnostics Program – Julian Tishkoff
- Topic: Hydrocarbon Combustion Chemistry
- 1:30 - 2:00 Chemical Kinetics and Aerodynamics of Ignition
Chung K. Law, Princeton University
- 2:00 - 2:30 Physical and Chemical Processes in Flames
Chung K. Law, Princeton University
- 2:30 - 3:00 Development of a Comprehensive and Predictive Reaction
Mechanism of Liquid Hydrocarbon Fuel Combustion
Hai Wang, University of Delaware
- 3:00 - 3:30 BREAK
- 3:30 - 4:00 Experimental and Detailed Numerical Studies of Fundamental
Flame Properties of Gaseous and Liquid Fuels
Fokion Egolfopoulos, University of Southern California
- 4:40 - 4:30 The Low Temperature Oxidation Chemistry of JP-8 and its
Surrogates at High Pressure
Nicholas Cernansky, Drexel University
- 4:30 - 5:00 Autoignition and Combustion of Diesel and JP-8
Kal Seshradi, University of California, San Diego
- 5:00 DINNER (on own)

TUESDAY, 8 JUNE

8:15 - 8:30 Announcements

TOPIC: Combustion Diagnostics

8:30 - 9:00 Experimental and Computational Characterization of
Combustion Phenomena
James Gord, AFRL/PRTS

9:00 - 9:30 Advanced Diagnostics for Reacting Flows
Ronald K. Hanson, Stanford University

9:30 - 10:00 Ramjet Research
Campbell Carter, AFRL/PRA

10:00 - 10:30 BREAK

10:30 - 11:00 Advanced Imaging of Premixed Turbulent Combustion Processes
Frederick Gouldin, Cornell University

11:00 - 11:30 Advanced Stimulated Scattering Measurements in
Supercritical Fluids
Gregory Faris, SRI International

11:30 - 12:00 Shock Tube Measurements of Ignition Processes in
Diesel-Related Fuels
Ronald K. Hanson, Stanford University

12:00 - 1:00 LUNCH

TOPIC: Particle-Laden Flows

1:00 - 1:30 Stabilization and Blowout of Gaseous and Spray Jet Flames
Kevin Lyons, North Carolina State University

1:30 - 2:00 Drop/Gas Interactions of Dense Sprays
Gerard M. Faeth, University of Michigan

2:00 - 2:30 LES of Sooting Flames
Suresh Menon, Georgia Institute of Technology

2:30 - 3:00 BREAK

TOPIC: Research Needs for Augmentors

3:00 - 3:20 In-House Augmentor High Impact Technology Research
Barry Kiel, AFRL/PRTC

- | | |
|-------------|--|
| 3:20 - 4:05 | Development Challenges and Progress for Gas Turbine Thrust Augmentors
Jeffery Lovett, Pratt and Whitney |
| 4:05 - 4:50 | Research Issues for the Augmentor Design and Development Process
Randy L. Lewis and John Koshoffer, General Electric Aircraft Engines |
| 4:50 - 6:15 | GENERAL DISCUSSION |
| 6:15 | DINNER (on own) |

WEDNESDAY, 9 JUNE

- | | |
|-------------|---------------|
| 8:15 - 8:30 | Announcements |
|-------------|---------------|

TOPIC: High Pressure Behavior

- | | |
|--------------|--|
| 8:30 - 9:00 | Advanced Supercritical Fuels/Supercritical Combustion
Timothy Edwards, AFRL/PRTG |
| 9:00 - 9:30 | Fuels Combustion Research: Supercritical Fuel Pyrolysis
Mary Julia (Judy) Wornat, Louisiana State University |
| 9:30 - 10:00 | Burning Speed Measurements of JP-8 Air Mixtures at High Pressure and Temperature
Hameed Metghalchi, Northeastern University |

- | | |
|---------------|-------|
| 10:00 - 10:30 | BREAK |
|---------------|-------|

TOPIC: General Combustion Research

- | | |
|---------------|---|
| 10:30 - 11:00 | Time Resolved Measurements and Reactive Pathways for Hypergolic Bipropellant Combustion
James Smith, University of Alabama, Huntsville |
| 11:00 - 11:30 | Plasma-Propellant Interaction Studies
Stefan Thynell, Pennsylvania State University |
| 11:30 - 12:00 | ARO BUSINESS SESSION – Contractors/Grantees in Dr. Mann's Program |
| 12:00 - 12:30 | AFOSR BUSINESS SESSION – Contractors/Grantees in Dr. Tishkoff's Program |
| 12:30 - 1:30 | LUNCH |
| 1:30 | ADJOURN |

The Army Research Office Program in Propulsion and Energetics

David M. Mann
Mechanical and Environmental Sciences Division
US Army Research Office

The Army is on a fast-paced path to transformation. That transformation involves the development of new classes of fighting vehicles, the Future Combat System, which are lighter and more mobile, while maintaining the levels of lethality and survivability offered by today's systems, e.g. the M1 Abrams tank. Over the years, ARO propulsion and energetics research has played a vital part in providing the options for the development of the new systems. Research in future years will yield breakthroughs that will enable new capabilities.

The Army Transformation and recent world events have re-emphasized the need for lightweight, high power density, high efficiency engines for air and ground vehicles. The ARO Propulsion program continues to focus on optimizing the combustion processes in diesel and gas turbine engines. Fundamental to that optimization is understanding and developing predictive models for the controlling mechanisms and processes. Particularly important research areas are fuel injection and fuel-air mixing dynamics, ignition, combustion and heat transfer. In order to be applicable to the environments of advanced engines, it is vitally important to address these areas in the appropriate parameter space of temperature, pressure and turbulence level. Ultimately the goal is to combine the detailed understanding of combustion that can be used with active control techniques and health monitoring systems.

Projectile and missile propulsion is the focus of the ARO Energetics program. The emphasis is on the development of higher energy systems, both through the utilization of current energetic materials under higher loading conditions and through the development of higher energy/output energetic materials, e.g. nanoscale materials. In the first instance, fixed volume systems, such as gun and missile combustion chambers, can deliver higher energies if higher charge densities (guns) or more compact combustors (liquid fueled missiles) are used. Here the challenges are the ignition and heat release dynamics at high density. In the second instance, the Army is exploring the potential of nano-scale energetic materials to provide higher energy and higher power for propulsion and explosive uses. In this new field, emphasis is being placed on the preparation and characterization of novel nanostructures and on understanding their reactivity.

Details on submitting proposals to ARO may be found on the ARO web site, www.aro.army.mil. The site contains the Broad Agency Announcement for the ARO and other Army Research Laboratory Directorates' research efforts. Prospective offerors to ARO are encouraged to informally discuss their research ideas with the appropriate ARO program manager prior to submitting a formal proposal.

AFOSR SPONSORED RESEARCH IN COMBUSTION AND DIAGNOSTICS

PROGRAM MANAGER: JULIAN M. TISHKOFF

**AFOSR/NA
4015 Wilson Boulevard, Room 713
Arlington VA 22203-1954**

SUMMARY/OVERVIEW: The Air Force Office of Scientific Research (AFOSR) program in combustion and diagnostics currently is focused on five areas of study: high-speed propulsion, turbulent combustion, diagnostics, supercritical fuel behavior, and plasma-enhanced combustion. An assessment of major research needs in each of these areas is presented.

TECHNICAL DISCUSSION

AFOSR is the single manager for Air Force basic research, including efforts based on external proposals and in-house work at the Air Force Research Laboratory (AFRL). Combustion and Diagnostics is assigned to the AFOSR Directorate of Aerospace and Materials Sciences along with programs in rocket and space propulsion, fluid and solid mechanics, and structural materials.

Interests of the AFOSR Combustion and Diagnostics subarea are given in the SUMMARY section above. Many achievements can be cited for these interests, yet imposing fundamental research challenges remain. The objective of the program is publications in the refereed scientific literature describing significant new understanding of multiphase turbulent reacting flow. Incremental improvements to existing scientific approaches, hardware development, and computer codes fall outside the scope of this objective.

The Combustion and Diagnostics subarea supports the Air Force commitment to aerospace propulsion through the Department of Defense National Aerospace Initiative (NAI). Accordingly, the research in this subarea will address research issues related to chemical propulsion for all Air Force aerospace missions, including combined cycle propulsion for access to space. This program will complement related research activities in space propulsion and energetic materials.

The primary focus of research in turbulent combustion is the creation of computational modeling tools for combustor designers that are both computationally tractable and quantitatively predictive. This research has been directed in two areas: the formulation of augmented reduced chemical kinetic mechanisms for the combustion of hydrocarbon fuels and the development of subgrid-scale models for large eddy simulation of turbulent combustion.

Future airbreathing and chemical rocket propulsion systems will require propellants to absorb substantial thermal energy, raising their temperatures to supercritical thermodynamic conditions. Understanding and controlling fluid properties at these conditions will be crucial for avoiding thermal degradation and for optimizing subsequent processes within the combustor. Research has focused on the role of supercritical transport in the thermal destabilization of hydrocarbon fuel prior to combustion and on primary and secondary fuel breakup under transcritical and supercritical conditions.

Plasma research is one of six AFOSR Theme topics selected for support beginning in Fiscal Year 2001. The focus primarily is on the utilization of plasmas for ignition and flame stabilization in scramjets; however, the extension of this technology to other modes of chemical propulsion and energy conversion also is of interest. The theme research has been supplemented by research coordinated between universities and small businesses under the Department of Defense Small Business Technology Transfer (STTR) Program. The Air Force also supports related research activity in Russia under the Air Force Research Laboratory Russian Research Initiative. The Theme and Russian research activity was presented as part of a Weakly Ionized Gas Dynamics (WIG) Workshop at the 32nd AIAA Aerospace Sciences Meeting and Exhibit in January 2004. The next workshop will take place in January 2005.

Decisions on support for research proposals are based on scientific opportunities and technology needs. Researchers interested in submitting proposals should contact Dr. Tishkoff for information on time constraints associated with proposal evaluations. Further information on research interests and proposal preparation can be found on the AFOSR web site, <http://www.afosr.af.mil>. The availability of funds places a major constraint on program redirection and growth. Figure 1 shows the recent trend of funding for basic research in combustion and diagnostics from Air Force and DOD sources. Informal inquiries for new research are encouraged throughout the year. Formal proposals should be submitted by 1 April for peer review by the National Research Council.

The purpose of this abstract has been to communicate AFOSR perceptions of research trends to the university and industrial research communities. However, communication from those communities back to AFOSR also is desirable and essential for creating new research opportunities. Therefore, all proposals and inquiries for fundamental research

are encouraged even if the content does not fall within the areas of emphasis described herein. Comments and criticisms of current AFOSR programs also are welcome.

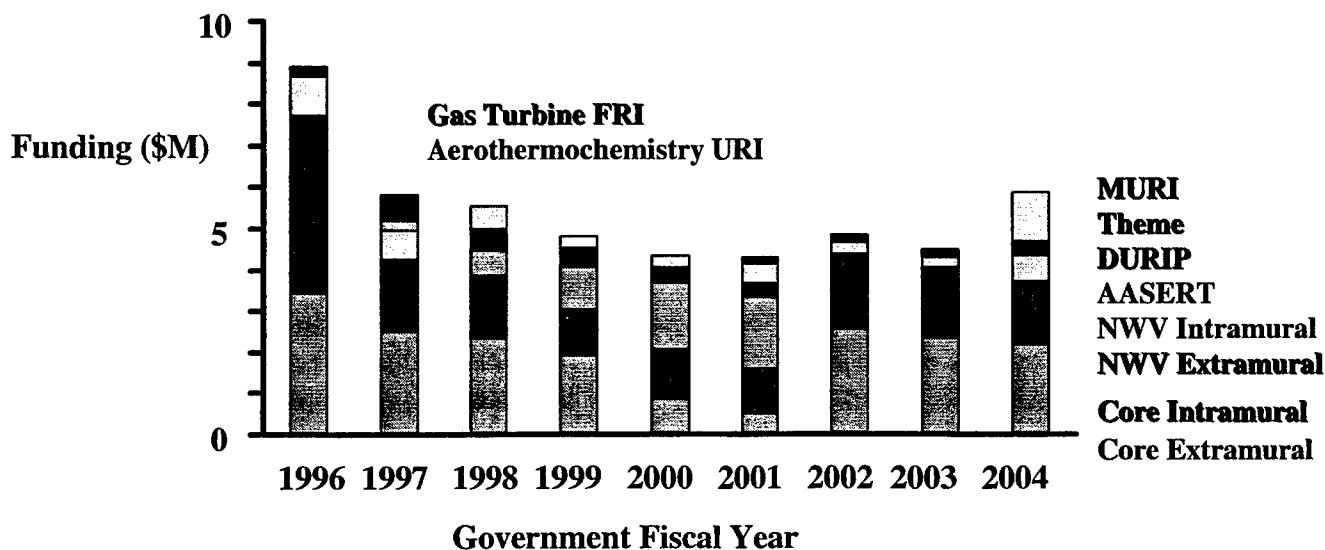


Figure 1. AFOSR Funding for Combustion and Diagnostics

CHEMICAL KINETICS AND AERODYNAMICS OF IGNITION

(ARO Grant No. DAAG19-01-0004)

Principal Investigator: Chung K. Law

Princeton University
Princeton, NJ 08544

SUMMARY/OVERVIEW

This program studies the individual and coupled effects of chemical kinetics and aerodynamics on ignition in laminar and turbulent hydrocarbon/air mixtures through experimental, computational, and analytical investigations. During the reporting period, three projects were undertaken, namely: (1) Experimental determination and computational calculation of the ignition temperatures of nonpremixed counterflow dimethyl ether (DME) versus air, leading to the validation of a recent mechanism that showed very close agreement with the experimental data; (2) experimental determination and computational calculation of the counterflow ignition temperatures and laminar flame speeds of several C2-C3 hydrocarbons, showing deficiencies in literature mechanisms; (3) computational simulation of the ignition of an nonpremixed hydrogen/air mixing layer with an embedded vortex, using detail chemistry, and a two-staged ignition process was observed.

TECHNICAL DISCUSSION

1. Ignition of Dimethyl Ether in Counterflow

Dimethyl Ether (DME), CH_3OCH_3 , is an attractive alternate fuel and fuel additive for diesel engines. The combination of its high cetane number and low boiling point of -25°C facilitates mixing, ignition, and cold start. The pyrolysis and oxidation process of DME have been studied mainly based on homogeneous systems, which has led to the development of two detailed mechanisms reported respectively in 1998 and 2003. However, their validity has not been experimentally scrutinized in nonhomogeneous systems, particularly at low temperatures relevant for ignition. In the present study the ignition temperatures of DME in nonpremixed counterflow were experimentally measured and subsequently used to evaluate the accuracy of these two mechanisms.

Specifically, the ignition temperatures of nitrogen-diluted DME by heated air in counterflow were experimentally determined for DME concentration from 5.9 to 30%, system pressure from 1.5 to 3.0 atmospheres, and pressure-weighted strain rate from 110 to 170s^{-1} . Figure 1 shows representative results for the ignition temperature as a function of DME mole fraction in nitrogen at 3atm and a pressure-weighted strain rate of 150s^{-1} . It is seen that the ignition temperature monotonically decreases with increasing fuel concentration in the fuel jet, and that such a dependence becomes stronger for lower fuel concentrations. Furthermore, while the 1998-mechanism substantially over-predicts the ignition temperature, the 2003-mechanism agrees very closely with the experimental data. This observation holds for all results obtained in the present study.

Sensitivity analysis was performed to identify the differences between these two mechanisms. Overall, the 1998-mechanism shows much reduced sensitivity to the low temperature oxidation sub-mechanism, while the 2003-mechanism shows that the majority of the

sensitivity comes from the low-temperature kinetics. For example, the 2003-mechanism exhibits a much stronger reactivity around 600K, as manifested by the turning point behavior (Fig. 2). On the contrary, the 1998-mechanism indicates the CH_3 radical concentration grows with the hot boundary temperature only gradually, which produces considerably less low temperature reactivity and therefore causes the ignition temperature to be 1039 K, which is about 100 K higher than that predicted by the 2003-mechanism. The reason that the low temperature kinetics contributes so much to ignition is that before the fuel enters the high-temperature ignition region around the hot-stream boundary, it is progressively heated from its low-temperature region.

The 2003-mechanism, consisting of 79 species and 398 elementary reactions, was then systematically simplified by using directed relation graph theory to a skeletal mechanism of 49 species and 251 elementary reactions, which in turn was further simplified by using computational singular perturbation and quasi-steady-state species assumption to a reduced mechanism consisting of 33 species and 28 lumped reactions. It was demonstrated that both the skeletal and reduced mechanisms mimic the performance of the detailed mechanism with high accuracy, as shown in Fig. 3.

This work is reported in Publication No. 5.

2. Counterflow Ignition Temperatures and Laminar Flame Speeds of C_2 - C_3 Hydrocarbons at Atmospheric and Elevated Pressures

While extensive kinetics data exist for hydrogen and methane, comparatively fewer data have been acquired for the hierarchically more complex C_2 and C_3 hydrocarbons, which are important fuels and intermediate constituents in the hydrocarbon combustion. Therefore, the primary objective of the present study is to acquire additional data on the nonpremixed counterflow ignition temperatures as well as the laminar flame speeds of most of the C_2 - C_3 hydrocarbons, namely acetylene (C_2H_2), ethylene (C_2H_4), ethane (C_2H_6), propylene (C_3H_6) and propane (C_3H_8). These data cover the regimes of high-temperature oxidation in flames and low- to intermediate-temperature oxidation relevant for ignition, in premixed as well as nonpremixed situations, and with substantial pressure variations. These data were then compared with those calculated by using an optimized mechanism for C_1 - C_3 (Z.W. Qin, V.V. Lissianski, H.X. Yang, W.C. Gardiner, S.G. Davis and H. Wang, *Proc. Combust. Inst.* 28, 1663-1669, 2000) and an ethylene ignition mechanism (B. Varatharajan and F.A. Williams, *J Propul. Power* 18, 344-351, 2002). These two mechanisms are referred to as the Q- and VW-mechanisms respectively.

Results (Figs. 4 and 5) show that, for all ignition cases, the Q-mechanism consistently predicts higher ignition temperature than the experiments, while the VW-mechanism agrees well with the experiments. On the other hand, the Q-mechanism agrees the laminar flame speed data moderately well. For acetylene and ethylene, the Q-mechanism slight over-predicts and under-predicts for the lean and rich mixtures, respectively as shown in Fig. 6 and 7. A possible source for the stronger reactivity of the Q-mechanism is that it was optimized against previous ethylene flame speed data based on linearly extrapolation, which yields higher laminar flame speeds. A fairly detailed exploration was conducted on the causes for the various disagreements between experiment and calculations.

This work is reported in Publication No. 6.

3. Nonpremixed Ignition of H_2 /Air in a Mixing Layer with a Vortex

Recent experimental studies on turbulent ignition have indicated the existence of optimal turbulent intensities and scales for ignition. To provide insight into turbulent ignition in general and optimize ignition in particular, nonpremixed ignition in an elemental structure of turbulent flows, namely the vortex, was computationally investigated for hydrogen/air in a mixing layer, with the fuel side being pure hydrogen at 300K, and the oxidize side being hot air at 2000K.

Figure 8 shows the maximum heat release rate for the mixing layers with and without (1D) the vortex. It is seen that, compared to the 1D case, the vortex case has higher heat release rates and an additional peak, hence signifying the presence of two-staged ignition. The first ignition occurs in a diffusion mode with chain branching reactions dominating. The second ignition takes place in the premixed mode, with more chemical reactions involved, and is substantially affected by the heat and species generated in the first ignition event. Results further show that the scalar dissipation rate is a crucial controlling factor for ignition, which causes a nonmonotonic dependence of ignition delay on all the vortex parameters.

This work is reported in Publication No. 7.

MAJOR PUBLICATIONS

- [1] "Ignition of premixed hydrogen/Air in heated counterflow," by X.L. Zheng, J.D. Blouch, D.L. Zhu, T.G. Kreutz and C.K. Law, *Proceedings of the Combustion Institute*, Vol. 29, pp. 1637-1644 (2003).
- [2] "A joint scalar PDF study of nonpremixed hydrogen ignition," by J.D. Blouch, J.Y. Chen and C.K. Law, *Combustion and Flame*, Vol. 135, pp. 209-225 (2003).
- [3] "Development of comprehensive detailed and reduced reaction mechanisms for combustion modeling," by C.K. Law, C.J. Sung, H. Wang and T. F. Lu, *AIAA Journal*, Vol.41, No. 9, pp. 1629-1646 (2003).
- [4] "Ignition of premixed hydrogen/air by heated counterflow under reduced and elevated pressures," by X.L. Zheng and C.K. Law, *Combustion and Flame*, Vol. 136, pp. 168-179 (2004).
- [5] "Experimental and computational study of nonpremixed ignition of dimethyl ether in counterflow," by X. L. Zheng, T. F. Lu, C.K. Law, and C. K. Westbrook, *Proceedings of the Combustion Institute*, Vol. 30, in press.
- [6] "Experimental determination of counterflow ignition temperatures and laminar flame speeds of C₂-C₃ hydrocarbons at atmospheric and elevated pressures," by G. Jomaas, X. L. Zheng, D. L. Zhu, and C. K. Law, *Proceedings of the Combustion Institute*, Vol. 30, in press.
- [7] "Nonpremixed ignition of H₂/Air in a mixing layer with a vortex," by X. L. Zheng, J. Yuan, and C. K. Law, *Proceedings of the Combustion Institute*, Vol. 30, in press.

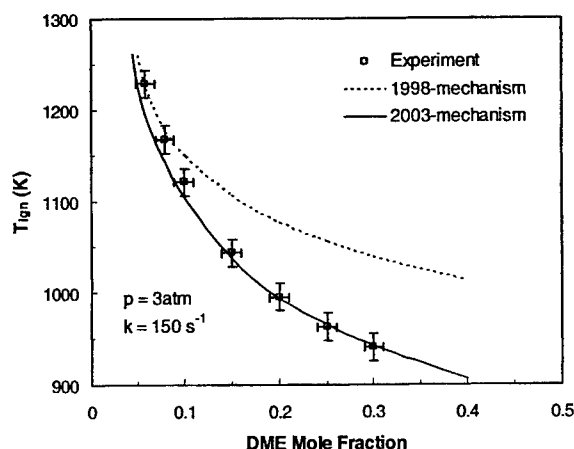


Figure 1. Effects of DME mole fraction on ignition temperature.

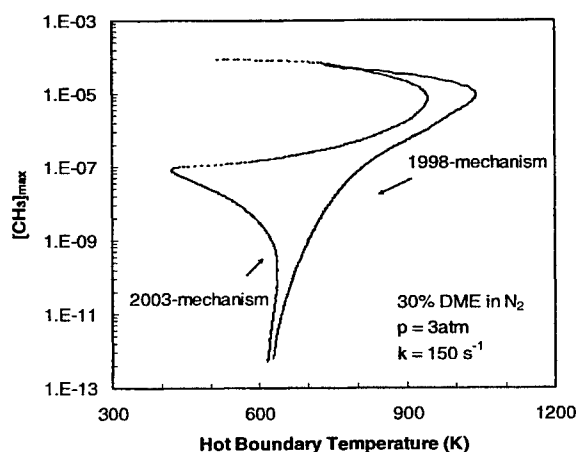


Figure 2. Calculated S-curves for 30% DME in N₂ mixture with 150 s⁻¹ strain rate at 3atm, using both mechanisms.

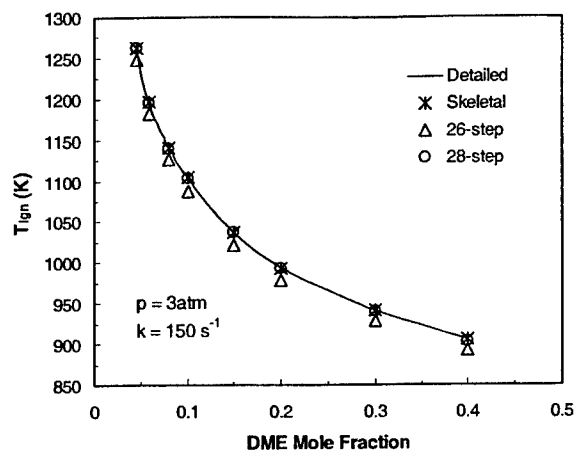


Figure 3. Comparison of the computed results using detailed, skeletal and reduced mechanisms for the ignition temperatures.

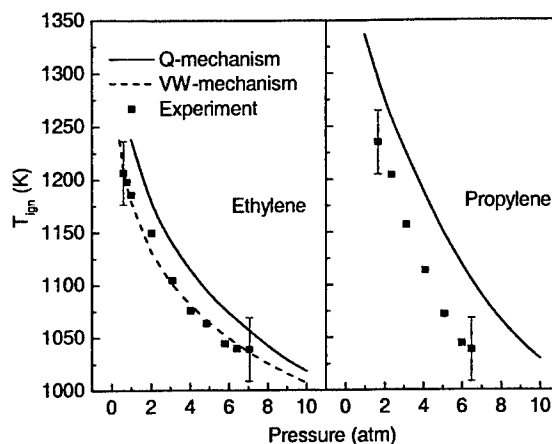


Figure 4. Effect of pressure on ignition temperatures for C_2H_4 and C_3H_6 . Conditions: 5.9% Fuel in N_2 and $k=150s^{-1}$.

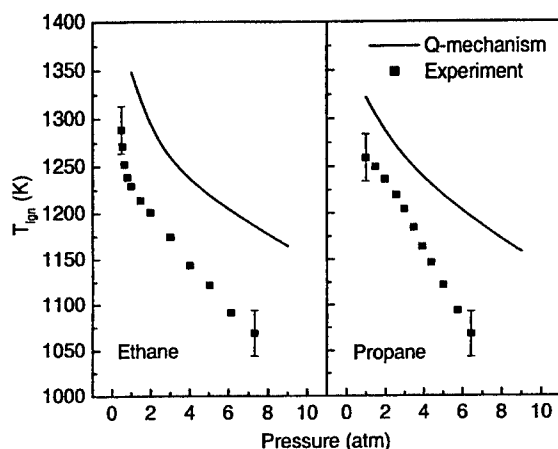


Figure 5. Effect of pressure on ignition temperatures for C_2H_6 and C_3H_8 . Conditions: 5.9% Fuel in N_2 and $k=150s^{-1}$.

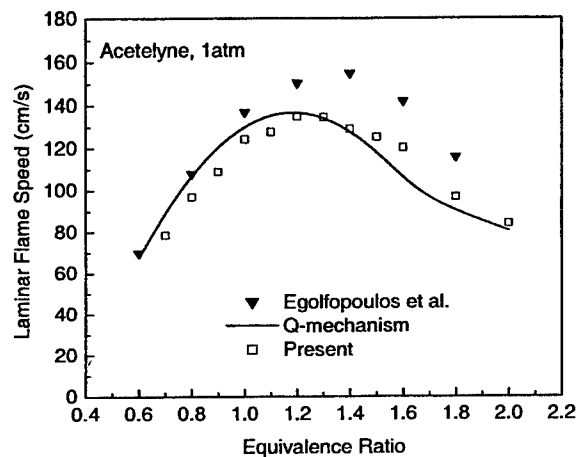


Figure 6. Laminar flame speed of acetylene (C_2H_2) in air at 1atm.

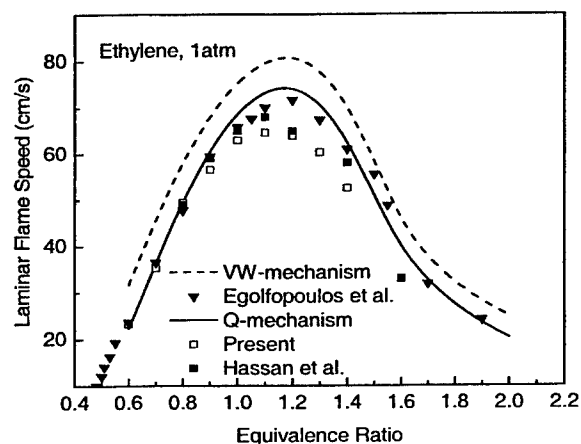


Figure 7. Laminar flame speed of ethylene (C_2H_4) in air at 1atm.

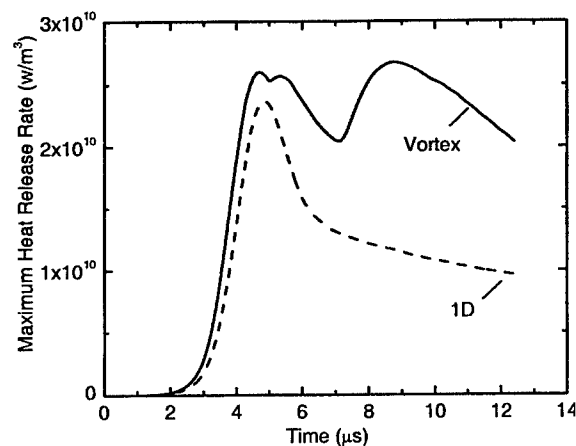


Figure 8. Time-dependent evolution history of the maximum heat release rate for ignition with and without (1D) vortex.

PHYSICAL AND CHEMICAL PROCESSES IN FLAMES

(AFOSR Grant No. F49620-01-1-0029)

Principle Investigator: Chung K. Law

Department of Mechanical and Aerospace Engineering
Princeton University, Princeton, NJ 08544

SUMMARY/OVERVIEW

The objectives of the present program are to develop detailed and simplified chemical kinetics models for hydrocarbon combustion, and to understand and quantify the dynamics of flames. During the reporting period progress were made in the following projects: (1) Further development of directed relation graph theory for skeletal reduction with linear-time algorithm, and its application to very large mechanisms such as that of heptane. (2) Integrated application of DRG, computational singular perturbation, and computation cost minimization towards developing fast algorithms. (3) Nonlinear analysis of pulsating instability of diffusion flames.

TECHNICAL DISCUSSION

1. Skeletal Mechanism Development Using Directed Relation Graph (DRG)

The method of directed relation graph (DRG), presented last year for the skeletal reduction of detailed reaction mechanisms, consists of three major steps, namely the construction of the graph, the graph searching, and the generation of candidate skeletal mechanisms. The previous effort embodied a linear-time algorithm in graph searching for the identification of major species. During the reporting period algorithms have been developed such that the steps involving graph construction and the generation of candidate skeletal mechanisms can also be conducted in linear time, being proportional to the number of species and reactions. Consequently the entire skeletal reduction can be carried out using linear-time algorithm.

To demonstrate the efficiency of the DRG method, a very large detailed mechanism, namely one for n-heptane oxidation consisting of 544 species and 2446 reactions, was reduced to skeletal mechanisms. The typical working conditions for the detailed mechanism were sampled from PSR and auto-ignition with equivalence ratio ranging from 0.5 to 1.5, and pressure ranging from 1 to 40 atms. The initial temperature range for auto-ignition was from 600K to 1800K, which covers the low-temperature NTC and moderately high-temperature ignition ranges. The number of data points sampled is larger than a thousand, which is sufficient to ensure the coverage of all the local behaviors in the parametric range. The entire reduction process, using the sample data points as input and outputting all the candidate skeletal mechanisms ordered with accuracy, takes only a few seconds. This is phenomenally shorter than the typical reduction times of months in previous works.

In the course of the study it was further recognized that because the number of species is very large in the detailed mechanism, the number of eliminated species by DRG is expected to be correspondingly large. Consequently, the properties of the retained species in the resulting skeletal mechanisms could be altered in a non-negligible manner, and as such it is likely that the resulting skeletal mechanism could be further reduced, by applying DRG again. This two-stage DRG reduction strategy has therefore also been applied to the reduction of the n-heptane mechanism.

Figure 1 shows dependence of the number of species retained in the skeletal mechanism on the assigned accuracy threshold value, ϵ , determined through the first stage reduction. It is seen that the reduction is most significant for small values of ϵ , which ensures high accuracy. In particular, a skeletal mechanism consisting of 260 species and 1097 reactions can be obtained with $\epsilon = 0.1$.

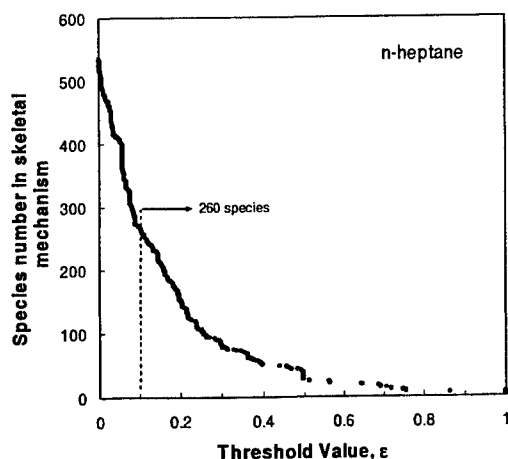


Figure 1. Dependence of the species number of the skeletal mechanisms on the threshold value ϵ , for detailed n-heptane oxidation mechanism.

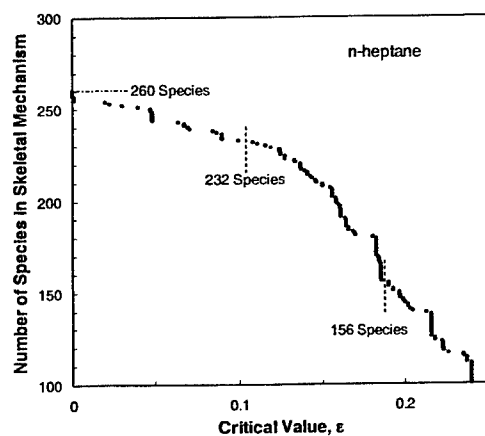


Figure 2. Dependence of the species number of the skeletal mechanisms in the second DRG reduction stage on the threshold value ϵ .

By applying the second stage reduction, Fig. 2 shows that skeletal mechanisms of 232 species and 902 reactions, and 156 species and 643 reactions can be obtained for $\epsilon = 0.1$ and 0.19 respectively, with the latter correspond to a state at which the species number exhibits a dramatic drop, indicating the release of a large group of coupled species.

The performance of the skeletal mechanisms obtained above was compared with those of the detailed mechanism for auto ignition with the same extensive parameter range of the reduction. Figure 3 shows that the 232 species skeletal mechanism agrees very well with the detailed mechanism in the entire parameter range including the NTC zone, while the 156 species skeletal mechanism shows only slight difference from the detailed mechanism for low or high temperature cases.

2. Integrated Algorithm of DRG, CSP, and CCM

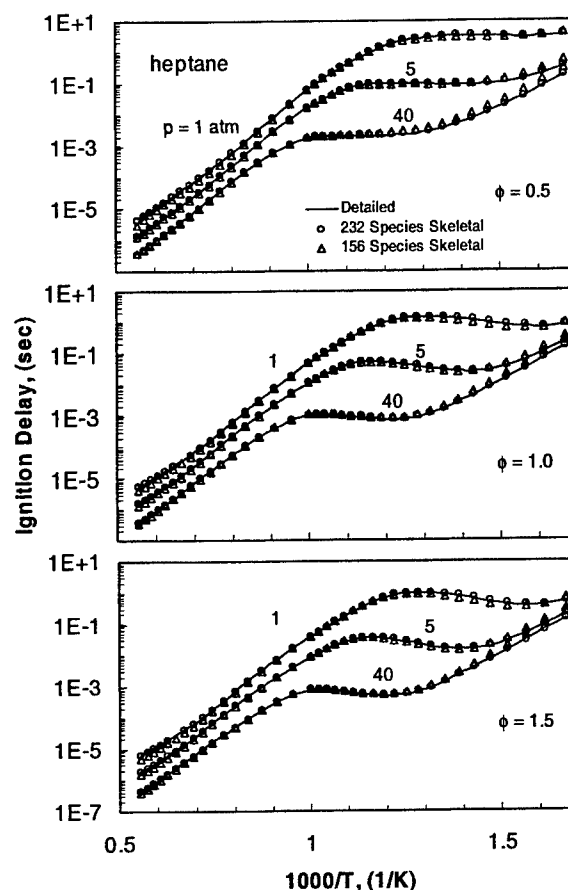


Figure 3. Comparison of calculated ignition delay of auto-ignition under constant pressure and constant enthalpy with detailed, 232 species, and 156 species skeletal mechanisms, for equivalence ratio from 0.5 to 1.5, pressure from 1 to 40 atms, and initial temperature from 600 to 1800K

The complete methodology toward facilitating computation of complex chemistry is now in place. Procedurally, the detailed mechanism is first simplified to the skeletal level using DRG. Next, computational singular perturbation (CSP) is applied to identify the quasi-steady state (QSS) species set. Finally, various strategies towards minimizing the computational cost (CCM), described in last year's report, is implemented such that a final algorithm can be generated with all the subroutines optimized for fast calculation.

Figure 4 shows the savings in the CPU time for a 33-species ethylene skeletal mechanism developed with DRG and optimized with CCM, as functions of the fraction of QSS species for different applications. It is seen that the time savings from using QSS assumptions is insignificant for both PSR and auto ignition, which implies that the computation of elementary rates dominates the CPU time in the simulation of these two applications. Significant time savings is observed for the premixed flame calculations, which implies that the CPU time for diffusive systems is a function of both the number of species and the number of reactions in the reduced mechanism. Further increasing the number of QSS species increases the simulation time because of the increased CPU time required for the internal algebraic loops. Furthermore, the accuracy of the QSS-reduced mechanisms decreases as the number of QSS species increases. Therefore an optimal size exists for the QSS-based reduced mechanisms for maximal CPU time saving and acceptable accuracy.

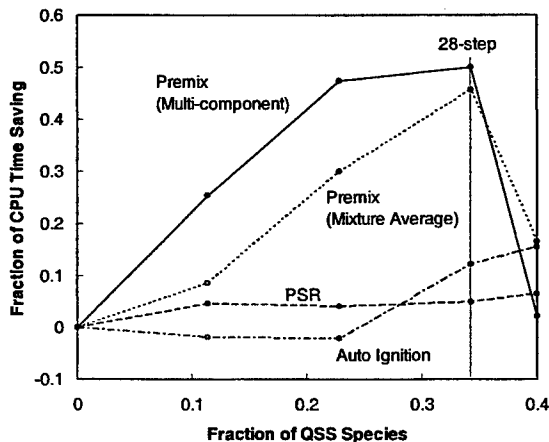


Figure 4. Comparison of CPU time savings with QSS-based reduced mechanism.

3. Nonlinear Analysis of Pulsating Instabilities of Diffusion Flames

Although extensive nonlinear analyses have been conducted for the instability of premixed flames, very few have been performed for diffusion flames. Recently Cheatham and Matalon performed a nonlinear analysis for the cellular instability of diffusion flames. This work is extended to pulsating instability of diffusion flames in the present investigation. It is to be noted that while linear stability analysis predicts the parametric boundaries for the onset of instability, nonlinear analysis is needed to describe the subsequent development. Furthermore, recent computational and experimental works, some of them performed by us, have shown a rich variety of flame responses.

The analysis employed the chambered flame configuration, with fuel and oxidizer Lewis numbers greater than unity in order to focus on pulsating instability. The Damkohler number D of interest is chosen to be very close to the critical Damkohler number D^* corresponding to the marginal stable state, namely $(D - D^*)/D^* \sim O(\varepsilon^2)$. Consequently, the transient flame oscillation behaviors exhibit weakly nonlinear characteristics. An evolution equation of perturbation amplitude was derived in order to study the nonlinear dynamics:

$$\frac{\partial A}{\partial \tau_2} + \alpha_1 A + \alpha_2 A|A|^2 = 0$$

where $\tau_2 = \varepsilon^2 t$ and $A(\tau_2)$ is the perturbation amplitude. The bifurcation analysis predicts three possible flame responses. Specifically, when $D < D^*$, the flame either extinguishes as the oscillation amplitude grows too large (Fig. 5a), or keeps oscillation in a limit cycle behavior (Fig.

5b). When $D > D^*$, the oscillation damps so that the flame is stable (Fig. 5c) unless a sufficiently large external perturbation is imposed (Fig. 5d). Thus, the pulsating instability of the diffusion flame is subcritical.

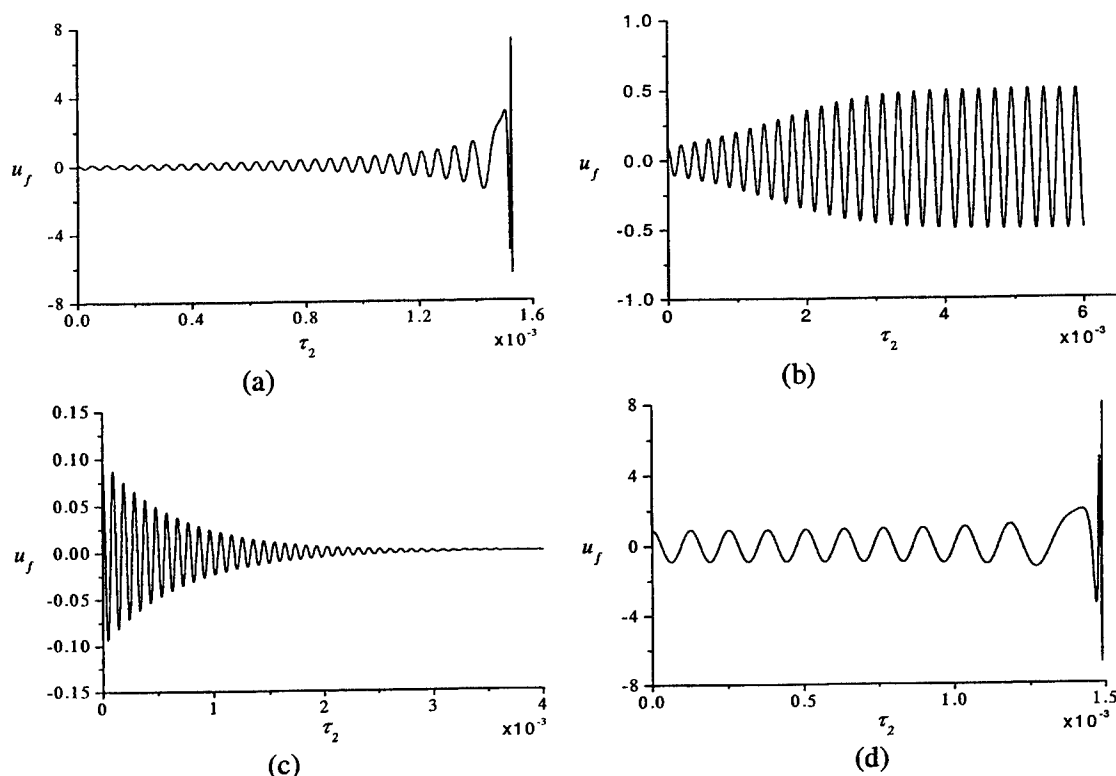


Figure 5 Long time behavior of the flame oscillations

MAJOR PUBLICATIONS

1. "Determination of laminar flame speeds of fuel blends using digital particle image velocimetry: ethylene, n-butane, and toluene mixtures," by T. Hirasawa, C.J. Sung, A. Joshi, H. Wang, and C.K. Law, *Proc. Combust. Inst.* Vol. 29, pp. 1427-1434 (2003).
2. "Outward propagation, burning velocities, and chemical effects of methane flames up to 60 atmospheres," *Proc. Combust. Inst.*, Vol. 29, pp. 1461-1470 (2003).
3. "Pulsating instability and extinction of stretched premixed flames," by E.W. Christiansen and C.K. Law, *Proc. Combust. Inst.*, Vol. 29, pp. 61-68 (2003).
4. "Oscillatory extinction of spherical diffusion flames," by S.W. Yoo, E.W. Christiansen, and C.K. Law, *Proc. Combust. Inst.*, Vol. 29, pp. 29-36 (2003).
5. "A computational study of oscillatory extinction of spherical diffusion flames," by E. W. Christiansen, S.D. Tse, and C.K. Law, *Combust. Flame*, Vol. 134, pp. 327-337 (2003).
6. "Development of comprehensive detailed and reduced reaction mechanisms for combustion modeling," by C.K. Law, C.J. Sung, H. Wang, and T.F. Lu, *AIAA J.*, Vol. 41, No. 9, pp. 1629-1646 (2003).
7. "A directed relation graph method for mechanism reduction," by T. F. Lu and C. K. Law, *Proceedings of the Combustion Institute*, Vol. 30, in press.
8. "Experimental determination of counterflow ignition temperatures and laminar flame speeds of C₂-C₃ hydrocarbons at atmospheric and elevated pressures," by G. Jomaas, X. L. Zheng, D. L. Zhu, and C. K. Law, *Proceedings of the Combustion Institute*, Vol. 30, in press.

DEVELOPMENT OF A COMPREHENSIVE AND PREDICTIVE REACTION MECHANISM OF LIQUID HYDROCARBON FUEL COMBUSTION

(Grant/Contract Number FA9550-04-1-0008)

Principal Investigator:

Hai Wang

Department of Mechanical Engineering
University of Delaware, Newark, DE 19716

SUMMARY/OVERVIEW:

The goal of this research program is to develop a comprehensive, predictive, and detailed kinetic model of hydrocarbon combustion for aeropropulsion simulations. During the reporting period progress has been made in a number of areas, including (1) the development of a predictive H_2/CO reaction model through multi-parameter optimization, (2) the development of a Monte Carlo code to determine the rate constants of unimolecular and chemically activated reactions of an arbitrary complexity, and (3) a theoretical kinetic study of the decomposition of ethylene oxide and the $C_2H_4 + O$ and benzene + O reactions. These projects represent the two key ingredients that are necessary for the success of the overall research program: (a) an accurate physico-chemical property database for combustion kinetics, and (b) a unified and optimized kinetic model for liquid aliphatic and aromatic fuel combustion.

TECHNICAL DISCUSSION:

1. Optimization of H_2/CO Combustion Chemistry

In this collaborative project (with Professor Fokion Egolfopoulos of USC), we propose a H_2 -CO kinetic model which incorporates the recent thermodynamic, kinetic, and species transport updates relevant to high-temperature H_2 and CO oxidation [1]. Attention has been placed on obtaining a comprehensive and kinetically accurate model able to predict a wide variety of H_2 -CO combustion data. The model was subject to systematic optimization and validation tests against reliable H_2 -CO combustion data, from global combustion properties (shock-tube ignition delays, laminar flame speeds, and extinction strain rates) to detailed species profiles during H_2 and CO oxidation in flow-reactor and in laminar premixed flames. Although some of the features of model optimization have been reported in the last contractors meeting, the model presented herein represents our final effort in this area. Validation tests now include the extinction stretch rates of ultra-lean H_2 -air flames, not considered previously [2]. The optimized model will be used as a kinetic foundation for future studies of aliphatics combustion mechanisms.

The unoptimized (trial) reaction model consists of 14 species and 30 reactions. The trial model was based on a careful review of recent kinetics literature, considering both direct data and compilations. The diffusion coefficients of key pairs have been updated, as reported in the last year's annual report. These updates are reported in [2]. A comprehensive review was conducted for a large number of H_2 -CO combustion data. Thirty-six experiments were chosen as optimization targets. The targets can be classified into four categories: (1) laminar flame speeds

of H₂-air, H₂-O₂-He, and H₂-CO-air mixtures, (2) the peak mole fractions of H and O in a low-pressure burner-stabilized H₂-O₂-Ar flame, (3) the consumption rates of H₂ and CO during the reaction of H₂-O₂-N₂ and CO-O₂-H₂O-N₂ mixtures in a turbulent flow reactor, and (4) ignition delay times of H₂-O₂-Ar and H₂-CO-O₂-Ar mixtures behind reflected shock waves. Active parameters were identified through sensitivity analysis. The entire set of active parameters consists of 28 *A*-factors and third-body efficiency factors. Minimization was carried out on the objective function $L^2 = \sum_i [(\eta_{i,\text{expt}} - \eta_{i,\text{calc}})/\sigma_i]^2$ subject to the constraints that the active parameters were bound by the ranges of their respective uncertainties. Each target was individually weighted by their uncertainty.

Selected validation results of the optimized model are briefly discussed here. Fig. 1 presents experimental and computed laminar flame speeds of H₂-air and air-equivalent mixtures where N₂ was replaced by Ar or He. It is seen that the flame speeds predicted with the optimized model are in an excellent agreement with the experimental data. Figures 2 shows that the optimized model reproduces experimental H₂-CO-air laminar flame speeds. Fig. 3 shows a plot of experimental and computed ignition delay times for H₂-O₂-Ar mixtures behind reflected shock waves. Here the experimental shock-tube ignition delay data were fitted into $\tau (\mu\text{s}) = [\text{H}_2]^{-0.154} [\text{O}_2]^{0.693} [\text{Ar}]^{0.04} [6.77 \times 10^{-8} T^{0.252} e^{9234/T}]$ for non “run-away” data, i.e., those fall on the nearly linear portion of the curves of Fig. 3, where $[\]$ denotes concentration in mol/cm³. Figure 4 depicts species profiles for 4 selected H₂ oxidation experiments in a turbulent flow reactor. Similar results for moist CO oxidation are presented in Fig. 5, over an extended pressure range. The trial and optimized models were also tested against extinction strain rates of ultra-lean H₂-air mixtures [2].

The optimization procedure also allows us to probe the residual kinetic uncertainties. For example, we found that the rate coefficient of H+O₂=OH+O always stayed within 5% of the trial value for all optimization runs made, including the use of a smaller number of targets and/or a reduced dimensionality of active parameter space.

This work is reported in Refs. 1 and 2.

2. A Monte Carlo Master Equation Solver

The temperature and pressure dependence of the rate constants of chemically activated reactions is essential in combustion modeling. Many gas phase reactions proceed through the formation of ro-vibrationally excited adducts. The fate of the excited species is determined by several competing processes. Energy is transferred to and from the molecule as a consequence of inelastic collisions with the surrounding bath gas molecules. Between collisions, the molecule can undergo internal rearrangement or isomerization, decompose to form new products or simply dissociate back to the reactants. Much progress has been made in our understanding of collisional energy transfer and its influence on the temperature and pressure dependence of unimolecular and chemically activated reactions. Troe introduced a collision efficiency factor β_c , such that the rate constant at low pressure was related to the strong collision rate constant through $k_0 \equiv \beta_c k_0^{sc}$. The modified strong collision (MSC) approach thus allowed for weak collisions with the efficiency of energy transfer dependent on the nature of the bath gas. Though the modified strong collision model was intended for use only for single-channel unimolecular reactions, over the years this model has been widely used for multi-channel chemically activated reactions. The fundamental validity of this approach is certainly questionable. For this reason a Monte Carlo code was developed that can solve the master equation of collision energy transfer for unimolecular and chemically activated reactions of an arbitrary complexity. The code was fully validated and optimized. Comparisons with the MSC model were made. These comparisons show that the MSC model lead to large errors in rate constant calculations.

A second motivation for the development of the Monte Carlo code arises from our interest to tackle a fundamental kinetic problem not tackled previously, namely chemically activated reactions that involve spin-state crossing. A methodology is currently being developed and tested for these reactions, including those to be discussed in section 3.

This work is reported in Ref. 3.

3. Reactions on C_2H_4O and C_6H_6O Potential Energy Surfaces.

There are several motivations for this work. The reactions on the C_2H_4O and C_6H_6O potential energy surface involve multiple triplet and singlet spin-state crossings. These reactions are ideal for use as test cases of our Monte Carlo approach. The reactions on the C_6H_6O potential energy surface are critical to the fundamental kinetics of aromatics oxidation. The reaction model of aromatics is currently under development by our research group. The C_2H_4O reactions are important to an predictive ethylene oxide reaction model also under development. The latter effort was initiated following the request by the USAF Research Laboratory.

Quantum chemistry calculations at G3 and CASSCF levels of theory were carried out. The potential energy surfaces for both C_2H_4O and C_6H_6O are now complete, including all feasible spin-state crossing. Unique kinetic features resulting from spin-state crossing will be examined using the developed Monte Carlo code.

Parts of this work are reported in Ref. 4.

AFOSR SPONSORED PUBLICATIONS AND PRESENTATIONS:

1. Davis, S. G., Joshi, A. V., Wang, H., and Egolfopoulos, F., "An optimized kinetic model of H_2/CO combustion," *Proceedings of the Combustion Institute*, accepted, 2003.
2. Dong, Y., Holley, A.T., Andac, M.G., Egolfopoulos, F.N. Davis, S. G., and Middha, P., Wang, H. "Experimental and Numerical Studies of Extinction of Premixed Lean H_2 /Air Flames," 2004 Spring Technical Meeting of the Western States of the Combustion Institute, University of California at Davis, Davis, California, March , 2004, paper 04S-19 and submitted to *Combustion and Flame*, 2004.
3. Joshi, A. V., Wang, H., and Davis, S. G., "Multi-Channel Chemically Activated Reactions: Comparison of Troe's Weak Collision Model and Exact Solution of the Master Equation by Monte Carlo Method," 2004 Spring Technical Meeting of the Western States of the Combustion Institute, University of California at Davis, Davis, California, March 29&30, 2004, paper 04S-25.
4. Joshi, A. V., Davis, S. G., and Wang, H. "Ab-initio Study of the $C_6H_5O + H$ Reaction: Viability of the $CO + C_5H_6$ Channel," in *Chemical and Physical Processes in Combustion*, 2003 Fall Technical Meeting of the Eastern States Section of the Combustion Institute, Pennsylvania State University, University Park, Pennsylvania, October 26-29, 2003.
5. Davis, S. G., Mhadeshwar, A. B., Vlachos, D. G., and Wang, H. "A new approach to response surface development for detailed gas-phase and surface reaction kinetic model development and optimization," *International Journal of Chemical Kinetics* 36: 94-106 (2003).
6. Law, C. K., Sung, C. J., Wang, H., and Lu, T. F. "Development of comprehensive detailed and reduced reaction mechanisms for combustion modeling," *AIChE Journal* 41: 1629-1646 (2003).

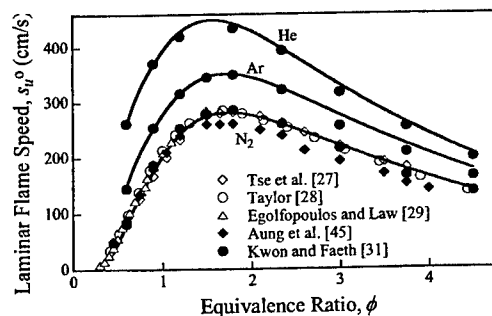


Figure 1. Experimental (symbols) [Tse, S. D., Zhu, D. L., and Law, C. K., *Proc. Combust. Inst.* 28, 1793-1800 (2000); Taylor, S. C., "Burning Velocity and the Influence of Flame Stretch," Ph.D. thesis, University of Leeds, 1991; Aung, K. T., Hassan, M. I., and Faeth, G. M., *Combust. Flame* 109, 1-24, (1997); Egolfopoulos, F. N. and Law, C. K., *Proc. Combust. Inst.* 23, 333-340 (1990); Kwon, O. C. and Faeth, G. M. *Combust. Flame* 124 590-610 (2001)] and computed (line) laminar flame speed of H₂-air and H₂-Ar- and He-substituted air mixtures at the atmospheric pressure.

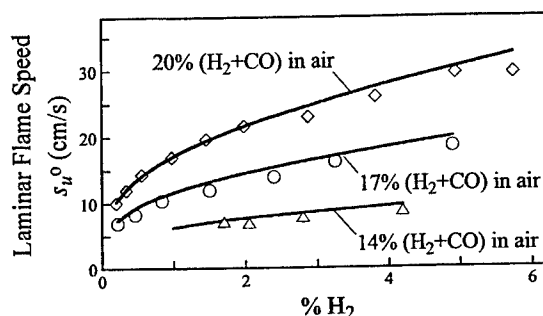


Figure 2. Experimental (symbols) [Vagelopoulos, C. M. and Egolfopoulos, F. N. *Proc. Combust. Inst.* 25, 1317-1323 (1994)] and computed (line) laminar flame speed of H₂-CO-air mixtures at the atmospheric pressure.

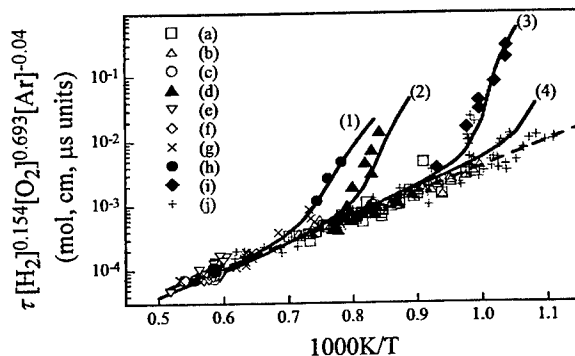


Figure 3. Experimental (symbols) and computed (lines) ignition delay times of H₂-O₂-Ar mixtures behind reflected shock waves. Symbols: (a) 6.67% H₂+3.33% O₂, $p_5=1.35-2.90$ atm; (b) 5% H₂+5% O₂, $p_5=1.35-2.90$ atm (onset of pressure rise, [R. K. Cheng, A. K. Oppenheim, *Combust. Flame* 58, (1984) 125-139]), (c) 0.5% H₂+0.25% O₂, $p_5=33$ atm, (d) 2% H₂+1% O₂, $p_5=33$ atm, (e) 0.5% H₂+0.25% O₂, $p_5=57$ atm, (f) 0.33% H₂+0.17% O₂, $p_5=64$ atm, (g) 0.1% H₂+0.05% O₂, $p_5=64$ atm, (h) 0.5% H₂+0.25% O₂, $p_5=87$ atm (maximum OH absorption rate, [E. L. Peterson, D. F. Davidson, M. Rohrig, R. K. Hanson, 20th Int. Symp. on Shock Waves, 1996, pp. 941-946]), (i) 8% H₂+2% O₂, $p_5=5$ atm (maximum OH emission) [G. B. Skinner, G. H. Ringrose, *J. Chem. Phys.* 42 (1965) 2190-2192], (j) four H₂+O₂ mixtures [A. Cohen, J. Larsen, Report BRL 1386, 1967]. Lines: (1) 0.5% H₂+0.25% O₂, $p_5=87$ atm (maximum [OH] rate), (2) 2% H₂+1% O₂, $p_5=33$ atm (maximum [OH] rate), (3) 8% H₂+2% O₂, $p_5=5$ atm (maximum [OH]), (4) 5% H₂+5% O₂, $p_5=2$ atm (maximum pressure gradient).

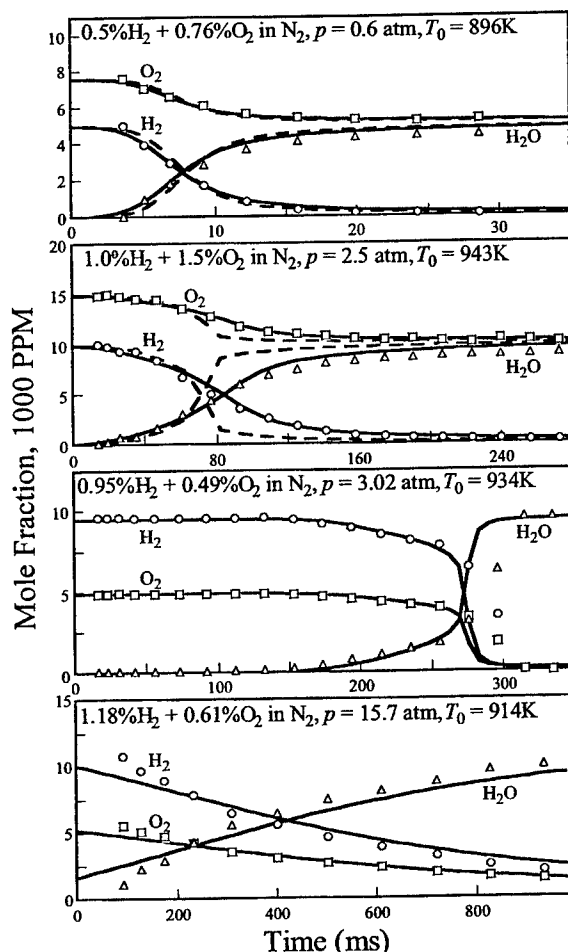


Figure 4. Experimental (symbols) [Mueller, M. A., Kim, T. J., Yetter, R. A., and Dryer, F. L. *Int. J. Chem. Kinet.* 31, 113-125 (1999)] and computed (lines) species mole fraction profiles during hydrogen oxidation in a flow reactor. Solid lines: optimized model; dashed lines: trial model.

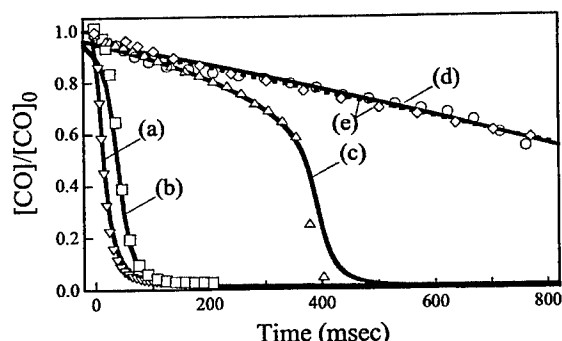


Figure 5. Experimental (symbols) [Kim, T. J., Yetter, R. A., Dryer, F. *Proc. Combust. Inst.* 25, 759-766 (1994)] and computed (lines) $[CO]/[CO]_0$ profiles during moist CO oxidation in a flow reactor. Cases: (a) 1.014% CO+0.517% O₂+0.65% H₂O in N₂, $p=1$ atm, $T_0=1038$ K, (b) 1.01% CO+0.496% O₂+0.65% H₂O in N₂, $p=2.44$ atm, $T_0=1038$ K, (c) 0.988% CO+0.494% O₂+0.65% H₂O in N₂, $p=3.46$ atm, $T_0=1038$ K, (d) 0.984% CO+0.497% O₂+0.65% H₂O in N₂, $p=6.5$ atm, $T_0=1040$ K, (e) 0.994% CO+1.47% O₂+0.65% H₂O in N₂, $p=9.6$ atm, $T_0=1039$ K.

EXPERIMENTAL AND DETAILED NUMERICAL STUDIES OF FUNDAMENTAL FLAME PROPERTIES OF GASEOUS AND LIQUID FUELS

(AFOSR Grant No. FA9550-04-1-0006)

Principal Investigator: Fokion N. Egolfopoulos

Department of Aerospace & Mechanical Engineering
University of Southern California
Los Angeles, California 90089-1453

SUMMARY/OVERVIEW

The main goal of this research is to provide archival experimental data and provide insight into the physical and chemical mechanisms that control various flame phenomena for a wide range of conditions. Fuel type, equivalence ratio, flame temperature, and combustion mode were the parameters considered. The experimental data are important for a number of reasons. First, they constitute a basis for *partially* validating the combustion chemistry of a large number of fuels ranging from hydrogen to gaseous and liquid hydrocarbons and alcohols. Second, they can be used in order to assess the effect of uncertainties of diffusion coefficients on the prediction of global flame properties. Finally, they can be used to assess whether prediction of laminar flame speeds is a sufficient condition to predict other high-temperature phenomena such as flame extinction. The results and findings of this program are of immediate interest to the design and performance of advanced air-breathing propulsion devices. During the reporting period, progress was made in the following: (1) Premixed flame extinction of lean and ultra-lean H_2 /air flames, (2) Premixed flame extinction of mixtures of liquid CH_3OH , C_2H_5OH , $n-C_7H_{16}$, and $iso-C_8H_{18}$ fuels with air, (3) Development of an alternative ignition methodology with which non-premixed and premixed ignition of H_2 , CO , and gaseous and liquid hydrocarbons was studied, and (4) Premixed flame ignition and extinction of mixtures of practical liquid JP-7, JP-8, JP-10, and RP-1 jet fuels with air. In all studies deficiencies of current state of the art chemical kinetics models were identified. The results of this work also suggest that uncertainties associated with the transport coefficients can have a notable effect on information derived for chemical kinetics in laminar flame studies. Finally, it was shown that predicting laminar flame speeds does *not* constitute a sufficient condition for predicting flame extinction conditions, a counterintuitive result.

TECHNICAL DISCUSSION

The studies include both experiments and detailed numerical simulations. The experiments are conducted in the opposed jet configuration that allows for the systematic determination of the fluid mechanics effects on flames and can be also modeled directly along its stagnation streamline. The experiments are performed in a variable pressure chamber. The reported measurements are performed at $p = 1 \text{ atm}$ through the use of a Digital Particle Image Velocimetry (DPIV) technique [1] and thermocouples. The numerical simulations include the

use of a CHEMKIN-based counterflow code [2]. Several chemical kinetics schemes have been tested. Furthermore, an updated molecular transport subroutine library developed under the AFOSR program of Professor Hai Wang (University of Delaware) [3] has been tested for H_2 /air flames.

1. Premixed Flame Extinction of Lean and Ultra-Lean H_2 /Air Mixtures

This is a collaborative effort with Professor Hai Wang, in which the oxidation kinetics of H_2 were tested for fuel-lean H_2 /air and $H_2/O_2/N_2$ mixtures. Under such conditions, the presence of thermo-diffusional instabilities does not allow for the determination of laminar flame speeds. Furthermore, the flame temperatures are well below those encountered in hydrocarbon flames, and such temperatures are of relevance to hydrocarbon ignition. The extinction strain rates, K_{ext} , were determined and used to validate the kinetics, as it is known that both extinction and propagation are controlled by similar chain mechanisms [e.g., 4]. Note that the presence of positive stretch suppresses the formation of cellular structures. Figure 1 depicts comparisons between the experimental and predicted K_{ext} 's by using the GRI30 [5] and Mueller et al. [6] ("MKYD99") H_2/O_2 mechanisms. It is of interest to note that the agreements are not satisfactory and that there is a difference in the "slope" of the results. Furthermore, it can be seen that while the predicted by the two mechanisms K_{ext} 's "merge" at high temperatures, they significantly deviate from each other at lower temperatures. The GRI30 mechanism appears to under-predict the K_{ext} 's by a factor of two (2) for the leaner fuel concentrations. At high temperatures, both mechanisms appear to over-predict the experimental K_{ext} 's by nearly 50%.

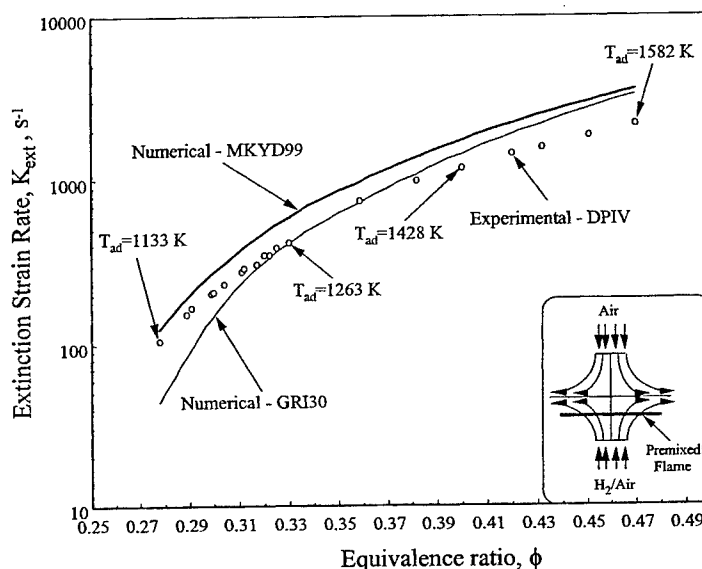


Fig. 1. K_{ext} for single H_2 /air flames

Through detailed sensitivity analysis, it was also shown that the K_{ext} 's of such mixtures are not only sensitive to the kinetics but also to the species diffusivities. Figure 2 depicts the logarithmic sensitivity coefficients of K_{ext} on the kinetics and mass diffusion coefficients for ultra-lean H_2 /air flames with $\phi = 0.289$ and $\phi = 0.314$. While the logarithmic sensitivity coefficients for kinetics are at most around the value of one (Fig. 2a), the corresponding ones for

diffusion (Fig. 2b) well exceed one and in particular for the H_2 species, values of the order of 10 to 30 are realized. Thus, a 5% uncertainty in diffusion coefficients could affect the predicted K_{ext} value by 25-30%, an uncertainty that could be casually attributed to kinetics. On the other hand, such flames are ideal candidates for assessing the validity of existing transport models.

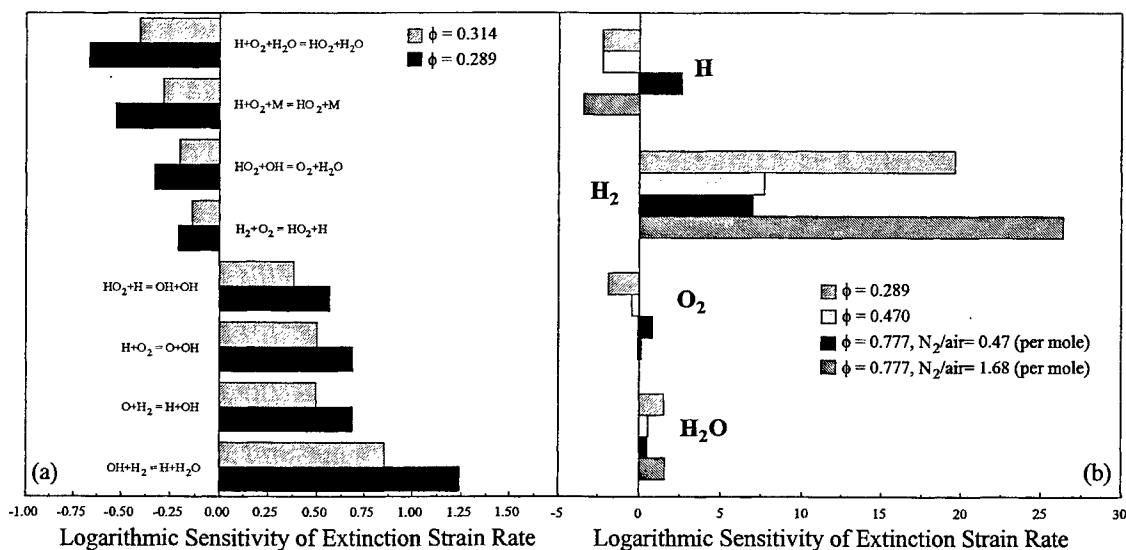


Fig. 2. Logarithmic sensitivity coefficients of K_{ext} on (a) reactions and (b) mass diffusion coefficients for ultra-lean and N_2 -diluted lean H_2 /air flames.

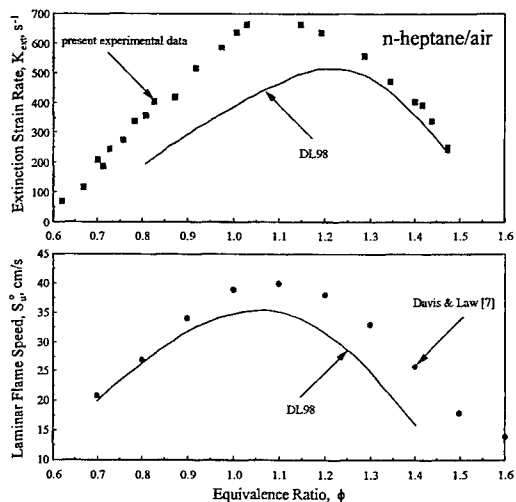


Fig. 3. K_{ext} and S_u^o for n-heptane/air flames

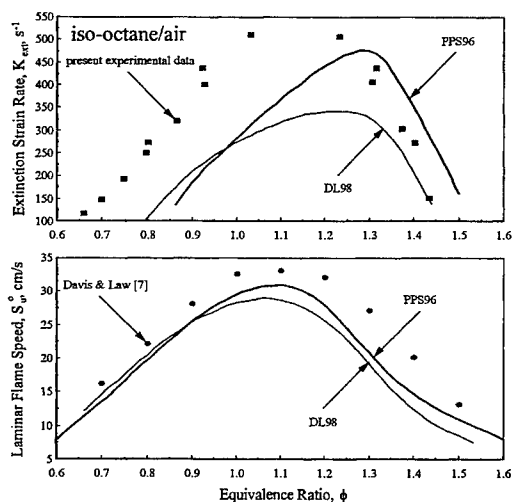


Fig. 4. K_{ext} and S_u^o for iso-octane/air flames

2. Premixed Flame Extinction of Mixtures of Liquid Fuels with Air

The extinction of mixtures of practical liquid fuels with air was also studied in the single flame configuration. The introduction of the liquid phase into the air under room temperature is achieved through the use of an evaporator and a high-precision liquid pump. The liquid is atomized into a stream of heated air and subsequently the temperature of the mixture is reduced to ambient. The liquid fuel exists in the vapor phase as long as its partial pressure is maintained below its vapor pressure at the prevailing ambient temperature. The liquid fuels that were tested are CH_3OH , C_2H_5OH , $n-C_7H_{16}$, and $iso-C_8H_{18}$.

Figures 3 and 4 depict the K_{ext} and S_u^o values for n-heptane/air and iso-octane/air mixtures. Those experiments were modeled using both the Davis & Law [7] mechanism (DL98) and Pitsch et al. [8] (PPS96) mechanisms. It is of interest to note that while both mechanisms predict closely S_u^o 's, they fail to predict the experimental K_{ext} 's, especially on the fuel-lean side where the experimental data are under-predicted by factors of the order of 2 to 3. Similar results were found for all liquid fuels studied.

3. Non-Premixed Ignition of H_2 , CO, and Hydrocarbons

A new methodology has been developed, allowing for ignition studies in the counterflow configuration. It includes the use of ultra-lean H_2 /air flames as ignition source, which eliminates the need for using heated air. The hot excess air dominates the composition of the post-flame products, while minor amounts of H_2O are present. In order to achieve a wide range of "ignition temperatures", from as low as 1,000 K to as high as 1,400 K, a platinum screen is used at the burner exit to catalytically support the H_2 /air flames. This also eliminates complications arising from the flame location, if the flame was stabilized by velocity gradients; these complications would pertain to data interpretation. Ignition of H_2 , CO, and various hydrocarbons was achieved and data were found to be in close agreement with those determined in past studies by Law and co-workers [e.g., 9], in which heated air was used as the ignition source.

4. Premixed Flame Ignition and Extinction of Mixtures of Practical Jet Fuels with Air

The ignition and extinction characteristics of mixtures of four practical jet fuels (JP-7, JP-8, JP-10, RP-1) with air were tested. The experiments were performed with unburned mixture temperatures around 110 °C, which is the capability of the existing liquid fuel system. At such temperatures, gaseous fuel-rich mixtures cannot be achieved. The mixture heating system is currently upgraded to allow for mixture temperature above the boiling points of these fuels. Preliminary results for fuel-lean mixtures show that JP-10 has better ignition characteristics while JP-7 appears to be the harder jet-fuel to ignite. As far as extinction under fuel-lean conditions, JP-7/air flames are less resistant to extinction while JP-10/air and RP-1/air flames are more resistant.

REFERENCES

1. Dong, Y., Vagelopoulos, C.M., Spedding, G.R. & Egolfopoulos, F.N. *Proc. Combust. Inst.* **29**, in press (2002).
2. Egolfopoulos, F.N. & Campbell, C.S., *J. Fluid Mech.* **318**, pp 1-29 (1996).
3. Dong, Y., Holley, A.T., Andac, M.G., Egolfopoulos, F.N., Davis, S.G., Middha, P., and Wang, H. "Premixed Extinction of H_2 /Air Flames: Chemical Kinetics and Diffusion Effects," submitted (2004).
4. Egolfopoulos, F.N. & Dimotakis, P.E., *Combust. Sci. Tech.* **162**, pp. 19-36, (2001).
5. G.P. Smith, D.M. Golden, M. Frenklach, N.W. Moriarty, B. Eiteneer, M. Goldenberg, C.T. Bowman, R.K. Hanson, S. Song, W.C. Gardiner, Jr., V. Lissianski & Z. Qin, GRI-Mech 3.0, http://www.me.berkeley.edu/gri_mech/ (2000).
6. Mueller, M.A., Kim, T.J., Yetter, R.A. & Dryer, F.L., *Int. J. Chem. Kin.* **31**, pp 113-119 (1999).
7. Davis, S.G. & Law, C.K., *Proc. Combust. Inst.* **27**: 521-527 (1998).
8. H. Pitsch, N. Peters, K. Seshadri, *Proc. Combust. Inst.* **26** (1996) 763-771.
9. C.G. Fotache, T.G. Kreutz, D.L. Zhu, C.K. Law, *Combust. Sci. Tech.* **109** (1995) 373-393.

THE LOW TEMPERATURE OXIDATION CHEMISTRY OF JP-8 AND ITS SURROGATES AT HIGH PRESSURE

Contract No. DAAD19-03-1-0070; 44458-EG

David L. Miller and Nicholas P. Cernansky

Department of Mechanical Engineering and Mechanics
Drexel University, Philadelphia, PA 19104

SUMMARY/OVERVIEW:

This is an experimental program to study of the ignition chemistry of JP-8 and its surrogates at high pressures. The purpose of this project is to map the effects of chemical variations on the oxidation behavior of JP-8, and to participate in the development of an acceptable surrogate that matches the general behavior of JP-8. In the JP-8 mapping and surrogate development effort, selected JP-8's, distillate fuels, and neat distillate fuel components will be examined to develop comparative kinetic and mechanistic information in the low and intermediate temperature ranges (600 – 1000 K) and at elevated pressures (up to 20 atm). Similarly, the various proposed JP-8 surrogates, components, and their mixtures will be examined as well. These single and multiple component fuels will be oxidized in a pressurized flow reactor and stable intermediate and product species will be identified and quantified using permanent gas analyzers, gas chromatography, gas chromatography with mass spectrometry (GC/MS), and on-line Fourier Transform Infrared Spectrometry (FT-IR) in order to provide key mechanistic information. The experimental results will be used to develop appropriate detailed and reduced kinetic models for the ignition and oxidation of these fuels. Ultimately, these low and intermediate temperature experimental and modeling results will be coupled with the efforts of other research groups to provide a comprehensive understanding of the oxidation and combustion behavior of JP-8 and its surrogates.

OVERVIEW OF RESEARCH PROGRAM:

“Average” JP-8 Reactivity

Due to the intentionally broad specification for JP-8, variations in cetane index, aromatic content, alkene content, sulfur content, API gravity, and additive content, namely the Fuel System Icing Inhibitor (FSII), are observed. However, the effect of these variations on the preignition oxidation process for JP-8 at conditions encountered in practical combustion devices is not well understood. In addition, if a “standard” chemical surrogate is to be developed, then the “average” combustion behavior of JP-8 must be determined. The composition and properties of JP-8 are very similar to civilian Jet-A and Jet A-1 fuel, and Jet-A has often been used as a substitute during the development of JP-8 surrogates. The fundamental difference between JP-8 and Jet-A is that JP-8 includes three additives: a lubricity improver/corrosion inhibitor, an anti-static additive, and a fuel system icing inhibitor (FSII). To elucidate the impact of JP-8

compositional variations and the differences between Jet-A and JP-8, several well-characterized samples of JP-8 and Jet-A from Wright-Patterson Air Force Base (WPAFB), one well-characterized sample of JP-7 from WPAFB, and one independently procured JP-8 sample from Phillips-66, were oxidized in Drexel University's Pressurized Flow Reactor (PFR).

During each experiment, a low and intermediate temperature reactivity map was generated using online CO/CO₂ gas analyzers. One major difference between the present work and previous flow reactor experiments is that a single volumetric fuel flow rate was used for all JP-8, Jet-A, and JP-7 fuel samples. This flow rate was determined by selecting one JP-8 sample and calibrating the flow rate of the fuel to the desired experimental settings, determined to be 1.050 ml/min. The fuel was metered into the flow reactor by an Isco high-pressure syringe pump, which has a flow rate accuracy of 0.5% and a resolution of 0.001 ml/min. The two motivating factors for this approach were that most aircraft do not compensate for the variations in the fuel and the empirical formula for JP-8 and Jet-A is not specifically known. The most commonly used empirical formula is C₁₁H₂₁, which was used during these experiments to determine approximate equivalence ratio, nitrogen dilution and other system parameters. During the oxidation of all fuel samples a clear negative temperature coefficient (NTC) behavior was observed at 8 atm, equivalence ratio of 0.3, nitrogen dilution of 80%, and residence time of 120 ms, Figure 1 and Figure 2. While the reactivity level of each sample was significantly different, with the JP-7 sample having the most reactivity, the temperature of peak reactivity, referred to as the start of the NTC regime, is nearly identical for all of the samples and occurred around 690 K despite the significant differences in composition. This confirms what previous work had suggested, that increasing the overall aromatic content of a fuel would tend to decrease reactivity, but not significantly affect the start of the NTC region.

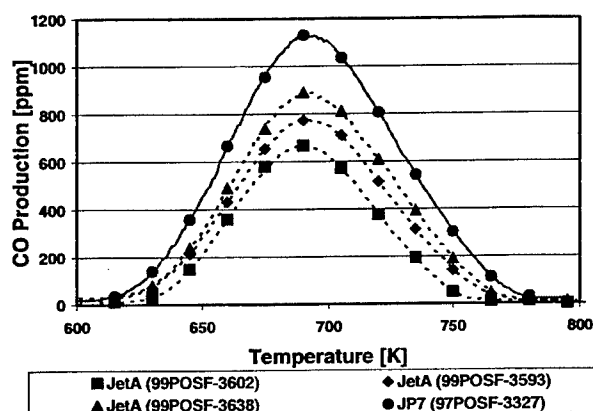


Figure 1: Reactivity maps of Jet-A and JP-7.

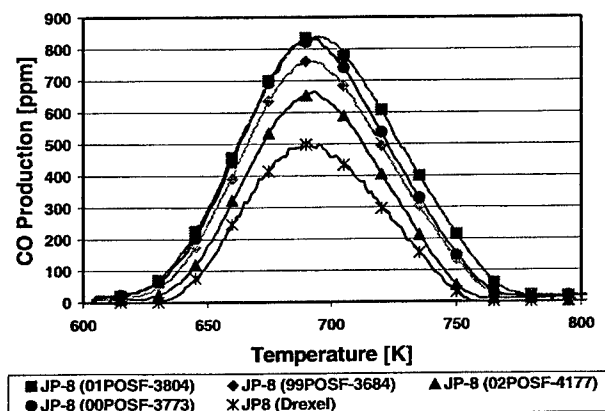


Figure 2: Reactivity Map of JP-8 Samples.

Comparison between the physical and chemical properties and the overall reactivity of the samples elucidated some interesting phenomena. First, due to the limited variation and low overall content of alkenes, < 2% vol, no impact of the alkenes were observed on the reactivity. Secondly, the API gravity of Jet-A is consistently lower for a given maximum CO concentration than for JP-8. Thirdly, the relationship between maximum CO production and aromatic content is nearly linear for the Jet-A and JP-7 samples. However, this same linear relationship is not apparent for the JP-8 samples. Specifically, two of the JP-8 samples, 01POSF-3804 and 02POSF-4177, deviate substantially from the behavior predicted by the Jet-A and other JP-8 samples. There is no readily apparent cause for the unexpected behavior of these samples. Both

JP-8 and Jet-A have considerable variation in sulfur content, yet the impact on the overall reactivity and the linearity of the aromatic/CO production relationships does not appear to be significant. However, additional investigation on the impact of sulfur, specifically sulfur oxides, on the oxidation process is necessary. Nevertheless, there does appear to be an "average" behavior at least in the domain of the low and intermediate temperature regime and using Jet-A in place of JP-8 for the development of surrogates is feasible so long as the composition of the Jet-A samples is near the average composition of JP-8. With respect to surrogate development, significant care should be taken when selecting either a Jet-A or JP-8 reference sample to ensure that the composition of the samples is representative of the average fuel composition, most notably aromatic content, otherwise significant tuning of the surrogate to a specific sample will occur. Of the samples provided by WPAFB, the Jet-A sample No. 99POSF-3593 and the JP-8 sample No. 99POSF-3684 appear to be the most "average" of the samples and will be utilized for comparisons to other surrogates.

Surrogate Studies

In an effort to begin the development of a "standard" surrogate for JP-8, preliminary studies of several surrogates proposed in publications have been conducted in the Pressurized Flow Reactor Facility. Utilizing the "average" JP-8 reactivity map previously identified, two surrogate mixtures developed at Drexel and one surrogate from Sarofim and coworkers at University of Utah have been investigated. Our previous work to develop a surrogate utilized the independently procured JP-8 sample from Phillips-66, however, this sample is considerably less reactive than the "average" behavior, Figure 2. Therefore, the previous five component surrogate (S9) was "tuned" to match the lower than average reactivity. This illustrates the dangers of utilizing only one sample of JP-8 or Jet-A. Of the developed surrogates, the mixture that matched the "average" JP-8 reactivity the closest was a four component mixture (S1) consisting of 43% n-dodecane, 27% iso-cetane, 15% methylcyclohexane, and 15% α -methyl-naphthalene, Figure 3.

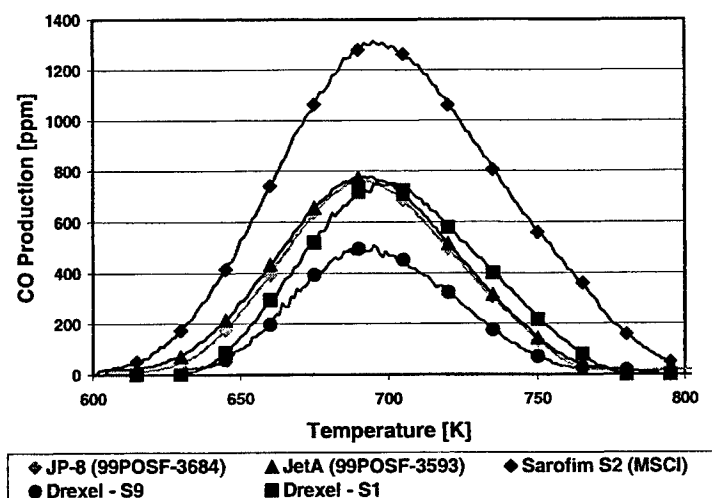


Figure 3: Surrogate comparison to "Average" JP-8 Reactivity Map.

Although the S1 surrogate reasonably matches the reactivity of JP-8, the peak of reactivity was shifted to a higher temperature by approximately 10 °C. The surrogate from Sarofim and coworkers was a mixture of 5% iso-octane, 5% methylcyclohexane, 20% toluene, 25% n-decane,

25% n-dodecane and 20% n-tetradecane¹. This surrogate was developed to simulate the volatility, sooting propensity, boiling-point curves, and compositional characteristics of JP-8. However, the reactivity mapping experiments are very sensitive to cetane number, thus, the Sarofim surrogate (CN \approx 62) is significantly more reactive than the JP-8 samples (CN \approx 42). During 2004, additional testing of other proposed surrogates will continue in an effort to identify a more standardized surrogate mixture.

Diesel Fuel Component Modeling Studies

Previously, using the CO reactivity mapping technique, the oxidation of neat and binary mixtures of n-dodecane, iso-cetane, methylcyclohexane, decalin, α -methylnaphthalene, and hexylbenzene was examined. Neat n-dodecane and decalin showed strong NTC behavior at the conditions examined, while decalin reacted over a very narrow temperature range. Conversely, methylcyclohexane did not oxidize at lean conditions, but it became unstable and explosive at richer conditions. The other pure hydrocarbons tested (the aromatics and iso-cetane) were resistant to ignition, and no reactivity was observed for the conditions tested. In an effort to expand kinetic and mechanistic information, a collaborative effort to model low and intermediate temperature reactivity of n-dodecane, iso-cetane, methylcyclohexane, α -methylnaphthalene and their binary mixtures has begun with Drs. Tiziano Faravelli and Eliseo Ranzi at Politecnico di Milano.

A semi-detailed kinetic scheme, developed in earlier works for hydrocarbons up to n-dodecane, was extended to include larger species. The scheme uses a lumped description of the primary propagation reactions and primary intermediates for the large species and then treats the successive reactions of smaller species with a detailed kinetic scheme. The lumped approach reduces the overall complexity of the resulting kinetic scheme both in terms of equivalent species and lumped or equivalent reactions. The 256 primary oxidation and propagation reactions of n-dodecane involve 72 new intermediate radicals and also 58 new intermediate components retaining the original n-C12 structure. A similar technique was utilized for iso-cetane (2,2,4,4,6,8,8-heptamethyl-nonane), methylcyclohexane, and α -methylnaphthalene. Figure 4 shows the predicted behavior of CO and CO₂ formation for two experimental conditions for n-dodecane, where ND1 was at $\phi=0.20$, $P = 8$ atm, and residence time = 120 ms and ND3 was at $\phi=0.30$, $P = 8$ atm, and residence time = 120 ms. The maximum CO formation at low temperatures corresponds to about 6% of the carbon input.

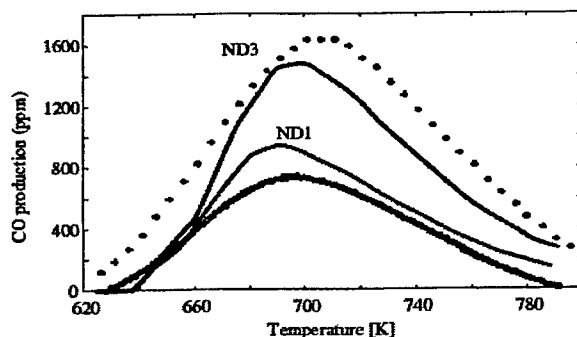


Figure 4: CO production vs. reactor temperature for two n-dodecane oxidation experiments
Comparison of experimental measures (points) vs. simulation results (lines).

¹ Violi, A., S. Yan, E. G. Eddings, A. F. Sarofim, S. Granata, T. Faravelli and E. Ranzi (2002). Experimental Formulation and Kinetic Model for JP-8 Surrogate Mixtures. Mediterranean Combustion Symposium, Sharm El Sheikh, Egypt

AUTOIGNITION AND COMBUSTION OF DIESEL AND JP-8

(Grant/Contract Number 45241-EG)

Principal Investigator: Dr. Kalyanasundaram Seshadri

Department of Mechanical and Aerospace Engineering
University of California at San Diego
La Jolla, California 92093

SUMMARY/OVERVIEW:

The objective of the research is to develop surrogate fuels that reproduce combustion characteristics of diesel and JP-8. Critical conditions of autoignition and extinction were measured for selected hydrocarbon fuels. These hydrocarbon fuels are considered to be possible components of surrogate fuels. The experimental part of the research was performed employing the counterflow configuration. Profiles of concentration of various species were measured in a nonpremixed toluene flame. An asymptotic analysis was carried out to predict autoignition in the counterflow configuration.

TECHNICAL DISCUSSION:

The Structure of Nonpremixed Toluene Flames

Toluene (C_7H_8) is considered to be a component of surrogate fuels for diesel and JP-8. An experimental and numerical study was performed to elucidate the structure and mechanisms of extinction and autoignition toluene flames in strained laminar flows under nonpremixed conditions. Experiments were conducted on flames stabilized between two counterflowing streams. The fuel-stream was a mixture of prevaporized toluene and nitrogen, and the oxidizer stream was air.

Concentration profiles of C_7H_8 , O_2 , N_2 , CO_2 , H_2O , CO , H_2 , benzene (C_6H_6), CH_4 , C_2 -hydrocarbons, C_3 -hydrocarbons, and C_4 -hydrocarbons, were measured. The measurements were made by removing gas samples from the reaction zone using a quartz microprobe and analyzing them in a gas chromatograph. A microprobe with an outer diameter of 180 microns and an inner diameter of 126 microns was employed. The inside of the probe was filled with glass fiber to filter out the soot. The gas chromatograph was equipped with a 4.5 ft molecular sieve (80/100 mesh) column and a 12 ft Porapak Q column. The molecular sieve column was used for separating H_2 , O_2 , Ar, N_2 , CH_4 , and CO . The Porapak Q column was used for separating all other species. Temperature programming and valve switching were employed to optimize the separation performance of both columns. The mole fractions of species in the gas mixture were determined using a thermo-conductivity-detector (TCD) and a flame-ionization-detector (FID). Figure 1 shows the mole fraction of C_7H_8 , O_2 , N_2 , CO_2 , H_2O , and CO as a function of distance. The points in Fig. 1 represent

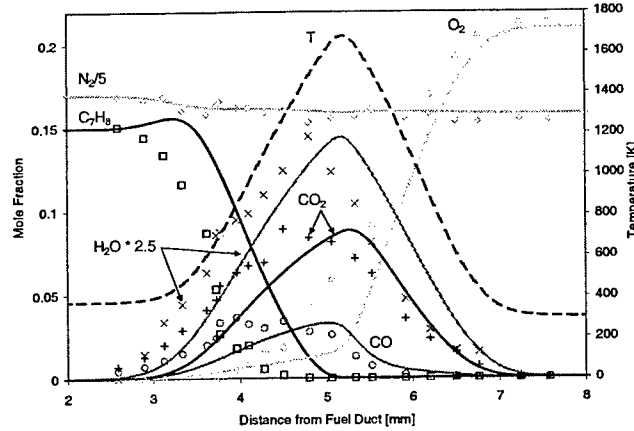


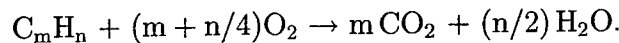
Figure 1: Experimental data showing the mole fraction of toluene (C_7H_8), O_2 , N_2 , CO_2 , H_2O , and CO as a function of distance. The points represent measurements and the lines are results of numerical calculations. The figure also shows numerically calculated temperature profile.

measurements and the lines are results of numerical calculations performed using a detailed chemical-kinetic mechanism.

The temperature profile was measured using an uncoated Pt-Pt13%Rh (Type R) thermocouple. The wire diameter was 60 microns and the bead diameter was 182 microns. The measurement was corrected for radiation by assuming spherical shape of the bead and a constant emissivity of 0.2. Catalytic effects were neglected. The numerically calculated temperature profile is shown in Fig. 1. The measured profile agreed well with the results of numerical calculations.

Asymptotic analysis of autoignition

An asymptotic analysis was carried out to describe autoignition in nonpremixed systems. Steady stagnation point laminar flow of an oxidizer toward a pool of liquid fuel was considered. A boundary layer was established over the surface of the liquid fuel. The chemical reaction between the fuel and oxygen is represented by the following one-step, irreversible process:



For diesel the proportion of the carbon and hydrogen is presumed to be $C_{14.7}H_{26.8}$, and for JP-8 it is presumed to be $C_{11}H_{21}$. The reaction rate, w , is given by

$$w = \rho^2 [Y_F Y_{O_2} / (W_F W_{O_2})] B \exp(-T_a/T). \quad (1)$$

Here Y_F and Y_{O_2} are mass fractions of fuel and oxygen, respectively, ρ is the density, T the temperature, B the frequency factor, and T_a the activation temperature. The activation energy, E , of the reaction was presumed to be large in comparison to the thermal energy. The asymptotic theory developed here makes available explicit formulas for predicting

Table 1: Activation temperature, T_a , Frequency factor B and activation energy E for one-step, irreversible reaction obtained from interpretation of experimental data using asymptotic analysis.

Fuel	T_a [K]	E [kJ/mol]	B [m ³ /(mol·s)]
<i>n</i> -hexadecane	1.191×10^4	99.01	1.259×10^5
<i>n</i> -dodecane	1.274×10^4	105.91	2.721×10^5
<i>n</i> -decane	1.305×10^4	108.51	3.855×10^5
<i>n</i> -octane	1.765×10^4	146.74	3.073×10^7
diesel	2.183×10^4	181.48	4.532×10^8
<i>n</i> -heptane	2.397×10^4	199.26	8.933×10^9
<i>o</i> -xylene	2.594×10^4	215.63	1.796×10^{10}
cyclohexane	2.676×10^4	222.49	1.680×10^{11}
JP-8	2.683×10^4	223.08	5.769×10^{10}
methylcyclohexane	2.713×10^4	225.53	1.136×10^{11}
<i>iso</i> -octane	2.880×10^4	239.41	4.093×10^{11}

autoignition. From these results a simple but reasonably accurate method was developed for deducing E and B . Experiments were conducted in a counterflow configuration. In this configuration an oxidizer stream made up of air and nitrogen flows toward a pool of liquid fuel. For a given injection velocity of the oxidizer stream, its temperature was increased until autoignition takes place. Fuels tested were *n*-heptane, *n*-octane, *iso*-octane, *n*-decane, *n*-dodecane, *n*-hexadecane, *o*-xylene, cyclohexane, methylcyclohexane, diesel, and JP-8. Figure 2 shows an arrhenius plot of $\ln G$ as a function of the reciprocal of the oxidizer stream temperature at autoignition, $T_{2,ign}^{-1}$. The quantity G depends on the strain rate. Overall activation energies were obtained from the slope of this plot and the frequency factor from the intercept. The overall rates are shown in Table 1.

Experimental studies on extinction

A new vaporizer was built to carry out experiments on multicomponent liquid fuels, for example diesel and JP-8. In this vaporizer liquid fuel is sprayed into a heated chamber where vaporization takes place. The fuel vapors are mixed with nitrogen and introduced into the counterflow burner. To test the performance of this new vaporizer extinction experiments were carried out. A flame was established between two counterflowing streams. One stream, called the fuel stream, was made up of prevaporized liquid fuel and nitrogen, and the other stream was air. The strain rate was increased until the flame extinguished. Figure 3 shows the strain rate at extinction as a function of the mass fraction of prevaporized liquid fuel in the fuel stream. Fuels tested are toluene, *n*-decane, *n*-heptane, and JP-8. The critical conditions of extinction obtained using the new vaporizer agreed well with previous experiments on toluene, *n*-decane, and *n*-heptane.

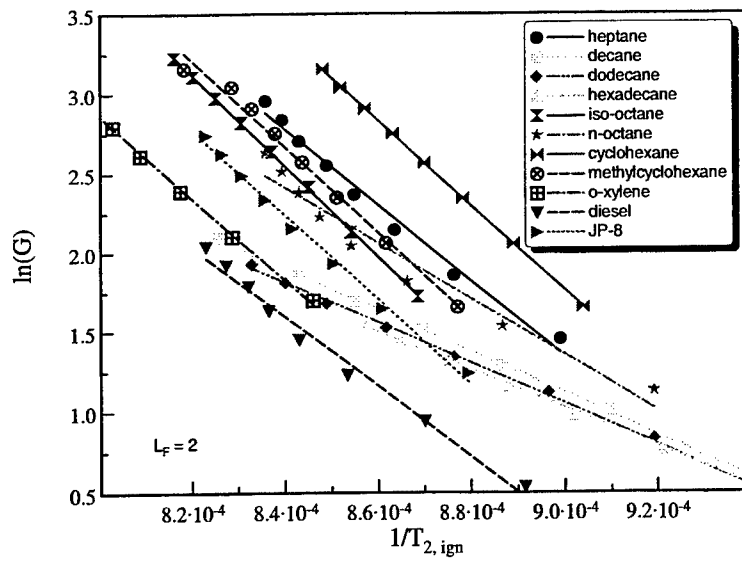


Figure 2: "Arrhenius" plot of $\ln G$ as a function of the reciprocal of the oxidizer stream temperature at autoignition, $T_{2,ign}^{-1}$.

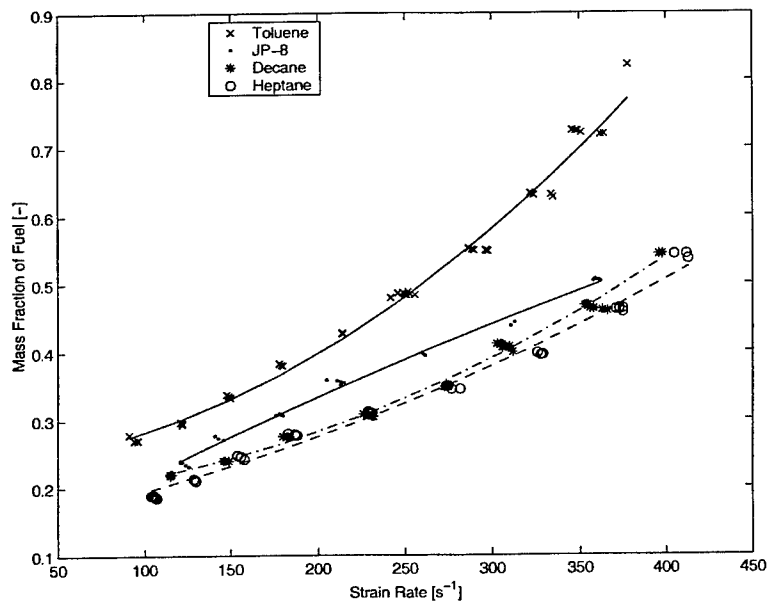


Figure 3: Experimental data showing the mass fraction of fuel in the fuel stream as a function of the strain rate, at extinction. The symbols represent measurements. The lines are best fits to the experimental data.

EXPERIMENTAL AND COMPUTATIONAL CHARACTERIZATION OF COMBUSTION PHENOMENA

AFOSR Task No. 02PR01COR

Principal Investigator: James R. Gord

Air Force Research Laboratory
AFRL/PRTC Bldg 5
1950 Fifth St
Wright-Patterson AFB OH 45433-7251

SUMMARY/OVERVIEW

Propulsions systems represent a substantial fraction of the cost, weight, and complexity of Air Force aircraft, spacecraft, and other weapon-system platforms. The vast majority of these propulsion systems are powered through combustion of fuel; therefore, the detailed study of combustion has emerged as a highly relevant and important field of endeavor. Much of the work performed by today's combustion scientists and engineers is devoted to the tasks of improving propulsion-system performance while simultaneously reducing pollutant emissions. Increasing the affordability, maintainability, and reliability of these critical propulsion systems is a major driver of activity as well. This research effort is designed to forward the scientific investigation of combustion phenomena through an integrated program of fundamental combustion studies, both experimental and computational, supported by parallel efforts to develop, demonstrate, and apply advanced techniques in laser-based/optical diagnostics and modeling and simulation.

TECHNICAL DISCUSSION

While this AFOSR-funded program involves numerous ongoing investigations, just a few recent advances are described in this abstract. Many other ongoing activities have been reviewed during recent AFOSR/ARO Contractors Meetings and are not discussed at length here.

Simultaneous OH PLIF and LII for Visualization of Flame Structure and Soot Inception in Swirl-Stabilized Liquid-Spray Flames. Much of the fundamental knowledge concerning soot formation is derived from investigations of laminar diffusion flames, with only a limited number of studies focusing on unsteady effects. The importance of considering unsteadiness and fluid-flame interactions was demonstrated by Shaddix et al. [Combust. Flame 99:723-732] who found that a forced methane/air diffusion flame produced a four-fold increase in soot volume fraction as compared with a steady flame having the same mean fuel-flow velocity. The goal of the current work is to study soot formation in the highly dynamic environment of a swirl-stabilized JP-8-fueled model combustor, which is characterized by high shear stresses and turbulent intensities that result in vortex breakdown and large-scale unsteady motions. This goal is accomplished by simultaneous imaging of the soot volume fraction and hydroxyl-radical (OH) distribution using laser-induced incandescence (LII) and OH planar laser-induced fluorescence (PLIF), respectively. Mie scattering from large droplets, which appears in the OH images but does not preclude signal interpretation, is used to a limited extent as a spray diagnostic. As shown in Fig. 1, the experimental set-up includes an Nd:YAG for saturated LII at 532 nm and a narrowband dye laser for OH PLIF using the $Q_1(9)$ line in the 1-0 band of the A-X system.

The injector geometry and sample instantaneous OH-PLIF images for JP-8 and a non-aromatic liquid fuel are shown in Fig. 2 at an equivalence ratio (ϕ) of 0.8. Such images provide a clear indication of the intermittency within the primary flame zone and are useful for characterizing the statistical behavior in terms of probability density functions. It is found, for example, that large-scale structures play a key role in the soot formation process. Intermittent regions of rich premixed fuel and air develop between the primary flame layer and recirculation zone that serve as sites for soot inception. The rate of soot production is dependent upon the frequency and spatial extent of these regions, while the rate of soot oxidation is dependent upon the availability of oxygen and OH in primary zone and recirculation region. Hence, the overall soot volume fraction is highly sensitive to the dynamics of the injection process as well as to the local, unsteady equivalence ratio. The importance of the former is highlighted by differences in the vaporization and soot formation characteristics of JP-8 versus non-aromatic fuels, as shown in Figs. 2(b) and 2(c).

In studies of soot-mitigating additives, performed in collaboration with the Fuels Branch of ARFL, the simultaneous OH-PLIF and LII measurements were used to determine whether changes in soot production result from changes in the chemical or physical properties of the fuel. Figs. 3(a) and 3(b) demonstrate the ability of the current measurement system to track local equivalence ratio and soot production, respectively. Using a droplet-free region in the recirculation zone, the time- and spatially averaged OH-PLIF signal is plotted with respect to equivalence ratio and compared with an equilibrium calculation. This provides a calibration for JP-8 that can be used qualitatively to track changes in equivalence ratio. The data in Fig. 3(a) include corrections for the effects of collisional

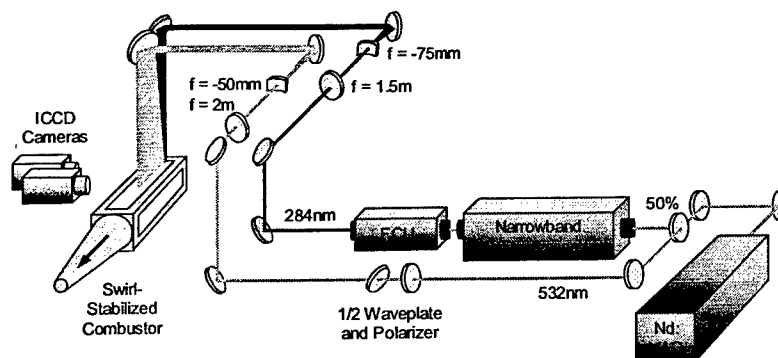


Fig. 1. Simultaneous OH PLIF and LII in atmospheric-pressure, swirl-stabilized, JP8-fueled, model gas-turbine combustor.

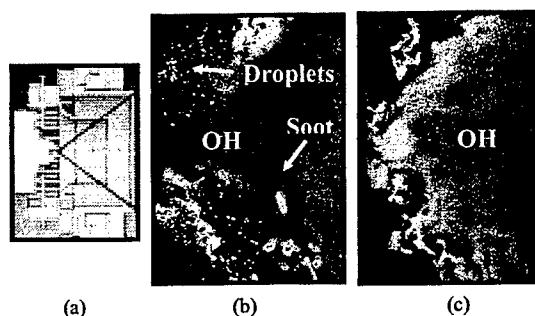


Fig. 2. (a) Dual-radial swirl cup with center-mounted pressure-swirl injector, (b) primary zone with JP-8 at $\phi = 0.8$, and (c) primary zone with non-aromatic fuel at $\phi = 0.8$.

Fig. 3(a) shows a plot of Equilibrium N_{OH} ($10^{22} m^{-3}$) versus Equivalence Ratio. The data points (OH PLIF) are fitted with a curve (Equilibrium OH). The data points show a peak around an equivalence ratio of 1.0. Fig. 3(b) shows a plot of Normalized Soot Volume Fraction versus Equivalence Ratio. The data points (LII with 50ns Gate, LII with 200ns Gate, and Sampling Probe) are compared. The Primary Zone is indicated by a shaded region, and the Exhaust is indicated by a dashed line.

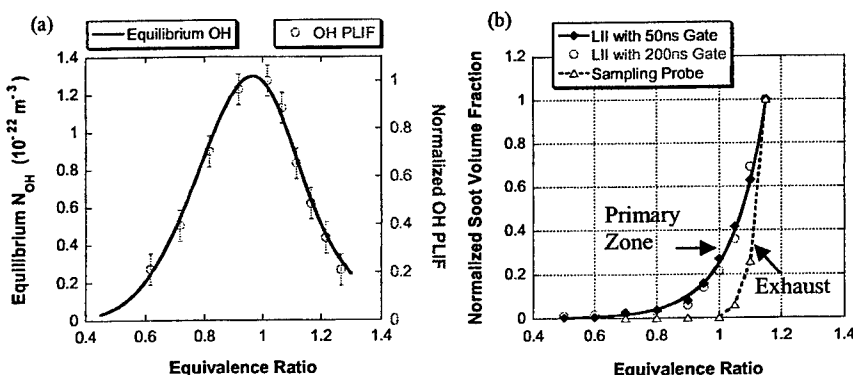


Fig. 3. (a) Fit of OH data in recirculation region with equilibrium calculations and (b) comparison of normalized soot volume fraction in primary zone with particle counts in the exhaust stream.

quenching and Boltzmann-fraction variations on the OH-PLIF signal. The LII data in Fig. 3(b) show an exponential increase of the soot volume fraction in the primary zone with respect to equivalence ratio. A subsequent test using an increased LII-gate period demonstrates minimal particle-size bias and measurement repeatability. Note that the exhaust-gas sampling probe displays a threshold effect at about $\phi = 1.0$, below which soot in the exhaust is effectively oxidized by OH and O_2 due to long residence times.

Since the dependence of soot on equivalence ratio is exponential, slight changes in equivalence ratio could easily be mistaken for changes in soot particle counts in the exhaust stream. This highlights the importance of tracking equivalence ratio while performing studies of soot-mitigating additives. An example is shown in Fig. 4 where methyl acetate is added to the fuel during a test. Note the large decrease in soot volume fraction during methyl-acetate addition, as measured by LII; this corresponds to a large decrease in particle counts from the sampling probe. Note also the increase in OH-PLIF signal that, according to the results of Fig. 3(a), indicates that the fuel mixture is becoming leaner. A certain ambiguity exists, however, because the final equivalence ratio could lie on either side of the peak OH signal. Using the exponential fit to the data in Fig. 3(b), however, the change in LII signal corresponds to an equivalence ratio that is slightly on the rich side of the OH peak. An overall equivalence-ratio decrease of 0.123 due to methyl-acetate addition is measured to within 1% for both the OH-PLIF and LII data, and to within 10% of flow calculations. The agreement between OH-PLIF and LII data indicates that methyl acetate in the current study did not have an effect on soot production, except for its effect on equivalence ratio. One can envision, therefore, the use of a combined LIF and LII system to track the performance of soot-mitigating additives without uncertainties in equivalence ratio.

Detection of Atomic Hydrogen in Reacting Flows Using Two-Color, Two-Photon Picosecond Laser-Induced Polarization Spectroscopy. Atomic hydrogen is an important species in hydrocarbon-based chemically reacting flows because of its high reactivity and diffusivity. In non-premixed flames interacting with vortices, the time evolution of the hydrogen atom closely follows that of heat release during the interaction and, therefore, will reveal information concerning the heat-release rate during the interaction process. Moreover, the hydrogen atom may play an important role in the formation of soot in hydrocarbon combustion. For example, in low-pressure diamond-synthesis environments, the hydrogen atom plays a significant role in determining the growth rate and quality of the diamond film. Therefore, the measurement of atomic-hydrogen concentration in flames is of fundamental importance in understanding relevant chemical and mass-transfer processes. In the current work, two-color, two-photon laser-induced polarization spectroscopy (LIPS) of atomic hydrogen using nearly transform-limited picosecond laser pulses is demonstrated. The use of short laser pulses (laser pulse width $\tau_L < \text{characteristic collision time } \tau_C$) significantly decreases the collision-rate dependence of the LIPS signal as compared to long laser pulses ($\tau_L > \tau_C$) interacting with atoms or molecules. The broadening of the spectral lines and the shift in transition frequencies with laser power is also investigated. This is, to our knowledge, the first reported two-color, two-photon LIPS experiment using

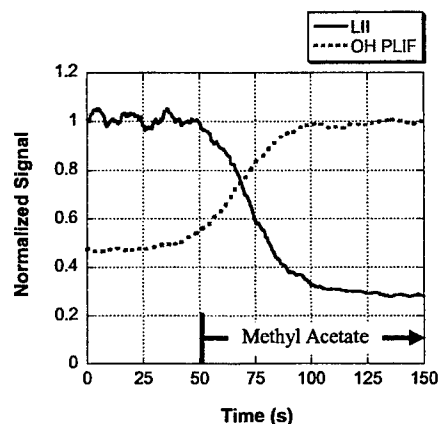


Fig. 4. Drop in soot due to methyl acetate addition corresponds to decrease in ϕ as verified by OH PLIF.

picosecond lasers for the detection of atomic hydrogen in reacting flows. The LIPS spectra of atomic hydrogen for pump beam energies of $\sim 13 \mu\text{J}$ and $\sim 30 \mu\text{J}$ are shown in Figure 6. The spectral line shapes shown in Fig. 5 were normalized to have maximum values of unity. Spectral broadening of the resonance line shape with laser power and the slight shift in transition frequency due to the ac Stark shift are evident in Fig. 5.

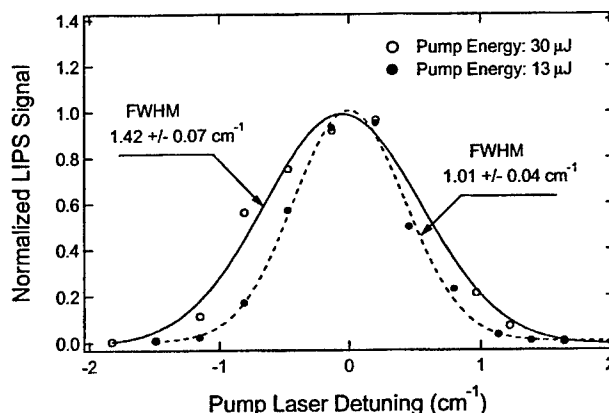


Fig. 5. LIPS spectrum of atomic hydrogen at two laser powers in a near-adiabatic hydrogen-air flame stabilized on a Hencken burner. The LIPS signal is normalized to have a maximum value of unity. The lines show Gaussian profiles fit through the experimental data points.

SELECTED RECENT PUBLICATIONS

- “Dual-Pump Dual-Broadband Coherent Anti-Stokes Raman Spectroscopy,” S. Roy, T. R. Meyer, R. P. Lucht, M. Afzelius, P.-E. Bengtsson, and J. R. Gord, accepted for publication in *Optics Letters*, 2004.
- “Simultaneous PLIF/PIV Investigation of Vortex-Induced Annular Extinction in H_2 -Air Counterflow Diffusion Flames,” T.R. Meyer, G.J. Fiechtner, S.P. Gogineni, C.D. Carter, and J.R. Gord, *Exp. Fluids* **36**, 259 (2004).
- “PIV/PLIF Investigation of Two-Phase Vortex-Flame Interactions: Effects of Vortex Size and Strength,” A. Lemaire, T.R. Meyer, K. Zähringer, J.R. Gord, and J.C. Rolon, *Exp. Fluids* **36**, 36 (2004).
- “Triple-Pump Coherent Anti-Stokes Raman Scattering (CARS): Temperature and Multiple-Species Concentration Measurements in Reacting Flows,” S. Roy, T. R. Meyer, M. S. Brown, V. N. Velur, R. P. Lucht, and J. R. Gord, *Opt. Comm.* **224**, 131 (2003).
- “Analysis of Transient-Grating Signals for Reacting-Flow Applications,” M. S. Brown, Y. Li, W. Roberts, and J. R. Gord, *Appl. Opt.* **42**, 566 (2003).
- “Lifetime Measurement and Calibration from Pressure-Sensitive Paint Luminescence Images,” T. F. Drouillard II, M. A. Linne, L. P. Goss, J. R. Gord, and G. J. Fiechtner, *Rev. Sci. Instrum.* **74**, 276 (2003).
- “Insights into Non-Adiabatic Flame Temperatures During Small-Scale-Vortex/Flame Interactions,” V. R. Katta, T. R. Meyer, J. R. Gord, and W. M. Roquemore, *Combust. Flame* **132**, 639 (2003).
- “Vortex-Induced Flame Extinction in Two-Phase Counterflow Diffusion Flames Using CH PLIF and PIV,” A. Lemaire, T. R. Meyer, K. Zähringer, J. C. Rolon, and J. R. Gord, *Appl. Opt.* **42**, 2063 (2003).
- “Dual-Pump Coherent Anti-Stokes Raman Scattering Temperature and CO_2 Concentration Measurements,” R. P. Lucht, V. N. Velur, C. D. Carter, K. D. Grinstead, J. R. Gord, P. M. Danehy, G. J. Fiechtner and R. L. Farrow, *AIAA J.* **41**, 679 (2003).

ADVANCED DIAGNOSTICS FOR REACTING FLOWS

AFOSR Grant F49620-04-1-0009

Principal Investigator: Ronald K. Hanson

Mechanical Engineering Department
Stanford University, Stanford, California 94305-3032

SUMMARY/OVERVIEW:

Recent advances in this program's research and development of non-intrusive diagnostics for air-breathing combustion applications are outlined below. Highlighted is progress on the use of toluene for fuel-air ratio PLIF measurements, temperature measurements using UV absorption of carbon dioxide, UV PLIF of carbon dioxide, IR PLIF of species with inaccessible electronic transitions, 2f wavelength-modulation techniques for temperature measurement, and wavelength-multiplexed extinction measurements for multiphase environments.

TECHNICAL DISCUSSION:

Fuel Tracer Photophysics for Quantitative PLIF Diagnostics

To facilitate the development and accurate use of quantitative PLIF diagnostics in a variety of applications, we quantify the absorption and fluorescence characteristics of tracers as a function of temperature, pressure (including bath gas), and excitation wavelength. Understanding the effects of these parameters on ketones has led to PLIF techniques that are widely used to spatially resolve temperature and concentration in applications ranging from fundamental fluid dynamics to mixing in propulsion engines. We have recently begun quantitative investigations of more realistic fuels and fuel surrogates. For example, toluene, an aromatic compound that comprises a significant fraction of gasoline and other fuels, has exhibited the potential for straightforward fuel-air ratio imaging. Like the ketones, toluene's attractive characteristics are easily recognized – a realistic fuel with accessible electronic transitions and strong red-shifted fluorescence signals that seem to be directly proportional to the local fuel-air ratio. However, realization of robust, quantitative diagnostic tools requires better fundamental understanding of the fluorescence behavior over a range of conditions.

Figure 1 exhibits measurements of toluene's relative fluorescence signal (per molecule) from 248 nm excitation as a function of the inverse oxygen number density (proportional to fuel-air ratio) at a total pressure of 1 bar. At 296 K, the signal is nearly linear over a wide range, indicating straightforward interpretation. As temperature increases, however, the overall signal levels decrease, the sensitivity to oxygen decreases, and systematic curvature may become important in certain situations. Mapping signal to fuel-air ratio is thus complex in non-isothermal flowfields. Preliminary studies suggest, however, that elevated total pressures and excitation using 266 nm may help simplify signal interpretation.

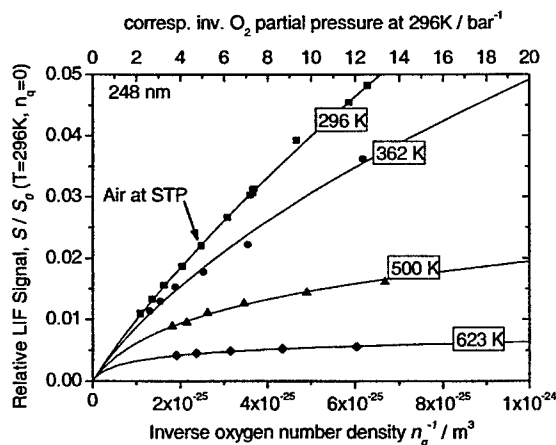


Figure 1. Relative toluene LIF signal (per molecule) from 248 nm excitation as a function of inverse oxygen concentration at several temperatures and 1 bar total pressure (diluted with nitrogen).

Temperature Measurements via UV Absorption of CO₂

At room temperature, CO₂ is transparent in the UV at wavelengths longer than 205nm; however, as discovered previously in this program, CO₂ absorption cross-sections become significant between 200nm and 320nm at temperatures above 1000K. Because CO₂ is a major product of hydrocarbon combustion and because the strength and the shape of the UV absorption spectrum vary strongly with temperature, CO₂ absorption offers the potential to infer gas temperature in combustion systems. During the past year, such temperature measurements have been demonstrated in five different applications. (1) Transmission measurements of cw laser light at 266nm have been used to determine time-resolved temperature in shock-heated CO₂, as illustrated in Fig. 2. The first 2 ms show the constant temperature and pressure expected after the reflected shock; this region comprises the normal test time for shock-heated chemistry experiments. The rise and fall of temperature and pressure in the region between 2 and 5 ms show the effects of shocks reflected from the contact surface. This time-resolved temperature diagnostic allows one to study reaction chemistry even when heat release alters the test gas temperature, thereby enabling an important extension of the normal shock tube operating envelope. (2) Similar transmission measurements have been used to infer temperature behind a detonation wave in a pulse-detonation engine using absorption from equilibrium concentrations

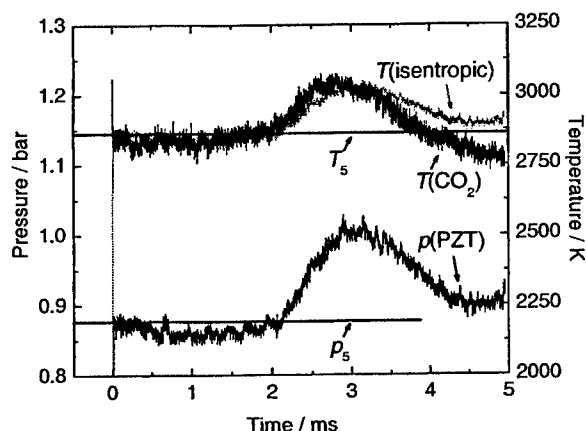


Figure 2. Time-resolved temperature and pressure measured in shock-heated mixture of 2% CO₂ in Ar. Time zero is the arrival of the reflected shock. The horizontal lines mark the T_5 and p_5 temperature and pressure expected from shock heating an ideal gas.

of the CO₂ combustion product. (3) The absorption of pulsed laser light near 226nm has been used to infer temperature in the burnt gases of a premixed high-pressure methane flame. (4) Absorption from a broad-band UV deuterium lamp has been detected with a kinetic spectrograph to measure temperature histories in a system with changing temperature and CO₂ mole fraction. (5) Time-gated, spectrally-resolved transmission of a deuterium lamp has been used to derive temperature at specific crank angles in a piston engine. These examples demonstrate that temperature measurements based on UV absorption of CO₂ are valuable in a wide variety of hydrocarbon combustion applications, especially for time-resolved measurements at high temperatures.

IR PLIF using Vibrational Transitions

Many molecules of interest for combustion (CO, CO₂, CH₄, C₂H₄, and higher hydrocarbons) do not have readily accessible electronic spectra making them unavailable for UV/visible PLIF measurements. Infrared PLIF, on the other hand, is possible using vibrational transitions if the molecule has an IR-active vibrational mode. IR PLIF differs from traditional UV/Vis PLIF because excited vibrational levels have much longer radiative lifetimes and smaller emission coefficients than excited electronic systems. In general the lifetime of molecules in the excited vibrational state is determined by multiple vibrational relaxation mechanisms. Therefore, detailed knowledge of vibrational energy transfer rates and processes is necessary for modeling of IR PLIF schemes and the quantitative interpretation of data.

Past work focused on CO and CO₂ IR PLIF. Currently, we are continuing the development of CO₂-based diagnostics for imaging combustion products and temperature. We are also working to extend the IR PLIF technique to new molecules and have begun the investigation of

diagnostics based on simple hydrocarbon fuels, CH_4 and C_2H_4 . Additionally we are working to capitalize on the simplicity of certain laser systems, such as TEA CO_2 lasers, to extend the capabilities of IR PLIF to harsh environments.

Carbon Dioxide (CO_2) UV PLIF

In applications involving UV excitation (190–320nm) of combustion species, hot CO_2 and H_2O can absorb both laser and fluorescent light. In the past year, we have identified the subsequent LIF spectrum from electronically excited CO_2 as a broad continuum (280–400nm) with a faint superimposed band structure. This signal increases linearly with pressure (from 10–60bar) and laser fluence and offers a unique opportunity for imaging CO_2 in high-pressure flames. Figure 3 shows the signal attenuation and CO_2 concentration in a 20 bar, laminar, flat flame (CH_4/air) with excitation wavelength at 239.34nm and 242.14nm. Excitation and detection wavelengths were chosen to minimize the contribution of nitric oxide (NO) and oxygen (O_2) LIF signals. Interference from O_2 LIF can be a serious problem due to the pervasive O_2 bands in this region and their subsequent overlap with the excitation wavelength. Spectrally-resolved point measurements were used to provide correction of oxygen interference. Further work is underway to enable single-shot CO_2 LIF imaging and to quantify the temperature and wavelength dependence of CO_2 fluorescence yield.

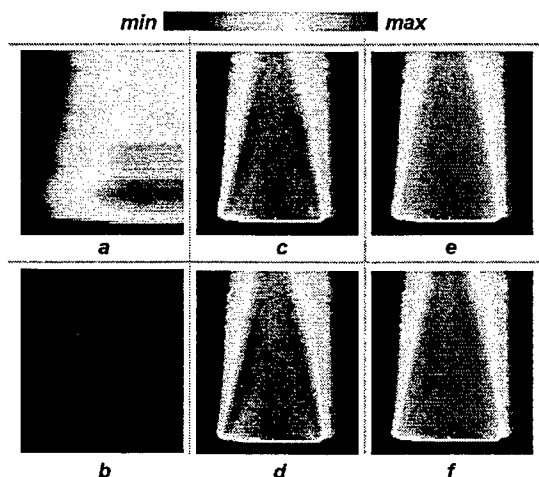


Figure 3. Visualization of CO_2 using UV PLIF. **a** total attenuation due to hot CO_2 and H_2O ; **b** O_2 contribution; **c** and **d** CO_2 and O_2 combined images at 239.34nm and 242.14nm, respectively; **e** and **f** final CO_2 images with O_2 correction at 239.34nm and 242.14nm, respectively.

Multiphase Diagnostics Based on Wavelength-Multiplexed Laser Extinction

In initial feasibility experiments, wavelength-multiplexed extinction diagnostics have shown high promise for near-real-time characterization of fuel sprays including fuel vapor concentration, temperature, and droplet size and density. Continuing studies of the relative magnitude of droplet extinction and vapor absorption for different fuels and droplet size ranges are underway to evaluate the performance and applicable domains of the diagnostic. New wavelengths over a broader spectral range (ranging from visible to 10 μm in the mid-infrared) have been incorporated, enhancing the droplet-sizing capability of this diagnostic. The multiplexed extinction diagnostic is being developed and applied in our aerosol shock tube for studies of shock wave interactions with fuel sprays. Such experiments have the potential to advance many aspects of liquid fuel combustion, including spray evaporation, droplet combustion, detonation of sprays, and combustion quenching.

2f Spectroscopy for Temperature Measurements in Combustion Flows

Wavelength modulation, in conjunction with second-harmonic (2f) detection, is well-known as a means to increase signal-to-noise ratios (SNR) in absorption spectroscopy, though to our knowledge past applications have been limited to atmospheric or reduced pressures. Current work at Stanford seeks to extend 2f methods for sensing temperature and species concentrations at elevated pressures with the objective of eliminating the limitation inherent in conventional scanned-wavelength direct absorption measurements, namely the difficulty in determining the zero-absorption baseline for laser intensity when spectral features become broadened and

overlap, as they do at high pressures. Our strategy is based on the fact that $2f$ spectroscopy is sensitive only to the shape of the broadened absorption features and does not require measurement of the zero-intensity baseline. Equally important, we have recognized that by forming the ratio of $2f$ signals from two different absorption features, most of the inherent complications of calibrating the $2f$ diagnostic are removed. A diagnostic based on these principles has been assembled and tested. Successful temperature measurements have been made with 15 kHz measurement bandwidth and precision better than 10 K, up to 20 atm and 1000K, limited only by the capabilities of our current static cell and oven. We believe that this new temperature sensor has very good potential for application in air-breathing propulsion, including gas turbine combustors and jet engine augmenters. The same sensor can be used to measure concentration from either of the two $2f$ signals, once the temperature has been inferred. We also expect that the advantage of this sensor for small absorption levels can be exploited to enable measurements at high temperatures where Boltzmann populations are small and direct-absorption signals become unacceptably weak.

AFOSR-SPONSORED PUBLICATIONS (2003-2004):

1. J.T.C. Liu, J.B. Jeffries and R.K. Hanson, "Large-Modulation-Depth $2f$ Spectroscopy with Diode Lasers for Rapid Temperature and Species Measurements in Gases with Blended and Broadened Spectra," *Appl. Opt.* submitted 2004.
2. W.G. Bessler, C. Schulz, T. Lee, J.B. Jeffries, and R.K. Hanson, "Strategies for Laser-Induced Fluorescence Detection of Nitric Oxide in High-Pressure Flames: II. A-X (0,1) Excitations," *Appl. Opt.* **42**, 2031-2042 (2003).
3. J.D. Koch and R.K. Hanson, "Temperature and Excitation Wavelength Dependences of 3-Pentanone Absorption and Fluorescence for PLIF Applications," *Appl. Phys. B*, **76**, 319-324 (2003).
4. S.T. Sanders, D.W. Mattison, J.B. Jeffries, and R.K. Hanson, "Time-of-flight Diode-laser Velocimetry using a Locally-seeded Atomic Absorber: Application in a Pulse Detonation Engine," *Shock Waves* **12**, 435-441 (2003).
5. W.G. Bessler, C. Schulz, T. Lee, J.B. Jeffries, and R.K. Hanson, "Strategies for Laser-Induced Fluorescence Detection of Nitric Oxide in High-Pressure Flames: III. Comparison of A-X Excitation Schemes," *Appl. Opt.* **42**, 4922-4936 (2003).
6. W.G. Bessler, C. Schulz, T. Lee, J.B. Jeffries, and R.K. Hanson, "Carbon Dioxide UV Laser-Induced Fluorescence in High-Pressure Flames," *Chem. Phys. Lett.* **375**, 344-349 (2003).
7. A. Ben-Yakar, M.G. Mungal, and R.K. Hanson, "Time Evolution of Coherent Structures and Mixing Characteristics of Hydrogen and Ethylene Jets in Supersonic Crossflow," *Phys. Fluids*, submitted 2003.
8. A. Ben-Yakar, M.G. Mungal, and R.K. Hanson, "The Effect of Velocity and Density Ratios on Transverse Jets in Supersonic Crossflows," *Phys. Fluids*, submitted 2003.
9. J.T.C. Liu, J.B. Jeffries, and R.K. Hanson, "Wavelength Modulation Absorption Spectroscopy with $2f$ Detection using Multiplexed Diode Lasers for Rapid Temperature Measurements in Gaseous Flows," *Appl. Phys. B* **78**, 503-511 (2004).
10. T. Rossmann, M.G. Mungal, and R.K. Hanson, "Nitric Oxide Planar Laser-induced Fluorescence applied to Low-pressure Hypersonic Flow Fields for the Imaging of Mixture Fraction," *Appl. Opt.* **42**, 6682-6695 (2003).
11. T. Rossmann, M.G. Mungal, and R.K. Hanson, "Mixing Efficiency Measurements using a Modified Cold-Chemistry Technique," *Experiments in Fluids*, submitted 2003.
12. J.B. Jeffries, C. Schulz, D.W. Mattison, M.A. Oelschlaeger, W.G. Bessler, T. Lee, D.F. Davidson, and R.K. Hanson, "UV Absorption of CO₂ for Temperature Diagnostics of Hydrocarbon Combustion Applications," *Proc. Comb. Inst.* **30**, in press.
13. W. Koban, J. Koch, V. Sick, N. Wermuth, R.K. Hanson, and C. Schulz, "Predicting LIF Signal Strength for Toluene and 3-Pentanone under Transient Temperature and Pressure Conditions," *Proc. Comb. Inst.* **30**, in press.
14. H. Li, R.K. Hanson, and J.B. Jeffries, "Diode Laser Induced Infrared Fluorescence of Water Vapor," *J. Meas. Sci.* in press.

TITLE: RAMJET RESEARCH

AFOSR TASK 2308BW

Principal Investigators: Campbell D. Carter
Mark R. Gruber

Aerospace Propulsion Division (PRA)
Propulsion Directorate
Air Force Research Laboratory
Wright-Patterson AFB OH 45433

SUMMARY/OVERVIEW

This research task includes work in three primary focus areas: (1) multiphase flows relevant to fuel injection into high-speed, oxidizing streams, (2) shock/boundary-layer interactions within the scramjet flowpath, and (3) multidisciplinary laser measurements for benchmarking modeling and simulation and for elucidating the physics of high-speed flows. Within each of these areas, there is a strong relevance to the scramjet propulsion system, and that relationship helps frame the context of our research. The motivation for this program is the need to develop the science basis to enable the design of high-speed, air-breathing propulsion systems. Lack of a science basis (and, in general, technology basis) is a limiting factor in design of scramjet vehicles. The approach will be to couple numerical computations and experimentation, to yield a thorough and fundamental understanding of each problem.

TECHNICAL DISCUSSION

Areas of focus in the past year have included the following:

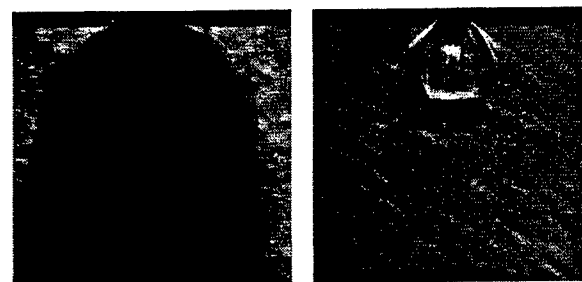
- 1) Study of fuel injection (in all its states, liquid, multi-phase—including plasma—supercritical, and gaseous) into a high-speed crossflow.
- 2) Investigation of cavity flameholding, particularly with regard to blow-out limits for different cavity configurations, fuels, fueling schemes, and cross-stream Mach numbers.
- 3) Study of shock/boundary-layer interactions within a model isolator.
- 4) Development/Application of laser diagnostic techniques for use in scramjet testing.

Note that four collaborations are ongoing or planned with AFOSR extramurally funded personnel: Profs. R. Hanson (Stanford, tunable diode laser absorption for scramjets), G. Faeth (U. Mich., fundamental aspects of liquid injection), M. Gundersen (USC, corona discharge ignition), and Y. Ju (Princeton, non-equilibrium discharges). Other university collaborators (and their respective contributions) include Profs. E. Gutmark (U. Cincinnati, advanced gaseous injector concepts), R. Pitz (Vanderbilt, NRC Summer Faculty, cavity flow-tagging velocimetry), J. Driscoll (U. Mich., URETI cavity flameholding), and J. Edwards (N.C.S.U., modeling of two-phase and supercritical injection). Two AFRL collaborations worth noting are those with Drs. J.T. Edwards (PRSF, supercritical fluids and injection) and S. Williams (VSBXI, ion chemistry and plasma-torch design). Drs. S. Lin, Taitech, and K.-Y. Hsu, Innovative Scientific Solutions, lead our in-house contractor efforts in studying fuel injection (both aerated fuel and the supercritical fuel) and cavity-flameholding/isolator research, respectively.

To study the plume formed by the aerated jet both holography (in the near field) and a phase-Doppler particle analysis (in the far field) have been performed as functions of gas loading, injector diameter, and liquid properties. The study using holography is a collaborative effort with Prof. G. Faeth and has included a series of measurements in a Mach-2 crossflow at WPAFB facilities. Here, two injection-seeded, Q-switched Nd:YAG lasers were used to create double-exposure images of the jet near its exit, for the purpose of measuring droplet/ligament size and velocity. The advantage that holography offers is that, in principle, the entire 3D spray volume can in principle be interrogated, on an instantaneous basis (though desired spatial resolution will ultimately limit the region of interrogation). The thickness of the liquid film is determined by the gas-liquid mass loading, physical properties of the fluids, and the length-to-diameter ratio of the injector tip (which drives differences in gas and liquid velocities within the injector). The initial structure of the issuing fuel plume depends on the film thickness and the velocity of both the liquid and gas flows. However, the penetration of the plume into the core flow is influenced by localized cross-stream properties such as the local boundary layer thickness and velocity profile, and the proximity of the free-stream shock system. One remarkable result of this work, and one that bears further investigation, is that primary drop sizes do not appear to be affected by any of the parameters considered in this study, including liquid/gas momentum flux ratio (or gas loading), liquid properties, or injector diameter.

Downstream in the Mach-2 flow, phase-Doppler particle analysis—an essential tool for determining a parameter of primary interest, the *volume-flux-weighted* SMD—shows that the atomization of the resulting spray is relatively complete at the axial location of $x/d_0 = 100$ (d_0 , the injector exit diameter, was 0.5 or 1 mm) and that the *flux-weighted* SMD is roughly constant at $10\text{ }\mu\text{m}$, regardless of aeration level (including no aeration); this result might be expected due to the strong aerodynamic forces acting on the spray. However, penetration with, say, 5% aeration level is significantly higher than with no aeration, and the area of the plume with drops diameters (SMD) of $\leq 20\text{ }\mu\text{m}$ is nearly twice as large (as that with no aeration) even at x/d_0 of 200. Measurements such as these are critical to understanding the resulting spray and to efforts at modeling these two-phase flows. In both cases (near and far fields), however, measurements are difficult due to the density of droplets. Indeed, a current challenge for the PDPA—even at x/d_0 values of 200 and beyond—is that the spray density leads to regions of the flow with significant data dropout, due, presumably, to multiple droplets within the probe region; one result is that the overall mass recovery ratio is poor (~ 20 to 30%), and droplet-diameter statistics may be biased. Currently efforts are underway to reduce the probe size and the likelihood that multiple droplets reside in the probe region.

Injection of a supercritical fluid into a superheated, low-pressure, high-speed crossflow—a problem relevant to much of the flight envelope—is vital to the scramjet, yet poorly understood. Extensive studies conducted in this laboratory have shown that the plume structure of supercritical fuel jets can be dramatically different from those of liquid or gaseous jets, due to the unique thermodynamic properties of the supercritical fluid and the occurrence of condensation phenomena. Typically, supercritical jets behave like ideal-gas jets when the injection temperatures are not too close to the critical temperature. A two-phase jet with a large quantity



P_{inj}/P_c	1.16	1.15
T_{inj}/T_c	1.03	1.23

Fig. 1 Shadowgraph images for methane/ethylene jets at various injection temperatures. $X_{CH_4}=0.1$ and $d=1.0\text{ mm}$.

of nucleated droplets, however, can be generated, presumably through the homogeneous nucleation processes, if the injection temperature is close to the critical temperature, as demonstrated in Fig. 1. Clearly, the liquid content within the jet indicates that a relatively long length/time will be needed for the injectant to reach the desired fuel/air mixing, and the issue of relevance to scramjet designer is what methodologies/techniques will be needed to efficiently and smoothly handle the continuously changing fuel state. Onset conditions for the condensation phenomena and the content and properties of the liquid phase within the injector are being studied—using mixtures with heavier components, such as $C_2H_4-SF_6$, instead of $C_2H_4-CH_4$, to simulate the presence of heavy hydrocarbons in the cracked fuel. These studies are being carried out in collaboration with Dr. J.T. Edwards (PRSF).

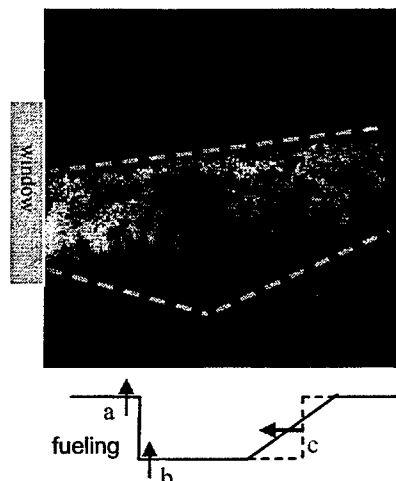


Fig. 2. Instantaneous spanwise image of OH distribution (half-span) with cavity flame in a Mach-2 crossflow. Potential fueling sites are indicated in the schematic above. The outline of the cavity is shown with red lines.

One key issue facing the design of a flameholder for hydrocarbon-fueled scramjets is the changing character of the flowfield that must be tolerated to ensure wide operability. Prior to ignition, the combustor flow is primarily supersonic. Assuming ignition takes place at a relatively low flight Mach number, the combustor operation is now dual-mode in character: a system of shock waves creates a distorted flowfield containing regions of both supersonic and subsonic flow (as well as separated boundary layer). As the vehicle accelerates, the shock-train weakens and the flowfield returns to mainly supersonic. Clearly, a robust flameholder must continually capture a small portion of the high-speed core flow, establish a stable combustible mixture, and hold the main-duct flame by providing a source of heat and radicals and to do all of this without excessive drag penalty. Local stoichiometry appears to vary widely in all three spatial dimensions and in time, regardless of the method for fueling the cavity (externally or internally). Some information on both the temporal and spatial behavior has been captured with OH planar laser-induce fluorescence measurements (Fig. 2, 19 mm from the leading edge). The spatial dependence of the mean flame location depends on fueling scheme, overall equivalence ratio (ϕ) within the cavity, and

Another related research topic is the investigation of the effects of ions, electrons, and their products on the reactivity of fuel-air mixture, especially when the fuel is a heavy hydrocarbon. Specifically, the goal of this task is to answer the question: how effective are ions and electrons in promoting ignition of heavy hydrocarbons. This topic relates to the efficacy of plasmas for scramjet ignition/ flameholding and is one aspect of our study of plasma ignition/flameholding (the other is in direct application of plasmas for ignition/flameholding in our scramjet tunnels). This effort is in collaboration with Dr. S. Williams and Prof. S. Sidhu (Univ. Dayton) and includes the development of detailed chemistry models (ones includes ions and electrons) for jet-fuel surrogates. In addition the change in ignition delay with the addition of the NO^+ ion (produced photolytically) has now been documented, and as predicted the effect is apparently small at $T \geq 1000$ K for $X_{NO^+} < 1000$ ppm. Ongoing efforts include the investigation of the influence of other species, such as atomic oxygen.

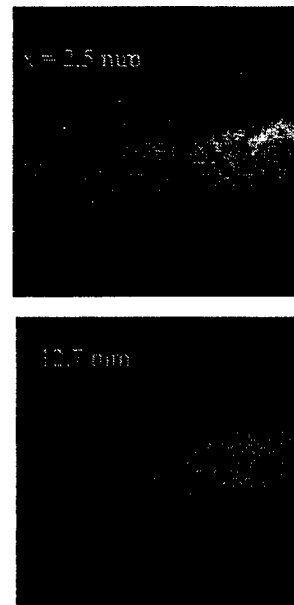


Fig. 3. NO PLIF showing mixing behavior of injection from location c.

coreflow conditions, particularly those that affect the shear layer. Our research shows that direct fueling via the cavity closeout face (ramp or rectangular), site c (Fig.2), allows for a broader range of cavity-flame operability (lean and rich blowout). It is clear from this research that some form of direct cavity fueling is desirable to improve lean and rich blowout characteristics. It is also interesting to note that while site b is also within the cavity, the resulting fuel jets tend to interact strongly with the shear layer, again making the cavity flame especially sensitive to shear-layer perturbations. Three observations are worth noting: 1) a cavity/core-flow shear layer flame is prominent, especially at intermediate fueling levels; 2) the upstream corner of the cavity flame appears important for flameholding; 3) at high fueling levels, most of the burning occurs at downstream locations (not in the upstream portion of the cavity). It is also worth noting that while the cavity is not a PSR, the fuel is reasonably well mixed near the leading edge of the cavity with close-out (c) injection, as is shown in Fig. 3 with single-shot NO PLIF. Indeed, the "patchy" flame apparently results from the locally rich mixture (and hence the presence of the shear-layer flame) in the central cavity span. One interesting aspect is that the use of a rectangular cavity—where acoustic forcing of the shear layer is stronger than with a ramped-cavity—does not adversely affect cavity stability in Mach-2 or 3 crossflows.

Regarding shock/boundary-layer effects on the isolator—that portion of the scramjet flow-path that "holds" the pre-combustion shock—efforts are underway to couple RANS-based CFD and measurements of the surface pressure using a recently developed high-speed (~1-kHz response time) Pressure-Sensitive Paint (PSP). The corner regions of low momentum flow in a rectangular duct increase the pressure loss, promote the flow separation—causing shock unsteadiness—and thus hurt isolator performance (potentially reducing shock-holding capability) while also impeding the simple characterization of the isolator flowfield. Thus, isolator performance can be improved by removing those corner regions (e.g., through modification of the isolator shape or by bleeding the boundary layer) in a rectangular duct, and this is a current research focus area. Pressure-field images clearly show the upstream propagation of the shock in the isolator corner region (as well as the extreme variability from shot to shot) and the improvement in performance with shape modification (though not as much as predicted). Two current challenges are in achieving adequate 1) characterization of the inflow boundary conditions and 2) predictive capability with the computations.

A particular focus of our effort has been on the development and application of advanced laser tools for the study of high-speed reacting flows. Examples of this effort are shown in some of the figures above, particularly with the application of PLIF, and as such this program element is described only in brief here. In general, these techniques are a principal means by which we address research topics. Clearly measurements shown in this proposal serve to illustrate the power of advanced imaging diagnostics to help interpret complex phenomena, such as flameholding. Particular focus areas in diagnostics have been in the development/application of 1) combined imaging methods, and 2) the iodine-filter techniques (filtered Rayleigh scattering and planar Doppler velocimetry). Particularly powerful are the combined imaging techniques of PLIF of a flamefront marker (such as OH or CH) and PIV. This combined technique allows study of many issues fundamental to flame stabilization and extinction, and though our applications have been in subsonic turbulent flame, the technique is suitable for high-speed flows. More recently, our group has sought means of employing tunable diode laser absorption spectroscopy, TDLAS, to a scramjet flowpath, in collaboration with Prof. R. Hanson and Dr. J. Jeffries. This joint effort to apply TDLAS for both test environments and flight vehicles will continue through our interaction with Stanford, and it is anticipated that advancements in the quality and accuracy of the absorption measurements will result. A particular point of emphasis will be the development of systems that can easily multiplex multiple beams—for multiple species—and that "pitch" and "catch" the diode-laser beams across multiple locations at once (or very rapidly).

ADVANCED IMAGING OF PREMIXED TURBULENT COMBUSTION PROCESSES

DAAD19-03-1-0251

Principal Investigator:

F. C. Gouldin

Mechanical and Aerospace Engineering
Cornell University, Ithaca, NY 14853

SUMMARY/OVERVIEW:

The goal of our current research is to exploit combined crossed-plane laser tomography (CPLT) and stereo particle image velocimetry (SPIV) in a systematic study of premixed turbulent combustion in a V-flame burner and a swirl burner. CPLT is used to image flamelets in two orthogonal, imaging planes and to measure the instantaneous spatial orientation of flamelets. SPIV is used to measure reactant velocity vectors in a vertical plane, $\underline{U}_r(x,y)$. These methods are combined to obtain a unique data base for V-flames and swirl stabilized flames that quantifies both flamelet wrinkling by turbulence (flamelet normal vectors, surface curvatures and surface density data) and velocities (reactant velocities, displacement speeds and velocity correlations at the flamelet surface). These data will quantify important measures of how turbulence distorts flamelets and will be of value in interpreting results from DNS and LES.

Introduction - Method and Quantities Measured

SPIV allows one to measure a 2-D distribution of the 3-D velocity field. For SPIV, two CCD cameras, mounted in a Scheimpflug configuration, are focused from different angles onto the same laser illumination plane. Each camera takes two exposures of laser light scattering from seed particles in the flow at two closely spaced points in time and the displacements of the seed particle images between exposures is used to determine particle and thereby gas velocities. A single camera can be used to obtain the in plane velocity components; images from a pair of cameras allow one to estimate also the out of plane velocity component.

In CPLT, images of seed particle scattering are taken simultaneously or near simultaneously from two intersecting, orthogonal laser sheets. The seed particles are micron sized silicone oil drops that evaporate on or near the 650 K isothermal surface [1]. In each image a curve marking the disappearance of the droplets and therefore the 650 K isotherm is identified. Tangent vectors to these curves projected onto the illumination planes are tangent vectors to the 650 K surface. Where this surface crosses the line of intersection between the two illumination planes, two tangent vectors can be determined and their cross product is normal to the 650 K surface at the instant the images are taken.

With combined SPIV and CPLT, one can obtain the distribution on a vertical plane of velocity in the reactants and 650 K surface normal vectors at the three points where this surface crosses the three horizontal lines of intersection between the tomography laser illumination planes and the SPIV laser illumination plane, Fig. 1. In addition, by staggering the pulse-timings of the tomography and the SPIV lasers by 1.5 milliseconds, displacement speeds of the 650 K surface in the laboratory frame and relative to the gas flow can be determined.

The data obtained from combined CPLT - SPIV measurements can be used in several different ways. Surface normal vector data can be used to find the flamelet surface density, an important modeling term. The PDF of the flamelet normal vector is a measure of the flamelet wrinkling by turbulence as is the PDF of flamelet curvature. Flamelet structure is perturbed by the turbulent flow field through imposed flow strain and curvature. The reactant field velocity data obtained with SPIV and CPLT can be used to estimate elements of imposed strain. Also of importance is the displacement speed on the cold side of the flamelet which is the relative velocity between the gas and the flamelet surface as marked by tomography.

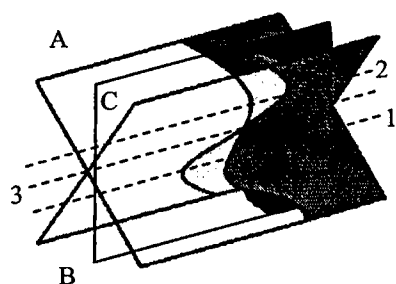


Figure 1. Schematic of combined CPLT-SPIV laser-sheet orientations. A and B are the perpendicular CPLT laser sheets and lie at 45° with respect to C, the vertical SPIV laser sheet. The sheets intersect forming three measurement lines: 1, 2, and 3. Flamelet normals and displacement speeds are measured along lines 1 and 2; normals are measured along 3.

Our goal is to apply combined CPLT-SPIV to obtain a large data set for a number of V-flames and for several swirl-stabilized turbulent flames. A swirl burner patterned on one developed by Robert Cheng at Lawrence Berkeley Laboratory has been built for this purpose. The imaging data will be analyzed for the quantities noted above. Our initial focus has been on the determination of displacement speeds and curvature from combined CPLT-SPIV. In this summary the data taken to date and work on displacement speed determination are outlined.

Results to Date

Data Taken: Data sets consisting of CPLT and SPIV images have been collected for 11 different V-flames. The flame parameters are listed in Table 1, and the locations of each flame on the regime diagram are shown in Figure 2. Each data realization consists of two tomography images and four SPIV images; for each flame condition images from approximately 2000 realizations have been obtained. Similar data sets for 5 swirl burner flames will be obtained soon.

Table 1. V-Flames Conditions

Flame #	l/l_f	u'/S_L^0	$U_0(m/s)$	ϕ	$M(mm)$
1	33.6	0.6	2	0.65	4.2
2	48	1.5	2	0.65	6
3	33.6	1.17	4	0.65	4.2
4	48	2.68	4	0.65	6
5	58.8	0.628	4	0.8	4.2
6	84	1.44	4	0.8	6
7	44.1	0.57	2.61	0.7	4.2
8	44.1	1.023	4.21	0.7	4.2
9	42	1	6	0.7	4.2
10	31.5	3.16	5.3	0.7	perforated plate
11	48	1.85	3	0.65	6

l/l_f is the ratio of the turbulence integral scale to the flame thickness; u'/S_L^0 is the turbulence intensity divided by the unstretched laminar flame speed; $U_0(m/s)$ is the mean reactant flow speed; ϕ is the equivalence ratio; and M is the mesh spacing of the turbulence generating grid.

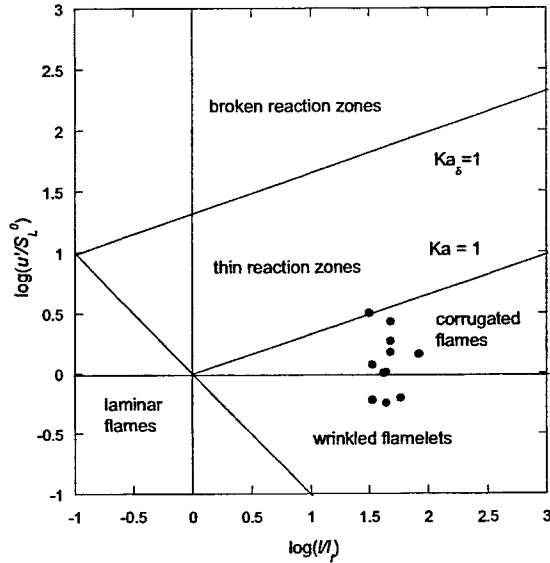


Figure 2. Regime diagram showing conditions of the 11 V-flames studied. Ka is the Karlovitz number based on l_f . Ka_δ is the Karlovitz number based on the high temperature reaction zone thickness, δ .

Flamelet Displacement Speed Measurements: For steady, unstretched premixed laminar flames, the mass flux across an isothermal surface is independent of the surface and when divided by the gas density at the surface yields the unstretched laminar burning velocity, S_L^0 . In a turbulent flame, the flow is unsteady; the flamelet is curved; and the local mass flux across isothermal surfaces varies in space and time. These variations are one measure

of flamelet distortion by turbulence. A related measure is the flamelet displacement speed, S_d , that we define here as the component of the instantaneous gas velocity relative to the flamelet and perpendicular to the instantaneous flamelet surface, as determined by crossed-plane tomography, the 650 K surface.

In combined CPLT and SPIV, \underline{N} is measured along three parallel measurement lines (see Figure 2) and $\underline{U}_r(x,y)$ is measured in a vertical plane. Along the measurement lines in the SPIV plane, \underline{N} , \underline{U}_r and displacement speeds are obtained. To determine displacement speed, data for the 650 K isotherm position along the two measurement lines in the SPIV plane are obtained in each of the tomography and SPIV camera images. The laser pulse timings of these images are staggered and the 650 K isotherm displacement speed along a measurement line in the laboratory reference frame is obtained by analyzing the stored images to determine the isotherm travel distance between the laser pulses. This distance is divided by the time between pulses, and the resulting speed is used along with the \underline{U}_r and \underline{N} data to estimate the normalized displacement speed, S_d/S_L^0 .

The technique has been used so far to measure S_d/S_L^0 in a lean, premixed, methane-air turbulent V-flame, flame 1 in Table 1. Flamelet normal data were also obtained. These latter data are consistent with previous CPLT studies of V and spark-ignition engine flames [2 - 5]. The measured probability density function of the flamelet normal is fit by a universal form characterized by a single fit parameter, ζ . ζ is the same on the three measurement lines, within experimental uncertainty.

Approximately 2000 realizations have been analyzed for the displacement speed and its PDF is shown in Figure 3 where it can be seen that the distribution of S_d/S_L^0 is peaked with a mean of approximately 1.7 ± 1 and broad ($-15 < S_d/S_L^0 < 20$) with a standard deviation of approximately 7.

The vertical error bars in the figure indicate statistical uncertainty and are proportional to $1/(n)^{1/2}$, where n is the number of samples in each histogram bin used to construct the distribution. The horizontal error bars are estimated by the rms error given in [5, 6] and the uncertainty analysis detailed in [7]. The experimental uncertainty estimates of the SPIV data are based on test results reported in [6]. The breadth of this distribution is explained in part by acceleration of the flow across the flamelet. For an unstretched laminar flamelet, continuity requires that S_d is approximately twice S_L^0 at 650K. Negative displacement speeds are not entirely unexpected. For example, they have been predicted to occur in highly strained opposed jet flames [8] and observed experimentally in double flames stabilized on an opposed jet burner [9]. In addition they have been seen in a DNS of the interaction of a flame with a counter-rotating vortex pair [10] and in a 2-D DNS of a turbulent methane-air flame [11]. The negative displacement speeds observed in the latter calculation are attributed to regions of high positive curvature and extensive tangential strain.

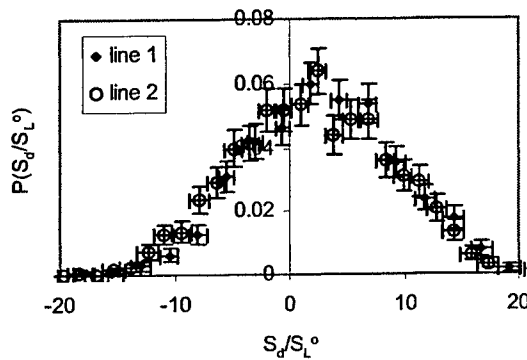


Figure 3. PDF of measured normalized displacement speeds obtained along the two measurement lines in the SPIV plane.

Summary

We have taken sets of combined CPLT-SPIV data for 11 different methane-air V-flames covering a region of the regime diagram. We have built a new swirl burner and plan to take similar data for five different flame conditions for this burner. From these image data flamelet normal data, displacement speed data and curvature data are to be extracted. A method for finding displacement speed has been demonstrated. Data of this type will improve our understanding of how turbulence effects premixed flames and will be of value for comparison with the results of direct numerical simulations and of large eddy simulations.

References

1. P. C. Miles, Conditional velocity statistics and time-resolved flamelet statistics in premixed turbulent V-shaped flames, Ph.D. Thesis, Cornell University, Ithaca, NY 1991.
2. D. C. Bingham, F. C. Gouldin and D. A. Knaus, *Proc. Comb. Inst.* **27**: 77-84 (1998).
3. D. A. Knaus, et. al., *SAE Trans.* **108**, paper no. 1999-01-3543 (1999).
4. D. A. Knaus and F. C. Gouldin, *Proc. Comb Inst* **28**: 367 (2000).
5. D. A. Knaus, F. C. Gouldin and D. C. Bingham, *Comb Sci. Tech* **174**: 101-134 (2002).
6. N. J. Lawson and J. Wu, *Meas. Sci. Technol* **8**:1455-1464 (1997).
7. M. R. Spiegel, et al, *Probability and Statistics*, 2nd ed., McGraw-Hill, New York, NY (2000).
8. P. A. Libby, and F. A. Williams, *Comb. Flame* **44**: 287-303 (1982).
9. S. H. Sohrab, Z. Y. Ye and C. K. Law, *Proc. Comb. Inst.* **26**: 1957 – 1965 (1984).
10. H. N. Najm and P. S. Wyckoff, *Comb. Flame* **110**: 92 - 112 (1997).
11. I. R. Gran, T. Echekki, and J. H. Chen, *Proc. Comb. Inst.* **26**: (1998).

ADVANCED STIMULATED SCATTERING MEASUREMENTS IN SUPERCRITICAL FLUIDS

(AFOSR Contract F49620-03-C-0015)

Principal Investigator: Gregory Faris

SRI International
Menlo Park, California 94025

SUMMARY/OVERVIEW

This project uses stimulated scattering (stimulated Rayleigh, Brillouin, and Raman scattering) as a tool to investigate supercritical fluids. From the measurements, we can determine thermal, compressional, and compositional properties of supercritical fluids in situ. This research effort addresses the need for new diagnostics in the study of the supercritical and near-critical regimes, where low-pressure diagnostics do not work well.

TECHNICAL DISCUSSION

Objectives

The objectives of this research are to develop stimulated scattering as a diagnostic for supercritical fluids, and use this technique to improve our understanding of fluids in the supercritical state.

The study of supercritical fluids and flows requires new diagnostic techniques. Currently available techniques such as laser-induced fluorescence (LIF) and coherent anti-Stokes Raman scattering (CARS) are complicated by increased molecular interactions, leading to stronger quenching, larger absorption and refractive index, and incomplete understanding of the influence of local conditions on spectroscopic parameters such as linewidths, nonresonant background contributions, and quenching rates. By comparison, application of stimulated scattering techniques to supercritical fluids is relatively straightforward.

Stimulated Scattering

Rayleigh, Brillouin, and Raman scattering occur commonly as spontaneous scattering. Rayleigh scattering results from refractive index variations due to thermal waves or diffusive density fluctuations and compositional fluctuations. Brillouin scattering results from refractive index variations due to sound waves or traveling density or pressure fluctuations. These scattering processes that arise from natural oscillation modes of materials can be used to determine the physical parameters responsible for those oscillations. When these collective modes are excited with a powerful laser, the mode oscillations can be driven so hard that they

grow exponentially. In this case, the oscillations cause stimulated scattering. The dominant advantage of stimulated scattering is that the scattered signal can be made arbitrarily large; otherwise, these processes produce extremely weak signals. By using a probe to measure the induced amplification, we can obtain very good quantitative results. This technique is distinct from the stimulated scattering that builds up from noise, in which case quantification is very difficult.

The large signals from stimulated scattering are particularly helpful for investigating Rayleigh and Brillouin scattering, where the weak signals available from spontaneous scattering are difficult to discriminate from background excitation light. Other advantages of stimulated scattering include excellent temporal resolution, and improved spectral resolution and signal-to-noise ratio. Furthermore, the use of two laser beams allows spatial registration and point measurement of local conditions. Stimulated Rayleigh, Brillouin, and Raman processes together provide measurements of a wide range of material properties. Rayleigh scattering provides information on thermal properties, Brillouin scattering on compressional or elastic properties, and Raman scattering on chemical and compositional properties, density, and temperature.

Experiment

We perform stimulated scattering measurements by producing strong scattering interactions using a pump laser and then probing the scattering using a second probe laser. As a pump laser we use an injection-seeded Nd:YAG laser and the probe laser is a tunable diode laser. The pump laser sets up an electric polarization oscillating at the characteristic frequency of a scattering mode of the material.¹ For strong laser driving, this polarization acts as a driving force, leading to amplification of both the material oscillation and the scattered optical wave. The optical amplification is detected as a gain or loss on the probe beam. The overlap volume of the pump and probe beams determines the spatial resolution. The stability of the probe and pump lasers has been optimized to allow for more reliable operation and narrower bandwidth, respectively. The cell is suitable for measurements in the supercritical and near-critical region.

The critical point for n-hexane occurs at a pressure 31 kPa and temperature of 234 °C.

Examples of stimulated Rayleigh / Brillouin scattering spectra measured at 1064 nm in n-hexane near the critical temperature at three different pressures are shown in Fig. 1. The peaks to the left and right of each spectrum are the gain and loss Brillouin peaks, respectively. The central peak is the stimulated Rayleigh peak. Optical absorption enhances the Rayleigh peak and produced asymmetry to the Brillouin peaks. Also shown in Fig. 1 are fits to the data. These fits include the appropriate lineshapes for each peak and the laser spectral width. Fits of this type enable the determination of linewidths, lineshifts, and peak heights. The electrostrictive Brillouin lineshape is described by the real part of the complex Lorentzian profile; the thermal Brillouin and Rayleigh lineshapes are described by the imaginary parts of a complex Lorentzian profile.² The measured lineshapes are given by the convolution of the Gaussian spectral lineshape of the Nd:YAG pump laser with

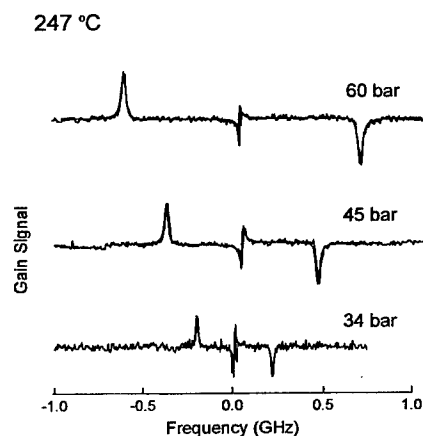


Fig. 1. Stimulated scattering spectra at 1064 nm for three different pressures.

these Lorentzian profiles. We have performed Rayleigh and Brillouin measurements in n-hexane over a wide range of temperatures and pressures at sub-, near-, and supercritical conditions.

Refractive Index Measurements

To provide the most accurate physical property measurements, we must know the refractive index. We have evaluated a number of methods for refractive index measurement, including beam translation, interferometric, and beam deflection methods. We prefer the beam deflection method because it provides larger signals than the beam translation method and is simpler to implement than the interferometric methods.

Enhanced Performance

One challenge for measurements in the supercritical region is that the Rayleigh peak becomes extremely narrow. In hexane, the Rayleigh peak is about 7 MHz at room temperature, but drops to values to a few MHz at elevated temperatures and pressures. The linewidth of the tunable diode laser that we use as a probe laser is not an issue. Although no active frequency stabilization is applied, it produces a linewidth of less than 300 kHz in 50 ms. However, the pump laser has important linewidth limitations due to the pulsewidth and the injection-seeding dither. Locking of the pump laser cavity to the injection-seeding ring laser is performed by dithering the pump laser cavity length with feedback stabilization to minimize the Q-switch buildup time. This dither corresponds to an alternating frequency shift of approximately 10 MHz on every other pulse. We prevent this dither from limiting the linewidth of the stimulated scattering measurements by acquiring the data at 5 Hz, i.e., on every other pulse. The pump laser also has a linewidth contribution related to the Fourier transform relationship between the pulsewidth in the time domain and the linewidth in the frequency domain. We can reduce this linewidth by lowering the cavity gain to produce long pulse lengths. We typically operate the pump laser with a pulsewidth of about 30 ns, which corresponds to a Fourier transform-limited linewidth of 15 MHz. There is also a linewidth contribution from the relative frequency drift between the pump and probe lasers. We have corrected for this drift by measuring the frequency of the heterodyne beat signal obtained by mixing a portion of the seed laser beam with a portion of the probe laser beam. The heterodyne frequency is then used to provide a corrected frequency axis for the stimulated scattering spectrum.

We are investigating methods to simplify the laser apparatus and improve the linewidth performance. With the steps taken to minimize the contributions from the injection-locking dither and pump-probe frequency drift, we still have the transform-limited pump laser linewidth of 15 MHz, which is significantly broader than the narrowest Rayleigh linewidths of a few MHz. Fortunately, the stimulated Rayleigh and Brillouin measurements require relatively low pump powers. To obtain gain signals of on the order of 1%, we require pump energies of tens of microjoules, or peak powers of near 1 KW. Thus it is practical to reach the required power levels through direct amplification of our probe laser. We first examined the amplification available from a cw Nd:YAG laser (Coherent Antares system). Although the cw laser provides a maximum power of only 10 W, with cw measurements we can use lock-in detection or related modulation techniques to measure smaller signals than possible with the pulsed laser. Furthermore, the Rayleigh peak will be larger when it is fully spectrally resolved, reducing the pump power requirement. We found that the single-pass gain of the cw laser was insufficient to

extract the full available power in a small number of amplification passes. Although extraction of the full power would be possible with injection locked laser operation of the cw laser, we chose to pursue pulsed amplification instead, which can provide higher peak powers and is a smaller departure from our current measurement approach.

As a first step toward pulse amplification, we made modifications to the injection-seeded pump laser to operate as an amplifier rather than a laser. The laser uses two quarterwave plates to produce circular polarization in the oscillator Nd:YAG rod to minimize multimode operation. Output coupling is obtained from an intracavity polarizer. By removing one of the quarterwave plates and adjusting the remaining waveplate, we can force the laser cavity to operate as a double-pass amplifier. We modified the layout of the second (amplifier) Nd:YAG rod to serve as a second double-pass amplifier through appropriate insertion of a polarizer, quarterwave plate, and mirror. With this arrangement, we were able to obtain pulse energies of several millijoules in a pulse of 100-microsecond duration, or powers of about 10 W. Much higher pulse energies can be obtained by further increasing the flashlamp pump energy. However, at higher energies, amplified spontaneous emission (ASE) occurred in the laser, leading a broadband contribution to the linewidth. To improve the narrowband laser energy, we used a second Nd:YAG laser (QuantaRay DCR) to amplify the pulses further. A spatial filter was placed between the two lasers to minimize contributions from ASE. This approach did not significantly improve the narrowband output energy. We attribute the broadband emission at higher lamp energies to parasitic oscillation from the various optical elements in the primary laser in its original configuration.

To overcome the parasitic oscillations and remaining ASE, we are completely rebuilding the primary laser as a direct double-stage double pass amplifier (Fig. 2). This configuration has a spatial filter between each stage of amplification and the fewest optical elements in the beam path. The laser rods can generate a single-pass gain of well over 100.³ Thus there is ample gain to saturate the final amplification stage, which would produce an energy of 1 J, or about 1 kW for a 100-microsecond pulse. We are also examining methods for stimulated scattering measurements based on a single laser source in which the second probe frequency is produced by frequency offset generation from the probe frequency.

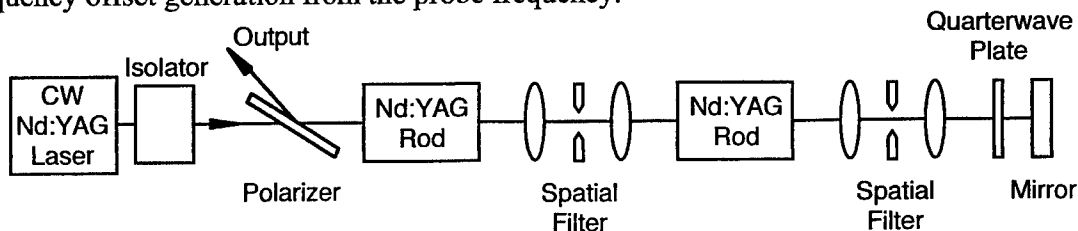


Fig. 2. Schematic of pulse amplified laser.

References

1. G. W. Faris, M. Gerken, C. Jirauschek, D. Hogan, and Y. Chen, "High-spectral-resolution stimulated Rayleigh-Brillouin scattering at 1 μm ," *Opt. Lett.* **26**, 1894-1896 (2001).
2. C. Jirauschek, E. M. Jeffrey, and G. W. Faris, "Electrostrictive and thermal stimulated Rayleigh spectroscopy in liquids," *Phys. Rev. Lett.* **87**, 233902 (2001).
3. G. W. Faris, M. J. Dyer, and W. K. Bischel, "Laser linewidth narrowing induced by amplifier gain saturation," *Opt. Lett.* **19**, 1529-1531 (1994).

SHOCK TUBE MEASUREMENTS OF IGNITION PROCESSES IN DIESEL-RELATED FUELS

ARO Contract No. DAAD19-01-1-0597

Principal Investigator: Ronald K. Hanson

Mechanical Engineering Department
Stanford University, Stanford CA 94305-3032

SUMMARY/OVERVIEW:

We report results from the third year of a three-year program of basic research aimed at improving knowledge of the combustion kinetics behavior of diesel-related fuels. The work is intended to develop a database of gas-phase chemical kinetic and two-phase spray reference measurements applicable to improving diesel engine modeling and performance. Research is being conducted in two Stanford shock tube facilities and focuses on two topics: (1) measurements of shock-induced ignition time and individual species concentration time-histories measurements during the combustion of diesel-related gas-phase fuels, and (2) fundamental studies of fuel sprays in a new aerosol shock tube using state-of-the-art optical diagnostic techniques.

TECHNICAL DISCUSSION:

Ignition Time and Species Concentration Time-History Measurements

Validation of hydrocarbon oxidation reaction mechanisms and development of new and improved reduced mechanisms require a reliable database of experimental combustion targets; such data are often drawn from experiments in shock tubes, flames or flow tube reactors. Though a limited amount of shock tube ignition time data presently exists for some fuels, these data exhibit substantial scatter and are of varying reliability. As well, stable species data in flames or bench-top reactors have often been used to tune reaction mechanisms, but little or no data is available on small transient radical species, such as OH or CH₃, that play an important role in ignition processes. To help remedy these deficiencies, we are currently working to establish a new database of ignition time and species concentration time-history measurements that will be acquired in shock tube studies of the major components of practical fuels and for surrogate fuel mixtures. This database will include studies of fuel components such as n-alkanes, branched alkanes, alkenes, aromatics, and diesel surrogate mixtures.

Recently, we have expanded the database by measuring shock tube ignition times and OH species concentrations for several new fuel components. Experimental details are given below.

1) Branched alkanes at low pressures: including iso-butane, iso-pentane, iso-octane at pressures of one to several atmospheres. Ignition time delays and OH radical concentration time histories were measured behind shock waves during the oxidation of these three branched alkanes over

initial reflected shock temperatures of 1177 to 2009 K, pressures of 1.1 to 12.6 atm, and in fuel dilutions of 100 ppm to 1.25 % and equivalence ratios of 0.25 to 2 [1,2]. Comparison of these data with current reaction models indicates the need for accurate measurements of rate constants for several key reactions, including the initial fuel decomposition reactions, which would substantially improve the performance of these models in predicting ignition time delays and species concentration. Figure 1 presents representative OH concentration time history data for iso-octane, n-heptane and toluene ignition. The wide variation in the small radical pool behavior, exemplified by the OH concentrations, is evident.

2) Aromatics and conjugated olefins at low pressures: including toluene and 1,3-butadiene. Ignition time delays and OH radical concentration time histories were measured behind shock waves during the oxidation of these two hydrocarbons over initial reflected shock temperatures of 1230 to 2000 K, pressures of 1.5 to 7.5 atm, and in dilute fuel concentrations of 250 ppm to 0.5 % and equivalence ratios of 0.25 to 2 [3,4]. In the case of toluene, we find that our ignition time measurements differ significantly from the recent toluene measurements in France. In the case of 1,3-butadiene, the OH time history measurements can be used to distinguish between the Frenklach et al. (1983) and Laskin et al. (2000) reaction models for soot precursors; the early formation of OH seen in the current shock tube measurement supports the proposed 1,3-butadiene decomposition pathway suggested by the Laskin et al. model.

3) Iso-octane/air and toluene/air mixtures at high pressures. Ignition time delay times and pressure time histories were measured behind shock waves during the oxidation of iso-octane and toluene over initial reflected shock temperatures of 855 to 1269 K, pressures of 14 to 59 atm, and equivalence ratios of 0.5 and 1 in air [5]. The iso-octane ignition time measurements serve to validate an earlier study by Adomeit in Aachen, Germany. The toluene ignition time measurements represent the first high-pressure study of this fuel. Pressure profiles from these two studies shows evidence of cool flame chemistry and pre-ignition energy release.

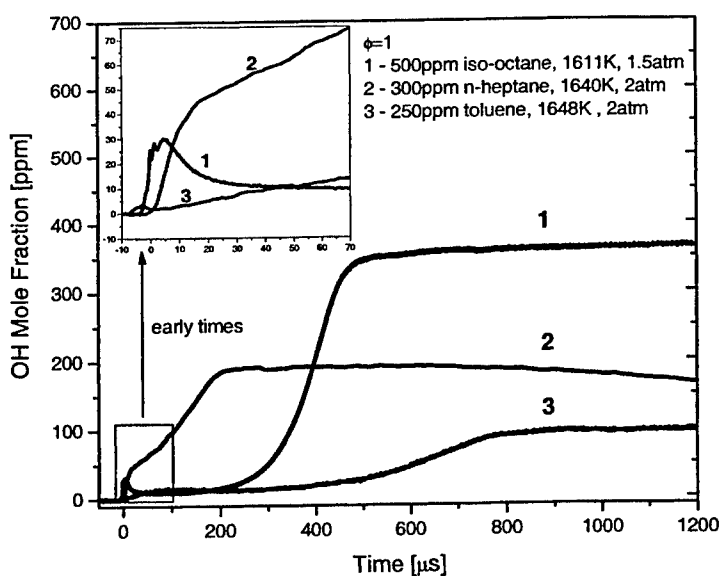


Figure 1. OH concentration time histories in these shock tube experiments were measured using narrow-linewidth ring-dye laser absorption at 306.5 nm. The initial OH concentration behavior is significantly different in the three fuel components: n-heptane, iso-octane and toluene, and is a result of different fuel decomposition products and oxidation pathways.

Shock Tube Studies of Fuel Sprays

Liquid fuels are predominant in mobile energy-conversion systems such as gas turbine combustors and internal combustion engines. While previous researchers have studied combustible sprays in shock tubes to learn about droplet breakup, evaporation, and ignition times, these studies generally have applied commercial injectors with wide droplet size distributions and relatively large droplets. Since the combustion of a two-phase mixture is strongly dependent on size-dependent droplet heating and evaporation rates, the results have largely been qualitative in nature, confused by the droplet size distribution, or quantitative only in specific situations.

To help remedy these deficiencies, we are developing a new spray test platform: an aerosol shock tube facility that can provide a relatively narrow droplet size distribution and a statistically uniform spatial distribution of droplets [6]. This facility should permit study of the full range of spray/shock interactions from simple evaporation, through ignition, to detonation. (See Fig. 2.) It will also be used as a test bench for the development of laser diagnostics for two-phase flows including diagnostics to measure droplet size and loading, fuel vapor concentration, temperature, transient species concentration time-histories, and to image reactive flow structures (e.g., detonation waves). This facility, based on a 10 cm diameter shock tube, provides a well-characterized two-phase flow with clear optical access for line-of-sight laser extinction and absorption measurements. A narrow aerosol size distribution is generated using an ultrasonic nebulizer. A uniform aerosol spatial distribution is provided by the use of pneumatically-controlled multiple inlet valves on the end wall. The spatial extent of the droplet-laden flow in the test section is controlled by timed valve closures and variations in the aerosol carrier gas flow rate.

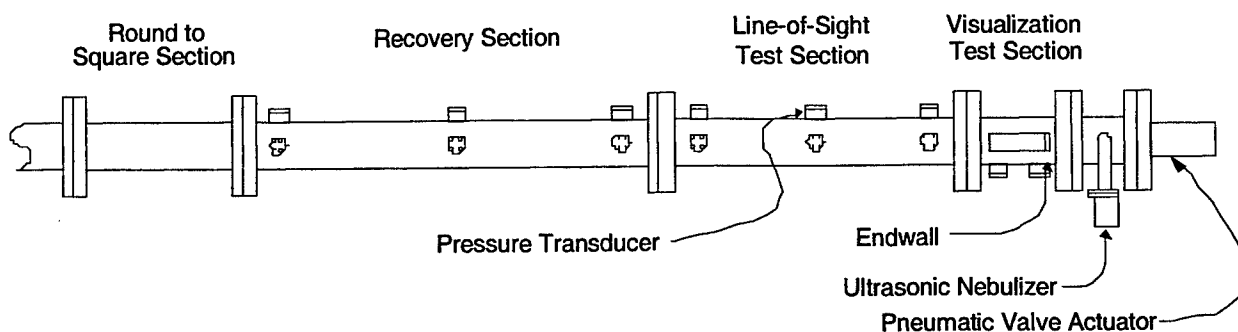


Figure 2. Schematic of aerosol shock tube facility. Incident shock waves travel from left to right, first entering a constant-area round-to-square section followed by a 1.25 m recovery section to ensure constant shock speed. Measurements may be performed in the line-of-sight test section (0.9 m in length) and visualization test section (0.3 m in length).

The facility is designed to permit extensive optical measurements. A visualization test section, with capabilities for large windows, is located at the end of the tube, allowing observation of phenomena occurring behind incident and reflected shock waves. Upstream of this section is another test section with numerous opposed windows allowing extensive line-of-sight diagnostics, such as wavelength-multiplexed extinction.

The first facility characterization tests are being carried out using water. We have fully characterizing the temporal evolution of droplet size distribution and loading and the spatial uniformity of a water aerosol in the shock tube test gas section, as well as concentration and temperature of the water vapor, during the filling phase and immediately before the arrival of the incident shock. These measurements have been made using both a commercial Mie scattering system and a multi-line IR laser extinction system developed in our laboratory (using 2 NIR lines near 1.39 microns for water vapor concentration and temperature, and four IR lines at 1.33, 1.997, 3.39 and 9.5 microns for droplet size distribution and loading.) Typical water aerosols generated are 4 microns in diameter with a volume log-normal distribution width of 2 microns with loading of the order of 10 ppmv; these exist in nearly 100% saturated water vapor at room temperature.

This multi-line system is currently being used to monitor water droplet time history (droplet size and loading, and vapor concentration and temperature) after passage of an incident and reflected shock wave. These data should provide new fundamental information on droplet evaporation rates behind shock waves.

Future work will concentrate on measurements of reactive mixtures: fuel/oxygen mixtures with n-alkanes fuels such as decane and dodecane, as well as with binary diesel fuel surrogates. In these reactive mixtures, we will study evaporation rates by measuring temperature, fuel droplet and vapor loading, as well as ignition delay times and radical species concentrations.

ARO-SPONSORED PUBLICATIONS (2003-2004):

1. M. A. Oehlschlaeger, D. F. Davidson, J. T. Herbon, and R. K. Hanson, "*Shock Tube Measurements of Branched Alkane Ignition Times and OH Concentration Time Histories*," International Journal of Chemical Kinetics 36: 67-78 (2004).
2. D. F. Davidson and R. K. Hanson, "*Interpreting Shock Tube Ignition Data*," in press, International Journal of Chemical Kinetics, January 2004; see also Western States Section/The Combustion Institute, Paper 03F-61 Fall Meeting, October 2003.
3. V. Vasudevan, D. F. Davidson and R. K. Hanson, "*Shock Tube Measurements of Toluene Ignition Times and OH Concentration Time Histories*," in press, Proceedings of the Combustion Institute 30, (2004).
4. C. S. Libby, D. F. Davidson and R. K. Hanson, "*A Shock Tube Study of the Oxidation of 1,3-Butadiene*," AIAA-2004-1322, 42nd Aerospace Sciences Meeting, January 2004.
5. D. F. Davidson, B. M. Gauthier and R. K. Hanson, "*Shock Tube Measurements of Iso-Octane/Air and Toluene/Air at High Pressures*," in press, Proceedings of the Combustion Institute 30, (2004); see also Western States Section/The Combustion Institute, Paper 03F-26 Fall Meeting, October 2003.
6. J. T. Kashdan, T. C. Hanson, E. L. Piper, D. F. Davidson, and R. K. Hanson, "*A New Facility for the Study of Shock Wave Induced Combustion of Liquid Fuels*," AIAA-2004-0468, 42nd Aerospace Sciences Meeting, January 2004.

STABILIZATION AND BLOWOUT OF GASEOUS- AND SPRAY-JET FLAMES

ARO Grant/Contract Number: AMSRL-RO-RI 40131-EG

Principal Investigator: Kevin M. Lyons

North Carolina State University
Department of Mechanical and Aerospace Engineering
Raleigh, NC 27695-7910

SUMMARY/OVERVIEW:

The focus of our efforts in this research program to date has been to determine the underlying mechanisms that control flame stabilization and blowout in lifted spray flames [1-2]. Extensive data exists for the characterization of gaseous diffusion flames as a result of past research performed by the combustion community. In these studies, mechanisms of stabilization, the role of premixing, and scalar dissipation have been examined to varying degrees in systems such as lifted laminar and turbulent diffusion flames. Interpretations of OH and smoke visualization measurements have been performed in our laboratory, to investigate the single and double flame structures that exist in spray flames, along with high-speed visualization of the reaction zone.

TECHNICAL DISCUSSION:

Findings Regarding Spray Flame Structure

The spray combustion system studied in this experimental investigation serves to both provide fundamental insight into the structure and stabilization of lifted spray flames and to provide qualitative data that is relevant to practical combustion devices. OH-PLIF and smoke visualization have been utilized to visualize combustion structures, air entrainment to support the inner reaction zone, and to develop a better understanding of how the flame-flow interaction is involved in lifted spray flame stabilization. Cases for no co-flow and 0.29 m/s co-flow have been presented to illuminate the response of the double reaction zone to changes in the oxidizer flow field. In the absence of a co-flowing air stream, the flame possesses a double reaction zone with an inner structure that burns intermittently with areas of local extinction occurring often at the most upstream locations near the leading edge. When the inner structure exists as a continuous reaction zone without local extinction, it burns predominately in a diffusion mode just inside the leading edge and transitions to partially premixed combustion farther downstream.

The addition of low-speed co-flow increases the liftoff height resulting in higher entrainment rates and enhanced inner zone combustion. There are no combustion cessation events with co-flow, and the leading edge widens as the flame base stabilizes in a location of the spray where there is a larger region possessing fuel vapor for combustion due to spreading of the spray cone and evaporation of the fuel droplets. One

key element associated with the double reaction zone, common to both cases presented here, is the role of turbulent mixing along the shear layer where the inner reaction zone resides. The OH-PLIF images and complementary smoke visualization clearly indicate that the inner zone is characterized by intense mixing which preferentially increases the residence time of small droplets in turbulent eddies and provides fuel vapor for partial premixing of reactants. Figure 1 shows some of the general findings of our study [3-6].

Characteristics of Double Flame Structure in Spray Flames:

Outer zone is a diffusion flame (external group combustion) Chiu et al. 1982 [7]

Inner zone shows properties of both diffusion and premixed flames

Lower region (sometimes combustion ceases) of the inner zone transitions between the outer diffusion flame (which wraps around the leading edge) and the thick OH zone seen at the upper inner reaction zone

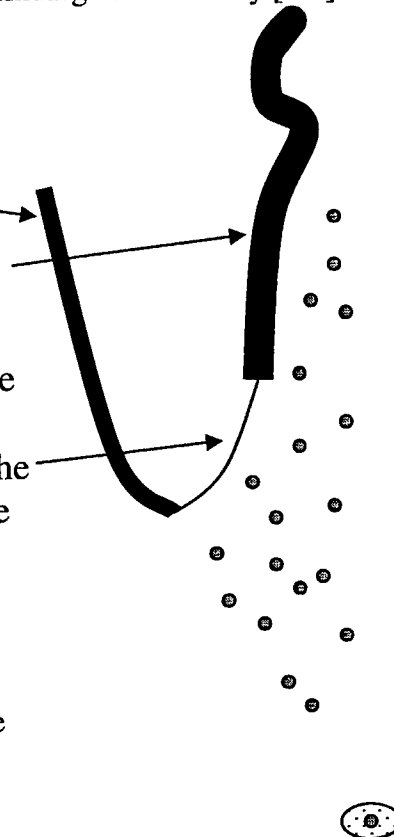


Figure 1: Schematic of what we have found on Spray Flame Structures

Flame without co-flow

The spray combustion system was initially operated without any co-flowing air stream, and representative OH and smoke visualization images are shown in Fig. 2. The flame base oscillates around an average liftoff height of 12.4 mm ($\pm 25\%$ fluctuation around average) as the flame responds to the turbulent fluctuations of the flow field. The OH images indicate that the flame exhibits the double reaction zone structure, with local extinction occurring at upstream positions of the inner reaction zone. The outer reaction zone has a stable and smooth OH contour that is largely free from the effects of large-scale turbulence and strain downstream of the stabilization point. The polydisperse spray distribution facilitates the existence of the double reaction zone. From the images it is reasoned that the smallest droplets, which possess high vaporization rates, are able to feed the inner reaction zone while the large droplet population can vaporize between the reaction zone structures to supply fuel vapor primarily to the outer diffusion flame

Generally, the flame without air co-flow exhibits weak entrainment of ambient air and an intermittent inner reaction zone. Results of MacGregor [9] indicate that sprays

typically are less efficient than gas jets at entraining ambient fluid [6]. This entrainment inefficiency, a result of poor momentum transfer, makes it difficult to sustain an inner flame structure due to minimal oxidizer availability and these regions where combustion has ceased are shown in Figure 2. In addition, this upstream region coincides with the spray cone boundary, contributing a high droplet mass flux, which can incur extinction as a result of quenching by droplets or possibly high strain/scalar dissipation rates, but quantitative measurements would be needed to support the latter possibility. Therefore, isolated pockets of combustion characterize the inner zone with continuous but diffuse regions of combustion occurring farther downstream. The broad “patches” of OH fluorescence suggest partial premixing of reactants along the wrinkled inner reaction zone. This wrinkled OH contour provides evidence that the inner reaction zone resides along the shear layer created between the momentum-dominated region of the spray and the entrained gas flow. As a result, it is reasoned that the inner zone burns in either a mixing-controlled mode, usually at the upstream locations when there is no local extinction (thin OH signal), or in a partially premixed mode downstream where there is sufficient time for partial premixing of reactants. It is important to note that the hot region bounded by the inner and outer reaction zones serves as a fuel vapor source to feed the stable outer diffusion flame and also supply fuel to the diffusive structures of the inner zone.

The smoke visualization images (also in Figure 2) further support the results obtained from the OH fluorescence data. Without co-flow, the smoke is injected only on one side of the flame beneath the spray nozzle. The smoke can be traced well into the core of the spray and flows just radially inside the inner reaction zone boundary. These streams of oxidizer within the flame demarcate the shear layer justifying the results from OH-PLIF and clearly indicating that these areas of mixing control the location (and appearance) of the inner reaction zone in conjunction with the polydisperse spray characteristics. Another interesting feature of the flow visualization is observed near the injector tip. The strong elastic scattering from the droplets, appearing as a V-shaped structure originating at the nozzle orifice, illuminates how the droplets are distributed as a hollow cone with the highest droplet counts occurring at the spray periphery. This result is important as each luminous branch of scattering intersects the base of the inner reaction zone just inside the leading edge, further indicating the contribution of the spray cone to local extinction due to a high drop flux. The flame leading edge is always positioned on the air side of the spray edge, where small droplets and fuel vapor populate recirculation zones created at the spray-air interface. These regions of recirculation create a combustible mixture ideally suited for flame stabilization and have been discussed previously in spray combustion studies [2,4,5].

Current emphasis of our research is aimed at resolving our conclusions with those provided by DNS researchers [8]. Results show strong agreement between models and experiment for the structures witnessed in the gaseous flame stabilization case. Spray flame correspondence to date has been less successful.

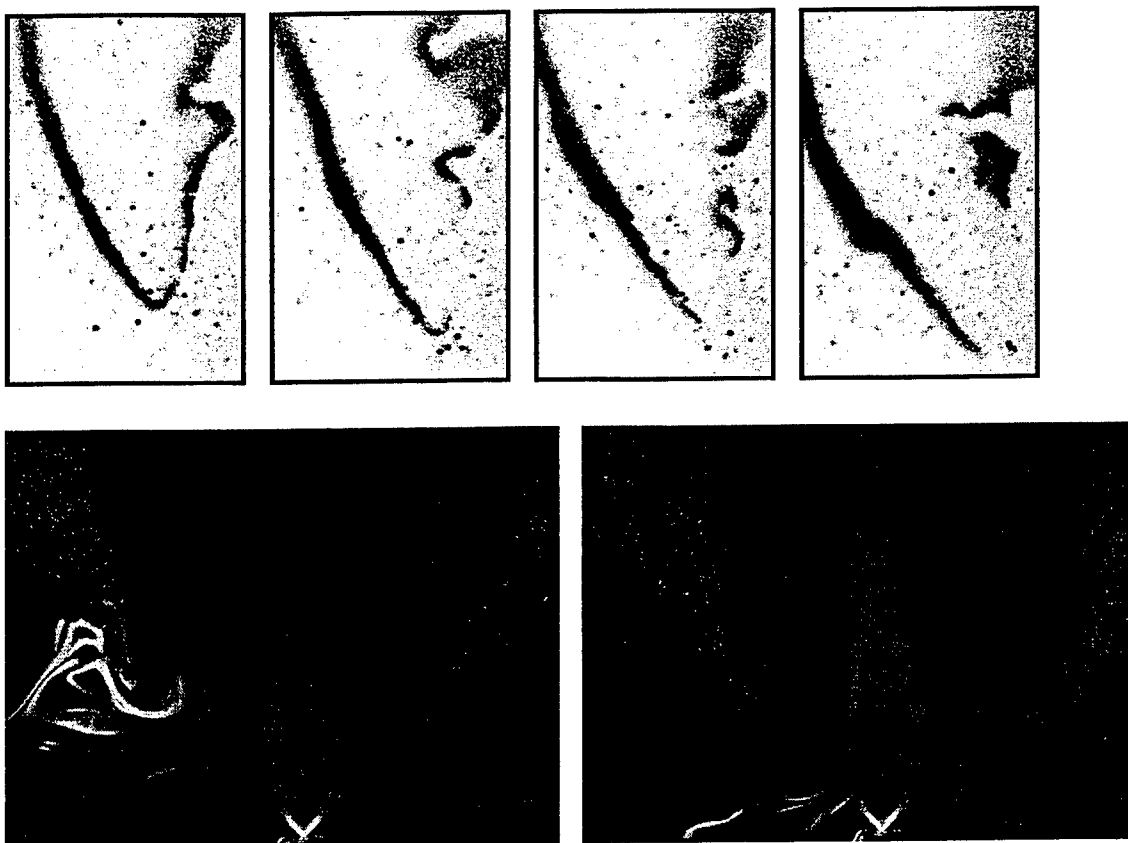


Figure 2: Images for hollow cone pressure-swirl nozzle without co-flow: single-shot OH-PLIF across the top, and two smoke visualization photographs. Low co-flow case shows frequent holes in the reaction zone near the leading edge (called the “lower region” in Fig. 1) as well as weak air entrainment.

References

1. Cessou, A., and Stepowski, D., “Planar Laser Induced Fluorescence Measurement of [OH] in the Stabilization Stage of a Spray Jet Flame”. *Combust. Sci. Technol.* 118 (1996) 361-381.
2. Stepowski, D., Cessou, A., and Goix, P., “Flame Stabilization and OH Fluorescence Mapping of the Combustion Structures in the Near Field of a Spray Jet”. *Combust. Flame* 99 (1994) 516-522.
3. Watson, K. A., Lyons, K. M., Donbar, J. M. and C. D. Carter, “Observations on the Leading Edge in Lifted Flame Stabilization”, *Combustion and Flame* 119 (1999) 199-202.
4. Marley, S. K., Welle, E. J. and Lyons, K. M. , “Combustion Structures in Lifted Ethanol Spray Flames”, *ASME Journal of Engineering for Gas Turbines and Power*, to appear.
5. Marley, S. K., Lyons, K. M. and Watson, K. A., “Comparison Study on the Leading Edge in Lifted-Jet Gaseous vs. Spray Flames”, *Flow, Turbulence and Combustion* 72 (1): 29-47(2004).
6. Marley, S.K., Welle, E. J., Lyons, K. M. and Roberts, W. L., “Effects of Leading Edge Entrainment on the Double Flame Structure in Lifted Ethanol Spray Flames”, *Experimental Fluid and Thermal Science*, to appear.
7. Chiu, H.H., Krim, H. Y. and Croke, E.J., “Internal Group Combustion of Liquid Droplets”, 19th Combustion Symposium International, The Combustion Institute , Pittsburgh, p. 971.
8. Domingo, P., Vervisch, L. and Reveillon, J. “ DNS Analysis of Partially Premixed Combustion in Spray and Gaseous Turbulent Flame-Bases Stabilized in Hot Air”. Manuscript, to be submitted to *Combustion and Flame*.
9. MacGregor, S.A., Air entrainment in spray jets, *International Journal of Heat and Fluid Flow* 12 (1991) 279-283.

DROP/GAS INTERACTIONS OF DENSE SPRAYS

(AFOSR Grant No. F49620-02-1-0074)

Principal Investigator: G. M. Faeth

Department of Aerospace Engineering
The University of Michigan
3000 François-Xavier Bagnoud Bldg.
Ann Arbor, Michigan 48109-2140, U.S.A.

SUMMARY/OVERVIEW:

Liquid breakup and turbulence generation are being studied due to their relevance to the dense combusting sprays found in propulsion systems. Secondary and primary liquid breakup are important because they are rate-controlling processes of dense sprays and fix the initial conditions of dilute sprays. Earlier experiments have shown that secondary drop breakup should be treated as a rate process and have provided the temporal properties of secondary drop breakup needed for this purpose. Current work is addressing three aspects of primary jet breakup of interest for air breathing propulsion systems by measuring spray properties using pulsed holography and shadowgraphy, and interpreting and correlating the measurements using phenomenological analysis, as follows: (1) breakup of round nonturbulent liquid jets in gaseous crossflows because this is a classical spray atomization configuration, (2) breakup of round turbulent liquid jets in gaseous crossflows because most practical injectors cause some degree of turbulent disturbance to liquid flows in injection passages, and (3) breakup of aerated-liquid jets in gaseous crossflows because this configuration has attractive atomization and penetration properties. In all cases, the following information is sought: definition of breakup regimes, liquid jet trajectories, conditions for the onset of breakup, conditions for jet breakup as a whole, drop size and velocity distributions after breakup as a function of distance along the jet and rates of breakup as a function of distance along the jet.

Turbulence generation is the main source of turbulence in dense sprays; it consists of drop (particle) wake disturbances embedded in a continuous turbulent interwake region. Both regions involve unusual flows that have received little attention in the past: the particle (drop) wakes are laminar-like turbulent wakes that are observed for intermediate Reynolds number spheres in turbulent environments whereas the turbulent interwake region consists of isotropic turbulence in the little-studied final decay period. Earlier work found the properties of these flows for monodisperse particle (drop) flows; current work is considering their properties for more practical polydisperse particle (drop) flows.

TECHNICAL DISCUSSION

BREAKUP OF NONTURBULENT LIQUID JETS IN CROSSFLOW. Past work has established the temporal properties of secondary drop breakup, see Chou et al. (1997) and Hsiang and Faeth (1995). In addition, Mazallon et al. (1999) initiated studies of breakup of round nonturbulent liquid jets in crossflow. Current work continued these studies by carrying out experimental observations using shock tube and wind tunnel tests combined with pulsed holography and shadowgraphy for measurements. Fig. 1 illustrates some typical results from these studies, involving the location of the end of the liquid jet in the streamwise and crosstream directions. Other results of this study include ligament and drop size distributions after breakup, drop velocity distributions after breakup, breakup regimes and rates of breakup, see Aalburg et al. (2003, 2004) and Sallam et al. (2004a) for a complete description of these results.

BREAKUP OF TURBULENT LIQUID JETS IN CROSSFLOW. The operation of most practical liquid injectors in gaseous crossflows invariably introduces some turbulence in the

liquid jet at the injection passage exit. The resulting properties of turbulent primary breakup have been studied extensively for turbulent round jets in still gases, see Sallam and Faeth (2003), Sallam et al. (2002) and references cited therein. Thus, study of primary breakup of nonturbulent round liquid jets in gaseous crossflows and turbulent round liquid jets in still gases was extended to consider the important case of primary breakup of turbulent liquid jets in gaseous crossflows. Similar to the earlier studies, this work involved experimental observations using shock tube and wind tunnel tests combined with pulsed holography and shadowgraphy for measurements. This work has just begun with some initial results illustrated in Fig. 2. Figure 2 is an illustration of mean drop diameters after turbulent primary breakup as a function of distance along the liquid jet. In this, as in other cases, simplified phenomenological analysis provides useful interpretation and correlation of the measurements. This work is continuing in order to complete the series of measurements reported for primary breakup of nonturbulent round liquid jets in gaseous crossflows.

BREAKUP OF AERATED LIQUID JETS IN CROSSFLOW. Aerated-liquid atomization was proposed by Lefebvre roughly twenty years ago and continues to attract attention due to demonstrated capabilities to improve both the atomization and penetration properties of sprays, see Wu et al. (1997) and references cited therein. Motivated by this observation, a joint investigation involving workers of AFRL/WPAFB (C.D. Carter, T.A. Jackson, K.-C. Lin) and workers at the University of Michigan was initiated to study the properties of this primary breakup process. This work involved observations of round aerated-liquid jet breakup in supersonic crossflow, with measurements involving pulsed holography and shadowgraphy at AFRL, combined with data reduction and analysis at Michigan. Only the first phase of this research has been completed and some example results of this study are discussed in the following, see Sallam et al. (2004b) for more details. The initial phase of this research established aerated-liquid jet primary breakup regimes and also indicated that breakup was dominated by the flow of gas in aerated liquid, with little effect of even supersonic crossflow on primary breakup. Some typical measurements of primary breakup properties giving the diameters of ligaments and drops near the liquid surface as a function of the gas/liquid mass flow-rate ratio (GLR), are illustrated in Fig. 3. It is evident that the size of ligaments and drops are negligibly affected by the GLR as long as the flow is in the annular breakup regime ($GLR > 2\%$). Remarkably, drop sizes after breakup illustrated in Fig. 3 are relatively independent of flow properties, which agrees with earlier observations of Kim and Lee (2001). Much remains to be done to provide information about aerated-liquid jet breakup equivalent to information available for nonturbulent round liquid jets in crossflow; fortunately, measurements to obtain this information can be undertaken in still gases, due to the small effect of crossflow on breakup properties, which will substantially simplify measurements of spray properties.

TURBULENCE GENERATION. Dispersed phases (particles or drops) moving through continuous gas or liquid phases generate turbulence that must be understood in order to understand the mixing properties of sprays. Recent studies of turbulence generation show that these flows involve particle wakes embedded in a continuous turbulent inter-wake region, see Chen and Faeth (2000), Chen et al. (2000) and references cited therein. Wu and Faeth (1995) have shown that the wakes behaved like laminar wakes but with fast mixing due to the presence of turbulence, and are called "laminar-like" turbulent wakes as a result. Studies of the turbulent inter-wake region for monodisperse particle flows showed that this region involved isotropic turbulence in the little-studied final-decay period (Chen and Faeth, 2001). Subsequent work during the current investigation extended these findings to polydisperse dispersed phases, developing successful mixing rules so that the properties of the turbulent inter-wake region could be estimated using an analogy with conventional isotropic turbulence in the initial- and final-decay periods (Lee et al., 2003). Work during the current report period sought to develop a better understanding of the one-dimensional energy spectra and scales of these flows based on measurements of both particle- and grid-generated turbulence.

An unusual property of turbulence in the final-decay period, observed in the turbulent interwake region of flows dominated by turbulence generation, is that the ratio of outer/inner length scales, e.g., the ratio of integral/Taylor length scales, decreases with increasing turbulence

Reynolds numbers rather than this ratio increasing with increasing turbulence Reynolds numbers typical of conventional isotropic turbulence in the initial-decay region. The effect of the reduction of the integral/Taylor length scale ratio with increasing turbulence Reynolds number in the final-decay period can be seen directly from the one-dimensional energy spectra illustrated in Fig. 4. Here it is clear that the frequency range of the inertial region of turbulence decreases with increasing turbulence Reynolds number, consistent with the observed variation of the outer/inner length scale ratio. Aside from this fundamental difference between isotropic turbulence in the initial- and final-decay regions, the energy spectra in the inertial range is still seen to decay with increasing frequency according to Kolmogorov's $-5/3$ power law. This behavior is not unexpected, however because Kolmogorov's decay law is found from dimensional considerations and only requires a large span of frequencies between the outer and inner scales – a property easily satisfied for turbulence at small turbulence Reynolds numbers in the final-decay period. Finally, these measurements show that rates of dissipation of turbulence kinetic energy in the final-decay period are orders of magnitude larger than the conventional turbulence. From this information, the mixing properties resulting from turbulence generation are reasonably well understood which should improve simulations of mixing in dense sprays.

REFERENCES

- Aalburg, C.M., van Leer, B. and Faeth, G.M. (2003) *AIAA J.* 41, 2371.
Aalburg, C.M., van Leer, B., Faeth, G.M. and Sallam, K.A. (2004) *Atom. Sprays*, in press
Chen, J.-H. and Faeth, G.M. (2000) *AIAA J.* 38, 995.
Chen, J.-H. and Faeth, G.M. (2001) *AIAA J.* 39, 180.
Chen, J.-H., Wu, J.-S. and Faeth, G.M. (2000) *AIAA J.* 38, 636.
Chou, W.-H., Hsiang, L.-P. and Faeth, G.M. (1997) *Int. J. Multiphase Flow* 23, 651.
Hsiang, L.-P. and Faeth, G.M. (1995) *Int. J. Multiphase Flow* 21, 545.
Kim, J.Y. and Lee, S.Y. (2001) *Atom. Sprays* 11, 734
Lee, K., Faeth, G.M. and Chen, J.-H. (2003) *AIAA J.* 41, 1332.
Mazallon, J., Dai, Z. and Faeth, G.M. (1999) *Atom. Sprays* 9, 291.
Sallam, K.A. and Faeth, G.M. (2003) *AIAA J.* 41, 1514.
Sallam, K.A., Dai, Z. and Faeth, G.M. (2002) *Int. J. Multiphase Flow* 28, 427.
Sallam, K.A., Aalburg, C.M. and Faeth, G.M. (2004a) *AIAA J.*, in press.
Sallam, K.A., Aalburg, C.M., Faeth, G.M. Lin, K.-C., Carter, C.D. and Jackson, J.A. (2004b) *Atom. Sprays*, in preparation.
Wu, J.-S. and Faeth, G.M. (1995) *AIAA J.* 33, 171.
Wu, P.-K., Kirkendall, K.A., Fuller, R.P. and Nejad, A.S. (1997) *AIAA J.* 13, 64.

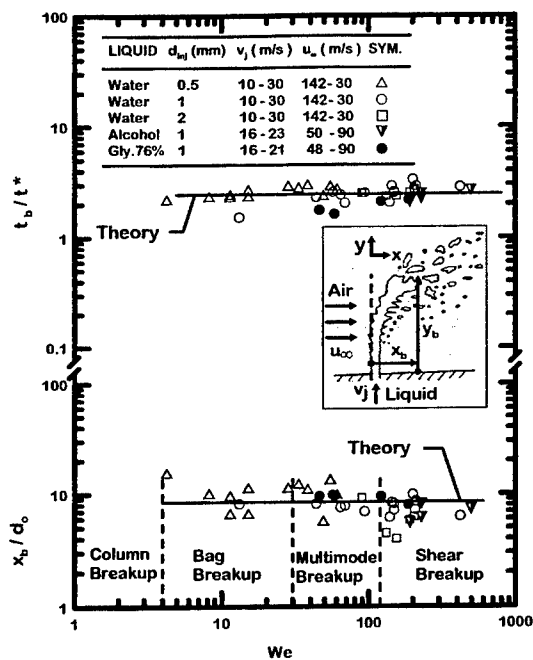


Fig. 1 Location of the end of the liquid jet in the streamwise and crossstream directions during primary breakup of nonturbulent round liquid jets in gaseous crossflows. From Sallam et al. (2004a)

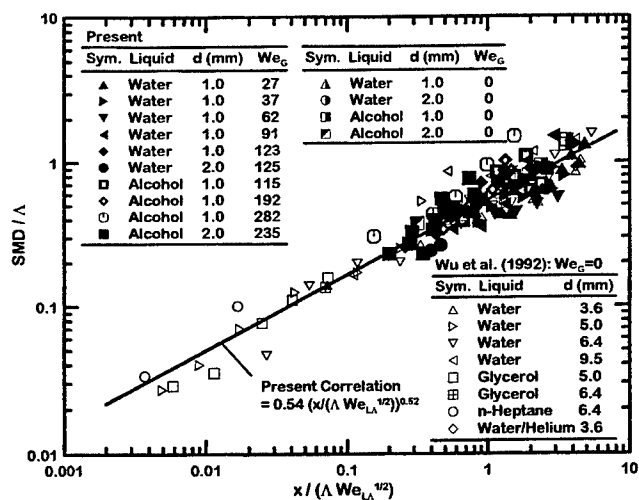


Fig. 2 Variation of drop diameters after primary breakup along the surface of round turbulent liquid jets in gaseous crossflows.

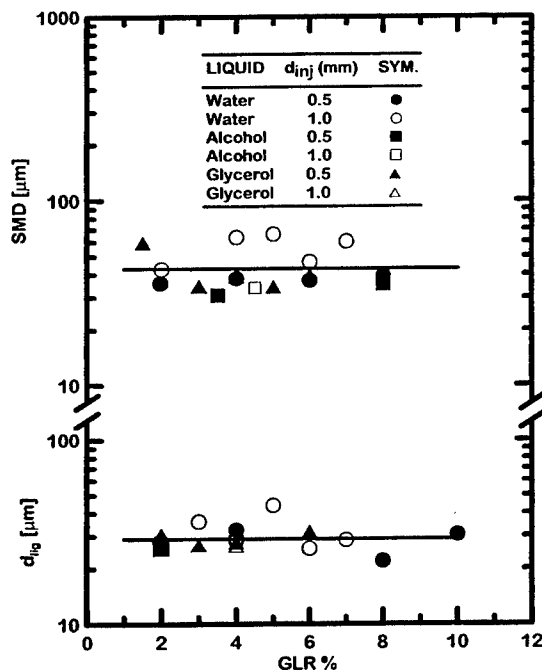


Fig. 3 Diameters of the ligaments and drops near the liquid surface during primary breakup as a function of the gas/liquid mass ratio for aerated-liquid injection. From Sallam et al. (2004b)

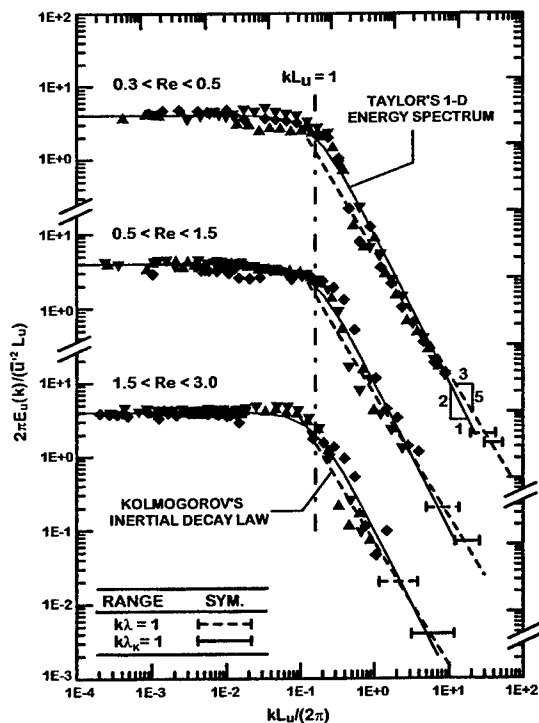


Fig. 4 Typical one-dimensional energy spectra of streamwise velocity fluctuations for various polydisperse particle phases and turbulence Reynolds numbers for conditions in the turbulent interwake region

LES OF SOOTING FLAMES

Grant/Contract Number: DAAD19-03-1-0049

Principal Investigator(s): Suresh Menon

School of Aerospace Engineering
Georgia Institute of Technology, Atlanta, GA 30332

SUMMARY/OVERVIEW

Soot results from incomplete combustion and typically occurs in fuel rich regions. Although some of these particles are oxidized in the flame zone, soot particles that escape oxidation are considered a serious health concern since both polycyclic aromatic hydrocarbons (PAHs) that are precursors of soot and soot associated organics have been identified as carcinogenic emission. Soot emission can result in unwanted thermal/IR signature that is unacceptable for various obvious military reasons. The formation of soot particles in flames is still a poorly understood phenomenon in spite of many seminal studies. It is commonly accepted that PAHs are precursors to soot and soot inception process can be modeled as the coagulation of PAHs under the influence of van der Waals forces. Further growth of these nascent soot particles occurs via PAH condensation and surface growth which then transitions to agglomeration of these particles into chain-like structures that in some cases can be as large as a few μm (Hamins, 1993). Determination of soot inception, the location where it occurs, and the conditions under which it begins is complicated since many of the PAHs that contribute to the soot formation process and many of the species (and the reactions) involved in soot formation are still unknown. Observations are also difficult since the largest observable gas phase molecule is approximately 300 atomic mass units (around 25 C-atoms) where as the smallest observable soot particle is around 5 nm (around 2.5×10^5 C-atoms, Hamins, 1993). Thus, where the precursor particles (0.1 - 1 nm) are forming in the flame zone are not known at this time.

To predict unsteady features such as where in the flame zone, soot inception, particles agglomerate and oxidization occurs a new approach within the context of large-eddy simulation (LES) methodology is being developed. We report on our recent progress here.

TECHNICAL DISCUSSION

The overall technical objective of this three year project (which began August 2003) is to develop a new subgrid closure to model soot precursor formation and subsequent growth into soot particles within the LES framework. We are currently focusing on two canonical flames: a turbulent jet diffusion flame and a stationary premixed flame. The current emphasis is on establishing (a) the minimum number of reactions and species needed to resolve proper chemical gas phase processes (in collaboration with Prof. Law's group), (b) the computational efficiency of this chemical kinetics model within a 3D LES, (c) the implementation of a baseline reduced soot mechanism, (d) the evaluation of these models in premixed and diffusion laminar and turbulent flames, and (e) the establishment of a collaboration with ARL to investigate soot precursor formation. The progress in these areas is summarized below.

(a) Evaluation of Reaction Mechanisms

For the present effort we are focusing on methane-air and ethylene-air combustion. For methane-air, we are using a 16-species, 12-reaction reduced mechanism (Sung and Law, 19xx), whereas for the ethylene-air combustion we are testing a new 20-species, 16-reaction reduced mechanism developed recently (Lu and Law, 2004). We compare the detailed mechanism (GRI-MECH 2.11 with 361 reactions and 61 species, up to C6 chemistry) with the reduced 16-species mechanism. The simplified soot model for both chemical mechanisms consists of a four-step reaction and employs two equations: conservation of soot mass and soot particle number density. The four steps are (1) formation of precursor species, (2) particle inception, (3) surface growth and particle agglomeration, and (4) particle oxidation. Lindstedt (1989) suggested a simplified reaction mechanism that assumed that the soot formation is dependent upon the breakdown path of the fuel and the presence of pyrolysis products. The present work uses benzene for the detailed mechanism and acetylene for the reduced mechanism (since it does not contain benzene) as the main pyrolysis products that lead to the soot formation process.

We compare in Fig. 1a the full mechanism and the reduced mechanism with experimental data (Beltrame et al., 2001) for a laminar opposed diffusion flame. The full GRI mechanism with the benzene-based soot model has a peak near stagnation point (SP), consistent with the experimental results, with a difference of only 4 percent. However, the numerical soot volume fractions in the fuel side from the stagnation point, SP, are under-predicted, and early oxidation is predicted after the SP. These results are consistent with past observations by Beltrame et al. On the other hand, the original reduced reaction model significantly over-predicts the soot volume fraction and an analysis of the results showed that, C₂H₂ is significantly over-predicted (when compared to the full mechanism). A modified mechanism that reduced C₂H₂ production (without affecting all major species) shows a more reasonable prediction of soot volume fraction. However, this type of adjustment is only possible for a particular case and is not general, as shown in Fig. 1b. It can be seen that the modified (at a strain rate of 20 1/s) reduced mechanism for 21% O₂ shows deviation the oxygen content and/or strain rate is changed.

Nevertheless, the present study confirms that the overall trend of the reduced mechanism with the acetylene soot model is reasonable and that the predictions are reasonably accurate with proper modifications. Since the current goal is to establish and integrate modeling tools for LES studies, the choice of the modified 16-species reduced mechanism with the modification for the 21% oxygen is considered acceptable. Eventually, it is expected that a more robust reaction model will be used when it becomes available.

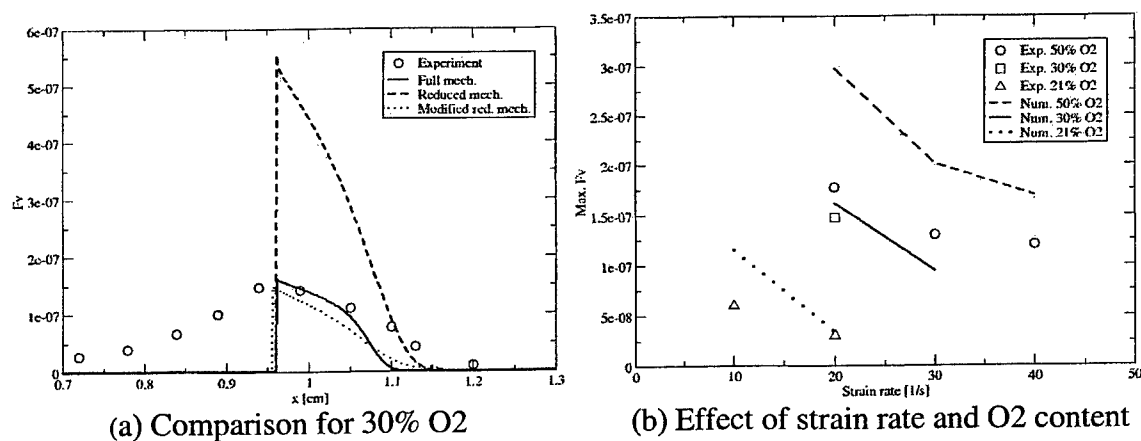


Figure 1 Comparison of predicted soot volume fraction with data. In (b), the reduced mechanism is tuned at 21% O₂ and at 20 (1/s) strain rate, and then used for other test conditions.

(b) LES of Sooting Turbulent Premixed Flames

The existing DNS/LES code is a fourth-order accurate finite-volume scheme that has been extensively validated for various applications in the past (e.g. Sankaran and Menon, 2004). Here, it has been simplified to study a premixed-flame-turbulence interaction problem. Our code uses the ISAT approach within a subgrid linear-eddy mixing (LEM) reaction-diffusion closure to simulate turbulent combustion. All LEMLES have been conducted using the reduced reaction mechanisms augmented by the two soot equations (thus, a total of 16 species and 18 scalar equations are in the subgrid model). At present, a $64 \times 64 \times 5$ grid with 12 LEM cells per LES cell is used in these simulations. Computational speed is considerably enhanced by the use of parallel optimization and ISAT. More detailed 3D LES are planned for the coming year.

Figure 2 shows some preliminary results for methane-air turbulent premixed flame LES at an equivalence of 1. In this coarse grid, the LES-resolved flame is captured in 2-3 cells. This is only possible since there are 12 LEM cells within each LES cell. Figure 2a shows the baseline case without the soot model, while Fig. 2 shows the case with soot model include. Soot formation in the flame zone (i.e., 2-3 cells) is captured in this LEMLES approach. Finally, Fig. 3 shows recent results (without the soot model) for the 20-species ethylene-air combustion.

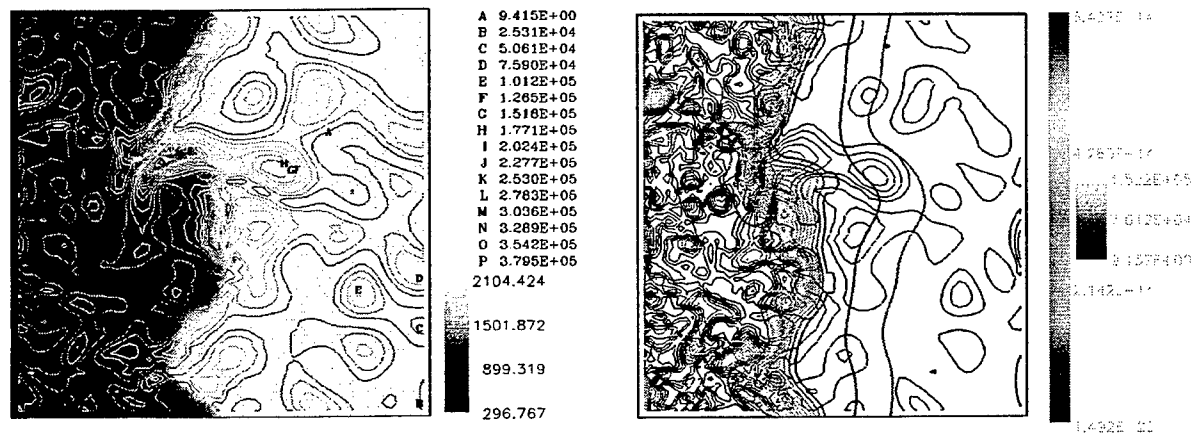


Figure 2 LES of premixed flame interaction with incoming turbulence. (a) Vorticity and temperature contours, (b) vorticity and soot mass fraction contours. Soot production within a 2-3 LES-resolved flame is captured within the subgrid LEM in these LEMLES studies.



Figure 3 Flame-vortex interactions in the ethylene-air system for condition similar to Fig. 2. Again, the flame is resolved on the LES grid within 2-3 cells due to the subgrid LEM approach.

(c) MD Simulations of Soot Precursor Formation

One of the key areas of research in this project is to determine the process of the formation of the soot precursor since this knowledge is essential to incorporate this effect into the LES model. This work is in collaboration with researchers (Dr. Mark Zottola) at ARL. We are focusing on a single mechanism involving benzene with the premise (developed at ARL) that benzene decomposes into three acetylene molecules at elevated temperatures. Acetylene can then fragment into two CH molecules and it is these CH molecules that agglomerate, expelling dihydrogen to form carbon clusters or soot. Molecular dynamics simulations (MDS) are being used at ARL to study the three distinct steps in this proposed mechanism: (a) transformation of benzene into acetylene, (b) fragmentation of acetylene into CH, and (c) agglomeration of CH to form carbon clusters. To perform ab-initio molecular dynamics, the VASP code is being used to explore both CH agglomeration and the process of hydrogen extrusion from those agglomerates, the penultimate and ultimate steps respectively, in soot formation. To date the ARL group has identified the transition state and energy barrier to the rearrangement of benzene into acetylene. Figure 4a shows the molecular rearrangement of the transformation at the transition state and the molecular arrangement for the transition state for C₂H₂ is shown in Fig. 4b. This figure shows the symmetric bond breaking to form the CH radicals. Exploring alternate spin states for this transformation and other potentially more appropriate and higher level of theory will also be investigated in the near future.

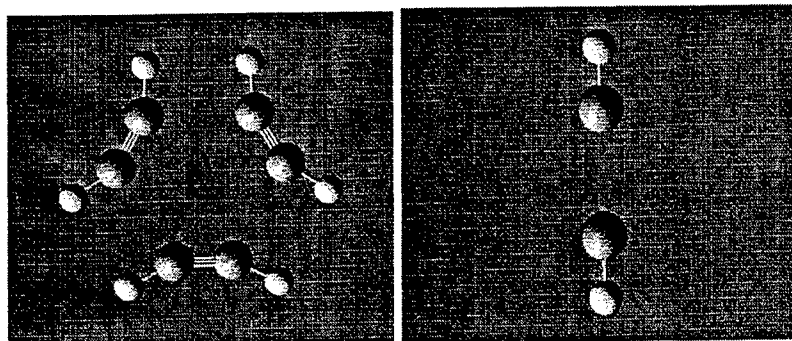


Figure 4 Molecular re-arrangement of benzene (a) and acetylene (b) at the transition state.

SUMMARY and FUTURE PLANS

The ability to carry out full 3D LES using our subgrid LEM approach with a relatively detailed (e.g. 16-20 species) reaction kinetics coupled with a soot model has been demonstrated for both methane and ethylene premixed flames. An initial collaborative effort with ARL to investigate the precursor formation using MDS has been initiated which will be continued in the coming year to develop precursor closure models for LES. Future LES studies will also focus on soot formation in ethylene premixed flames in collaboration with the Princeton group with a goal to validate this approach and to establish a new LES capability to simulate sooting flames.

References

- Beltrame, A., Porshnev, W., Merchan, W, and Kennedy, L. (2001), Comb. Flame, 124:295-310.
- Hamins, A. (1993) In Environmental Implications of Combustion Processes, 71-95, CRC Press.
- Lindstedt, P. (1989) Simplified Soot Nucleation and Surface Growth Steps for Non-Premixed Flames, John Wiley & Sons, Inc., 1989.
- Lu, T. and Law, C. K. (2004), Proceedings of the Combustion Institute, 30 (to appear).
- Sankaran, V. and Menon, S. (2004), Proceedings of the Combustion Institute, 30 (to appear).
- Sung, C. J., Law, C. K., and Chen, J.-Y. (2001), Comb. Flame, 125:906-919.

ADVANCED SUPERCRITICAL FUELS

LRIR 93PR02COR

Principal Investigators: Tim Edwards, Chris Bunker, Tom Jackson

Air Force Research Laboratory
AFRL/PRTG Bldg 490
1790 Loop Rd N
Wright Patterson AFB, OH 45433-7103

SUMMARY/OVERVIEW:

Increases in aircraft and engine performance are increasing the heat load being transferred into an aircraft's primary coolant--the fuel. This research is aimed at understanding the limitations of operation of fuel heated to 480 C (900 F) and beyond. Important issues are expected to be thermal stability, injection/combustion properties, and fuel characterization.

TECHNICAL DISCUSSION

Thermal Stability

A significant effort in this task is the construction of fuel models that include thermal-oxidative and pyrolytic behavior "upstream" of the engine combustor. As thermal-oxidative deposition models progress beyond "global" models, a better understanding of fuel-surface interactions [1] and trace species reactions [2,3] is being developed. Treating the effect of the surface in terms of catalysis of hydroperoxide decomposition allows effective simulation of fuel oxidation rates on various surfaces (Figure 1). In fact, model predictions of measured hydroperoxide concentrations are fairly well simulated (Figure 2). The effect of added fuel anti-oxidants is also well-simulated (Figure 3). Ultimately, the goal is to allow simulation of any jet fuel with only a few-easily measured fuel species concentrations (such as sulfur and "polars") – rather than treating rate parameters as adjustable constants [2,3]. Modeling of fuel thermal cracking (Figure 4) and pyrolytic deposition is also continuing [4], with the effect of supercritical pressures being of special interest (Figure 5).

Fuel-Quality Diagnostics

Research efforts focused on developing sensors and sensor technologies to support rapid, field-level fuel quality analysis are continuing. With respect to sensor development, efforts to incorporate environment-sensitive luminescent nanoparticles into thin-film devices have begun. The effects of the thin-film material on the photophysical properties of the nanoparticles have been investigated using polymethylmethacrylate (PMMA), polyvinylpyrrolidone (PVP), and a tetraethyl orthosilicate (TEOS)-based sol-gels. Figure 7 demonstrates the changes observed in the luminescent properties of CdS nanoparticles [5] in these environments. Sensitivity of the emission spectra to various sulfur containing compounds (models for those compounds found in aviation fuel) has

also been investigated. Figure 8 demonstrates the significant enhancement of the photoluminescence yield with exposure of a sol-gel-based CdS thin-film sensor to hexanethiol. The increase in emission intensity is almost 100% for a concentration of 5 mM.

With respect to the development of sensor technologies, efforts to predict various physical and chemical properties of aviation fuels using analytical techniques amenable to field-level usage continues. The concept of *Fuels Topology Mapping* (FTM) focuses on visualizing the fuel by its properties and characteristics along with its history and intended use; taking the fuel from an unknown state to a known state using *first-principles* knowledge. Data (Figure 9) collected using gas chromatography-mass spectrometry, near-infrared absorption spectroscopy, and a chemical vapor sensor (Cyrano Sciences, Inc.) is analyzed using the partial least squares (PLS) method. Results from the PLS analysis demonstrate good predictive capabilities for a number of important physical properties (freeze point, density, D86 synthetic distillation). Figure 10 plots measured vs. predicted freeze point temperatures for 45 different aviation fuels (17 Jet A, 23 JP-8, 3 JP-8+100, 1 JP-4, 1 Fischer-Tropsch). The dotted lines represent current accepted errors for freeze point determination; the predicted results are well within these limits. Efforts to combine the separate analytical data sets into a single data matrix and to explore the effects of such multidimensional systems on the ability to predict these properties are underway.

Fuel Additives

Research is continuing on the development of additive technologies able to provide heat-sinks required for a JP-900 fuel (working temperature limit of 900°F). Our approach has been to synthesize iron-based core-shell nanoparticles that are stable under ambient conditions but will react with oxygen at elevated temperatures. TEM analysis of these particles shows diameters of ~7 nm (Figure 11). Temperature studies in hexane using the luminescence decay of pyrene as a measure of dissolved oxygen concentration show no reactivity at low temperatures ($T < 110^{\circ}\text{C}$) but efficient oxygen scavenging at temperature above 110°C (~240°F, autooxidation onset). Data for a zero oxygen baseline analysis and two separate additive analyses is shown in Figure 12. Above a temperature of 120°C , the cell appears to be devoid of oxygen. Further efforts are underway to explore the application of these materials as reactive sensors and highly energetic materials.

[1] Ervin, J.S., Williams, T.F., Ward, T.A., and Bento, J., "Surface Deposition within Treated and Untreated Stainless-Steel Tubes Resulting from Thermal-Oxidative and Pyrolytic Degradation of Jet Fuel," *Energy & Fuels*, Vol. 17, pp. 577-586, 2003.

[2] Balster, L., Zabarnick, S., Striebich, R., DeWitt, M., "Predicting the Thermal Stability of Jet Fuel: Analytical Techniques Toward Model Validation," 8th Int'l Conference on Stability and Handling of Liquid Fuels (IASH), Sep 2003.

[3] N.J. Kuprowicz, J.S. Ervin, and S. Zabarnick, "Modeling the Liquid-Phase Oxidation of Hydrocarbons over a Range of Temperatures and Dissolved Oxygen Concentrations with Pseudo-Detailed Chemical Kinetics," accepted for *Fuel*, 2004.

[4] T.A. Ward, J.S. Ervin, R.C. Striebich, and S. Zabarnick, "Two-Dimensional Simulations of Flowing Mildly-Cracked Normal Alkanes Incorporating Proportional Product Distributions," *AIAA Journal of Propulsion and Power*, in press, 2003.

[5] Bunker, C. E.; Harruff, B. A.; Pathak, P.; Payzant, A.; Allard, L. F.; Sun, Y.-P. "Formation of Cadmium Sulfide Nanoparticles in Reverse Micelles: Extreme Sensitivity to Preparation Procedure" Langmuir, accepted for publication.

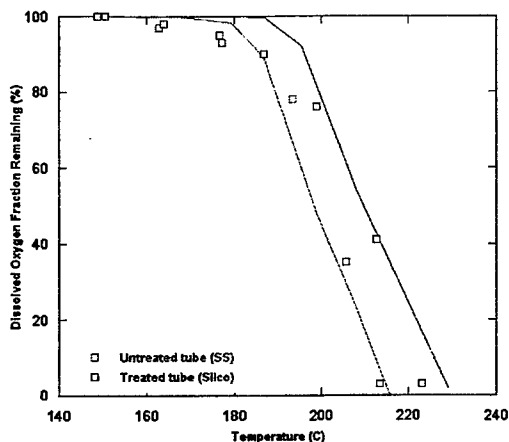


Figure 1. Effect of bare stainless steel and silica-coated surfaces on fuel oxidation [1].

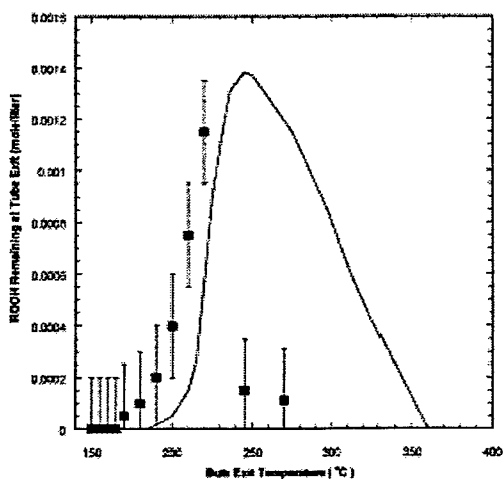


Figure 2. Predicted and measured levels of fuel hydroperoxides [2,3].

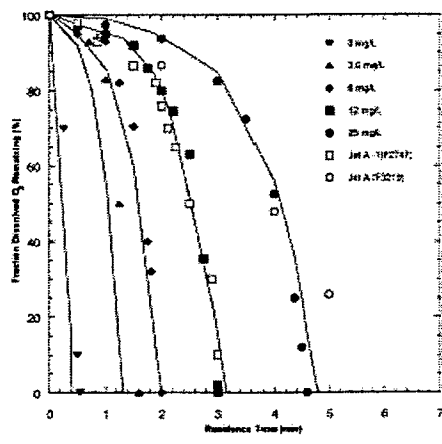


Figure 3. Effect of varying anti-oxidant levels in jet fuel on oxidation rate.

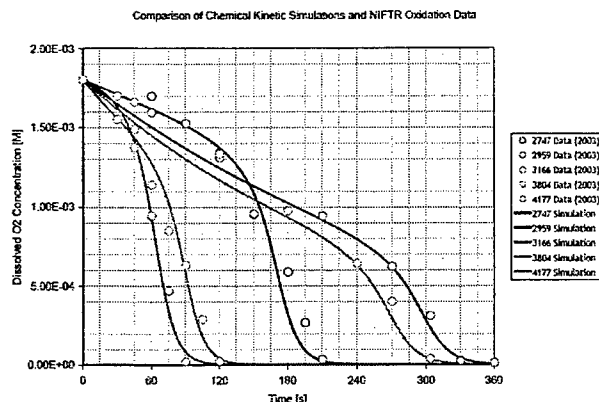


Figure 4. Predicted and measured dissolved oxygen consumption in 5 fuels using measured fuel parameters.

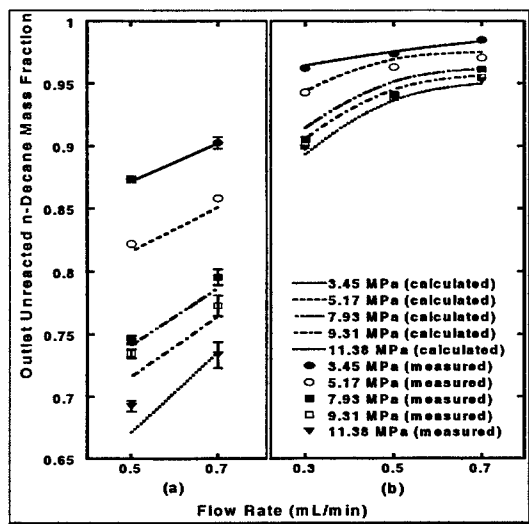


Figure 5. Model results and experimental data for fuel thermal cracking using PPD model [4].

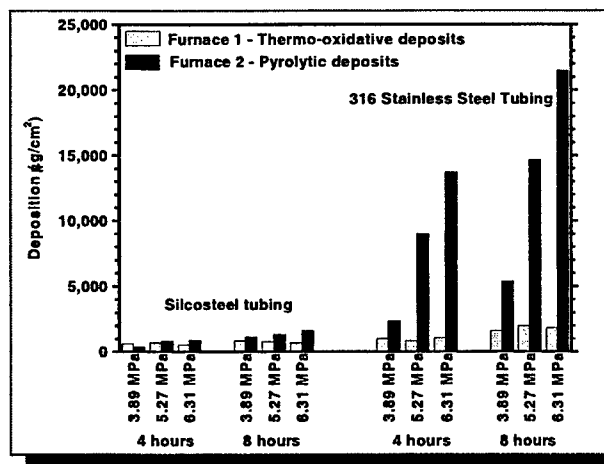


Figure 6. Effect of pressure on fuel thermal-oxidative and pyrolytic deposition [1,4].

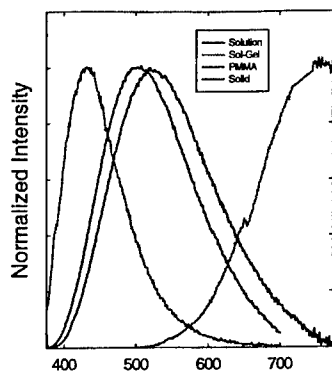


Figure 7. Emission spectra for CdS nanoparticles in various thin-film matrices.

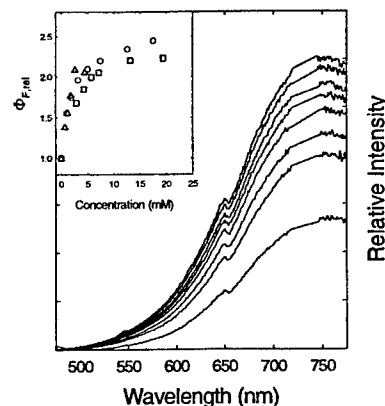


Figure 8. Emission spectra for CdS nanoparticles exposed to increasing concentration of hexanethiol. Inset is quantum efficiency vs. concentration.

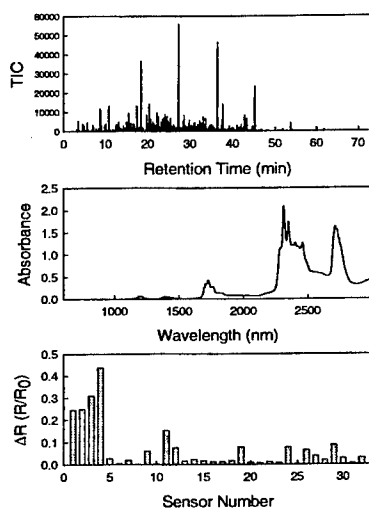


Figure 9. Representative JP-8+100 data obtained from gas chromatography-mass spectrometry (top), near-infrared absorption spectroscopy (middle), and chemical vapor sensor (bottom)

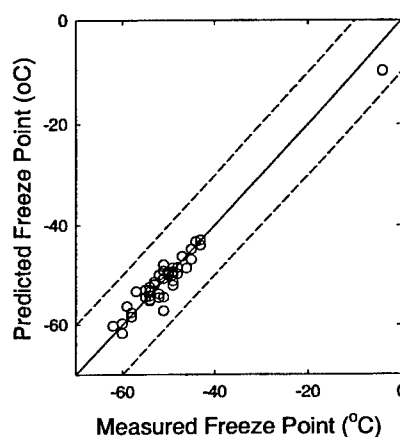


Figure 10. Measured vs. predicted freeze point temperatures determined from PLS analysis using GC-MS data.

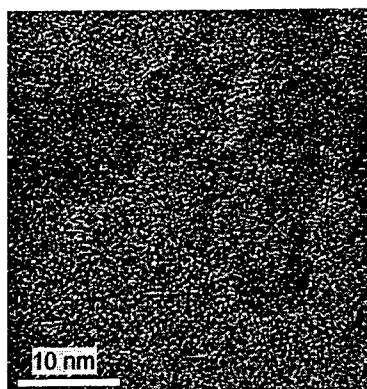


Figure 11. TEM image of iron-based core-shell nanoparticles used as JP-900 additive.

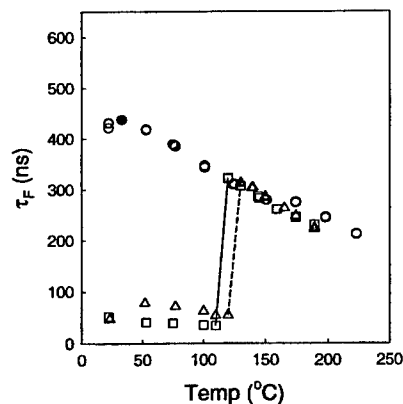


Figure 12. Plot of pyrene lifetime vs. temperature for no oxygen (\circ) and two additized solutions (\square , \bullet). The abrupt change indicates additive activity.

SUPERCRITICAL FUEL PYROLYSIS

AFOSR Grant No. FA9550-04-1-0005

Principal Investigator: Mary Julia (Judy) Wornat

Louisiana State University
Department of Chemical Engineering
Baton Rouge, Louisiana 70803

SUMMARY/OVERVIEW:

The fuels used in the next generation of hypersonic aircraft will have to operate under very high pressures (beyond the critical pressures of most hydrocarbons) and will have to sustain very high heat loads in order to meet aircraft cooling requirements [1,2,3]. Critical to the development of the fuel systems in these aircraft is an understanding of the fuel pyrolysis reaction mechanisms under the conditions that the fuels will be operating. Of particular interest are the reactions leading to polycyclic aromatic hydrocarbons (PAH), which can serve as precursors to fuel-line deposits [3,4], a problem of critical importance to avoid, for safe aircraft operation. In order to better elucidate the mechanisms and kinetics of the reactions of fuel pyrolysis and PAH formation under supercritical conditions, pyrolysis experiments are being conducted, under the present research program, with model fuels at temperatures of 300-600 °C, pressures of 20-100 atm, and residence times of 30-1000 sec. The model fuels include the jet fuel components toluene, 1-methylnaphthalene, and mixtures of toluene and *n*-heptane—as well as the "endothermic" fuel methylcyclohexane. The supercritical pyrolysis experiments are conducted in an isothermal silica-lined stainless-steel coil reactor specially designed [4,5] for such experiments, and PAH reaction products are analyzed by high-pressure liquid chromatography with diode-array ultraviolet-visible absorbance detection (HPLC/UV), an isomer-specific technique ideally suited for the analysis of PAH [6]. It is anticipated that the results from this research will provide information of critical importance to the design and development of fuel systems for high-speed aircraft.

TECHNICAL DISCUSSION

Supercritical pyrolysis experiments have been conducted with the model fuel toluene (critical temperature 319 °C, critical pressure 41 atm), and the reaction products have been analyzed by gas chromatography and HPLC/UV. For experiments at 535 °C and 140 sec, Figures 1-6 present the yields, versus pressure, of benzene and twenty-three of the PAH unequivocally identified as products of supercritical toluene pyrolysis [7,8]. The quantified PAH range in size from two to nine fused aromatic rings and are grouped as follows: Fig. 1—benzene, naphthalene, indene, and fluorene; Fig. 2—phenanthrene, anthracene, chrysene, and benz[*a*]anthracene; Fig. 3—pyrene and three pyrene benzologues; Fig. 4—fluoranthene and three fluoranthene benzologues; Fig. 5—benzo[*ghi*]perylene and three of its benzologues; and Fig. 6—1-methylnaphthalene, 2-methylnaphthalene, 2-methylanthracene, and 1-methylpyrene. In each of the plots of Figs. 1-6,

the filled circles are experimentally measured points; all of the curves represent fits of the data to first-order global kinetics expressions, as explained below.

The first thing to notice in Figs. 1-6 is that all of the PAH product yields are low, corresponding to the low level of toluene conversion in our experiments [7]. Even this low level of PAH production is important, however, with regard to the formation of carbonaceous solids. Experiments run at just 50 °C higher than the conditions of Figs. 1-6 result in repeated plugging of our reactor, due to the production of solid deposits. Under the high-pressure conditions of the toluene pyrolysis environment, therefore, it appears that even small levels of large PAH can serve as kernels for growth leading to carbonaceous solids.

As Figs. 1-6 demonstrate, the experimentally measured yields of all the PAH increase continuously with pressure, rising particularly dramatically at pressures above the toluene critical pressure of 41 atm. These pressure-dependent product yield data, taken at constant temperature and residence time, permit us to determine the pressure dependency of the global kinetic rate constants for formation of PAH in supercritical toluene pyrolysis. For our global kinetic analysis, we assume that the rate of production of each product B is first order in the concentration of toluene A, so

$$d[B]/dt = k[A] \quad (1)$$

where k is the global kinetic rate constant (in sec^{-1}) for the formation of B. For the range of conditions examined in our supercritical toluene pyrolysis experiments, the level of toluene conversion is very small, less than 1 %, so the concentration of A is effectively constant with time, at its initial value of $[A]_0$. Therefore, integration of Eq. 1 over time gives:

$$[B] = k[A]_0 t \quad (2)$$

or

$$[B]/[A]_0 = kt \quad (3)$$

where $[B]/[A]_0$ is just the yield of B, as plotted in Figs. 1-6.

For constant temperature (and pressures < 1500 atm), the pressure dependency of the rate constant k is given [9,10] as:

$$k = A \exp[(-\Delta V^\ddagger/RT)p] \quad (4)$$

where A is the preexponential factor (in sec^{-1}) and ΔV^\ddagger is the activation volume (in L/mole), defined as the difference between the partial molar volumes of the transition state and the reactants [10]. Substitution of Eq. 4 into Eq. 3 gives:

$$[B]/[A]_0 = At\{\exp[(-\Delta V^\ddagger/RT)p]\} \quad (5)$$

Therefore a set of product yield data at constant temperature and residence time but varying pressure lends itself to determining ΔV^\ddagger and A , if the data conform to the assumed first-order global kinetics.

Using the data from our supercritical toluene pyrolysis at 535 °C and 140 sec, we fit the experimentally measured yield/pressure data for each product to Eq. 5, determining the values of ΔV^\ddagger and A that best fit the data for each product species. A yield/pressure curve is then generated from the derived values of ΔV^\ddagger and A , to examine how well the experimental data conform to the assumed first-order behavior.

The curves in Figs. 1-6 show the results of this exercise for the yield data of benzene and twenty-three of the PAH produced from the supercritical pyrolysis of toluene at 535 °C and 140 sec. The close matching of the data points and curves for almost all of the PAH in Figs. 1-6—and the high values of the correlation coefficient R^2 (mostly > .99)—show that the data conform very well to the assumed first-order global kinetics model.

Figures 1-6 also display the values of $\ln A$ and ΔV^\ddagger that best fit the experimental data for each product. For most of the compounds, ΔV^\ddagger falls between -2.5 and -4 L/mole. The negative values of ΔV^\ddagger of course indicate that higher pressures favor formation of the PAH products, as the experiments demonstrate. The magnitudes of the ΔV^\ddagger values in Figs. 1-6 are typical for

reactions in supercritical fluids (two orders of magnitude higher than for liquid-phase reactions) [10,11].

The activation volumes in Figs. 1-6 are good indicators of just how highly pressure-sensitive PAH formation is in the supercritical toluene pyrolysis environment. For an activation volume of -2.5 L/mole at 535 °C, it takes an 18.4-atm rise in pressure to double the formation rate of the product PAH; for an activation volume of -4 L/mole, the formation rate doubles with a pressure increase of only 11.5 atm. Some of the larger PAH in Figs. 1-6, such as the 8-ring benzo[*pqr*]naphtho[8,1,2-*bcd*]perylene and the 9-ring naphtho[8,1,2-*abc*]coronene, exhibit negative activation volumes of even greater magnitude, underlining the extreme sensitivity to pressure of the formation rates of these large PAH. This result is of particular relevance to the formation of carbonaceous solid deposits, as large PAH are thought to be precursors to these solids [4]. The reaction mechanisms responsible for the formation of PAH in the supercritical toluene pyrolysis environment remain a principal focus of our ongoing research.

REFERENCES

1. Heneghan, S.P., Zabarnick, S., Ballal, D.R., Harrison W.E. III. "JP-8+100: The Development of High-Thermal Stability Jet Fuel," *Journal of Energy Resources Technology* 118: 170-179 (1996).
2. Doughtip, T., Ervin, J.S., Williams, T.F., and Bento, J. "Studies of Injection of Jet Fuel at Supercritical Conditions," *Industrial and Engineering Chemistry Research* 41: 5856-5866 (2002).
3. Edwards, T., Zabarnick, S. "Supercritical Fuel Deposition Mechanisms," *Industrial and Engineering Chemistry Research* 32: 3117-3122 (1993).
4. Stewart, J.F. "Supercritical Pyrolysis of Endothermic Fuels," Ph.D. Thesis, Department of Mechanical and Aerospace Engineering, Princeton University, 1999.
5. Davis, G.D. "An Experimental Study of Supercritical Methylcyclohexane Pyrolysis," M.S.E. Thesis, Department of Mechanical and Aerospace Engineering, Princeton University, 1994.
6. Wornat, M.J., Ledesma, E.B., and Marsh, N.D. "Polycyclic Aromatic Hydrocarbons from the Pyrolysis of Catechol (*ortho*-Dihydroxybenzene), a Model Fuel Representative of Entities in Tobacco, Coal, and Lignin," *Fuel* 80:1711-1726 (2001).
7. Wornat, M.J., AFOSR Grant No. F49620-00-1-0298 Final Technical Report (2003).
8. Ledesma, E.B., Wornat, M.J., Felton, P.G., and Sivo, J.A. "The Effects of Pressure on the Yields of Polycyclic Aromatic Hydrocarbons Produced During the Supercritical Pyrolysis of Toluene," accepted to *Proceedings of the Combustion Institute* 30 (2004).
9. Hubbard, C.D., van Eldik, R. In: R. van Eldik, C.D. Hubbard (Eds.). *Chemistry Under Extreme or Non-Classical Conditions*. John Wiley & Sons, Inc. and Spektrum Akademischer Verlag, New York, NY, and Heidelberg, Germany, 1999, p. 53.
10. Eckert, C.A., Knutson, B.E., and Debenedetti, P.G. "Supercritical Fluids as Solvents for Chemical and Materials Processing," *Nature* 383: 313-318 (1996).
11. Johnston, K.P., Haynes, C. "Extreme Solvent Effects on Reaction Rate Constants at Supercritical Fluid Conditions," *AIChE Journal* 33: 2017-2026 (1987).

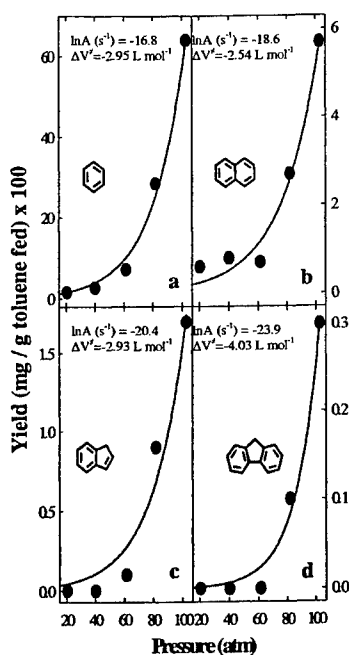


Figure 1. Yields, versus pressure, from toluene pyrolysis at 535 °C and 140 sec: (a) benzene; (b) naphthalene; (c) indene; (d) fluorene. Circles: experimental data. Curves: fits of the data to Eq. 5.

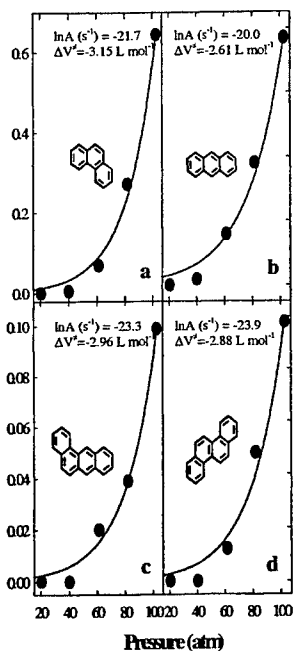


Figure 2. Yields, versus pressure, from toluene pyrolysis at 535 °C and 140 sec: (a) phenanthrene; (b) anthracene; (c) benz[a]anthracene; (d) chrysene. Circles: experimental data. Curves: fits of the data to Eq. 5.

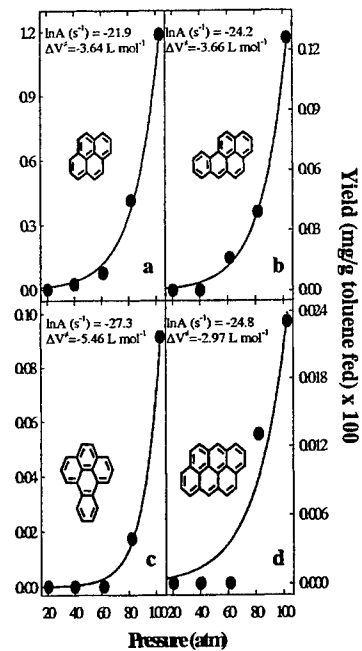


Figure 3. Yields, versus pressure, from toluene pyrolysis at 535 °C and 140 sec: (a) pyrene; (b) benzo[a]pyrene; (c) benzo[e]pyrene; (d) anthanthrene. Circles: experimental data. Curves: fits of the data to Eq. 5.

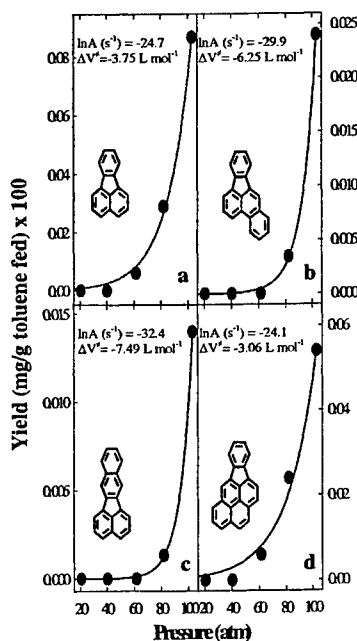


Figure 4. Yields, versus pressure, from toluene pyrolysis at 535 °C and 140 sec: (a) fluoranthene; (b) benzo[b]fluoranthene; (c) benzo[k]fluoranthene; (d) indeno[1,2,3-cd]pyrene. Circles: experimental data. Curves: fits of the data to Eq. 5.

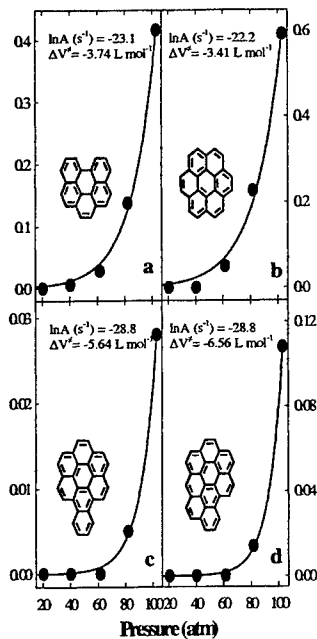


Figure 5. Yields, versus pressure, from toluene pyrolysis at 535 °C and 140 sec: (a) benzo[ghi]perylene; (b) coronene; (c) benzo[a]coronene; (d) naphtho[8,1,2-abc]coronene. Circles: experimental data. Curves: fits of the data to Eq. 5.

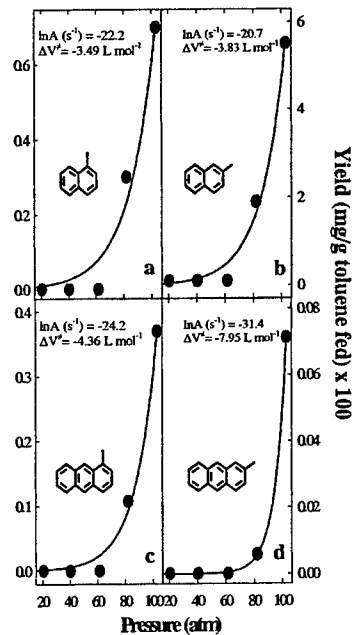


Figure 6. Yields, versus pressure, from toluene pyrolysis at 535 °C and 140 sec: (a) 1-methyl naphthalene; (b) 2-methyl naphthalene; (c) 1-methyl anthracene; (d) 1-methyl pyrene. Circles: experimental data. Curves: fits of the data to Eq. 5.

BURNING SPEED MEASUREMENTS OF JP-8 AIR MIXTURES AT HIGH PRESSURE AND TEMPERATURE

(Grant/Contract Number DAAD19-01-1-0587)

Principal Investigator: Hameed Metghalchi

Mechanical, Industrial and Manufacturing Engineering Department
Northeastern University
Boston, MA 02115

SUMMARY/OVERVIEW:

The objective of this research is to obtain a physical and fundamental understanding of JP-8 fuel characteristics as the U.S. Army's single fuel in battle field. The burning speed is a fundamental property of homogenous fuel/oxygen/diluent gas mixtures. It is of basic importance both for developing and testing chemical kinetic models of hydrocarbon oxidation and for a wide range of practical applications in the fields of engines, burners, explosions, and chemical processors. The research was focused in burning speed measurement of JP-8 air mixtures experimentally at a wide range of temperature and pressure. Measurements have been made in two constant volume combustion chambers; one spherical and the other a cylindrical with glass at both end caps which is used to visualize flame.

TECHNICAL DISCUSSION:

Measurement Methods

A number of different methods have been used to experimentally determine the burning speed. They can be characterized as being either constant pressure or constant volume methods. In this study, measurements have been done in constant volume chambers. Pressure as the primary output of the experiments is collected and is stored in a PC. A thermodynamic model that correlates the combustion vessel pressure rise to burning speed has been developed and is incorporated with the measurements. Structure of the flame has been observed using the cylindrical vessel and a Schlieren set up. The flame propagation has been optically recorded using a high speed CCD camera.

Theoretical Model

Burning speed is calculated using the equation below:

$$S_u = m v_u \&/ A_f \quad (1)$$

Where:

S_u : Burning speed

m : Mass of the gas mixture in the chamber

v_u : Specific volume of the unburned gas

\dot{x} : Mass fraction burning rate

A_f : Flame area

Using the volume and energy equations, temperature and mass fraction of burned gas are determined iteratively. Knowing the mass fraction burned one can calculate burned volume and then flame area. The unburned gas properties can be found in JANAF tables.

Results

Some experimental results are shown in the following.

Figure 1 shows the pressure-time history of stoichiometric JP8-air mixtures with initial temperature of 450 K and initial pressure of 1 atmosphere. In order to monitor the arrival time of the flame at the vessel wall and also to learn whether the flame was buoyant or not, three ionization probes have been used. Ionization signals are also shown in this figure. The signals verify that for this particular flame there is no buoyancy effect and flame is symmetrical. However increasing the initial pressure reduces the flame speed and also makes the flame buoyant.

Figure 2 shows Shadowgraph pictures of premixed stoichiometric mixture of JP-8 and air at initial temperature of 450 K and pressure of 1 atm. Each snapshot is taken 3 ms after the previous one starting from left to right and up to down. First picture is at $t = 0$. It can be seen that flame initially is laminar and smooth up to the point where pressure and temperature are about 5 atm and 650 K respectively. This is the onset of instability on the flame and where it turns to turbulent flame. Turbulent flames are faster than laminar ones partly since the flame area increases, hence increasing the mass flow rate of unburned gas into reaction zone.

Figures 3 and 4 show the burning speed measurements for JP-8 at a range of pressure and temperature for different stoichiometric ratios. Figure 3 indicates that the burning speed of JP-8 at 450 K and 1 atm is about 60 cm/sec. It can be seen in Figure 4 that increasing the pressure will decrease the burning speed.

The next step of this research is to study the characteristics of autoignition of premixed JP-8 air. Autoignition is determined by the sudden combustion pressure rise in the vessel. More results will be presented in the near future.

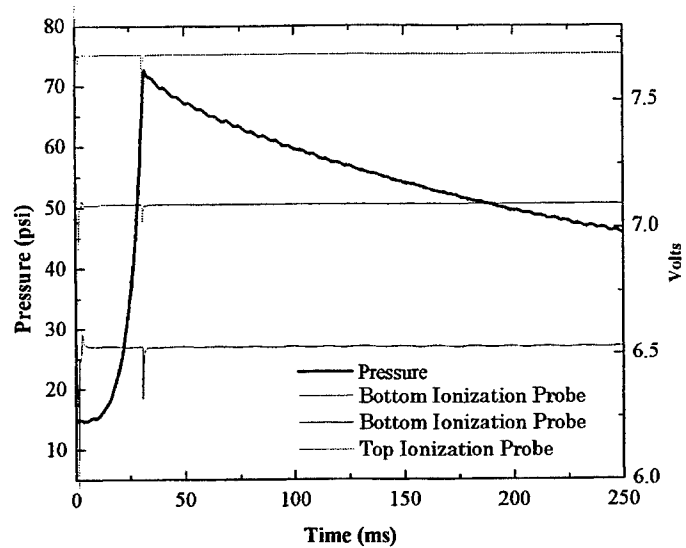


Figure 1: Pressure variation in a constant volume chamber for normal combustion without autoignition. JP8-Air, $P_i = 1$ atm, $T_i = 450$ K, $\phi = 1$.

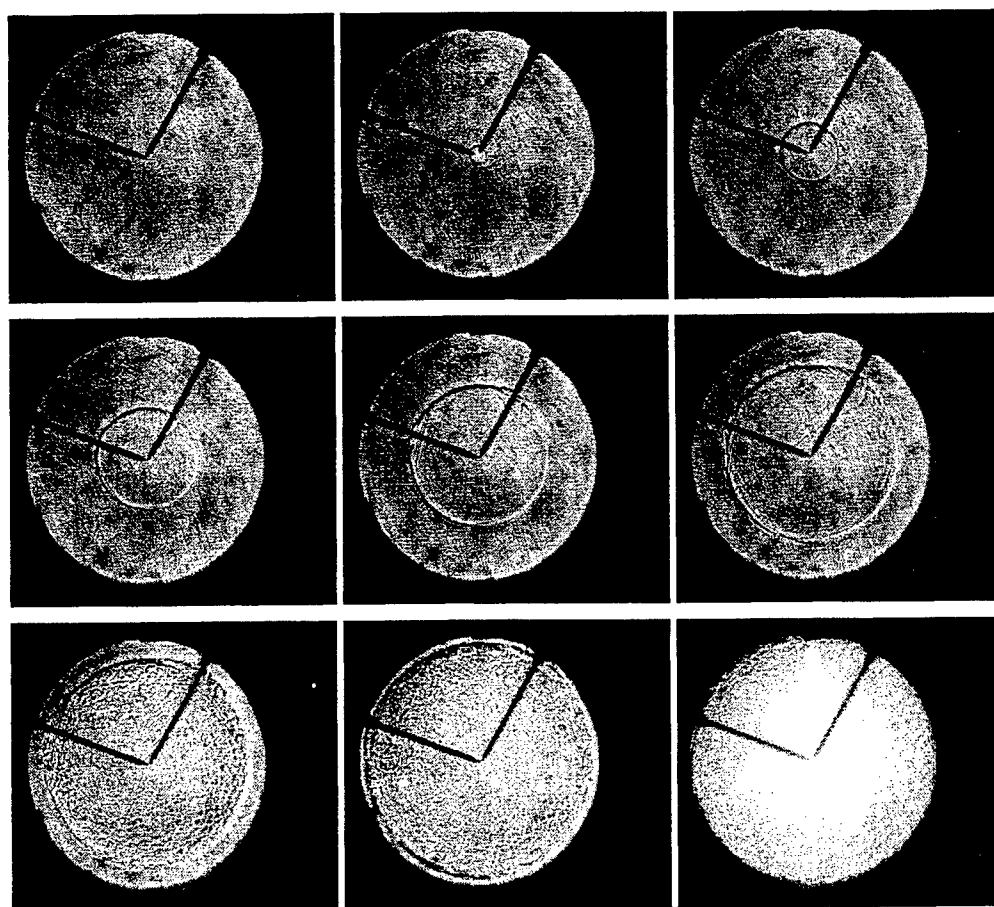


Figure 2: Flame propagation of stoichiometric JP-8 and air mixture at initial temperature and pressure of 450 K and 1 atm.

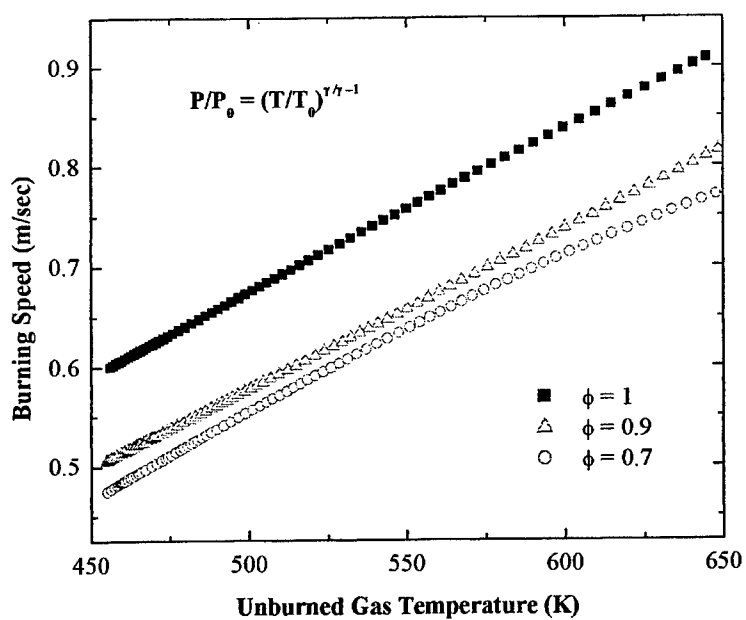


Figure 3: Burning speed measurements for mixtures of JP-8 and air at initial temperature of 450 K and initial pressure of 1 atm

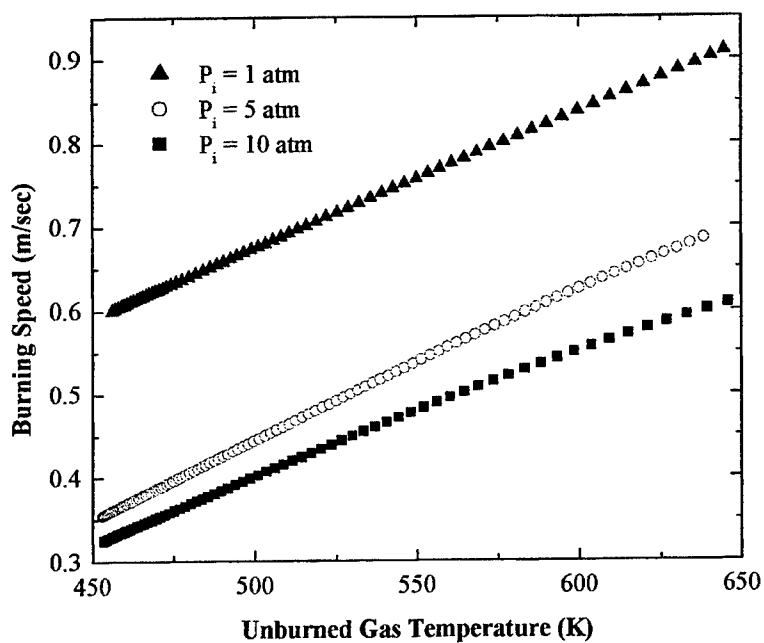


Figure 4: Burning speed measurements for stoichiometric mixtures of JP-8 and air at initial temperature of 450 K.

TIME RESOLVED MEASUREMENTS AND REACTIVE PATHWAYS FOR HYPERGOLIC BIPROPELLANT COMBUSTION

Grant Number DAAD190210356

Principal Investigator: James E. Smith Jr.

University of Alabama in Huntsville
Department of Chemical and Materials Engineering
Huntsville, Alabama 35899

SUMMARY

A modified laser diagnostic system was used to measure the chemical delay time (CDT) of pure components, mixtures, and oxygenated hydrazines reacted with red fuming nitric acid (RFNA) with improved resolution. The CDT of pure components, as well as binary and ternary mixtures of the three hydrazines reacted with RFNA under air were compared with respect to the Carbon/ Nitrogen atomic ratios. It was shown that greater performance across the entire domain can be achieved by carefully controlling tertiary mixtures to control the C/N ratio. With tertiary mixtures the toxicity of a given hydrazine is reduced from that of the pure component. It also suggests that adding an asymmetric polar compound, such as MMH, could reduce the CDT for other hydrazines or azides. The addition of an oxygenating agent, methanol, showed only significant increases with MMH, and not Hydrazine or UDMH. The CDT for MMH/Methanol mixtures at certain concentrations are faster than pure MMH suggesting that the addition of oxygenating compounds to asymmetric polar hydrazines or azides could reduce the CDT. When MMH/Methanol mixtures were created a heat of mixing was observed which led to the discovery that a change of volume upon mixing also existed for the mixture. The importance of carbon, oxygen, polarity and mass transfer resistance to the reaction mechanism of hypergolic bipropellants and reductions in toxicity relative to pure hypergols are discussed

TECHNICAL DISCUSSION

The CDT of pure components Hydrazine, MMH, and UDMH reacted with RFNA were compared to mixtures of the same species under both air and inert atmospheres.¹ UDMH demonstrated no significant difference, Hydrazine showed only a 4 % difference and for MMH there was a 23 % maximum difference in CDT between air and Argon gas. For hydrazine and MMH all results showed that CDT measurements conducted under air were faster than Argon.

MMH has at least one major difference, it is a highly asymmetric polar compound and this may be a contributing factor to the enhancements discussed. MMH can utilize more atmospheric oxygen than either Hydrazine or UDMH. In previous studies it was shown that 50 volume % UDMH in Hydrazine decreases the CDT by 71% relative to ideal mixture, making this mixture as reactive as MMH/RFNA.² Thus, the presence of carbon influences the CDT, clearly showing that carbon is important to the reaction mechanism. It is also obvious that too much carbon or no carbon at all slows the reaction.

In Figure 1, mixtures of Hydrazine/MMH were varied from 0-100 molar % MMH which resulted in a set of mixtures with C/N ratio in the range of 0-0.5. For mixtures with C/N ratios from 0.5-1, the addition of UDMH was necessary to increase the C/N atom ratio. Previous data contained only Hydrazine/UDMH mixtures with a C/N of 0-1. This addition of the asymmetric

polar compound MMH to Hydrazine/UDMH mixtures resulted in improvements in the CDT. Greater performance across the entire domain was achieved by carefully controlling tertiary mixtures to control the C/N atom ratio at the desired level. Using tertiary mixtures, the toxicity of a given hydrazine is reduced relative to the pure component.

There are several important aspects of Figure 1, the first is that previous data, triangles, are for mixtures of only Hydrazine/UDMH, while the new data, circles, are for mixtures of Hydrazine/MMH with a C/N of 0-0.5 and Hydrazine/UDMH/MMH mixtures with a C/N of 0.5-1. For the C/N of 0-0.5 the CDT of Hydrazine/MMH mixtures differed slightly from Hydrazine/UDMH mixtures. Another important fact is that with the system modifications, the CDT results are within the previous data range and have less relative error.

Therefore, the overall precision of the technique has been increased with the modifications in the experimental apparatus as well as CDT measurement techniques.¹ Also notice the differences in CDT for a C/N ratio from 0.5-1, shown in Figure 1. For the range of C/N ratio of 0.5-1.0 there is on average about a 46% decrease in CDT for the new data compared to the previous data. This is due to the fact that in previous data MMH was not included in the mixtures. This suggests that adding an asymmetric polar compound could reduce the CDT for other hydrazines and azides.

The data point shown as a square in Figure 1, previously measured by Mays (1998) at 0.4 ± 0.2 msec represented 8 measurements at an oxidizer to fuel mass ratio of 1.4.² This measurement was confirmed by Anderson (1999) of Talley Defense Inc. for the TRW Corporation.³ The modified laser diagnostic system discussed in previous papers has produced higher resolutions and increased precision as shown in Figure 1. Results at a C/N of 0.5 represent 6 measurements with a CDT of 0.2 ± 0.02 msec at an oxidizer to fuel mass ratio of 1.9.

It was shown previously that the presence of atmospheric oxygen during the combustion greatly effects MMH/RFNA reactions and only a slight to no effect for Hydrazine and UDMH/RFNA reactions.¹ Pure methanol was tested with RFNA and was not hypergolic. The reactions with Hydrazine and UDMH mixed with methanol produced two different combustion phenomena when reacted with RFNA. During several tests, the methanol evaporated and the remaining pool of hydrazine ignited, similar to normal hypergolic combustion of hydrazines, triggering an explosion of the now premixed methanol air mixture above the initial combustion zone. However at high concentrations (>10%) of methanol with pure Hydrazine and UDMH, contact with RFNA produced an immediate detonation which completely filled the combustion chamber with smoke, typical of incomplete combustion. Mixtures of UDMH, Hydrazine, and methanol at a constant C/N ratio of 0.3 were reacted with RFNA as shown in Figure 2. The C/N ratio of 0.3 was chosen because earlier CDT measurements of Hydrazine/UDMH mixtures showed that the minimum CDT occurred 50 % Hydrazine in UDMH by volume. For each Hydrazine/UDMH/Methanol mixture the concentrations of Hydrazine and UDMH were adjusted so that the resulting C/N atom ratio would be 0.3. By maintaining the C/N ratio constant at 0.3 on an atomic scale the only difference between the Hydrazine/UDMH mixtures without methanol and mixtures with methanol is the addition of oxygen and hydrogen atoms to the mix.

Figure 2 clearly shows that the CDT measurements for Hydrazine/UDMH/Methanol mixtures are constant with only slight fluctuations. Thus only a small amount of methanol can be added to the Hydrazine/UDMH mixtures. At the higher concentration, two separate phenomena,

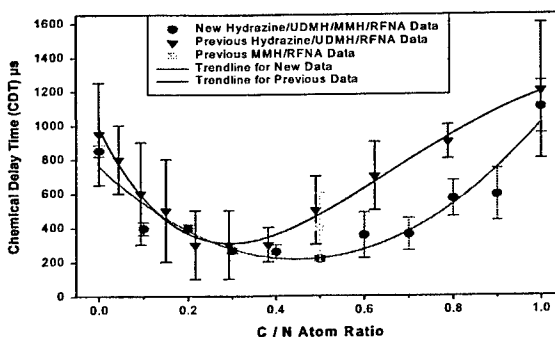


Figure 1: Comparison of CDT with Different C/N Atom Ratios

described above, often occurred. Methanol evaporation and the resulting explosion triggered by hypergolic ignition suggests that mixtures with higher contents of methanol be run at high pressure to prevent rapid evaporation of the methanol and permitting greater contact time between the hypergolic bipropellant mixtures. Methods are being considered to safely extend our experimental technique to operate at higher pressures to study such mixtures.

Previous experiments under Argon and air showed that MMH uses more oxygen during the combustion with RFNA.¹ This suggested that MMH could benefit from oxygenation. MMH was oxygenated with methanol up to 45 mole % and reacted with RFNA. Mixtures above 45 mole % immediately detonated similar to that discussed above, for Hydrazine and UDMH. CDT experiments for the range of 0-30 mole % methanol were conducted with fuel lead while experiments in the range of 35-45 mole % methanol were performed with oxidizer lead. The method of experimentation was changed at 30 mole % methanol from fuel lead to oxidizer lead in an effort to suppress detonation, as described above. For oxidizer lead in the range of 35-45 mole % methanol, detonation seldom occurred. Having to switch between fuel and oxidizer leads to prevent detonation again suggests that higher pressure operation could shift the combustion from a detonation to a deflagration.

Figure 3 shows the resulting CDT measurements for the MMH/Methanol mixtures reacted with RFNA. There exist two distinct regions, fuel lead (0-30 mole % methanol) and oxidizer lead (35-45 mole % methanol). The large errors at the higher concentrations are attributed to combustion instabilities associated with hypergolicity and methanol evaporation. Notice that the CDT for MMH/Methanol mixtures actually decreases from that of pure MMH to compositions of 20 mole %

methanol. A 23 mole % methanol mixture produced the same average CDT as pure MMH. Beyond the 20 molar % methanol the CDT increased. This suggests that the addition of oxygenating compounds to asymmetric polar hydrazines or azides could reduce the CDT.

Another important effect of oxygenating MMH with methanol is the reduced toxicity of the MMH/Methanol mixtures compared to pure MMH. Further investigations into the effects of oxygenating hydrazines and azides may reduce CDT and toxicity.

When the MMH/Methanol mixtures were prepared for CDT measurements, the solutions heated. Since both methanol and MMH are polar compounds, and polar mixtures often produce excess thermodynamic properties, a series of experiments were conducted to determine if both volume change and heat of mixing occurred for this system. The results in Figures 4 show that the density of the mixtures does not follow ideal solution behavior. For methanol concentrations below 23 mass % the mixture density was actually greater than that of MMH, as noted by the horizontal line added to Figure 4. The data point in Figure 4 at 32 mass % methanol does not

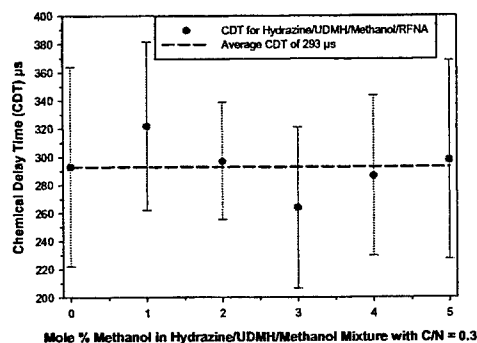


Figure 2: CDT for hydrazine/UDMH /Methanol/RFNA Mixtures

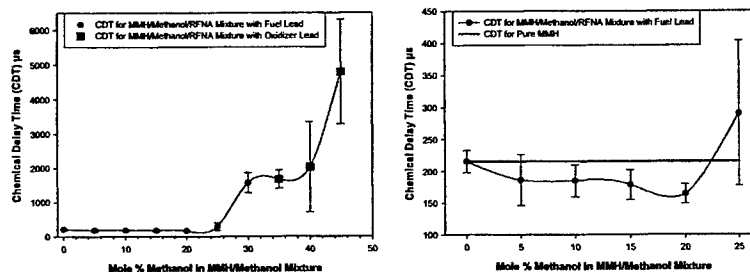


Figure 3: CDT Measurements for MMH/Methanol

appear to follow the trend of the other data points in the figure. We measured this point several times and each time the same result was obtained. This inflection point could suggest that two phenomena are taking place within this system that begin at ~23 mass % methanol and extends to 41 mass % methanol. Below 23 mass % methanol, stable hypergolic combustion occurred.

It is known that water additions to hydrazine produce hydrates, however, no references to a similar phenomena occurring in MMH could be found.⁴ It may be possible that an intermediate compound is being formed at compositions less than 32 mass % methanol, which is responsible for the decrease in CDT previously discussed. For compositions past 32 mass % methanol, pure volume change on mixing may explain the detonation phenomena observed in the system. The maximum increase in density is 3.5 % relative to ideal solution behavior.

Generally, the mixtures of hydrazines with other polar compounds are exothermic.⁴ For MMH/Methanol mixtures the heat of mixing was also exothermic. Figure 5 shows the heat of solution for MMH/Methanol mixtures. The maximum heat of mixing for the MMH/Methanol mixtures occurs between 40-50 mass % methanol. In this figure three distinct zones are apparent. The first is a well behaved zone extending to ~20 mass % methanol (~24 mole % methanol), this is followed by an inflection point that occurs at the identical concentration as seen in the volume change on mixing results, and within the region of 23 – 41 mass % methanol. Finally a third zone shows well behaved heat of solution data. Again with the exception of the single point (32 mass % methanol) that was confirmed several times the data follows what would be a typical heat of solution diagram. Below 23 mass % methanol stable hypergolic combustion occurred, while above 41 mass % methanol combustion was unstable and detonated.

CONCLUSION

The importance of carbon, oxygen, polarity and mass transfer resistance to the reaction mechanism of hypergolic bipropellants and reductions in toxicity relative to pure hypergols are important findings as we progress towards finding green replacements for pure hydrazines.

REFERENCES

1. Hampton, C. S., Ramesh, K. K., Berry, J. B., Smith, Jr., J. E., "Atmospheric Effects on the Chemical Delay Time for Hypergolic Bipropellants," AIAA Paper 2004-1381, AIAA 42nd Aerospace Sciences Meeting and Exhibit, Reno, NV, January 2004.
2. Hampton, C. S., Ramesh, K. K., and Smith, Jr., J. E., "Importance of Chemical Delay Time in Understanding Hypergolic Behaviors," AIAA Paper 2003-1359, AIAA 41st Aerospace Science Meeting and Exhibit, Reno, NV, January 2003.
3. Anderson, B. B., "Tertiary Amine Azide Hypergolicity and Hazards Evaluation," 1999 JANNAF SEPS/PDCS Meeting, San Diego, CA, April 1999 (Limited Distribution).
4. Schmidt, Eckart W., Hydrazine and its Derivatives, Vol 1 & 2, Wiley-Interscience; New York, (2001).

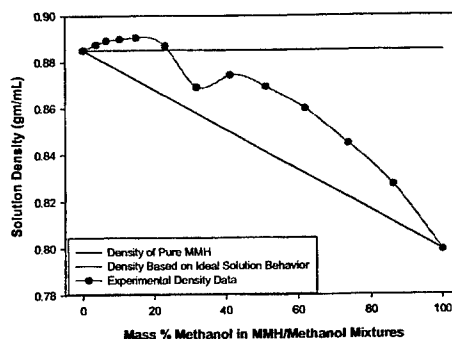


Figure 4: Change in Density

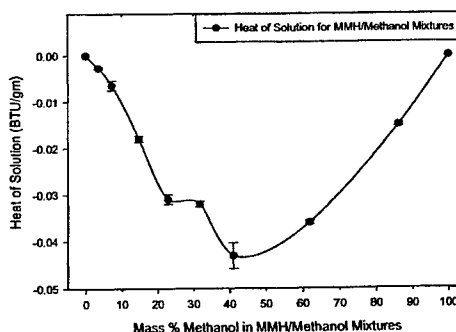


Figure 5: Heat of Mixing

PLASMA-PROPELLANT INTERACTION STUDIES

Grant Number DAAD19-03-1-0340

Principal Investigators: Stefan T. Thynell and Thomas A. Litzinger

Department of Mechanical and Nuclear Engineering
The Pennsylvania State University
University Park, PA 16802

SUMMARY

The overall objective is to gain insights about of the various chemical and physical processes that occur during ignition of a solid propellant by a high-pressure and high-temperature plasma. Two experimental approaches are being applied. A triple-quadrupole mass spectrometer is employed to examine species from the plasma and the pyrolysis products from the propellant generated by interactions with the plasma. A fast-response heat flux gauge has been designed and utilized to determine the transient variation of the radiant heat flux, with specific emphasis on the UV to near-visible components. Based on the experimental findings, radicals from the plasma are present near the surface to enhance the ignition of the propellant. Additionally, the UV-near-visible component of the emitted radiant energy is significant in the early portion of the event, and may augment the ignition event by both surface and in-depth radiation absorption.

TECHNICAL DISCUSSION

Species Measurement

Information of species in the plasma-propellant interface region is very important to the understanding of possible chemical enhancement. Species measurement over this region proved to be very challenging. Direct measurement in closed-chamber configuration is desired, but the chance for the sampler to survive the harsh conditions in the closed chamber is quite small. Moreover, the short time duration of the open-air plasma does not match the TQMS response. Additionally, since the plasma jet has a very low density, it is hard to detect any species within the jet with a relatively high intensity. These difficulties were overcome to some extent by the setup shown in Fig. 1.

The plasma-holding chamber is a long cylindrical chamber with one end attached to the plasma generator and the other extending to a test chamber. A tubular sleeve of polyethylene (PE) or Lexan was inserted in the holding chamber to vary its actual volume, and more importantly, to weaken the heat transfer from the plasma to chamber walls. On the bottom wall of the holding chamber is installed a small nozzle (1 ~ 2 mm I.D.) that uses elkonite to minimize material erosion. The test chamber has a 4x4x4 inch³ volume and is equipped with a 2.6 inch circular window for photography. The plasma-holding chamber coupled with a closed test chamber was considered as a promising setup in that the holding chamber prolongs the sampling duration through sampling a secondary jet from it rather than the primary plasma jet from the plasma generator.

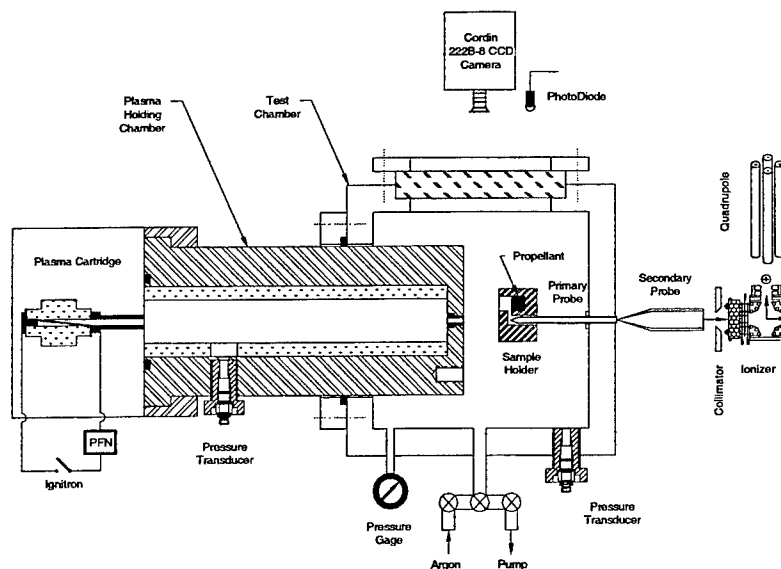


Figure 1. Setup for species measurement in a closed environment.

As an example, Fig. 2 displays the detected species as a result of recombination from the plasma species, i.e., C, H, C⁺, H⁺ and electrons. The left plot shows three species of higher intensities, including C₂H₂, C₂H₃, and H₂. Other species having relatively low intensities are CH₄, H, CH₃ and NO, and they are plotted in the right graph.

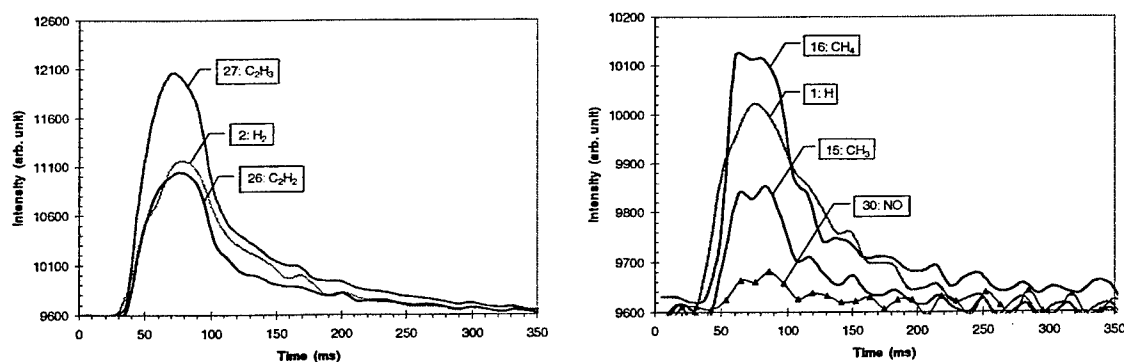


Figure 2. Recombined species from plasma: major (left) and minor (right).
Test conditions: 4kV, 3.2mm PE capillary, trigger plasma at 20ms.

Propellant species measurements were done with a double base propellant, JA2, and a composite propellant, M43. The propellant sample was placed about 13 mm downstream the secondary nozzle exit, and a 1.5mm hole provides a passage for any products from the propellant decomposition induced by the plasma interaction to reach the microprobe tip for sampling. Typical results are presented in Fig. 3 for JA2. In addition to the recombined species from the plasma, two other species coming from decomposition of the propellants were consistently detected for both propellants, which are NO and HCO.

Radiant Heat Flux Measurements

Sputtering has been employed to produce Pt-based, thin film heat flux gauges. The obtained electrical properties are adequate for measuring voltage drops, and therefore deducing the transient temperature variations. The typical heat flux gauge is 12 mm long, 80 nm thick, and 0.25 mm wide. The connections to the gauge are made via a 3mm wide, 500nm thick Cu film.

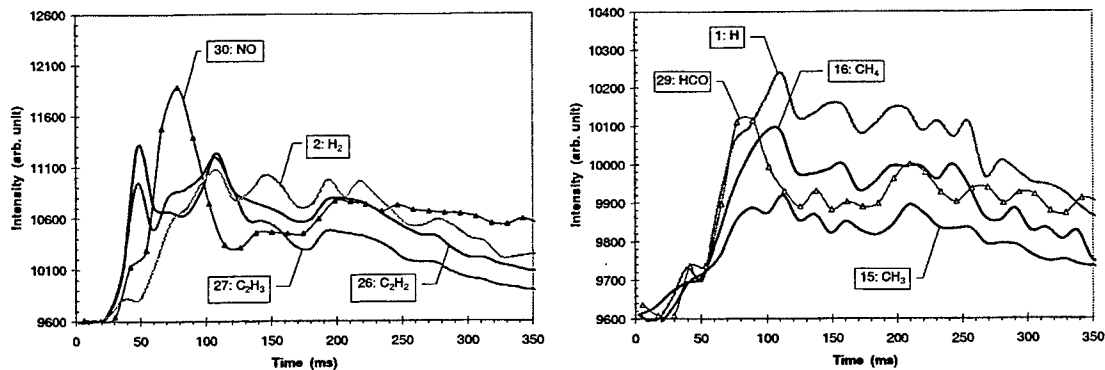


Figure 3. Species from plasma and decomposed JA2: major (left) and minor (right).
Test conditions: 5kV, 3.2mm PE capillary, trigger plasma at 20ms.

Figures 4 and 5 show the results from open-air testing involving a 3kV (870 J) plasma, with a distance between plasma exit port to stagnation plate of 75 mm. The heat flux gauges were covered with two S1-UV fused silica windows from ESCO Products (one is 1/16" thick, whereas the other is 3/16" thick); this window material is very pure and allows transmission over the wavelength range from about 170 nm to 2,500nm. The thin window is replaced after every test, since some slight degradation occurs of the surface, and only a small amount of sooty residue remains on the surface. Diode 1 (Si) is located directly below the plasma exit port, and is used to determine the time when the plasma emerges from the capillary into the ambient air environment. Diode 2 is also located below the plasma flow, but is placed about 25 mm in front of the stagnation plate. Both diodes thus have a side view of the plasma; their spectral range covers 300 to 900 nm. The heat flux and pressure gauges are located at the stagnation point, directly opposite to the plasma exit port.

Inspection of current I1 in Fig. 4 reveals that the current flow reaches a peak value at 83 μ s into the event, and that the plasma ceases to exist at around 200 μ s. Current I1 represents the current flow through the plasma chamber. At the end of the I1 current flow, there is still some residual energy in capacitor. It is slowly dissipated in the noninductive bypass resistor, which is used to deduce the instantaneous voltage drop. At this relatively low energy level of 870J, the plasma enters the ambient air 37 μ s after triggering. The second diode does sense the plasma emergence too, but this is caused by multiple reflections within the test facility. Diode 1, however, records a peak radiant heat flux that is approximately 100-fold larger than Diode 2. The occurrence of the peak value of the heat flux of Diode 1 is close to the occurrence of the peak value of the current I1. Diode 2 detects reemission near 280 μ s, which is probably due to interaction between plasma species and air as well as recombination reactions among the plasma products.

Figure 5 shows that the gauge temperature reaches a peak temperature of 140°C, the pressure reaches a peak value of 76 psig, and that the radiant heat flux reaches a peak value of 8.4 MW/m². The gas dynamic phenomena are complex as discussed previously, and captured modeling efforts by Nusca at ARL. The temperature rise is dominated by plasma emission during the time period prior to arrival of the precursor shock and thus shows a fairly smooth variation. The plasma quickly loses its sensible energy largely by radiation, and thus the gauge temperature decreases quickly due to surface emission and heat conduction into the substrate. Furthermore, inspection of Fig. 5 reveals that the early portion of the plasma emission is the most intense, corresponding to the time period up to peak current flow, or peak power dissipation.

From other measurements, the plasma has traveled only about 50 mm at a time of 80 μs into the event. Additionally, when using the S1-UV window material, the UV radiation component is so intense that at 1.5kJ of energy (4kV) and a distance of 50 mm, the gauges become vaporized; using pyrex windows, the films remain intact. Hence, the UV component is strong and its magnitude will be determined in upcoming series of experiments and data analysis.

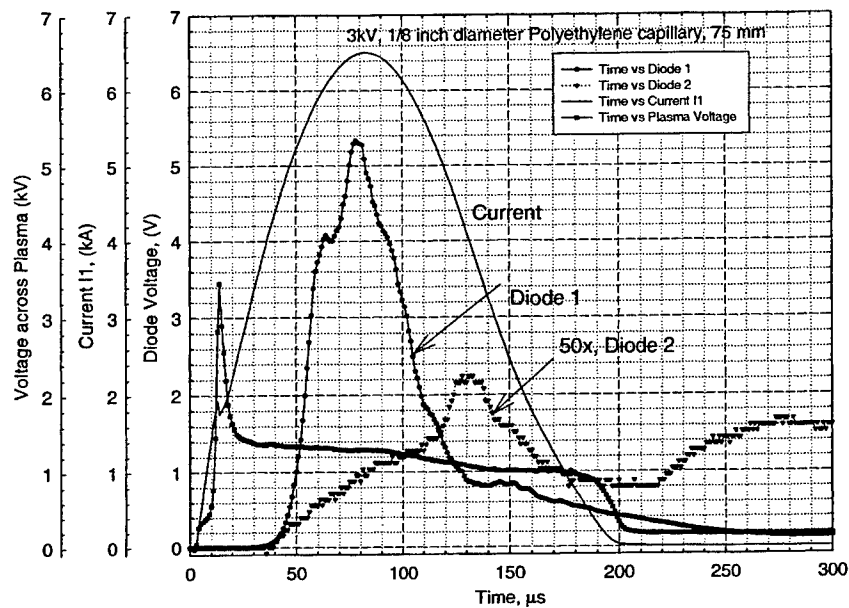


Figure 4. Current, voltage and diode traces for a 3kV (870J) plasma using a polyethylene capillary.

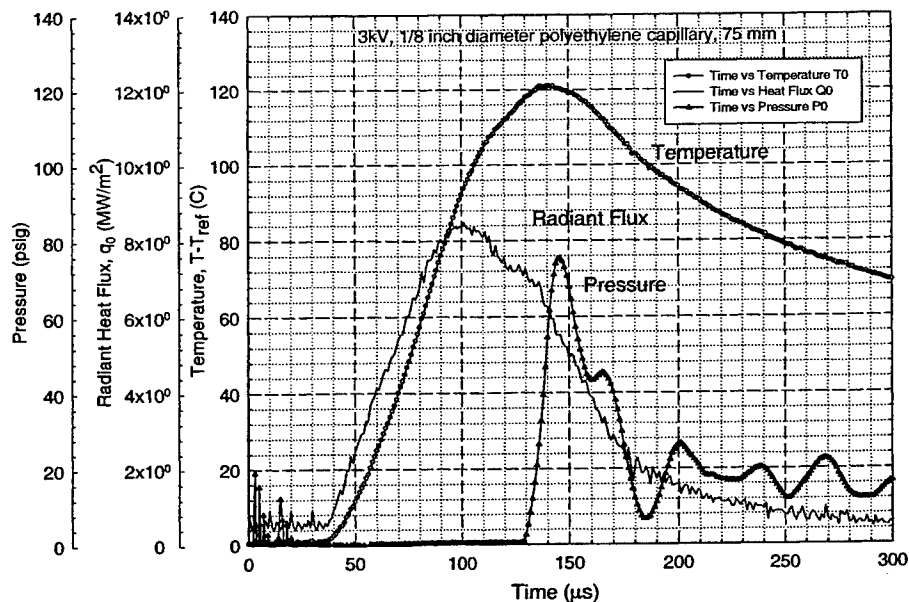


Figure 5. Measured temperature and stagnation pressure, as well as deduced absorbed radiant heat flux due to a 3kV (870J) due to plasma formed within a polyethylene capillary.

initial reflected shock temperatures of 1177 to 2009 K, pressures of 1.1 to 12.6 atm, and in fuel dilutions of 100 ppm to 1.25 % and equivalence ratios of 0.25 to 2 [1,2]. Comparison of these data with current reaction models indicates the need for accurate measurements of rate constants for several key reactions, including the initial fuel decomposition reactions, which would substantially improve the performance of these models in predicting ignition time delays and species concentration. Figure 1 presents representative OH concentration time history data for iso-octane, n-heptane and toluene ignition. The wide variation in the small radical pool behavior, exemplified by the OH concentrations, is evident.

2) Aromatics and conjugated olefins at low pressures: including toluene and 1,3-butadiene. Ignition time delays and OH radical concentration time histories were measured behind shock waves during the oxidation of these two hydrocarbons over initial reflected shock temperatures of 1230 to 2000 K, pressures of 1.5 to 7.5 atm, and in dilute fuel concentrations of 250 ppm to 0.5 % and equivalence ratios of 0.25 to 2 [3,4]. In the case of toluene, we find that our ignition time measurements differ significantly from the recent toluene measurements in France. In the case of 1,3-butadiene, the OH time history measurements can be used to distinguish between the Frenklach et al. (1983) and Laskin et al. (2000) reaction models for soot precursors; the early formation of OH seen in the current shock tube measurement supports the proposed 1,3-butadiene decomposition pathway suggested by the Laskin et al. model.

3) Iso-octane/air and toluene/air mixtures at high pressures. Ignition time delay times and pressure time histories were measured behind shock waves during the oxidation of iso-octane and toluene over initial reflected shock temperatures of 855 to 1269 K, pressures of 14 to 59 atm, and equivalence ratios of 0.5 and 1 in air [5]. The iso-octane ignition time measurements serve to validate an earlier study by Adomeit in Aachen, Germany. The toluene ignition time measurements represent the first high-pressure study of this fuel. Pressure profiles from these two studies shows evidence of cool flame chemistry and pre-ignition energy release.

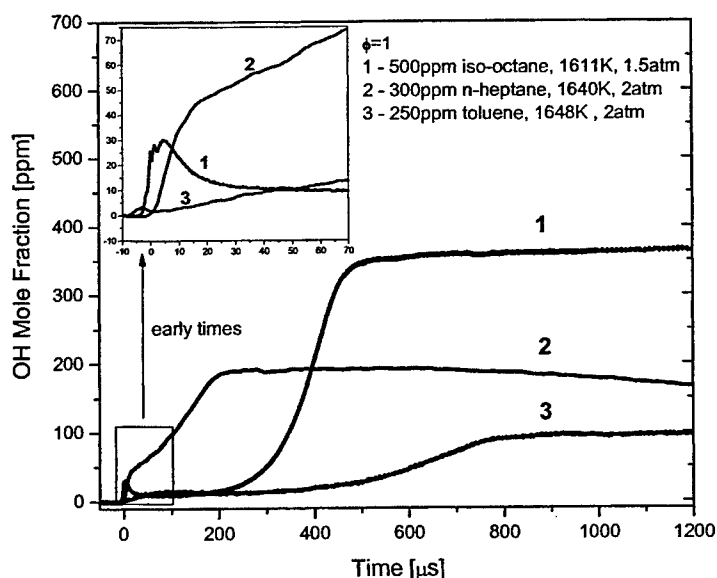


Figure 1. OH concentration time histories in these shock tube experiments were measured using narrow-linewidth ring-dye laser absorption at 306.5 nm. The initial OH concentration behavior is significantly different in the three fuel components: n-heptane, iso-octane and toluene, and is a result of different fuel decomposition products and oxidation pathways.

Shock Tube Studies of Fuel Sprays

Liquid fuels are predominant in mobile energy-conversion systems such as gas turbine combustors and internal combustion engines. While previous researchers have studied combustible sprays in shock tubes to learn about droplet breakup, evaporation, and ignition times, these studies generally have applied commercial injectors with wide droplet size distributions and relatively large droplets. Since the combustion of a two-phase mixture is strongly dependent on size-dependent droplet heating and evaporation rates, the results have largely been qualitative in nature, confused by the droplet size distribution, or quantitative only in specific situations.

To help remedy these deficiencies, we are developing a new spray test platform: an aerosol shock tube facility that can provide a relatively narrow droplet size distribution and a statistically uniform spatial distribution of droplets [6]. This facility should permit study of the full range of spray/shock interactions from simple evaporation, through ignition, to detonation. (See Fig. 2.) It will also be used as a test bench for the development of laser diagnostics for two-phase flows including diagnostics to measure droplet size and loading, fuel vapor concentration, temperature, transient species concentration time-histories, and to image reactive flow structures (e.g., detonation waves). This facility, based on a 10 cm diameter shock tube, provides a well-characterized two-phase flow with clear optical access for line-of-sight laser extinction and absorption measurements. A narrow aerosol size distribution is generated using an ultrasonic nebulizer. A uniform aerosol spatial distribution is provided by the use of pneumatically-controlled multiple inlet valves on the end wall. The spatial extent of the droplet-laden flow in the test section is controlled by timed valve closures and variations in the aerosol carrier gas flow rate.

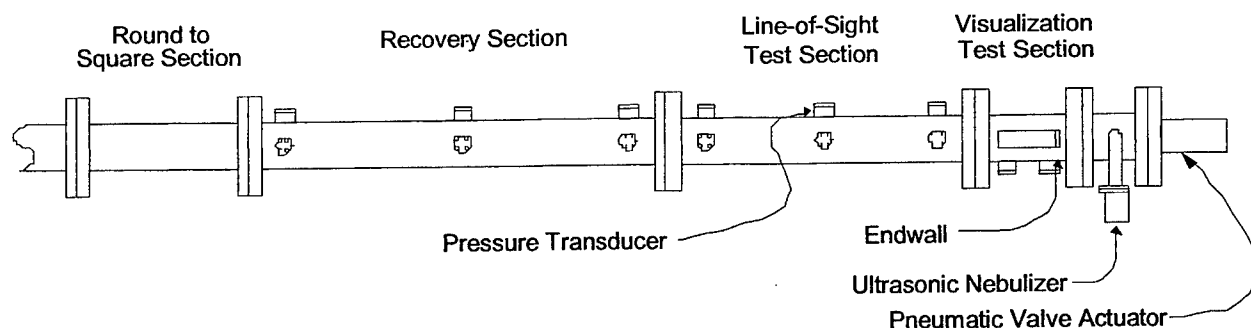


Figure 2. Schematic of aerosol shock tube facility. Incident shock waves travel from left to right, first entering a constant-area round-to-square section followed by a 1.25 m recovery section to ensure constant shock speed. Measurements may be performed in the line-of-sight test section (0.9 m in length) and visualization test section (0.3 m in length).

The facility is designed to permit extensive optical measurements. A visualization test section, with capabilities for large windows, is located at the end of the tube, allowing observation of phenomena occurring behind incident and reflected shock waves. Upstream of this section is another test section with numerous opposed windows allowing extensive line-of-sight diagnostics, such as wavelength-multiplexed extinction.

The first facility characterization tests are being carried out using water. We have fully characterizing the temporal evolution of droplet size distribution and loading and the spatial uniformity of a water aerosol in the shock tube test gas section, as well as concentration and temperature of the water vapor, during the filling phase and immediately before the arrival of the incident shock. These measurements have been made using both a commercial Mie scattering system and a multi-line IR laser extinction system developed in our laboratory (using 2 NIR lines near 1.39 microns for water vapor concentration and temperature, and four IR lines at 1.33, 1.997, 3.39 and 9.5 microns for droplet size distribution and loading.) Typical water aerosols generated are 4 microns in diameter with a volume log-normal distribution width of 2 microns with loading of the order of 10 ppmv; these exist in nearly 100% saturated water vapor at room temperature.

This multi-line system is currently being used to monitor water droplet time history (droplet size and loading, and vapor concentration and temperature) after passage of an incident and reflected shock wave. These data should provide new fundamental information on droplet evaporation rates behind shock waves.

Future work will concentrate on measurements of reactive mixtures: fuel/oxygen mixtures with n-alkanes fuels such as decane and dodecane, as well as with binary diesel fuel surrogates. In these reactive mixtures, we will study evaporation rates by measuring temperature, fuel droplet and vapor loading, as well as ignition delay times and radical species concentrations.

ARO-SPONSORED PUBLICATIONS (2003-2004):

1. M. A. Oehlschlaeger, D. F. Davidson, J. T. Herbon, and R. K. Hanson, "*Shock Tube Measurements of Branched Alkane Ignition Times and OH Concentration Time Histories*," International Journal of Chemical Kinetics 36: 67-78 (2004).
2. D. F. Davidson and R. K. Hanson, "*Interpreting Shock Tube Ignition Data*," in press, International Journal of Chemical Kinetics, January 2004; see also Western States Section/The Combustion Institute, Paper 03F-61 Fall Meeting, October 2003.
3. V. Vasudevan, D. F. Davidson and R. K. Hanson, "*Shock Tube Measurements of Toluene Ignition Times and OH Concentration Time Histories*," in press, Proceedings of the Combustion Institute 30, (2004).
4. C. S. Libby, D. F. Davidson and R. K. Hanson, "*A Shock Tube Study of the Oxidation of 1,3-Butadiene*," AIAA-2004-1322, 42nd Aerospace Sciences Meeting, January 2004.
5. D. F. Davidson, B. M. Gauthier and R. K. Hanson, "*Shock Tube Measurements of Iso-Octane/Air and Toluene/Air at High Pressures*," in press, Proceedings of the Combustion Institute 30, (2004); see also Western States Section/The Combustion Institute, Paper 03F-26 Fall Meeting, October 2003.
6. J. T. Kashdan, T. C. Hanson, E. L. Piper, D. F. Davidson, and R. K. Hanson, "*A New Facility for the Study of Shock Wave Induced Combustion of Liquid Fuels*," AIAA-2004-0468, 42nd Aerospace Sciences Meeting, January 2004.

POROUS MEDIA COMBUSTION CONCEPTS FOR PROPULSION GAS TURBINES

(Grant/Contract Number DAAD 190210082)

Principal Investigators: Ajay K. Agrawal, and Subramanayam R. Gollahalli

School of Aerospace and Mechanical Engineering
University of Oklahoma, Norman, OK 73019

SUMMARY/OVERVIEW:

Combustion using porous inert media offers several benefits for propulsion gas turbines such as high power density, stable operation over a wider turn-down ratio, homogeneous temperature field, lower combustion noise and reduced emissions of NO_x and CO. In this study fuel atomization, fuel/air mixing, and combustion processes using porous inert media are investigated experimentally and computationally. Pre-combustion and combustion processes are studied independently to demarcate the underlying physics of fuel preparation and chemical reactions. Specific tasks include characterization of droplet distribution and fuel vaporization upstream of the porous media. Combustion experiments involve NO_x and CO emissions measurements with the flame stabilized either on the surface or inside the porous media. Results demonstrate extension of lean-blow off limit with flame stabilized inside the porous media leading to lower NO_x and CO emissions.

TECHNICAL DISCUSSION

Liquid fuels account for a significant portion of combustion today as they are used in a wide range of applications including power generation, transportation and heating. Liquid fuels are traditionally burned in the form of sprays created by an injector. The injector must produce fine droplets, which are dispersed to produce a uniform fuel-air ratio distribution across the burner. These requirements allow greater control of the flame temperature to reduce the emissions of soot, nitric oxides (NO_x) and carbon monoxide (CO). Recent concepts include lean premixed/pre-vaporized (LPP) combustion and lean direct injection (LDI) combustion. In LPP combustion, a premixer is used to achieve complete vaporization and fuel-air mixing upstream of the combustion zone. However, the residence time needed to fully evaporate and mix fuel with air requires a long premixer, which is undesirable in most applications. Flashback, lean blow off (LBO), and acoustic resonance are other problems of LPP combustion. In LDI combustion, the fuel is injected directly into the air stream from multiple locations to allow rapid fuel vaporization and distributed fuel-air mixing.

Combustion within porous inert media (PIM) is another approach with the potential to improve vaporization and fuel-air mixing. PIM combustor typically consists of two regions. On the upstream end, a PIM of small pores is used to prevent flashback and to preheat reactants. The flame is stabilized within a PIM of large pores in the downstream region. The PIM promotes transfer of energy by conduction and radiation from the reaction zone to the incoming reactants. PIM combustion is of particular interest for liquid fuels because the energy transferred upstream may assist fuel vaporization and the twisting pathways of the PIM may promote fuel-air mixing.

Although gaseous fuel combustion using PIM has been investigated extensively, few studies have been conducted on liquid fuel combustion within PIM. Kaplan and Hall [1] tested several PIM combustors using heptane supplied from an oil spray nozzle. They found that the combustion stability depended upon parameters such as the properties of the porous material, the distance between the injector and PIM, and the pore size configuration. Trimis et al. [2] developed a liquid fuel burner that combines PIM combustion with cool flame vaporization. This burner was shown to produce low emissions over a power modulation range of 1:10. Jugjai et al [3] achieved combustion of kerosene by dripping the fuel onto a porous surface with the flame stabilized underneath. Heat transfer from the flame zone was shown to enhance fuel vaporization. A major challenge facing PIM combustion is the material properties of the porous media. So far, ceramics are the most widely used materials for PIM combustion. Although ceramics can withstand high temperatures, they lack structural strength to sustain thermal cycling for extended periods. Flow and combustion uniformity is another issue facing PIM combustion. Wharton et al. [4] found that "clogged pores" in the PIM created a non-uniform flowfield at the exit of a zirconia porous burner. The clogged pores were inherent to the manufacturing technique used to produce the porous material. New high temperature materials have become available in recent years. Examples include carbon-carbon composite or carbon foam with a coating of a high temperature material such as silicon carbide (SiC), rhenium, hafnium, or iridium, applied using the chemical vapor deposition technique. These materials offer the structural rigidity and oxidation resistance required for many combustion applications.

In this study, the carbon foam porous media coated with SiC is utilized to alleviate the materials issues. The spray characteristics are measured upstream of the PIM using a phase Doppler particle analyzer. The flow uniformity is evaluated by measuring axial velocity and turbulence intensity profiles at the PIM exit and pressure drop across the PIM. The combustion performance is quantified by measurements of temperature and NO_x and CO emissions at various operating conditions. The study seeks to investigate the potential of SiC coated carbon foam PIM to assist vaporization and fuel-air mixing with minimum pollutant emissions in liquid fuel combustion.

The experimental setup shown in Fig. 1 consists of four sections, namely, the inlet plenum, the vaporization and mixing section, the PIM section, and the emissions shield. The combustion air entered through fittings mounted on the inlet plenum on the upstream end of the apparatus. An air-assist atomizer (Delvan Type SNA) was used because of its excellent atomization characteristics over a wide range of fuel flow rates utilizing low-pressure air. The atomizer could be located at any axial position within the vaporization and mixing section. The combustion section was 10 cm long with 4.2 cm x 4.2 cm flow cross section and wall thickness of 0.64 cm. A 2.5 cm thick, 26 pores per cm (ppcm) porous piece was placed on the upstream end of the combustor to preheat the reactants and to prevent flashback. The combustion section consisted of three 4 ppcm porous pieces occupying the 7.5 cm length downstream of the preheat zone. Each porous piece fit tightly into the combustion section. A 0.3cm wide lip was placed around the walls to contain porous pieces within the PIM section. A 7.6 cm long emissions shield was mounted

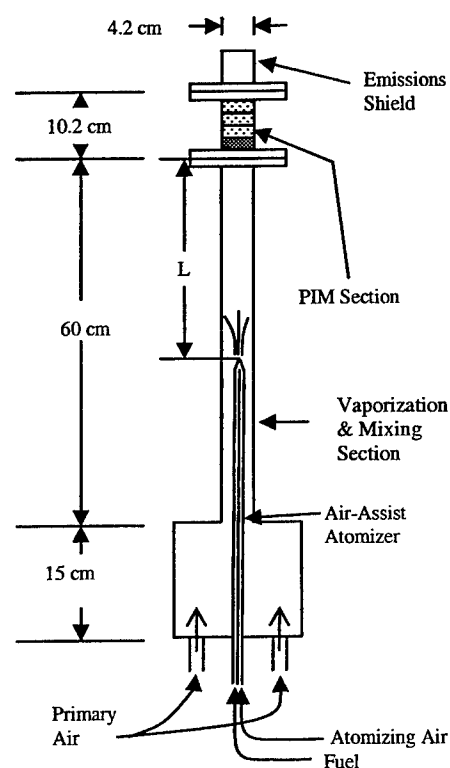


Figure 1. Schematic Diagram of the Combustor Setup

downstream of the combustion section to allow sampling of the combustion products. The entire assembly upstream of the combustion zone was insulated with 2.5 cm thick insulation.

An air compressor was used to supply the combustion air, which was dried and measured by a laminar flow element calibrated for 0-300 slm. Then, the air passed through an electrical heater and entered the experimental apparatus through two fittings attached symmetrically to the inlet plenum. The air temperature upstream of the combustor was monitored and maintained at 475 K. The atomizer air was unheated and its flowrate was measured with a calibrated mass flowmeter. The atomizer air flowrate was held constant at approximately 5% of the total air flowrate. Kerosene was supplied to the atomizer by a peristaltic pump (Masterflex M/S Variable Speed). A phase Doppler particle analyzer was used to measure the droplet diameter and axial velocity of the fuel spray in a separate but similar experimental setup. Axial velocity and turbulence measurements at the PIM exit were taken by a single hot-wire anemometer (TSI IFA 300). A traversing system was used to accurately move the probe to collect data at various locations. Three wall pressure taps were placed upstream of the PIM section. The pressure drop in the PIM combustor was found by averaging the wall pressure readings measured with a pressure transducer calibrated for ± 6.3 cm water. Emission concentrations were measured by a gas analyzer with electrochemical sensors. A quartz probe with a tapered tip was used to collect the gas sample. A bare fine-wire R-type thermocouple with 0.25 mm bead diameter was used for temperature measurements.

Figure 2 shows the radial mass flux distribution 1.4cm upstream of the PIM for different equivalence ratios. Higher mass flux is recorded away from the core region because of the swirling action imparted to the atomizing air. The axial velocity contours in Fig. 3 show nearly uniform flow exiting the PIM, indicating that the manufacturing technique used to produce the PIM did not create plugged pores. Turbulence intensity profiles indicated values of 1 to 4%. Figure 4 presents the drop for cold flow, air heated to 475K, and combustion within PIM. The pressure drop increased by 50% with combustion in PIM.

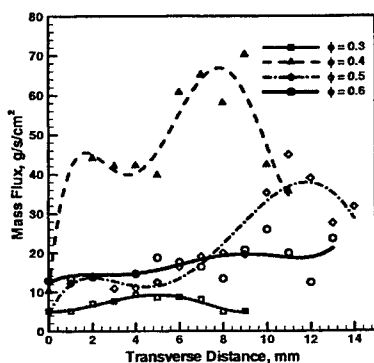
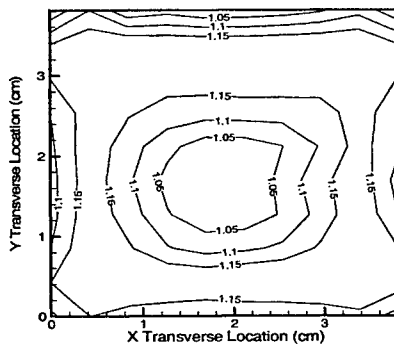


Figure 2. Radial Mass Flux Distribution



walls. The data obtained in the middle region of the combustor represent the performance of a large-scale PIM burner, without significant heat loss through the walls.

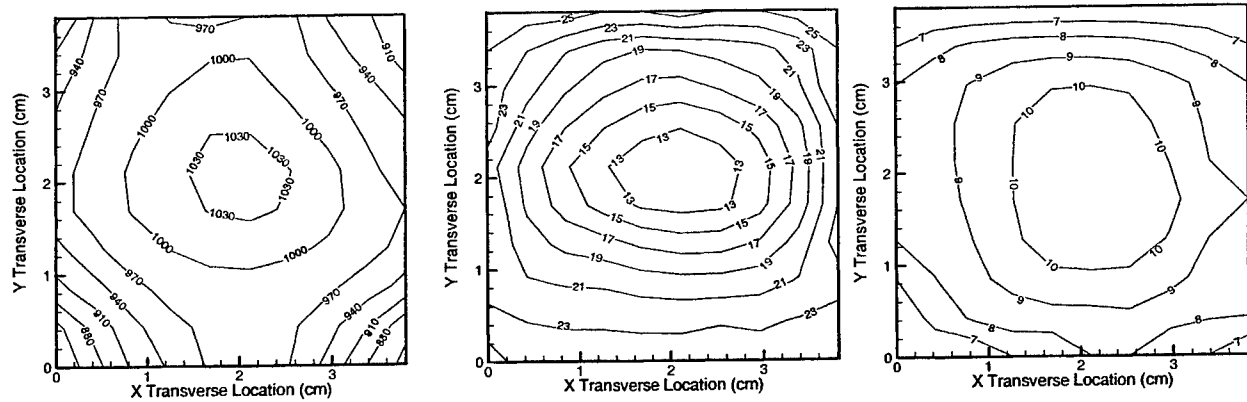


Figure 5. Contour plots of (a) Temperature, (b) CO Concentration, (c) NOx Concentration

Next, emission data were obtained by varying the atomizer location or L for $Q = 3.3$ kW and $\Phi = 0.67$. The profiles in Fig. 6 show nearly constant CO concentration in the middle region and a rise near the wall for all values of L . The variation in NOx concentration with the x-transverse location is less dramatic. The rise in CO and a slight decrease in NOx near the wall are caused by heat loss through the wall. Results show that CO and NOx concentrations are nearly the same for $L = 60$ cm and $L = 30$ cm. Thus, fuel and air were fully premixed at these locations. The NOx and CO emissions increased for $L=15$ cm, indicating inadequate vaporization and/or fuel-air mixing. For $L=10$ cm, the CO concentration increased dramatically to above 100 ppm for all equivalence ratio. An increase in soot particles was also observed visually. Measurements at different equivalence ratios indicated that in PIM combustion, locally fuel rich regions transfer energy to locally fuel lean regions to sustain burning at conditions leaner than the fully premixed case.

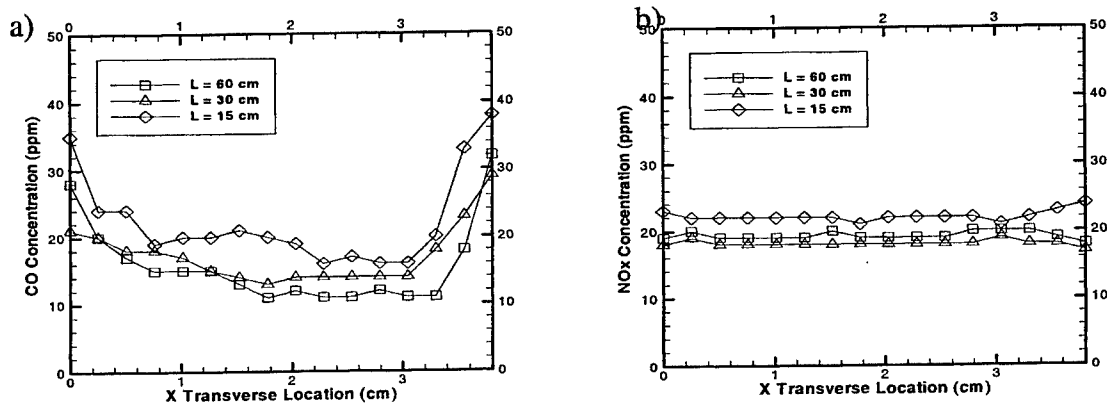


Figure 6. Profiles of a) CO and b) NOx concentration for $Q = 3.3$ kW, $\Phi = 0.67$

REFERENCES

1. Kaplan, M. and Hall, M.J., 1995, *Exp. Thermal Fluid Science*, vol. 11, pp. 13-20.
2. D. Trimis, K. Wawrzinek, O. Hatzfeld, K. Lucka, A. Rutsche, F. Haase, K. Kruger, C. Kuchen, *Proc. Of the Int. Conf. On Tech. And Combust. For Clean Environ.* 6 (2001).
3. S. Jugjai, W. Narongsak, T. Laoketkan, S. Nokkaew, *Exp. Therm Fluid Sci.* 26 (2002) 15-23.
4. J.A. Wharton, J.L. Ellzey, D.G. Bogard, *Joint Meeting of the U.S. Section of the Combust. Inst.* 3 (2003).

TURBULENT MIXING AND COMBUSTION FOR HIGH-SPEED, AIR-BREATHING PROPULSION APPLICATIONS

AFOSR Grant FA9550-04-1-0020

Paul E. Dimotakis

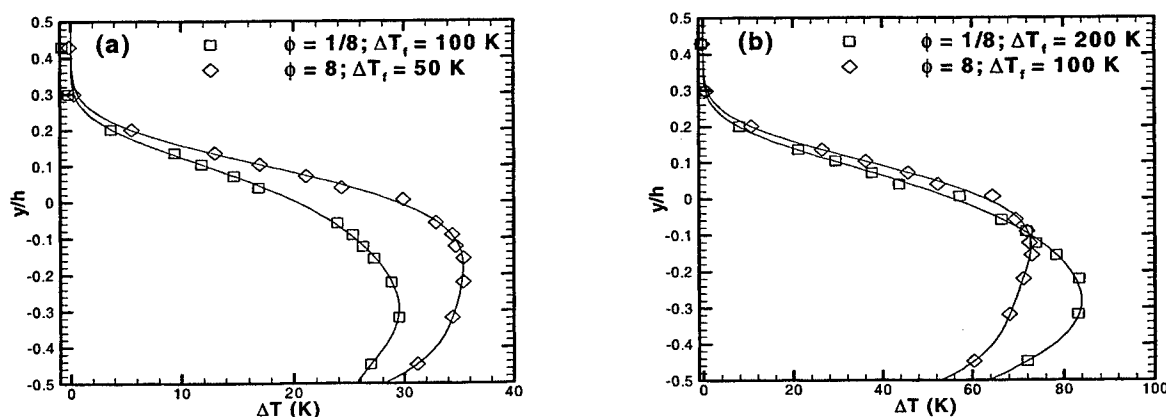
Graduate Aeronautical Laboratories, California Institute of Technology, Pasadena, CA 91125

Summary/Overview

This research focuses on investigations of mixing, chemical-reaction, and combustion, in turbulent, subsonic, and supersonic flows. It is comprised of an experimental effort; an analytical, modeling, and computational effort; and a diagnostics- and instrumentation-development effort. This is a brief report of work that began 1 January 2004 under this grant.

Technical discussion

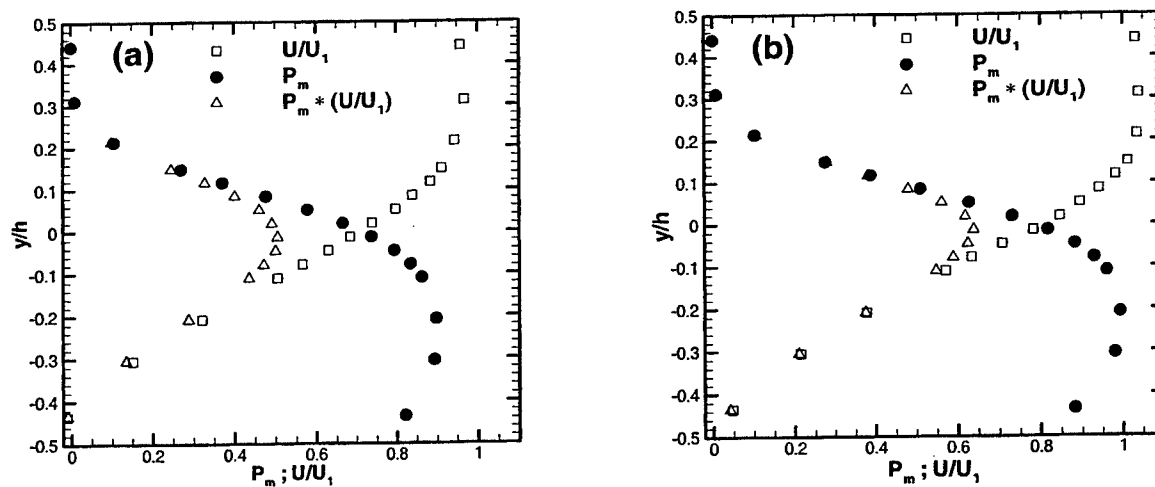
Work on mixing in scramjet-like geometries employed “flip” experiments (Mungal & Dimotakis 1984, Koochesfahani & Dimotakis 1986) at subsonic speeds to measure the amount of molecular mixing between freestream and injected fluids, and to quantify the benefits of a recirculation zone. Experiments were performed with freestream velocity $U_1 \approx 120$ m/s and an injection velocity $U_2 \approx 11$ m/s. A low-heat-release case (maximum temperature rise ~ 30 K) and a higher-heat-release case (maximum temperature rise ~ 80 K) were studied. The figure below illustrates the characteristic shift of the peak temperature-rise location towards the stream with the lean reactant. Case (a) is at low heat release and (b) is at higher heat release. $\phi=1/8$ means that the upper-stream reactant concentration is high and it is necessary to mix only 1/8-parts of upper-stream fluid per part of lower-stream fluid for complete consumption. For $\phi=8$, 8 parts (moles) of upper-stream fluid are required to fully consume reactants in 1 part (mole) of lower-stream fluid.



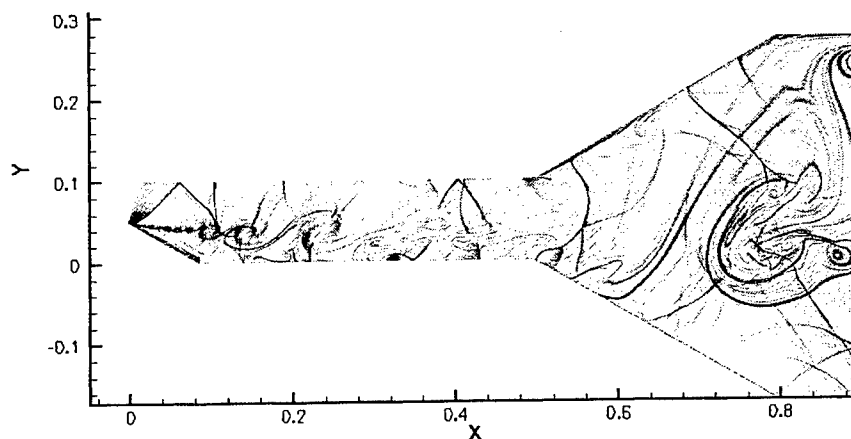
Using the shear-layer-entrainment model (Dimotakis 1986), a shear layer with a velocity ratio as in these experiments would have a volumetric (molar) entrainment ratio, $E_n = 1.57$. In free shear layers, this correlates well with mixed-fluid mean composition ratio. A composition ratio of 2.37 for Case (a) and 1.87 for Case (b) was measured with flip experiments, an increase of 50% and 20%, respectively, over a classical free shear layer, i.e., a significantly higher fraction of upper-stream fluid entrained and mixed in this flow.

Flip experiments also yield the (molecularly) mixed-fluid fraction, δ_m/δ . Dimotakis (1991) quotes a value for gas-phase shear layers of $\delta_m/\delta = 0.49$. Measured values are $\delta_m/\delta = 0.64$ and 0.71 for Cases (a) and (b), i.e., an increase of 31% and 45%, respectively, over classical shear layers. As found in previous work on heat-release effects, mixing initially increases with

increasing heat release. Experiments with higher heat release levels are required to see how far this trend continues before heat release decreases mixing benefits of the recirculation zone.



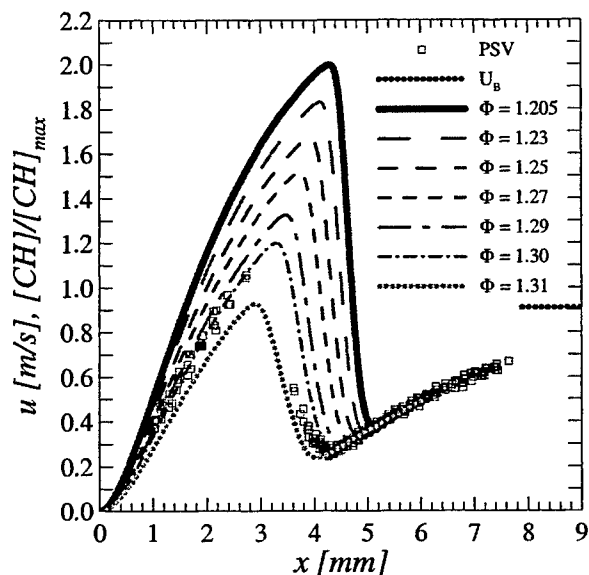
An important quantity for supersonic combustor flows is the exiting mixed-fluid flux. The figure above plots the normalized exit velocity, the probability of mixed fluid, and their product for the two cases studied. Case (a) is at low heat release and Case (b) is at higher heat release. In the recirculation zone, the probability of mixed fluid nearly reaches unity, demonstrating the good mixing properties for this flow. Integrating the profiles of mixed-fluid probability and normalized exit velocity yields a mixed-fluid volume fraction exiting the test section of 0.32 for Case (a) and 0.37 for Case (b). As with the mixed fluid fraction, δ_m/δ , this increases with increasing heat release. Further experiments are required to see how far this trend continues. Work in progress will focus on flip experiments at higher inlet velocities. This work is part of the graduate research of M. Johnson and E. Iglesias.



This flow is also under study computationally, using Euler equations and an improved geometry. Recent improvements rely on a downstream section with inclined top and bottom walls and a ramp represented with "open" (inflow jets) and "closed" (wall) portions. The figure on the left depicts a simulated schlieren image.

These improvements have brought simulations closer to experiment. The static pressure ratio between the top and bottom stream is used to control the angle of the shear layer and thus the angle of the oblique waves that form in the top (supersonic) stream. The computed flow is unsteady, with the angle of the shear layer changing during the simulation, qualitatively similar to the experimentally observed behavior. These simulations are two-dimensional, at this time. The work is part of the graduate research of G. Matheou and performed in collaboration with the Caltech DOE/ASCI program.

Other research targets the properties of strained, premixed hydrocarbon flames and their ignition and extinction characteristics, with a preliminary focus on methane-air flames. This study is important to both validate the experimental methodology, provide a dataset to improve current C_1 kinetics mechanisms, and yield data for scramjet design. Results of the work to date are documented in Bergthorson *et al.* (2004) and indicate good agreement between experiment and simulations for near-stoichiometric flames. One-dimensional simulations are performed using the *Cantera* reacting-flow software package (Goodwin 2003), with the GRI-Mech 3.0 chemical kinetics model (Smith *et al.*). Disagreement is found for both lean and rich flames. In an



attempt to isolate the source of this disagreement, the sensitivity of the solutions to the various boundary conditions is tested. The greatest sensitivity is found for the composition of the mixture. The figure on the left presents the experimental velocity data for a $\Phi = 1.205$ methane-air flame, compared to simulations at the measured equivalence ratio, at Φ increments toward better agreement. An error of $\approx 8\%$ in Φ would be required to achieve approximate agreement, which exceeds the maximum estimated measurement uncertainty (2%) for this quantity, indicating that the chemistry and/or transport models may be inadequate, even for methane-air flames at 1 atm.

The hydrodynamic, transport, and kinetics models used in this study are well documented. *Cantera*, however, is relatively new and the stagnation flame solver has not been thoroughly tested. To validate the solver, laminar flame speed estimates from *Cantera* are compared to simulations performed using the PREMIX package (Grcar *et al.* 1986). Flames are simulated, using *Cantera*, in a stagnation-flow geometry, as in the experiments, with a zero velocity gradient inlet boundary condition and varying inlet mass flux. This results in a family of flames with various imposed strain rates. The reference flame speed is taken as the minimum of the velocity profile (preheat zone) and the strain rate is defined as the maximum velocity gradient upstream of the flame (Wu & Law 1984). The strained flame data is then extrapolated to zero strain-rate, with only low-strain rate flames being used in the extrapolation. This minimizes errors due to the nonlinear dependence of the reference flame speed with strain-rate (Tien & Matalon 1991). The extrapolated results are compared to the simulated results using the PREMIX laminar flame code. The agreement is quite good near stoichiometry, with slight disagreement for very lean flames. The lean flames are near extinction in the simulated setup and extrapolation is difficult in this region. The results help verify the *Cantera* performance.

Sensitivity analysis was also performed for a $\Phi = 0.88$ flame with respect to the predicted CH-profile peak location, x_{CH} . The highest sensitivity is to the main chain-branching reaction [R38]; increasing this reaction rate increases the burning intensity, and x_{CH} , in the direction of agreement. Increasing the radical recombination reaction rate [R52] leads to decreased burning and the flame moves towards the plate (smaller x_{CH}). Such analyses can help assess kinetics models, as well as indicate the conditions where experiments should be performed. This work is part of the graduate research of J. Bergthorson.

A parallel research effort focuses on unsteady axisymmetric Direct Numerical Simulations (DNS) of this flow. Such a multi-dimensional simulation of chemically reacting flow is challenging with high computational costs. For such large-scale simulations, solver efficiency is

paramount. Several methods were investigated. Computational time was compared for Conjugate Gradient (CG), Static Condensation (SC) with CG, and static condensation with Cholesky decomposition, on an incompressible Navier-Stokes spectral-element solver for impinging jet flow. The study showed a two order of magnitude savings in computational time using static condensation with Cholesky. This is the method that will be used. We are currently in the process of parallelizing the code to perform a large-scale simulation. The table below lists the results of the study. Case A: pure CG. Case Ba: SC+CG. Case Bb: SC+Cholesky. Numbers are average time (ms) used per iteration. This work is part of the graduate research of K. Sone, is co-funded by the Caltech DOE/ASCI program, and co-advised by D. Meiron.

	Elements	Polynomial order	Case A	Case Ba	Case Bb
Test 1	62	8	3,268	296	45
Test 2	62	12	15,009	814	118
Test 3	62	20	115,717	2,661	660
Test 4	248	12	108,083	5,259	597

Work on a new experiment to study scalar dispersion has begun. This requires a new facility with digitally controlled optical scanning/imaging/acquisition. The facility consists of an 8'-long Plexiglas tow tank. A pulley system with stepper-motor controls will move suitable bodies to create the turbulence/dispersion to be studied. Fabrication of the facility has begun. Illumination will rely on a custom-built Nd:Yag laser, pulsed at 200 Hz. Imaging will rely on our custom-built low-noise KFS digital camera. With suitable collimating and sheet-aligning optics, the laser will sweep a rectangular 3D volume 200/ N times/s, where N is the number of steps per sweep. This part of the work is performed in collaboration with G. Katzenstein and D. Lang.

References

- BERGTHORSON, J.M., GOODWIN, D.G., AND DIMOTAKIS, P.E., 2004. Particle streak velocimetry and CH laser-induced fluorescence diagnostics in strained, premixed, methane-air flames. *Proc. Comb. Inst.* **30** (accepted).
- DIMOTAKIS, P.E. 1986 Two-Dimensional Shear-Layer Entrainment. *AIAA J.* **24**, 1791–1796.
- DIMOTAKIS, P.E. 1991 Turbulent Free Shear Layer Mixing and Combustion. *Prog. Astro. & Aeronautics* **137**, Ch. 5, 265–340.
- GOODWIN, D.G., 2003. An open-source, extensible software suite for CVD process simulation. *Proc. of CVD XVI and EuroCVD Fourteen, Electrochem. Soc.*, p. 155–162.
- GRGAR, J.F., KEE, R.J., SMOOKE, M.D., AND MILLER, J.A., 1986. A hybrid Newton/time-integration procedure for the solution of steady, laminar, one-dimensional, premixed flames. *Proc. Combust. Inst.* **21**, 1773–1782.
- KOOCHESFAHANI, M.M., & DIMOTAKIS, P.E. 1986 Mixing and chemical reactions in a turbulent mixing layer. *J. Fluid Mech.* **170**, 83–112.
- MUNGAL, M.G., & DIMOTAKIS, P.E. 1984 Mixing and combustion with low heat release in a turbulent shear flow. *J. Fluid Mech.* **148**, 349–382.
- SMITH, G.P., *et al.* http://www.me.berkeley.edu/gri_mech/.
- TIEN, J.H., AND MATALON, M., 1991. On the burning velocity of stretched flames. *Comb. Flame* **84**, 238–248.
- WU, C.K. AND LAW, C.K., 1984. On the determination of laminar flame speeds from stretched flames. *Proc. Combust. Inst.* **20**, 1941–1949.

A NEW CLASS OF HYBRID SCHEMES BASED ON LARGE-EDDY SIMULATION AND LOW-DIMENSIONAL STOCHASTIC MODELS

(Grant/Contract Number F49620-03-1-0023)

Principal Investigator: Tarek Echekki

Department of Mechanical and Aerospace Engineering
North Carolina State University
2601 Stinson Drive, Raleigh, NC 27695-7910

SUMMARY/OVERVIEW

The objective of this work is to develop and validate a novel class of hybrid schemes of Large Eddy Simulations (LES) and the One-Dimensional Turbulence (ODT) model for turbulent mixing and combustion. The proposed modeling approach provides an alternative strategy for the evaluation of closure terms in the momentum and scalar equations through fine-grained ODT simulations that are solved concurrently with or instead of LES. Challenges in the implementation of hybrid schemes include the actual coupling of a fine-grained and a coarse-grained simulations and the prediction of important physical phenomena related to the coupling of mixing and chemistry.

TECHNICAL DISCUSSION

Introduction

Turbulent mixing and combustion are governed by multiscale processes. In turbulent non-reacting flows, the multiscale nature of turbulent flows has given rise to an increasingly popular simulation approach, Large-Eddy Simulations (LES). The solution approach in LES is based on coarse-grained simulations, where physical phenomena are resolved down to a prescribed cut-off length scale, the LES spatial filter. The contribution of unresolved subgrid scales is modeled. The key assumption in such models is that smaller scales generally follow universal rules; while, the bulk of kinetic energy responsible for entrainment and transport resides in the large scales. However, important combustion processes, such as flames and ignition phenomena, may occur at scales below the LES cut-off filter size. The coupling between chemistry and transport occurs at LES-resolved and unresolved scales.

The Proposed Approach

In the context of turbulent mixing and combustion predictions, the principal hypothesis of this research proposal is as follows: hybrid schemes of LES coupled with low-dimensional stochastic formulations (such as the One-Dimensional Turbulence, ODT, Model) will lead to a better prediction of mixing and finite-rate chemistry effects in turbulent flows. The objective of the proposed work is to develop and validate a novel LES formulation for turbulent mixing and combustion flows that is based on the coupling of large-eddy simulation (LES) and One-Dimensional Turbulence (ODT) in the same computational domain.

Model Governing Equations

The proposed LES-ODT formulation is based on a distribution of ODT domains or elements, which are embedded in the LES domain. ODT solutions of scalar and momentum equations are filtered on the LES grid to provide filtered moments of the LES momentum and species

equations, including closure for the subgrid stresses, subgrid scalar fluxes, diffusive transport and chemistry.

LES Governing Equations for Turbulent Mixing and Combustion

The basic equations that govern both scalar mixing and combustion are the mass, momentum and scalar transport equations. Here the term 'scalar equations' is inclusive of many scalars of interest, which are used to track the progress of mixing, reaction, and other mechanisms including phase change. The LES-filtered governing equations are:

✦ Continuity equation

$$\frac{\partial \bar{\rho}}{\partial t} + \frac{\partial}{\partial x_j} (\bar{\rho} \tilde{u}_j) = 0 \quad (1)$$

✦ Momentum equations

$$\frac{\partial \bar{\rho} \tilde{u}_i}{\partial t} + \frac{\partial}{\partial x_j} (\bar{\rho} \tilde{u}_i \tilde{u}_j) = \frac{\partial \bar{\tau}_{ij}}{\partial x_j} - \frac{\partial}{\partial x_j} \left[\bar{\rho} (\widetilde{u_i u_j} - \tilde{u}_i \tilde{u}_j) \right] + \bar{\rho} \tilde{f}_i, \quad i=1,2,3 \quad (2)$$

Here, the ' \sim ' corresponds to a density-weighted (Favre-averaged) filtering of a given quantity, $\phi = \tilde{\phi} + \phi''$, which is expressed by $\tilde{\phi} = \frac{\bar{\rho} \phi}{\bar{\rho}}$. The quantity, ϕ'' , corresponds to the unresolved contribution to ϕ . $\bar{\rho} (\widetilde{u_i u_j} - \tilde{u}_i \tilde{u}_j)$ is the subgrid stress tensor.

✦ Scalars Transport Equations: Similarly, filtered equations for thermo-chemical scalars, \tilde{Z}_α , with an index α , may be formulated:

$$\frac{\partial \bar{\rho} \tilde{Z}_\alpha}{\partial t} + \frac{\partial}{\partial x_j} (\bar{\rho} \tilde{u}_j \tilde{Z}_\alpha) = \frac{\partial \bar{J}_{\alpha,j}}{\partial x_j} - \frac{\partial}{\partial x_j} \left[\bar{\rho} (\widetilde{u_j Z_\alpha} - \tilde{u}_j \tilde{Z}_\alpha) \right] + \bar{S}_\alpha \quad (3)$$

The terms on the right-hand side correspond to diffusive transport, the subgrid scalar flux and the filtered source term for \tilde{Z}_α , respectively.

ODT Governing Equations

The ODT equations for momentum, species and energy contain both resolved and unresolved contributions to their transport. The resolved contributions correspond to terms with values (including chemistry) and gradients along the ODT elements. The unresolved contributions correspond to transport terms from directions normal to the 1D domain. Here, the ODT 1D spatial coordinate is denoted as η , and (out-of-line) normal coordinates to η are x_1 and x_2 . The ODT element equations are as follows:

✦ ODT three-component momentum equation

$$\begin{aligned} \frac{\partial u_i}{\partial t} + \tilde{u} \frac{\partial u_i}{\partial \eta} = & -\frac{1}{\rho} \frac{\partial P}{\partial \eta} + \frac{1}{\rho} \frac{\partial}{\partial \eta} \left(\frac{\partial u_i}{\partial \eta} \right) + f_i \\ & + \frac{1}{\rho} \left\{ -\bar{\rho} \tilde{u}_1 \frac{\partial \tilde{u}_i}{\partial x_1} - \bar{\rho} \tilde{u}_2 \frac{\partial \tilde{u}_i}{\partial x_2} + \frac{\partial \bar{\tau}_{i1}}{\partial x_1} + \frac{\partial \bar{\tau}_{i2}}{\partial x_2} - \frac{\partial}{\partial x_j} \left[\bar{\rho} (\widetilde{u_i u_j} - \tilde{u}_i \tilde{u}_j) \right] \right\} \end{aligned} \quad (4)$$

✦ ODT species equation, $k=1, \dots, N$

$$\begin{aligned} & \left(\frac{Y_k}{t} + \tilde{u} \frac{Y_k}{x} = \frac{1}{\rho} \frac{J_k}{x} + \frac{\dot{\cdot}}{\rho} \right) \\ & + \frac{1}{\rho} \left\{ -\bar{\rho} \tilde{u}_1 \frac{\tilde{Y}_k}{x_1} - \bar{\rho} \tilde{u}_2 \frac{\tilde{Y}_k}{x_2} + \frac{\bar{J}_{k,1}}{x_1} + \frac{\bar{J}_{k,2}}{x_2} - \frac{1}{x_j} \left[\bar{\rho} u_j Y_k - \tilde{u}_j \tilde{Y}_k \right] \right\}, \end{aligned} \quad (5)$$

✦ ODT energy equation

$$\begin{aligned} & \left(\frac{\partial T}{\partial t} + \tilde{u} \frac{\partial T}{\partial \eta} = \frac{1}{\rho c_p} \frac{\partial P}{\partial t} + \frac{\dot{q}''}{\rho c_p} - \frac{1}{\rho c_p} \sum_k h_k \dot{\omega}_k \right) \\ & + \frac{1}{\rho c_p} \left\{ -\tilde{u}_1 \frac{\partial \tilde{T}}{\partial x_1} - \tilde{u}_2 \frac{\partial \tilde{T}}{\partial x_2} + \tilde{q}_1'' + \tilde{q}_2'' - \frac{\partial}{\partial x_j} \left[\bar{\rho} u_j T - \tilde{u}_j \tilde{T} \right] \right\}, \end{aligned} \quad (6)$$

where \dot{q}'' is the heat flux term. The terms inside the brackets “{.}” in the ODT governing equations correspond to contributions from out-of-line transport terms; therefore, they are not resolved by a single ODT element. Their contribution may be evaluated either by 1) filtering of the ODT solutions in the entire domain or by 2) using the solution from the filtered LES governing equations. These terms are crucial for momentum and scalar transfer between ODT elements. In combustion, these transfers may provide robust mechanisms for ignition stabilization and propagation, especially in inherently non-parabolic problems.

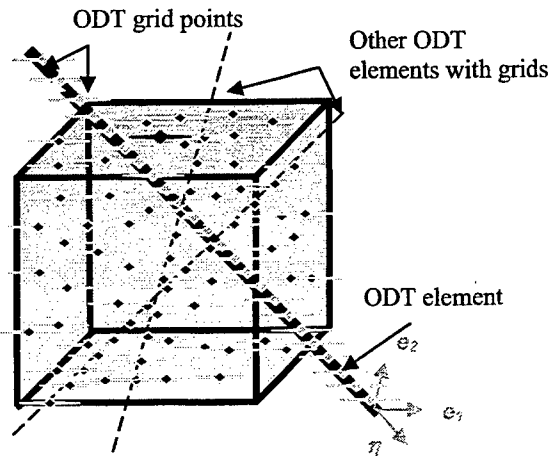


Figure 1. Illustration of ODT elements within a LES grid. Filtering of data to the LES grid may be treated the same way as in particle or vortex methods to represent a weighted contribution from ODT grid points. However, the most important distinction from particle methods is that diffusive transport and mixing (through stirring events) are represented in a resolved manner along ODT elements, potentially improving the representation of transport.

Model Illustration: Scalar mixing in decaying homogeneous isotropic turbulence

The above formulation is implemented for the mixing of a passive scalar in decaying homogenous isotropic turbulence. Although the ultimate goal of this work is to implement a Lagrangian formulation of ODT elements to better represent combustion phenomena, the formulation is tested first using a fixed matrix of ODT elements embedded along a Cartesian grid, as shown in Fig. 1. Both the initial turbulence and scalar fields are imposed using a Passot-Pouquet spectrum of the form $B k^4 \exp \left(-k/k_r \right)^2$, where B is the amplitude and k_r is a reference wave number that determines the characteristic length scale associated with velocity and scalar fluctuations. The simulations below are illustrated for a Taylor scale Reynolds number of 80. A number of implementation approaches have been attempted. The results shown below are based the approach of combining the solution of the LES equations (1)-(3) and the ODT equations (4)-(5). The ODT solution provides closure for the subgrid stress and the subgrid scalar fluxes. The turbulence is maintained at a fixed level by the

forcing of the LES-resolved velocity field. Initial ODT profiles are obtained by linear interpolation from the LES grid of the velocity components and the scalar field. The LES resolution is 16^3 over a domain size of 2^3 .

Figure 2 shows two representative 1D ODT scalar profiles and correspond 3D LES scalar fields at two different times of the scalar evolution. The ODT profiles show both small scale and large scale variations of the scalar field, in contrast with the 3D LES scalar fields.

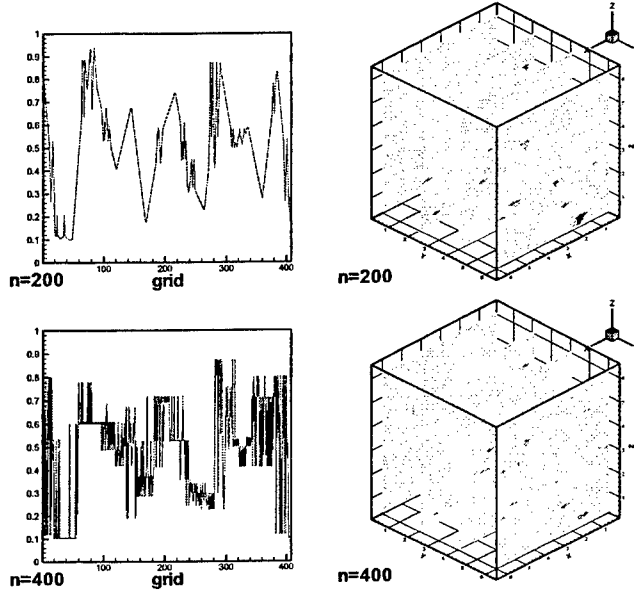


Figure 2. Typical ODT profiles and LES contours of the scalar field.

Figure 3 shows ODT scalar spectra evolutions from the initial field, and is presented at regular time intervals. The spectra are normalized by the correlation, $\overline{\phi''^2}$. The figure shows that initially, the bulk of the 'energy' of scalar fluctuations are in the range resolved in LES because of the linear interpolation process. As the solution for the scalar and velocity fields evolves, the scalar spectra extend to the high-frequency ODT-resolved range, and the mixture evolves to a more homogeneous mixture.

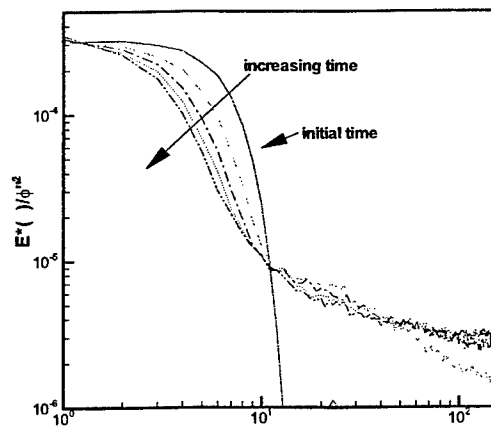


Figure 3. Evolution of the scalar spectra at different times of the LES-ODT solution.

PARTICULATE SIZE AND COMPOSITION

(DAAD19-00-1-0487)

Principal Investigator(s): D. Foster

Engine Research Center
University of Wisconsin-Madison
1500 Engineering Drive, Madison, WI 53706

SUMMARY/OVERVIEW:

Particulate mass is the regulated quantity for Diesel engines. The size, number, and composition of particulates in Diesel exhaust varies with engine operating condition. As particulate characteristics vary, so too will the detectability and health hazard characteristics. The project outlined here shows a sample of recent results measuring the variation in particulate number, size and composition.

TECHNICAL DISCUSSION:

During this research, we were fortunate to have the opportunity to use an atmospheric time of flight mass spectrometer (ATOFMS). The instrument was brought to the Engine Research Center as part of a NSF collaborative equipment use research grant. The instrument is capable of sampling individual particles at a rate of up to 150 particles per minute and measuring their size (within a size range of 0.15 to 5.0 μm) and chemical composition. An example of these data is shown in below, which shows the percentage of particles containing organic carbon versus particle size for three different loads at 1200 RPM. It appears that there is a tendency for organic carbon to be found in the smaller particles. This is consistent with the conceptual picture that the organic carbon originates from semi-volatile organics that nucleate, forming small particles, which dominate the smaller size distribution.

Detailed chemical analysis was done on the particulate samples in an attempt to identify the origin of the organic carbon found in the particulate matter. The relative distribution by carbon number of elutable hydrocarbon is given in Figure 2. The fraction of carbon compounds that would most likely be attributed to lubricating oil, carbon numbers greater than 30, only constitutes a small portion, less than approximately 25%, of the organic carbon found in the particulate. It cannot be determined whether the smaller carbon number molecules are fragments of the larger oil molecule, or originate from the fuel.

Further resolution of the organic carbon species is shown in Figures 3 and 4. As shown in Figure 3, the chemical compounds have been classified by their structural groups. The results are plotted as specific emissions, $\mu\text{g}/\text{ihp-hr}$, so one should not correlate the magnitude of the bar graph with the actual mass of the emission from the engine. What can be seen from this plot is the range of chemical compounds that are found in the particulate matter. For example, the families of compounds of hopanes and steranes are only found in the lubricating oil. The n-alkanes can be found in either the lubricating oil or the fuel, depending on the size of the base chain. The alkylcyclohexanes and the polycyclic aromatic compounds are probably from

pyrolysis reactions during combustion. One trend that is seen in studying Figure 3 is that the relative contribution of fuel, lubricating oil and combustion pyrolysis products changes with engine operating conditions.

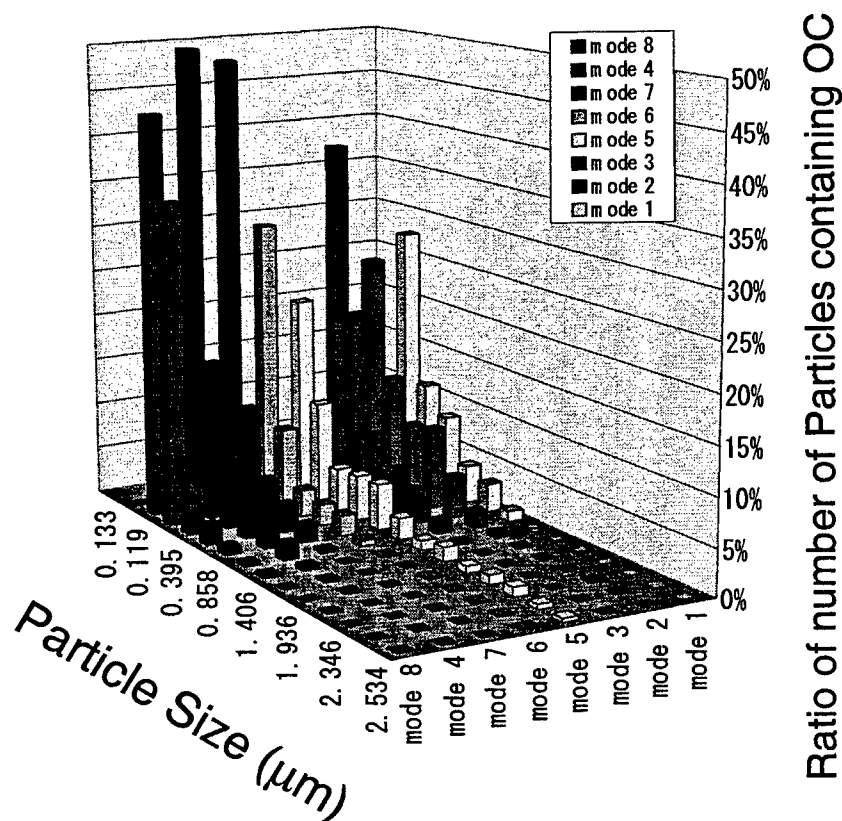


Figure 1. An Example of ATOFMS data. The partitioning of the particulates into size categories and the percent of particles in each size category that contain organic carbon. Fuel A – D2

An even more detailed analysis of the polycyclic aromatic hydrocarbon (PAH) compounds is shown in Figure 4. It is seen from the data that the PAH are only present for the in the light load conditions, where the organic carbon proportion of the particulate matter is high.

Particle size distributions were measured using an SMPS for a wide range of operating conditions. One can see that at idle and light load conditions the particle distribution is skewed towards the smaller particles. These small particles contribute very little to the total mass loading, even though their number density is very high. At the heavier loads the number of nano-sized particles decreases and more accumulation mode particles are present. From the distributions shown in Figure 5 it is readily observed that the increase in particulate mass emissions from the engine with increases in load is the result of a larger number of accumulation mode particles being emitted.

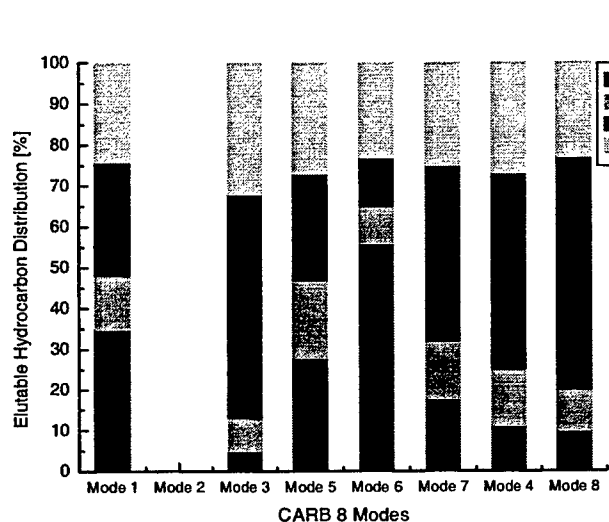


Figure 2. Distribution of elutable hydrocarbons within the particulate matter in terms of carbon number for the different engine operating modes.

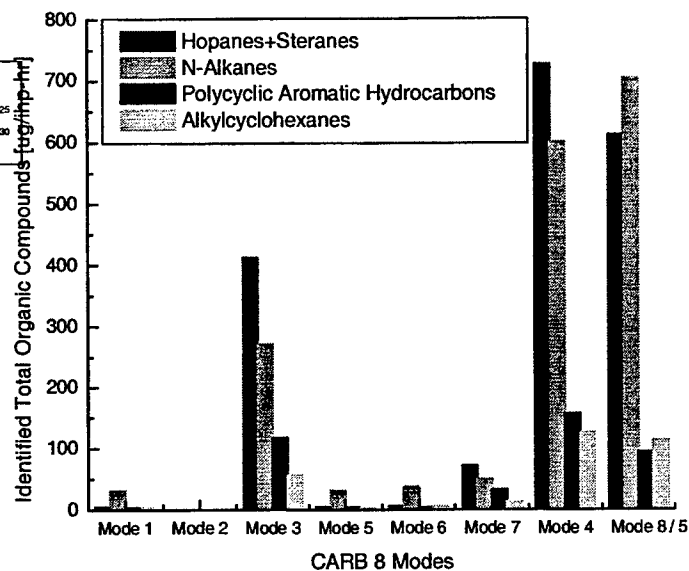


Figure 3. Summary of the distribution of chemical structural groups observed in diesel particulate matter. Fuel is D2

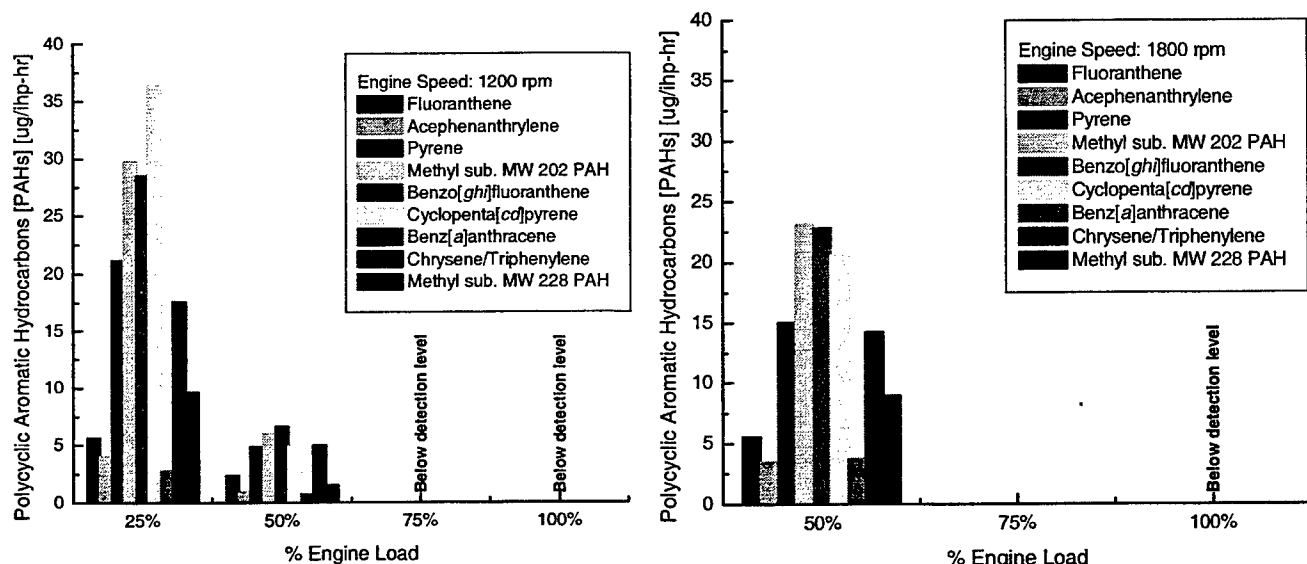


Figure 4: Particle phase PAH versus engine load and speed. Fuel A – D2

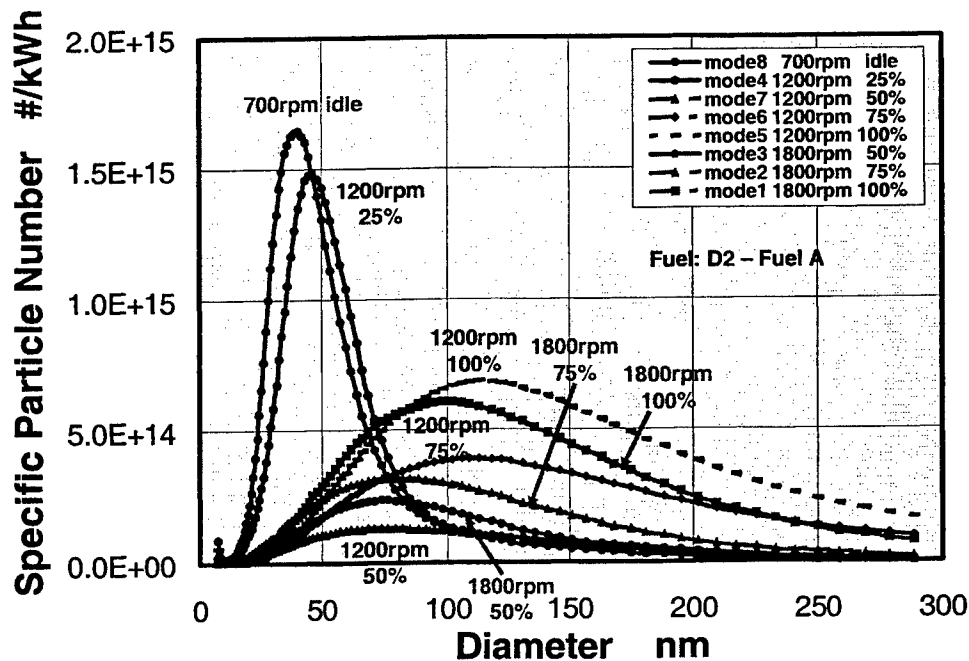


Figure 5: Particle size distributions for a range of engine speeds and loads.

Figure 6 shows the median particle size and number for the different operating conditions tested. The data is plotted as median particle size and number versus peak injection pressure. With the unit injector used on this engine, the peak injection pressure also correlates with load. Note that, in general, as the load increased, the median particle size and number also increased. The exceptions to this trend are the mode 4 and mode 8 operating conditions. Closer analysis of the SMPS data showed that the particle number is high because of a very high number of nucleation, or nano, particles. This is a direct result of the predominance of organic carbon contributing to the particulate at these operating conditions.

As one pushes to higher power density, the limiting condition for air utilization, as evidenced by increases in particulate emissions, the result will be larger particles that are predominantly elemental carbon. At idle conditions; there will be a very large number of nano particles that are largely organic carbon. The chemical kinetic processes occurring at the air utilization limits for the two engine operating conditions are different.

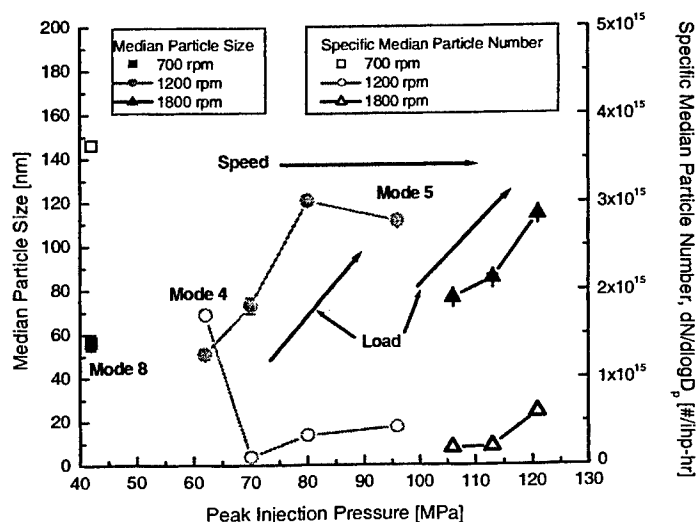


Figure 6. Median Particle Size and Specific Median Particle Number for the different engine operating conditions. The results are plotted against peak injection pressure, which is indicative of the engine load.

PLASMA RESEARCH FOR AEROSPACE APPLICATIONS

Principal Investigator(s): Biswa Ganguly

AFRL/PRPE, Wright-Patterson AFB OH 45433

SUMMARY/OVERVIEW:

Nonequilibrium plasma research is conducted to determine its potential application to reduce ignition delay in hydrocarbon/ air combustor. Also, the effect of pressure scaling on the minimum ignition kernel size dependence will be investigated by quantifying the PD, P is the pressure and D is spark gap, scaling of nonequilibrium plasma. Flame holding improvement with plasma generated radical injection and applied voltage will be measured.

TECHNICAL DISCUSSION

In supersonic combustion (scramjet) systems the flow speed is very high so that mixing and reaction times are limited¹⁻³. Some flow conditions also give rise to very low mixture temperatures¹. For either condition, additional sources of ignition or combustion enhancement are needed. Plasma torch ignitors^{1,2} have been investigated widely, and microwave discharges³ have been studied, both as means of providing reliable scramjet combustion. However, such approaches require multi-kilowatt electrical power inputs and are not easily volume scaleable. Highly nonequilibrium plasma production of energetic reactive hydrocarbon fragments could have application in situations where more conventional means of promoting and sustaining combustion are degraded^{4,5}.

The attractiveness of high E/n , where E is the electric field and n is the gas density, pulsed discharges for dissociation, and electronic excitation and ionization is clear from both theoretical^{6,7} and experimental⁸ work performed on corona and dielectric barrier discharges. Pulsed dc discharges in gaseous hydrocarbon mixtures can provide substantial amounts of atomic hydrogen, as well as electronically excited hydrocarbon fragment neutrals and ions. Such discharge products would be useful in promoting combustion in a wide variety of fuel to air mixtures.

The plasma volume and energy scaling of highly nonequilibrium plasma assisted ignition could improve overall efficiency of combustion. It is, therefore, important to quantify the radical production efficiency of a plasma device which could be used to replace a conventional spark

ignition module. We have developed a short pulse excited discharge device⁹ which can operate at high reduced electric field (E/n) with PD, P is the gas pressure and D is the gap distance, scaling up to 50 Torr.cm. Actinometric measurements performed in this high reduced electric field plasma device indicated that the CH_4 dissociation efficiency can be more than an order of magnitude greater than thermal dissociation process⁹. Although those measurements gave indications that a short pulse discharge can produce radicals with higher efficiency, compared to the thermal dissociation, those measurements were performed at low current density (2 Amp/cm²) and low energy density (0.7mJ/cm²). In this work we report absolute H atom ground state density measurements in a short pulse methane discharge by two-photon allowed LIF (TALIF) technique at current densities exceeding 20 Amp/cm². The H atom TALIF intensity has been calibrated by comparing TALIF intensity from Kr atom ground state¹⁰ to obtain absolute H atom density.

The goals of this study are: 1) construct a high E/n discharge system capable of producing discharges over a substantial range of input energy density, and 2) conduct spectroscopic measurements of the absolute H-atom production to estimate plasma dissociation efficiency of CH_4 in high E/n discharges. Pulsed gas discharges in CH_4 produce all possible methane fragments (CH_3 , CH_2 , CH , C and H) and their ions in varying ratios depending upon the discharge E/n . In the present study, we provide an accurate estimate of the direct electron impact dissociation efficiency of CH_4 in short pulse excited, high E/n discharge, with nearly two orders of magnitude higher energy density compared to the previous measurement⁹, using absolute H atom number density measurement by calibration of H atom TALIF signal with near isoenergetic Kr ground state atom TALIF measurement¹⁰. Figures 1a and 1b show the voltage-current waveforms.

Pressure dependent krypton TALIF calibration signal were measured and was found to be linear with pressure. Calibration transfer was made via a measurement at 0.318 Torr, where Kr signal amplitude was comparable to the H atom TALIF. Immediately following the Kr atom TALIF measurement, ground state H atom production in CH_4 discharge was measured. The H atom TALIF intensity has been calibrated by comparing TALIF intensity from Kr atom ground state¹⁰ to obtain absolute H atom density using the equation given below.

$$n_H = \kappa \frac{a_{23}(\text{Kr}) \sigma^{(2)}(\text{Kr}) S_{\text{PMT}}(\text{H}) \left(\frac{I_L(\text{Kr})}{I_L(\text{H})} \right)^2}{a_{23}(\text{H}) \sigma^{(2)}(\text{H}) S_{\text{PMT}}(\text{Kr})} n_{\text{Kr}} \quad (1)$$

where n_H and n_{Kr} are the absolute number density of the H- and Kr-atoms respectively, κ is a transmission and sensitivity factor for the optical set-up and detector at the two wavelengths, a_{23} is the optical branching ratio ($a_{23} = A_{23} / \sum A_{2i}$, A_{23} is the spontaneous emission coefficient and $\sum A_{2i}$ is the sum of spontaneous emission and collisional quenching coefficients), $\sigma^{(2)}$ is the two-photon cross section, S_{PMT} is the measured TALIF signal, and I_L is the intensity of the laser radiation. The ratio of the two-photon cross-sections, Kr atom optical branching ratio and collisional quenching rate of H atom 3d and 3s states by CH_4 are given in reference 10. Under our measurement conditions, the value of κ depends on the ratio of the PMT response sensitivity at 656.3 nm and 826.3 nm, which is obtained from the manufacturer's data sheet. Thus from a measurement of both the H-atom and Kr-atom TALIF signals, the absolute number density of H-atoms can be calibrated with a known number density of ground state Kr atom. Figure 2 shows H atom TALIF signals, calibrated in absolute H atom number density by comparing with Kr atom TALIF signal, obtained with three different applied drive voltages from 4 kV to 6 kV, with 480

ns pulse duration. The total input energy for these discharges were 6.5, 8.7, 11.4 mJ, respectively. For the corresponding discharge conditions, the measured H atom density ranged from $\sim 9.8 \times 10^{15}$ per cm^3 at 4 kV to 2.2×10^{16} per cm^3 at 6 kV (TALIF pulse peak-to-area ratio is essentially constant so the peak values are used), i.e., nearly 4.5% of CH_4 was dissociated at 6 kV applied voltage, assuming 400 K gas temperature at 20 Torr, across the 5 mm gap discharge. Based on the energy deposited in the discharge volume near the cathode, an estimate of the direct electron impact dissociation efficiency of $\text{CH}_4 + e \rightarrow \text{CH}_3 + \text{H} + e$ can be obtained from the measured H atom yield in this pulsed discharge. The product of the direct electron impact dissociation rate coefficient and electron density in plasma is proportional to the fraction of discharge energy deposited to that process multiplied by the energy deposited in the gas, i.e.:

$$k_{ei}^{CH_4} n_e^{CH_4} \propto Y(E/n) P_{CH_4} \quad (2)$$

where $Y(E/n)$ is the fractional energy deposited into electron impact production of $\text{CH}_3 + \text{H}(n=1)$ as a function of E/n in methane discharges, $k_{ei}^{CH_4}$ is the electron impact dissociation rate, $n_e^{CH_4}$ is the electron density, and P_{CH_4} is total discharge energy. For this discharge operating condition with 700 V sheath voltage drop along with about 80 V/cm plasma electric field in the 5 mm gap discharge, 70 to 75% of the energy is deposited in the discharge volume within 2 mm from the cathode surface. For the 6 kV applied voltage, discharge with 11.4 mJ total discharge energy, this would correspond to the discharge energy density $\sim 70 \text{ mJ/cm}^3$. Assuming an average CH_4 dissociation energy cost of 10 eV, the total energy required to produce H atom density of 2.2×10^{16} per cm^3 would be 35 mJ/cm^3 (direct electron impact dissociation threshold¹² of $\text{CH}_4 + e \rightarrow \text{CH}_3 + \text{H} + e$ is 8.5 eV, and at the threshold energy the dissociation rate is very small. The higher dissociation rate, $k_{ei}^{CH_4}$, with average electron energy cost of 10 eV would be more appropriate for this short pulse discharge). This would imply about 50% efficiency of the direct electron dissociation of CH_4 in this 6 kV short pulse discharge. Similarly for the 4 and 5 kV discharges, the corresponding energy densities are ~ 40 and 53 mJ/cm^3 , respectively. The energy required to produce 9.8×10^{15} per cm^3 H atom density, at 4 kV, would be 15.7 mJ/cm^3 and the CH_4 dissociation efficiency is $\sim 40\%$. For the 5 kV discharge, the energy required to produce H atom density of 1.44×10^{16} per cm^3 would be 23 mJ/cm^3 and the dissociation efficiency is nearly the same as the 4 kV discharge. The measurable difference in the CH_4 dissociation efficiency at higher applied voltage may be caused by the increase in the discharge energy deposition in the sheath, where nonlocal electron impact excitation can dissociate CH_4 at higher efficiency than in the volume plasma. Note that volume plasma E/n is essentially constant for all the applied voltages. Although the importance of initial energy deposition near the breakdown under higher E/n can not be directly quantified from these measurements, these measurements clearly show the advantage of operation at higher applied voltage even for a relatively long pulse duration discharge compared to the initial high peak power pulse duration

REFERENCES

1. T.C. Wagner, W.F. O'Brien, G.B. Northam and J.M. Eggers, J. Propulsion 5, 548 (1989)
2. T. Mitani, Combust. Flame 101, 347 (1995).
3. K. Khodataev and A. Ershov, in 2nd Weakly Ionized Gases Workshop, Proceedings Supplement, Norfolk, VA, p. 341-350, (1998).

4. Y. Y. Buriko, V. A. Vinogradov, V. A. Goltsev, and P. J. Waltrup, *J. Propulsion and Power* 18, 1049 (2002).
5. S. A. Bozhenkov, S. M. Starikovskia, A. Yu. Starikovskii, *Combustion and Flame* 133, 133 (2003).
6. R. Dorai, K. Hassouni, and M. J. Kushner, *J. Appl. Phys* 88, 6060 (2000).
7. V. Puchkarev and M. Gundersen, *Appl. Phys. Lett.* 71, 3364 (1997).
8. R. S. Sigmond and M. Goldman in *Electrical breakdown and discharges in gases* eds. E. E. Kundhart and L. H. Luessen, Plenum, New York, 1981, pp 1-64.
9. S. D. Marcum, J. W. Parish, and B. N. Ganguly, *J. Propulsion and Power* (to be published).
10. K. Niemi, V. S. von der Gathen, and H. F. Dobeles, *J. Phys. D: Appl. Phys.* 34 2330 (2001).
11. A. von Engel, *Ionized Gases*, American Institute of Physics, New York, 1995, pp 222-236.
12. R. K. Janev, and D. Reiter, *Phys. Plasmas* 9, 4071 (2002).

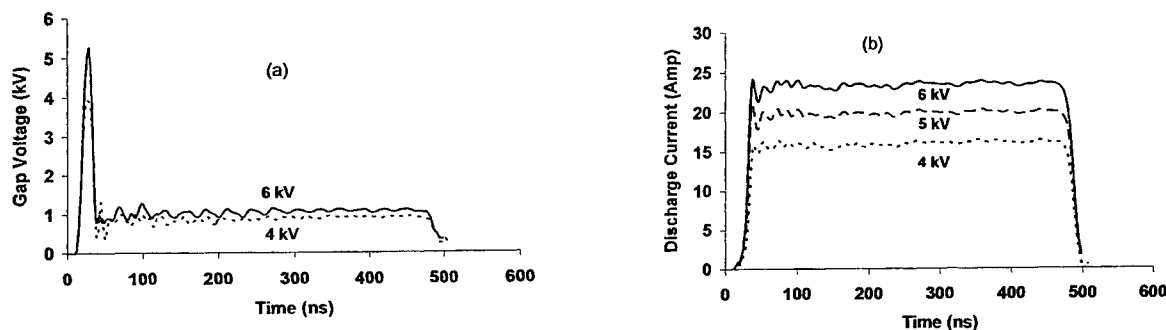


Figure 1. Discharge voltage (a) and current (b) for 480 ns pulse width 4, 5 and 6 kV applied voltages across a 5 mm gap, 1 cm diameter electrodes, at 20 Torr CH₄.

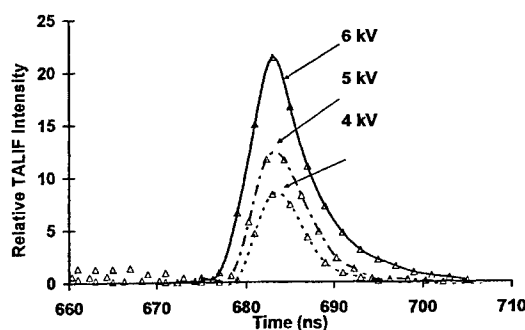


Figure 2. TALIF measurement of absolute H atom densities are obtained from the Kr atom TALIF calibration, yielding H atom density of 9.8×10^{15} per cm³ at 4 kV, 1.44×10^{16} per cm³ at 5 kV, and 2.2×10^{16} per cm³ at 6 kV.

FILTERED MASS DENSITY FUNCTION FOR SUBGRID SCALE MODELING OF TURBULENT DIFFUSION FLAMES

Grant Number F49620-03-1-0022

Principal Investigator: Peyman Givi

Department of Mechanical Engineering
University of Pittsburgh
Pittsburgh, PA 15261

SUMMARY/OVERVIEW:

The specific objectives of this work are:

- i. To further develop and improve the "filtered density function" (FDF) methodology for closure of the subgrid scales (SGS) in turbulent reacting flows.
- ii. To implement the resulting SGS closure for large eddy simulation (LES) of non-premixed turbulent flames.

TECHNICAL DISCUSSION

The filtered density function (FDF) [1] methodology has proven effective for large eddy simulation (LES) of turbulent reacting flows. The fundamental property of the FDF method is exhibited by the closed form nature of the chemical source term appearing in the transport equation governing the FDF. This property is very important as evidenced in several applications of FDF for LES of a variety of turbulent reacting flows; see Ref. [2] for a recent review. The encouraging results attained thus far warrant further improvements and implementations of LES/FDF for a wider class of reacting flows. Our efforts within the past year have been concentrated on doing exactly that. Specifically, we have been working on:

- I. Implementation of our previously developed scalar filtered mass density function (SFMDf) for LES of turbulent flames.
- II. Development of the joint velocity-scalar filtered mass density function (VSFMDf) methodology.

In efforts pertaining to (I), we have used our previously developed SFMDf [3] methodology for LES of a piloted jet flame and a bluff-body stabilized flame. Both of these configurations are detailed in the experiments of the Combustion Research Facility at the Sandia National Laboratories and the University of Sydney. These flames have been the subject of broad investigations by other computational/modeling methodologies [4]. In the piloted jet flame experiments, three basic flames are considered, identified by Flames D, E, and F. The geometrical configuration in these flames is the same, but the jet inlet velocity is varied. In Flame D, the fuel jet velocity is the lowest and the flame is close to equilibrium. The jet velocity increases from flames D to E to F, with noticeable non-equilibrium effects in the latter two [5]. For the bluff body, the Sydney experiments [6] with 50% Methane and 50% Hydrogen by volume fuel jet is considered. The fuel jet of diameter 3.6 mm is surrounded by a round ceramic bluff-body of 50 mm diameter and encompassed by an air co-flow. Various fuel jet and air co-flow speeds are studied to create an experimental database for different levels of flame blow-off. In all of our work thus far, combustion is modeled via the near-equilibrium oxidation model.

This model is enacted via "flamelet" simulations which consider a laminar counterflow (opposed jet) flame configuration [7]. The full methane oxidation mechanism of the Gas Research Institute (GRI) [8] accounting for 53 species and 325 elementary reactions is used. At low strain rates, the flame is close to equilibrium. Thus, the thermo-chemical variables are determined completely by the "mixture fraction." This flamelet library is coupled with our LES/SFMDF solver in which transport of the mixture fraction is considered. It is important to emphasize that the PDF of the mixture fraction is not "assumed" a priori (as done in almost all other flamelet based LES [9-13]). Rather, it is calculated explicitly via the SFMDF. Simulation of the piloted jet flame has been completed and some of our results are presented in Ref. [14]. Simulations of the bluff body flame are ongoing. These simulations are being conducted via a hybrid finite-difference/Monte-Carlo methodology as documented in Refs. [15,16]. The grid resolution is $101 \times 181 \times 181$ in stream-wise, cross-stream and span-wise directions, respectively. This grid space spans a physical space of $1.44 \times 1.30 \times 1.30$ bluff-body diameters, where the fuel jet is located at the center of the domain's cross-section. Consequently, this LES considers a recirculation zone (up to about 1.3 bluff-body diameters) of the experimental flame. In Figs. 1-2 the Reynolds averaged profiles of the filtered values of the mixture fraction and the temperature are compared with experimental data. While the agreement is encouraging, these results are very preliminary and more work is needed (and is underway) for further assessments of the FDF methodology.

In efforts pertaining to (II), we have completed the mathematical formulation for the "velocity-scalar filtered mass density function" (VSFMDf). Compared to our previous velocity-scalar FDF (VSFDF), this methodology has an added advantage that it allows for variable density effects. An exact transport equation is derived for the VSFMDf. In this equation, the unclosed terms are modeled in a fashion similar to probability density function (PDF) methods as used in Reynolds-averaged simulations (RAS) [17]. A system of stochastic differential equations which yield statistically equivalent results to the modeled VSFDF transport equation is constructed. These SDEs are solved numerically by a Lagrangian Monte Carlo procedure in which the Ito character of the SDEs is preserved. The consistency of the proposed SDEs and the convergence of the Monte Carlo solution are assessed in a format similar to that in our previous work [15,16]. All of the results are assessed via detailed comparisons with direct numerical simulation (DNS) Data. Excellent agreements are observed.

WORK IN PROGRESS

Our current work is concentrated on the following issues: (1) Fine-tuning and further implementation of the LES/SFMDF methodology for prediction of Sandia piloted flamed E, & F and the bluff-body flame. (2) Completion of the work on LES/VSFMDf by assessing its consistency and also its predictive capability by the procedure followed in our previous work [16].

ACKNOWLEDGMENT

We are indebted to Professor Stephen B. Pope (Cornell University) for his valuable collaboration on various aspects of this work.

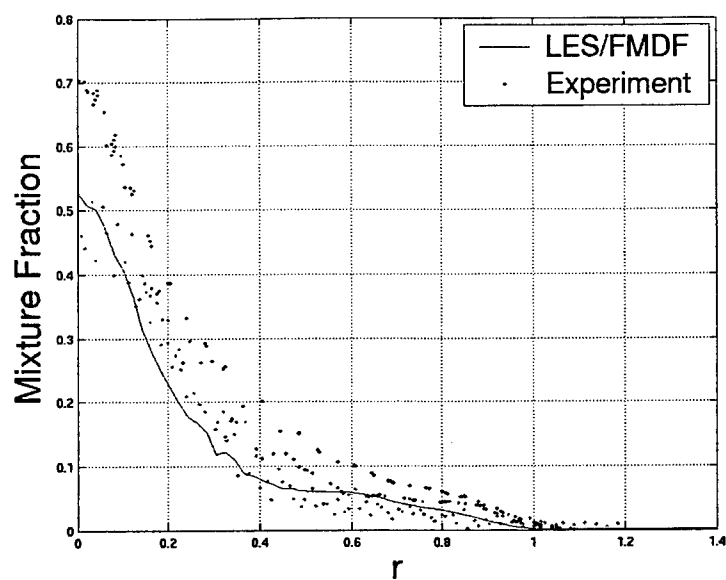


Figure 1. Reynolds averaged values of the filtered mixture fraction.

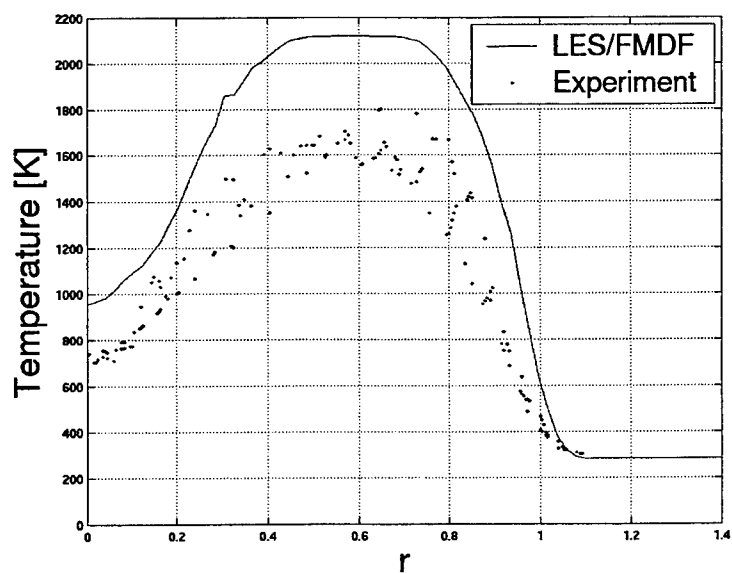


Figure 2. Reynolds averaged values of the filtered temperature.

REFERENCES

1. Pope, S. B., *Turbulent Flows*, Cambridge University Press, Cambridge, UK, 2000.
2. Givi, P. AIAA Paper 2003-5081, 2003.
3. Jaber, F. A., Colucci, P. J., James, S., Givi, P., and Pope, S. B., *J. Fluid Mech.*, **401**:85-121 (1999).
4. Sandia National Laboratories website <http://www.ca.sandia.gov/tdf/Workshop.html>, 2004.
5. Nooren, P. A., Versuijs, M., Van der Meer, T. H., Barlow, R. S., and Frank, J. H., *Applied Physics*, **B71**: 95 (2000).
6. Dally, B. B., Fletcher, D. F., and Masri, A. R., *Combust. Theory Modeling*, **2**: 193-219 (1998).
7. Peters, N., *Turbulent Combustion*, Cambridge University Press, Cambridge, UK, 2000.
8. Smith, G. P., Golden, D. M., Frenklach, M., Moriarty, N. W., Eiteneer, B., Goldenberg, M., Bowman, C. T., Hanson, R., Song, S., Gardiner, W. C., Lissianski, V., and Qin, Z., <http://www.me.berkeley.edu/gri-mech>.
9. De Bruyn Kops, S. M., Riley, J. J., Kosály, G., and Cook, A. W., *Combust. Flame*, **60**:105-122 (1998).
10. DesJardin, P. E. and Frankel, S. H., *Combust. Flame* **119**:121-132 (1999).
11. Pitsch, H. and Steiner, H., *Phys. Fluids*, **12**(10):2541-2554 (2000).
12. Ladeinde, F., Cai, X., Sekar, B., and Kiel, B., AIAA Paper 2001-0634, 2001.
13. Kempf, A., Forkel, H., Chen, J. Y., Sadiki, A., and Janicka, J., *Proc. Combust. Inst.*, **28**:35-40 (2000).
14. Sheikhi, M. R. H., Drozda, T. G., Givi, P., Jaber, F. A. and Pope, S. B., *Proc. Combust. Inst.*, **30**: in press (2004).
15. Gicquel, L. Y. M., Givi, P., Jaber, F. A., and Pope, S. B., *Phys. Fluids*, **14** (3): 1196-1213 (2002).
16. Sheikhi, M. R. H., Drozda, T. G., Givi, P. and Pope, S. B., *Phys. Fluids*, **15** (8): 2321-2337 (2003).
17. Pope, S. B., *Ann. Rev. Fluid Mech.*, **26**: 23-63 (1994).

COMPUTER-BASED ADAPTATION TOOL FOR ADVANCED DIESEL ENGINES USED IN MILITARY APPLICATIONS

(Grant Number DAAD 19-03-1-0338)

Principal Investigator(s): N. A. Henein, D. Taraza and N. Chalhoub

Wayne State University
Center for Automotive Research
Engineering Building
Detroit, MI 48202
Tel. (313) 577 3887, Fax: (313) 577 8789
email:henein@wayne.edu

SUMMARY

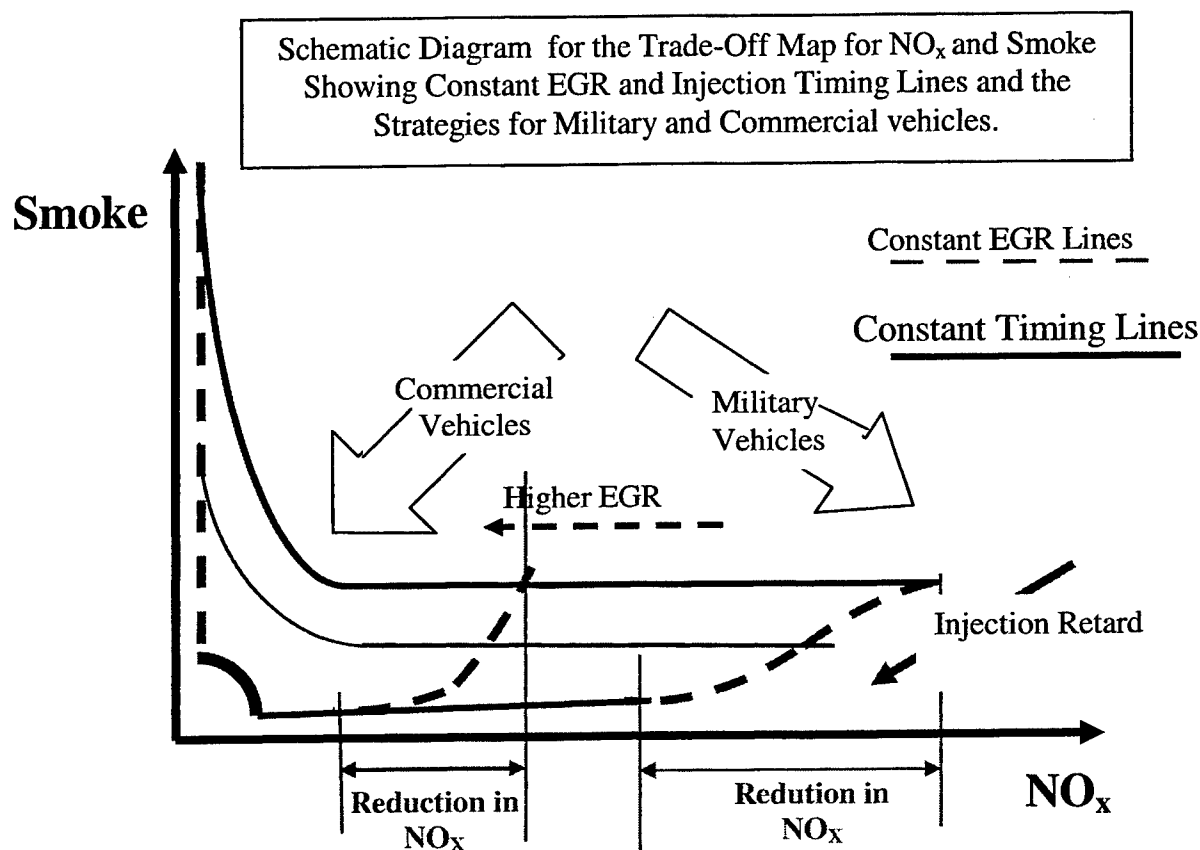
The goal of this project is to develop a user friendly platform for designing and assessing new control strategies that optimize the fuel economy and maximize the power density of advanced commercial diesel engines while satisfying the military requirement of low smoke visibility in the field. The project has three thrust areas: I. Development of new electronic control strategies based on a generic MATLAB/ Simulink model for heavy duty diesel engines, II. Determining tribological limitations of engine bearings under extreme loading conditions, and III. Determining tribological limitations of the piston assembly. The strategy would enable the engine to run on JP-8 instead of the regular DF-2 fuel.

I. Development Of New Electronic Control Strategies Based On A Generic MATLAB/ Simulink Model For Heavy Duty Diesel Engines

The engine cycle simulation is for a detailed multi-zone model for direct injection (DI) diesel engines. The model covers the entire engine cycle and accounts for the gas exchange system, in-cylinder processes, engine-out emissions, and engine dynamics. The formulation of the gas exchange system captures the filling and emptying of the intake and exhaust manifolds. For the in-cylinder processes, the charge will be considered as a single zone till the fuel injection process begins. Beyond that point, a multi-zone combustion model will be used whereby the injected fuel is partitioned into numerous packages/zones with each package having its own history of temperature, composition and equivalence ratio. A uniform pressure will be considered for the entire cylinder. At the moment of its inception, each package is considered to contain fuel droplets and air. Its location inside the cylinder will be determined from the formulation of spray penetration and spray angle. A specific pattern of introducing the packages has been adopted based on the duration and the fuel spray profile. Each package will be considered to go through an atomization process, fuel droplets evaporation process, air entrainment into the package, ignition delay and the combustion process. The amount of fuel that will be burned in each package and at any given time step will be determined by an empirical formulation, which takes into consideration the local molar fraction of the vaporized fuel and entrained oxygen. Consequently, the energy (heat) release rate in each package will be computed and the overall energy release rate inside the cylinder will be determined from the contributions of all packages. The formation of engine-out emissions in each package will be

governed by a reduced 11-specie chemical kinetic model enhanced by the extended Zeldovich mechanism for predicting NO emissions. The overall concentration for any given specie will be determined from the concentrations in all zones defined inside the cylinder. An empirical model, based on the formation and burning rates of soot, will be used to determine the net amount of soot formation. The thermodynamics portion of the model will be coupled with the engine dynamics submodel through the overall cylinder pressure and crankshaft angular velocity. The model will account for the rigid body motion of the crankshaft/connecting-rod/piston mechanism.

The engine cycle simulation model will be validated by comparing its results to those obtained experimentally. Furthermore, the engine cycle simulation models will be used to develop control strategies for reducing EGR and determining the appropriate injection timing. These strategies will be validated through experimental results as shown in the figure below.



II. Tribology of the Main Engine bearings

Engine bearings are one of the most vulnerable parts in high power density diesel engines. If the minimum oil film thickness (OFT) becomes less than 2 μm damage of the bearing could occur. The accurate determination of the OFT must consider bearing and shaft deformation.

The following computer codes have been developed.

(A) The code “Polar Diagram” calculates the loading of the bearings and displays the polar diagram of the bearing according to two separate assumptions:

- a) Statically determined cranks
- b) Statically Undetermined crankshaft structure

The inputs needed for the code are: the cylinder pressure variation and basic engine dimensions (bore, stroke, and connecting rod length, mass of the piston assembly, mass of the connecting rod, dimensions and mass of the crankshaft)

(B) The code “Journal Orbit” calculates the orbit of the journal using the mobility method and displays the orbit inside the clearance circle showing also the variation of the oil film thickness

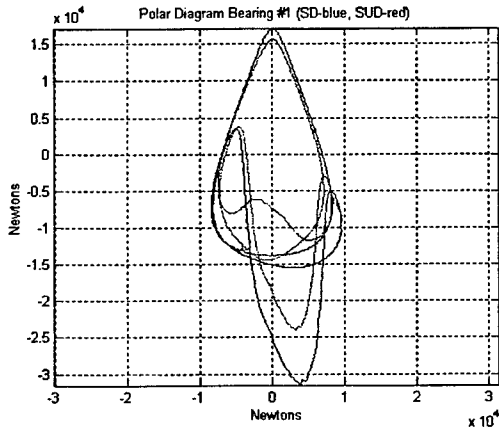


Fig. 1. Polar diagrams of the first main bearing four-stroke, four-cylinder diesel engine (2500 rpm)

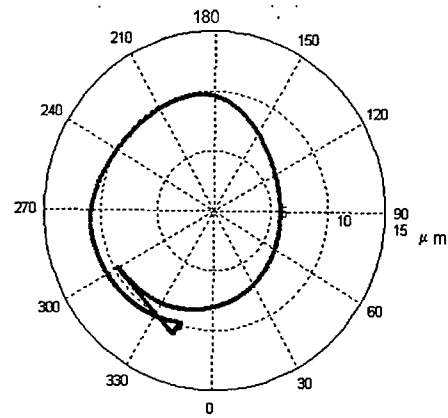


Fig. 2. Journal orbit calculated for the Bearing load shown in Fig.1

(c) The code “Oil Pressure” uses a finite difference method to integrate the Reynolds equation and calculate the oil pressure variation inside the bearing. This code is used for a more accurate determination of the oil film thickness and also to obtain the detailed bearing load for the Finite Element model of the bearing to determine the deformation of the bearing. The code is capable to simulate the oil-feeding groove in the bearing and the effect of the shaft misalignment. The following figures show the influence of these parameters on the minimum oil film thickness.

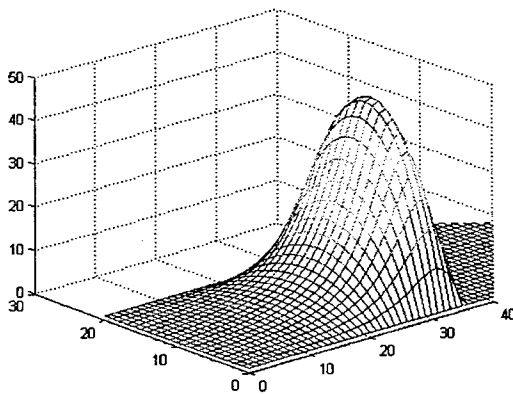


Fig. 3.a. Minimum OFT 3.5 μm

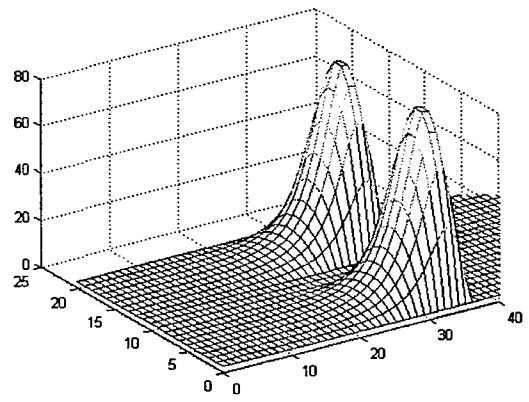


Fig. 3. b. Minimum OFT 1.8 μm

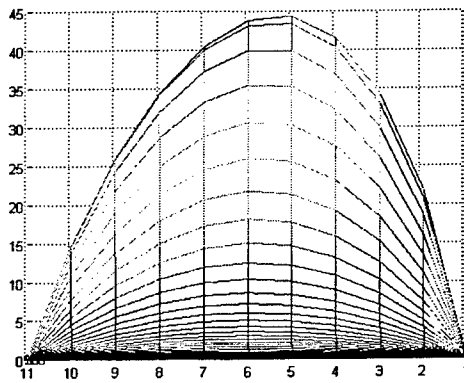


Fig. 3.c. Minimum OFT 2.82 μm
Load center offset 0.645 mm

Fig. 3. Oil film pressure variation in the bearing for the load of 42,500 N at 1500 rpm

The main bearing at the flywheel end of the crankshaft of the experimental engine has been instrumented with two gap sensors for the measurement of the journal orbit. Preliminary measurements have shown a very good repeatability and the sensors are now calibrated for the validation of the simulation model. Also the finite element model (FEM) of the bearing has been generated and the deformation of the bearing under oil pressure load was determined.

Future work

The code "Oil Pressure" will be developed to include bearing deformation from the FEM and determine the oil film pressure distribution in the deformed bearing housing. Boundary and Elasto-Hydrodynamic lubrication models will be incorporated in the simulation code.

The simulation code will be validated by experimental results from the single cylinder diesel engine.

III. Tribology of the piston assembly

A tribology test rig has been built to provide direct measurements of both frictional losses in the piston assembly and secondary motions of the piston (i.e., piston slap and piston tilting). The code of the data acquisition system has now been written. However, the current DC motor, used in motoring the engine, was not powerful to conduct tests at high-speeds. Thus, we are currently acquiring a large DC motor along with its accessories to enhance the capability of the WSU piston tribology test rig.

STATISTICAL INTERPRETATION OF SCALAR TIME-SERIES MEASUREMENTS IN TURBULENT PARTIALLY PREMIXED FLAMES

AFOSR Grant Number F49620-03-1-0026

Principal Investigators: Normand M. Laurendeau, Galen B. King and Michael W. Renfro

School of Mechanical Engineering, Purdue University, West Lafayette, IN 47907-1288
Department of Mechanical Engineering, University of Connecticut, Storrs, CT 06269-3139

SUMMARY/OVERVIEW

This research is concerned with systematic comparisons of scalar autocorrelation functions, power spectral densities and integral time scales measured by picosecond time-resolved laser-induced fluorescence (PITLIF) and Laser Rayleigh Scattering (LRS), and their comparisons to large-eddy simulations (LES). Such assessments should lead to the development of improved LES models for turbulent combustion processes crucial to practical gas-turbine combustors.

During this past year, hydroxyl and number density time-series have been obtained using PITLIF and LRS in turbulent $H_2/CH_4/N_2$ -air jet flames. The particular fuel used in the investigation was selected because its Rayleigh cross-section is essentially the same for air as for the exhaust gases. Therefore, the resulting LRS measurements depend only on number density and thus inversely on temperature. The measured power spectral densities for OH and LRS were found to collapse to the same shape when normalized by their integral time scales. The OH and LRS integral time-scales at the peak radial temperature location were found to scale similarly versus Reynolds number as $Re^{-1.41}$. The ratios of OH to LRS time scales at various axial distances on the jet centerline for a given Re were found to be constant. This result suggests important relationships between OH and LRS time scales. These data represent the first reported assessment and comparisons of fluctuation rates for OH and number density in turbulent reactive flows.

TECHNICAL DISCUSSION

A variety of non-intrusive laser-based techniques with high temporal and spatial resolution have been developed in recent years to gain insight into the complex physical and chemical processes occurring during turbulent non-premixed combustion. Jet flames have been extensively studied because they provide a relatively simple and well-defined flow field. Measurements of minor species concentrations in turbulent flames are of interest owing to their importance in pollutant chemistry and their use as markers of instantaneous flame structure.

Time-scale information can be provided by scalar time series when measurement repetition rates are sufficiently fast to resolve turbulent fluctuations. This approach has been demonstrated for many scalars such as temperature¹, OH² and CH³. Such time series of minor-species concentrations are recovered by use of picosecond time-resolved laser-induced fluorescence (PITLIF), which directly accounts for potential variations in both the electronic quenching rate coefficient and background flame emission. Information on time scales for OH

¹ M.Q. McQuay, S.M. Cannon, Combust. Sci. Tech. 119 (1996) 13.

² M.W. Renfro, G.B. King, N.M. Laurendeau, Appl. Opt. 38 (1999) 4596.

³ M.W. Renfro, G.B. King, N.M. Laurendeau, Combust. Flame 122 (2000) 139.

concentration ($[\text{OH}]$) and temperature (or number density), if available in the same set of flames, would clarify the relationship between temperature and species fluctuations.

In the current investigation, $[\text{OH}]$ and LRS time-series measurements have been obtained in a set of non-premixed flames in the range $13,100 \leq \text{Re} \leq 21,500$ using a fuel composed of 22.1% CH_4 , 33.2% H_2 and 45.7% N_2 . This particular fuel mixture was selected because its Rayleigh cross-section is essentially the same for air as for the exhaust gases. Therefore, the resulting LRS measurements depend only on number density (n) and thus inversely on temperature. This particular fuel mixture has been extensively studied by Bergmann *et al.*⁴, Meier *et al.*⁵ and Schneider *et al.*⁶ They report mixture fraction, temperature, velocity, and minor species concentrations for a variety of axial locations and provide a comprehensive database for two standard flames at $\text{Re} = 15,200$ and $\text{Re} = 22,800$. These flames have been chosen as benchmarks for the Turbulent Non-premixed Flame (TNF) Workshops. The time-series measurements reported in this study further characterize a standard flame and thus complement the previous data for this flame.

The laser and detection system used for the OH measurements is identical to that employed by Renfro *et al.*² The system consists of a mode-locked laser and a photon-counting assembly that records the LIF signal and fluorescence lifetime with temporal resolution and bandwidth sufficient for time-series measurements. For the LRS measurements, a continuous-wave Ar^+ laser was used at a nominal power of 22 W and a wavelength of 488 nm. The resulting LRS signal was collected by a Hamamatsu PMT. The signal was first amplified and then counted by utilizing a single ungated bin of the photon counting system used for the OH measurements. For the current measurements, the spatial resolution for both $[\text{OH}]$ and LRS was $100 \times 100 \times 90 \mu\text{m}^3$ based on the beam diameter and the monochromator entrance slit width for the detection system. A fixed sampling rate of 16129 Hz was used for both the LRS and OH measurements. Signal-to-noise ratios were typically 2-3 for the OH measurements, and 4-6 for the LRS measurements.

The burner for the turbulent nonpremixed flames was identical to that used by Bergmann *et al.*⁴ and consisted of an 8-mm diameter (D) tube with a thinned rim at the exit. Co-flowing air with an exit velocity of 0.3 m/s was provided using a contoured 140-mm nozzle. The burner could be translated in axial and radial directions to change the position of the measuring location. Time series of 4096 points were collected at each measurement location. Probability density function (PDFs), power spectral density (PSDs), autocorrelation functions (ρ), and integral time scales were computed in the same manner as reported by Renfro *et al.*² including a correction for the measured contribution of shot noise. The statistics were averaged over fifty time series to reduce noise.

Figure 1 shows time-averaged $[\text{OH}]$ and temperature profiles measured at different radial locations in a $\text{Re} = 15,200$ flame at an axial height, x , of $x/D = 20$. Each point on these profiles was sampled at 10 Hz and the data were averaged over 25 samples to give clean statistics. At every point, flame emission and background corrections were made by taking measurements in

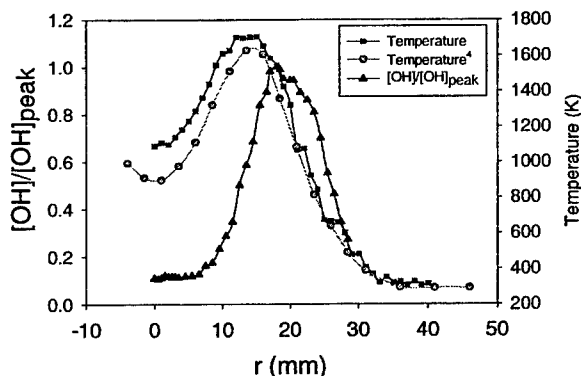


Fig. 1: Comparison of radial temperature and $[\text{OH}]$ profiles at $x/D = 20$ for $\text{Re} = 15,200$.

⁴ V. Bergmann, W. Meier, D. Wolff, W. Stricker: Appl. Phys. B. 66 (1998) 489.

⁵ W. Meier, R.S. Barlow, Y.-L. Chen, J. -Y. Chen, Combust. Flame 123 (2000) 326.

⁶ Ch. Schneider, A. Dreizler, J. Janicka, Combust. Flame 135 (2003) 185.

the absence of a laser beam. The temperature profile was calibrated using number density measurements taken in ambient air at room temperature. The measured temperature profile shows good agreement with temperature measurements made by Bergmann *et al.*⁴. The peak [OH] is offset from the peak temperature by a few millimeters, as expected for this diffusion flame.

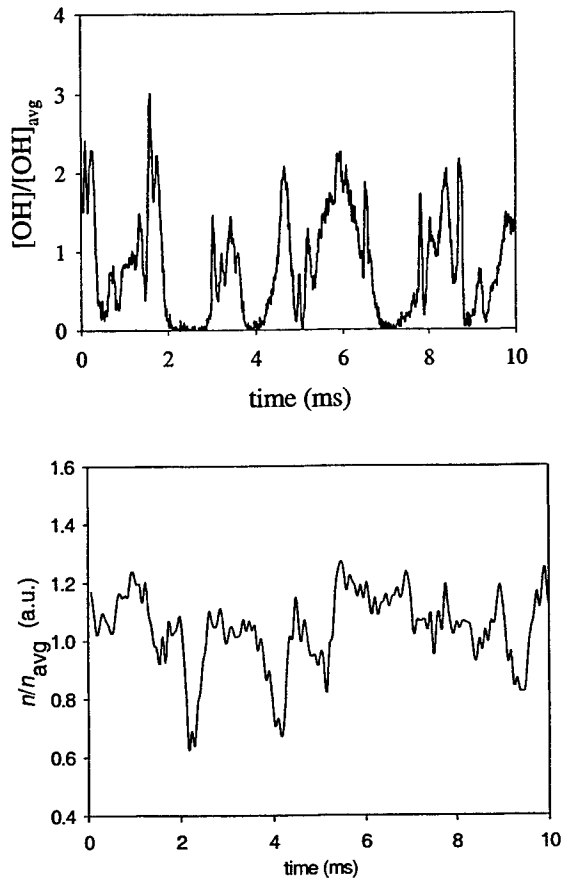


Figure 2: Representative OH (top) and LRS (bottom) time series at the centerline for $x/D = 28$ and $Re = 17,300$.

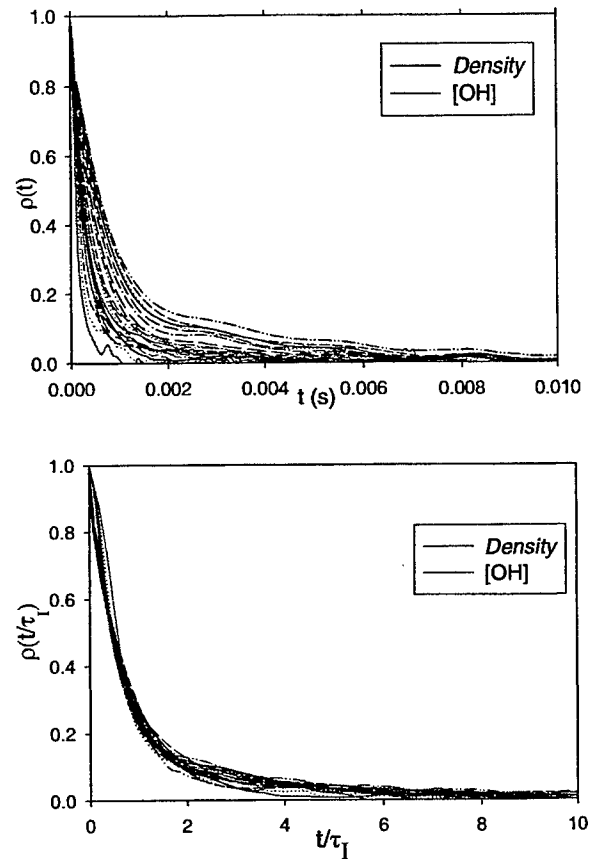


Figure 3: LRS and [OH] autocorrelation functions for $Re = 15,200$ (top) at different axial locations along the jet centerline, and (bottom) normalized by their integral time scales.

A representative time-series measurement at the peak radial location for $x/D = 20$ is shown in Fig. 2. The trace represents the first 10 ms of data collected and visually demonstrates fluctuations in [OH] fluorescence and number density as these two layers fluctuate with respect to the fixed laser beam. The fluctuations observed in these time-series can be characterized by the autocorrelation function, the power spectral density and the integral time scale.

The [OH] and LRS autocorrelation functions for different axial locations along the jet centerline in a $Re = 15,200$ flame are shown in Fig. 3. Figure 3 also shows the same autocorrelation functions normalized by their respective integral time scales. Integral time scales, τ_I , were calculated by numerically integrating the autocorrelation functions over 100 data points. We note that the normalized curves essentially collapse to a single autocorrelation function for both the LRS and [OH] measurements. The collapse implies that the relative distribution of fluctuation rates at a single point in the turbulent flow is the same as that at a different point for both the density and OH fluctuations. Figure 4 compares [OH] and density integral time scales at various axial locations for the five flames of this investigation. In general, the integral time scales rise with increasing distance from the nozzle tip, but also drop with

increasing Reynolds number. The density time scales in each of the flames are approximately twice the [OH] time scales. This feature can be attributed to the higher scalar intermittency for [OH]. In particular, since the OH layer is thin, small fluctuations in the flame can yield large OH fluctuations which would not be present in the number density fluctuations.

To investigate the effect of Reynolds number on integral time scale, a series of LRS measurements were made by fixing the laser beam at a single radial position for $x/D = 20$ using 23 different Reynolds numbers. This location was selected because [OH] and temperature peaks are relatively invariant with Re at this particular point. Figure 5 shows the density time scales for these 23 different flames compared with [OH] measurements made in 18 different flames by Renfro *et al.*⁷ in a 3.4-mm tube burner with the same fuel mixture.

For the range $Re = 2980 - 19,200$ the density time scales are proportional to $Re^{-1.42}$, while the [OH] time scales are proportional to $Re^{-1.41}$. Hence, the [OH] and density fluctuations scale similarly with Re. Recent [OH] time-series measurements in turbulent non-premixed counter-flow flames⁸ suggest that this relationship might result from combined strain and Reynolds number effects. In contrast, velocity and mixture fraction statistics from the literature display a Re^{-1} dependence for non-reacting jets. However, to our knowledge, no study has systematically examined time scales for mixture fraction in flames, although some sparse data exist⁹.

The similar scaling for the [OH] and density time scales with Re suggests a linear relation between them. Figure 6 shows the ratio of density to [OH] time scales at various axial locations along the jet centerline for all flames investigated. It is interesting to note that for a given Re, this ratio of time scales is mostly invariant with x/D . This result requires further investigation, but appears to suggest an enhanced reduction in the [OH] time scale at greater Re owing to more discernable fluctuations of the thin [OH] layer as compared to the wider density layer.

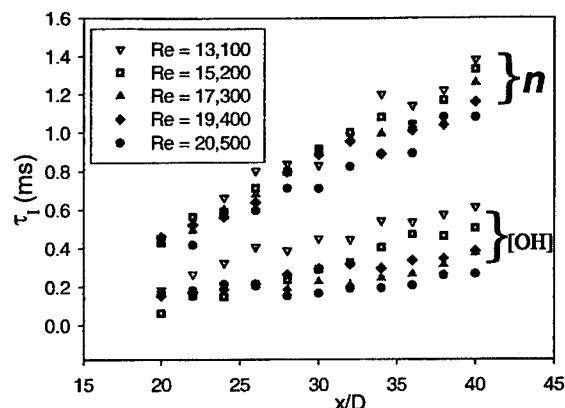


Figure 4: Centerline [OH] and density time scales.

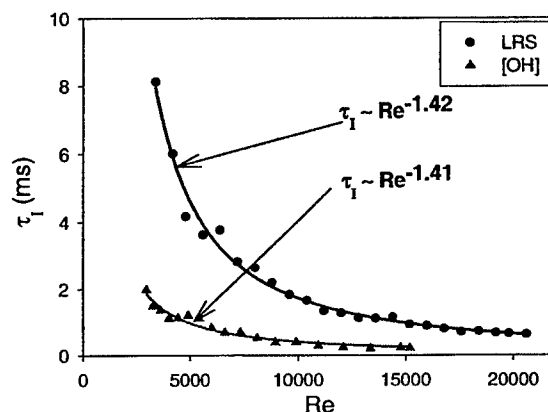


Figure 5: Hydroxyl and density integral time scales for different Reynolds

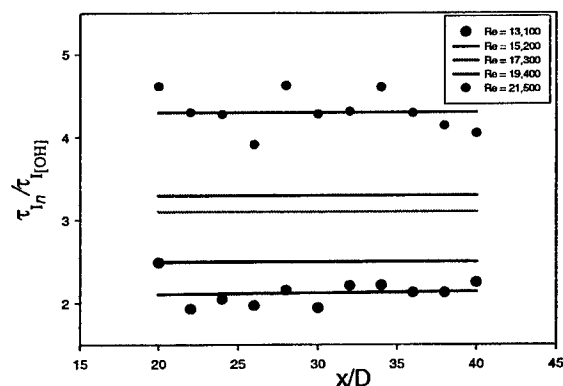


Figure 6: Ratio of integral time scales.

⁷ M.W. Renfro, J. P. Gore, N.M. Laurendeau, Combust. Flame 129 (2002) 120.

⁸ K.K.Venkatesan, Hydroxyl time series measurements in turbulent counter-flow partially premixed and non-premixed flames, M.S. Thesis, Purdue University, West Lafayette, IN (2003).

⁹ M.E. Kounalakis, Y.R. Sivathanu, G.M. Faeth, J. Heat Tran. 113 (1991) 437.

Acoustic Sensing and Actuation in Gaseous Flows

Contract # DAAD19-01-0571

Principal Investigator: Tim Lieuwen

School of Aerospace Engineering
Georgia Institute of Technology
Atlanta, GA 30332-0150

SUMMARY/OVERVIEW:

Controlling and/or monitoring the degree of mixing between constituents of a multi-component media is a key problem in a variety of applications. Monitoring such mixing processes necessarily requires capabilities for quantification of the level of "mixedness". However, quantification of *molecular* mixedness levels, as opposed to macro-scale entrainment, is difficult. Under this program, we have demonstrated the use of acoustic absorption measurements to characterize an average level of molecular mixedness between gases across the wave propagation path. This abstract presents the results of example calculations and experiments demonstrating the feasibility of this technique and the significant sensitivity of acoustic absorption levels upon gas mixedness ; e.g., measurements reported here show acoustic amplitude differences of up to a factor of ten between identical gas mixtures whose only difference is the level of mixedness of their constituent gases.

TECHNICAL DISCUSSION:

Controlling, enhancing and/or monitoring the degree of mixing between constituents of a multi-component media is a key problem in a variety of applications; e.g., in various chemical processes or in developing fuel/air mixers for low NO_x combustors. In particular, for applications where the rate of chemical reactions is controlled by the molecular collision rate between mixture constituents, control and/or enhancement of mixedness at the molecular level, as opposed to simply macro-scale entrainment, is needed. Optimization of such mixing enhancement strategies necessarily requires capabilities for quantification of the level of "mixedness". However, quantification of *molecular* levels of mixedness, as opposed to macro-scale entrainment, is difficult. This objective of this program is to develop acoustic techniques to characterize the level of gas mixedness at the molecular level. Under this program, extensive theoretical and experimental work was performed. Because of space limitations, we emphasize the experimental results in this abstract.

A photograph and drawing of the facility are shown in Figure 1.

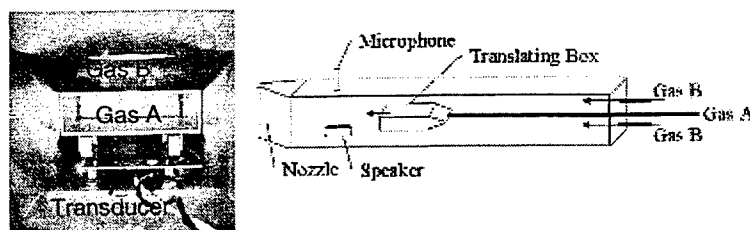


Figure 1. Photo (flow coming out of page) and drawing of facility developed for acoustic absorption measurements.

It consists of an 244 cm long, 20 x 28 cm section aluminum duct that is capped at one side and open at the other side. A translating box 30.5 x 27.9 x 6.4 cm with one open end slides inside the duct. Two gases of arbitrary composition, denoted as Gas "A" and Gas "B", flow through the main chamber and the translating box and mix at the translating box exit. For this experiment, gases "A" and "B" simply consisted of two CO₂ sources with different levels of some secondary gas. We used both H₂O and propane (C₃H₈) as the secondary gases. Water vapor was used because of the abundance of existing data on its effect on CO₂ vibrational relaxation rates.

In a typical experiment, two initially unmixed gas streams enter the facility in the positions noted in Figure 1. At the point where gas A exits the translating box, it mixes with gas B. As these gases convect down the duct and mix, the acoustic amplitude is measured at different axial locations, accomplished by pulling the translating box away from the transducers.

Typical transverse C₃H₈ concentration profiles at different axial locations are shown in Figure 2. The two vertical lines indicate the edges of the translating box. It can be seen that the profile at the translating box exit is smoothed out somewhat from the discontinuous change in concentration, at least partially due to the averaging of the 1.3 cm diameter measurement probe in the transverse direction. As expected, the profiles smooth out with increasing axial mixing distance, and at 120 cm, the propane concentration is completely uniform.

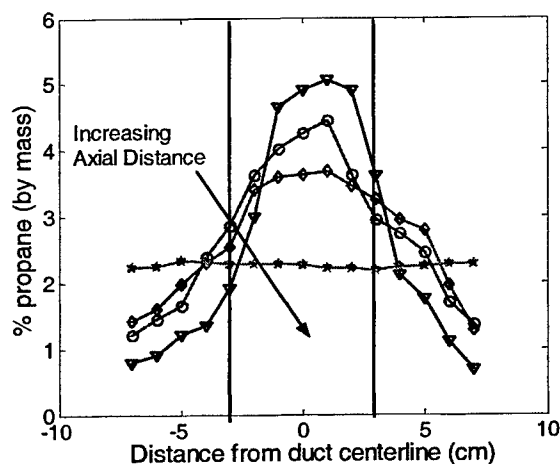


Figure 2. Measured transverse propane concentration profile at mixing distances of 0, 2.5, 5 and 120 cm (axial flow velocity = 3 cm/s). Vertical lines denote translating box edges.

The typical dependence of the acoustic amplitude upon axial mixing distance, normalized by its values at the perfectly mixed $x = 120$ cm axial location, are shown in Figure 3. The figure shows the substantial, generally monotonic, increase in acoustic amplitudes as the gases become

more mixed. Data are not shown for 80 or 90 kHz because the absorption was so high that the amplitude could not be accurately measured in all cases. The dependence of the ratio of the acoustic amplitude in the most unmixed and mixed, $A(x=0)/A(x=1.2\text{ m})$, cases upon frequency also is plotted.

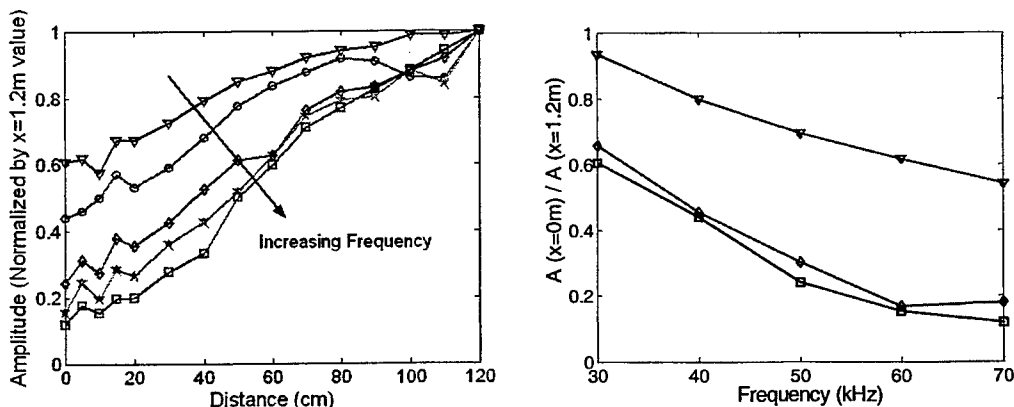


Figure 3. (Left) Dependence of 30, 40, 50, 60 and 70 kHz amplitude signal upon axial distance between gas stream origination point and acoustic transducer (initial propane concentration of 8.5%). (Right) Comparison of theoretical, ∇ , (based upon measured C_3H_8 concentration at box exit in 8.5% propane case) and measured (initial C_3H_8 concentrations at translating box exit of 8.5%, \diamond , and 9.4 %, \square) ratio of acoustic amplitude at $x=0$ and 120 cm. Axial flow velocity = 3 cm/s

It shows that the acoustic amplitude increases by a factor of roughly 2 and 10 in the 30 and 70 kHz cases, making the point that the effect of mixedness upon acoustic amplitude is by no means minor! The figure also shows a comparison of the predicted dependence of this ratio upon frequency, calculated using the measured absorption at each C_3H_8 level in the perfectly mixed case and assuming that the total absorption could be approximated as $\exp\left(-\int \alpha dy\right)$. The two results have similar qualitative trends, although the theoretical predicted frequency sensitivity of the amplitude ratio is significantly less than what was experimentally observed. These differences are due in part to the sensitivity of the theoretical result to the exact details of the C_3H_8 profile. For example, the true profile likely changes much more sharply at the translating box edges, but is smeared out somewhat in the measurements because of the transverse averaging of the measurement probe. We ran sensitivity studies to evaluate the manner in which the predicted amplitude ratio would change with deviations in C_3H_8 profile. By using a "flat-top" exit profile whose concentration changed discontinuously from 2% in the outer flow to 8.25% in the translating box, the frequency sensitivity changed to approximately 0.85 and 0.35 at 30 and 70 kHz, respectively. These values are much closer to our measurements.

Analogous data were obtained for the case where water vapor was used at the secondary gas. Because of space limitations, these are not included here.

While the data shown here deliberately focused on steady state, laminar mixing cases so that the corresponding gas concentration profiles could be readily measured, we have obtained ample data in cases where unsteady mixing is clearly prominent. For example, by intentionally causing the flow velocities of the outer flow and the translating box to differ we could observe what is apparently the unsteady rollup of the shear layer between the two streams. This behavior can be seen in Figure 4, where the average velocity of the outer flow has intentionally been set 60% higher than in the translating box. Pure CO_2 is used in both flows in curve (1) to illustrate

that the amplitude is essentially constant in the absence of unsteady species mixing, illustrating that the bouncing observed in the signal amplitude in other cases is not due to velocity fluctuations. Approximately 30% propane is added to the translating box flow in curves (2-7), which are taken at successive axial locations downstream. At the translating box exit (curve 2), the signal oscillates only slightly. The level of oscillations (as well as the average amplitude) grows monotonically with downstream distances of 5, 15, and 30 cm. The unsteadiness in amplitude is particularly evident at 30 cm. The amplitude of oscillations then decreases with further distance, indicating that the two streams are nearly mixed. Although not shown, at 120 cm the signal is essentially flat with no bouncing.

In closing it should be pointed out the implementation of the technique is gas specific, depending upon the nature of the vibrational-translational and vibrational-vibrational interactions between the gases being mixed. The technique may not work in all situations, such as with two monotonic gases or two gases with little effect upon each other's vibrational relaxation rates. However, a possible way to extend the technique to such cases would be to mix one or more of the gases with a third gas that does impact the other's relaxation rates.

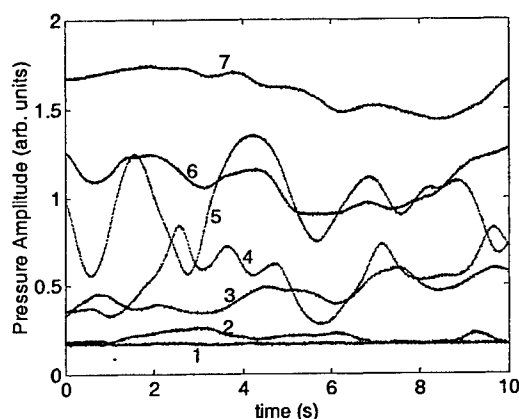


Figure 4. Temporal dependence of amplitude of 50 kHz signal with (1) pure CO₂, and (2-7) C₃H₈-CO₂ mixtures at axial distances of $x=0, 5, 15, 30, 40$ and 60 cm (average velocities of 1.3 and 2.1 cm/s in the translating box and outer flow, respectively; 30% propane in translating box flow in cases 2-7).

BALLISTIC IMAGING IN THE PRIMARY BREAKUP REGION OF DIESEL INJECTOR SPRAYS

Contract Number DAAD19-02-1-0221

Principal Investigators: Mark Linne and Terrence Parker

Division of Engineering
Colorado School of Mines
Golden, CO 80401

SUMMARY/OVERVIEW:

We are developing a technique for imaging the near-field, liquid core in the primary breakup region of a diesel spray, under operating temperatures and pressures typical of a diesel engine. This technique, called "ballistic imaging", has been used primarily in the medical community for imaging through tissue. To-date, the existence and behavior of a liquid core for diesel sprays have been a subject of debate. Our goal is to contribute to the understanding of the liquid spray core and its breakup by adapting ballistic imaging to this important flowfield.

TECHNICAL DISCUSSION:

When light passes through a highly turbid medium, some of the photons actually pass straight through without scattering, exiting the medium within roughly the same solid angle that they entered (see Figure 1a). These relatively few photons are termed "ballistic". Because they travel the shortest path, they also exit first (see Figure 1b). A somewhat larger group of photons is called the "snake" photon group, because they are scattered just once or twice. They exit the medium in the same direction as the input light but with a somewhat larger solid angle than the ballistic photons. Because they travel a bit further, they exit just after the ballistic photons. Light exiting the medium that has scattered multiply ("diffuse photons") has a larger photon number density, but it also is scattered into a very large solid angle and it exits last.

Due to their undisturbed path, ballistic photons retain an undistorted image of structures that may be embedded within the turbid material. If used in a shadowgram arrangement, the ballistic photons can provide diffraction limited imaging performance of these structures. Unfortunately, in most highly scattering and/or absorbing environments, the number of transmitted ballistic photons is often insufficient to provide the necessary signal to noise ratios (SNR) to form an image. In such a case, the snake photons retain slightly distorted information and can be used in imaging,

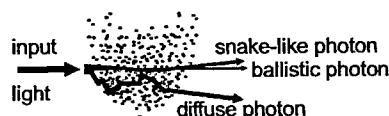


Figure 1a. Geometric schematic of ballistic imaging.

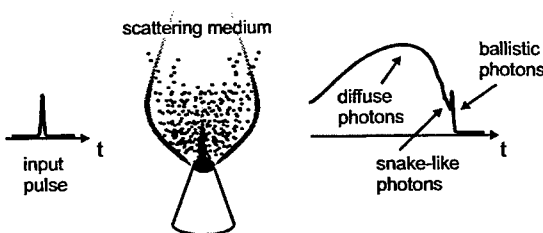


Figure 1b. Time-domain schematic of ballistic imaging with a short pulse.

together with the ballistic photons, with little degradation of resolution. We make use of them in this work. In contrast, diffuse photons retain no memory of the structure within the material. If allowed to participate in the formation of an image, the various paths these multiply scattered photons take through the material will cause any image point they form to appear as if it came from an entirely different part of the object, and this will seriously degrade image resolution. Unfortunately, diffuse photons are the most numerous when light is transmitted through highly scattering media. The problem of obtaining a high-resolution image through highly scattering materials is thus a matter of separating and eliminating the diffuse light from the ballistic and snake light. This can be done using discrimination methods that make use of the properties that are retained by the ballistic and snake light but are lost in multiple scattering events. As already alluded, the direction taken by transmitted light, together with exit time, can help to segregate diffuse photons from the imaging photons. This is done here via spatial filtering (to select the light exiting at narrow scattering angles), together with time gating. In time gating, a very fast shutter (an optical Kerr gate¹) is used to select just the leading edge containing ballistic and snake photons.

Based upon a detailed evaluation described by Paciaroni and Linne², we have chosen the time-gated system shown in Figure 2. A 1-kHz repetition rate Spectra-Physics Spitfire Ti:Sapphire regenerative amplifier, seeded with a Spectra-Physics Tsunami Ti:Sapphire mode-locked laser, generates 80 fs, 1mJ pulses centered at ~ 800 nm. The linearly polarized beam is split into OKE gating and imaging beams; 30% of the optical power is used as the imaging beam while the remaining power is used to create the OKE time gate. Our initial work² demonstrates that we can routinely achieve a spatial resolution around 40-50 μm (depending upon the level of extinction imposed by the droplet mist).

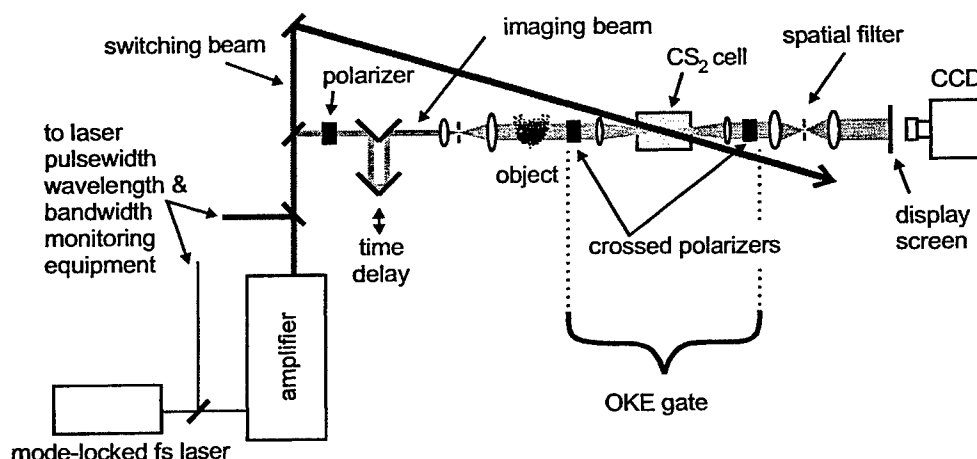


Figure 2. Layout of OKE-switched ballistic imaging system.

As shown in Figure 2, the polarization state of the imaging beam is first cleaned up with a polarizer and then rotated 45°, because the OKE gate relies upon polarization switching. The imaging beam is then time delayed using an adjustable length delay arm. This allows one to control the delay between the arrival of the switching and imaging pulses at the OKE gate, for optimum time gating. The imaging beam then passes through an optics train consisting of a

¹ Wang, Ho, Liu and Alfano, "Ballistic 2-D Imaging Through Scattering Walls Using an Ultrafast Optical Kerr Gate", *Science*, 253:769, (1991), Wang, Liu, and Alfano, "Ballistic Imaging of Biomedical Samples Using a Picosecond Optical Kerr Gate", *Proceedings of the SPIE*, 143:97, (1991), Yoo, Das, Liu, Xing and Alfano, "Femtosecond Time-gated Imaging of Translucent Objects Hidden in Highly Scattering Media", *Springer Series in Chemical Physics: Ultrafast Phenomena VIII*, 55:124, (1993).

² "Single-shot two-dimensional ballistic imaging through scattering media", Megan Paciaroni and Mark Linne, under review in *Applied Optics*.

telescope (with spatial filter) that controls the imaging beam size at the object, a system to relay the beam through the OKE switch, and a combined spatial filter/telescope for imaging onto a display screen. This system was been designed using OSLO®, a commercial ray-trace code. By careful choice of optics, we have ensured that the optical train itself is diffraction limited. There are no spurious aberrations or distortions introduced by the imaging optics themselves in this system.

The OKE gate works in the following manner. When there is no switching pulse present, no image is transferred to the display screen. This is because the OKE gate uses crossed calcite polarizers. The first polarizer in the OKE gate (second polarizer used in the imaging beam) is oriented to pass the polarization orientation of the imaging beam. The second OKE polarizer is oriented normal to the first, blocking an unperturbed imaging beam. The measured extinction ratio of the polarizers is $>10^5$; without a switching pulse present there is $<10^{-5}$ transmission of the imaging beam through the second polarizer. Following the first polarizer, the imaging beam is focused into the Kerr active liquid (CS_2 in this case) with an F/#5 achromat, and then up-collimated with an F/#10 achromat. At the arrival of a switching pulse, the intense electric field of the pulse causes the CS_2 dipoles in a to align along the polarization vector of the switching beam, creating temporary birefringence in the liquid. This birefringence rotates the polarization of the imaging beam (about $\pi/3$ radians for switching with the fundamental of Ti:sapphire), allowing most of the imaging beam ($\sim 70 - 75\%$) to pass through the second polarizer. The imaging beam time delay is adjusted while switching for maximum signal transmission through the OKE gate. This OKE induced birefringence is limited in time by either the duration of the laser pulse or the molecular response time of the Kerr medium, whichever is longer. In our case, the incident laser pulse is of much shorter duration than the molecular relaxation time of ~ 2 ps for CS_2 ; our gate time of 2 ps has been confirmed by direct measurement.

As a first test of this imaging system, we set up a quasi-steady water jet experiment using a piston-accumulator system to provide high pressure (up to 2500 psi) over about 1 minute of spray time. This allowed us to develop and prove a ballistic imaging system for sprays without having to deal with triggering issues. It has also generated some very interesting results. The nozzle used here has a constant area passage length of 0.219 mm, an exit diameter of 0.457 mm, and therefore a length-to-diameter ratio of 3.01. The pressure control available in this system thus provides access to a range of Reynolds and Weber numbers along with the associated range of expected liquid core lengths. The system generates a spray that is well into the atomization regime. The specific spray images contained in this report were acquired at a Reynolds number $Re = 103000$, Ohnesorge number $Oh = 0.0047$, and Weber number $We = 233000$.

Representative ballistic images of the spray are shown in Figure 3. The images are characterized by dark areas representing a continuous fluid phase and light areas representing the gas phase. Small features at the limit of spatial resolution can be seen in both sections of the images. In the fluid phase, the grainy texture is dark noise in the camera; in the gas phase, spurious dark spots that are smaller than the resolution limit of the system are caused by diffraction. These should not be interpreted as small droplets.

These are the first detailed images of the liquid core in such a spray, and we find some unexpected features in these images. At the nozzle exit a dense core is evident and there is no indication of spray breakup; however, two of the three images suggest the presence of large-scale turbulent structures in the jet, or perhaps harmonic oscillations. The wavelength of these disturbances, or oscillations, is approximately 1.5 - 2 mm. The velocity of the fluid at the nozzle exit is 190 m/s. If we use this as the characteristic velocity, these oscillations have an estimated frequency of ~ 95 kHz. The complete time series of these images past the exit

reveal a flow field undergoing turbulent primary breakup. One can also detect potential signatures of harmonic behavior, shedding of droplets from an intact core, and small voids that seem to appear and then coalesce with distance. The evolution of the liquid core is characterized by the growth of these structures with downstream position. A classical breakup, with organized stripping from the sides and mass ejection from the end is not supported by these images. Rather, we observe violent ejection of mass from the sides and loss of an organized jet structure. Much more information about this spray is presented in a forthcoming article³.

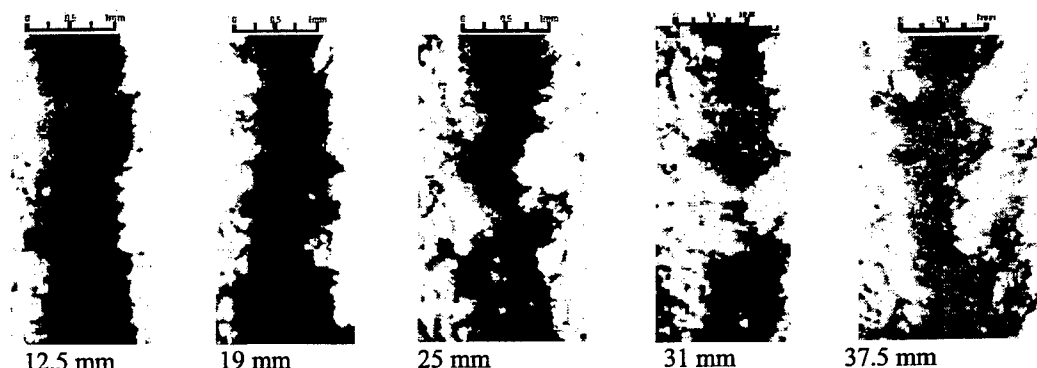


Figure 3. Ballistic images of the liquid core as a function of distance from the jet exit.

Next, we have acquired one ballistic image in a diesel fuel spray produced by a Sturman® diesel fuel injector (Figure 4). The nozzle for this system is manufactured by Siemens and includes a ring of six holes, each with an orifice diameter of 195 μm . Imaging for the system was arranged to view a single hole. Figure 4 shows the structure of the diesel jet very near the injector outlet. The top of the image shows the injector edge with the spray exiting from this edge. Very near the outlet the lighter gray regions indicate voids in the spray which could possibly be due to cavitation in the injector outlet, as speculated by Smallwood and Gülder⁴, or aggressive breakup and entrainment of the jet itself. The jet also appears to have a spiral mode as suggested by Soteriou *et al.*⁵. This is the first image confirming what were speculative notions about the liquid core.



Figure 4. Ballistic image of a diesel spray.

As our ability to synchronize the injection and laser systems matures, we expect to be able to provide high quality images of the near injector region that shows the time evolution of the jet over a range of injection conditions. Ongoing work is focused upon acquisition of such a time series of ballistic images in this diesel fuel spray, into one atmosphere for the initial diesel experiments.

³ M. Paciaroni, M. Linne, T. Hall, J-P Deloplanque and T. Parker, "Single-Shot Two-Dimensional Ballistic Imaging of the Liquid Core in a Spray", under review in *Atomization and Sprays*

⁴ G. J. Smallwood and Ö. L. Gülder, "Views on the Structure of Transient Diesel Sprays", *Atomization and Sprays*, Vol. 10, (2000), pp. 355-386.

⁵ C. Soteriou, R. Andrews, N. Torres, M. Smith & R. Kunkulagunta, "Through the Diesel Nozzle Hole - a Journey of Discovery", ILASS Americas, (2001)

LARGE-EDDY SIMULATION OF TURBULENT COMBUSTION

Grant number: F4962-03-1-0258
Principal Investigator: Heinz Pitsch

Flow Physics and Computation Group
Department of Mechanical Engineering
Stanford University
Stanford, CA 94305-3030

SUMMARY/OVERVIEW

The present research program has two major components: (I) the development of improved turbulence/chemistry interaction models for large-eddy simulations (LES), and (II) the development of reduced kinetic mechanisms for JP-8 surrogate fuels, including the definition of surrogate fuels and the systematic reduction of the detailed chemical mechanisms. During this performance period we have analyzed sub-filter models for the scalar variance, which have been found to be of crucial importance in non-premixed combustion simulations. We have developed two new models, one based on the solution of a second moment transport equation, one based on a dynamic localization approach. These models have been evaluated in LES and will in the future be validated with DNS and experimental data. Further, we have developed a new method to evaluate the filtered density in the Combined Conserved Scalar/Level Set Flamelet model, which accounts for the turbulent broadening of the preheat zone of premixed flames in the thin reaction zones regime. This method has been applied in the simulation of an aircraft engine model combustor. The results are compared with experimental data showing good agreement for temperature, major species, and CO. For the chemistry part of this project, a semi-detailed multi-component mechanism has been assessed and analyzed, and first attempts to reduce the mechanism have been made.

TECHNICAL DISCUSSION

Combustion Models for LES

Modeling Sub-filter Scalar Variance in Turbulent Combustion Simulations

Flamelet models used in LES simulations of turbulent combustion typically utilize the local mixture-fraction and scalar dissipation rate for the description of flame chemistry. Since LES simulations only resolve the large-scale part of the turbulent motion, the sub-filter mixture-fraction variations are described using a model. Typically, the variance of the mixture-fraction is used along with the filtered mixture-fraction field to define a sub-filter probability density function (PDF). DNS and experimental studies have shown that this PDF can be approximated by a beta-function. The filtered mixture-fraction field is obtained through the solution of a transport equation, while typically an algebraic model is used for estimating the sub-filter variance as well as the local scalar dissipation rate.

Pierce and Moin have proposed a dynamic modeling (DM) procedure for the sub-filter variance based on the assumption of local equilibrium. Using a modeled dissipation rate, the variance model can then be written as

$$\overline{Z''^2} = C\Delta^2(\nabla\overline{Z})^2 \quad (1)$$

where Δ is the filter width and C is a coefficient to be determined. The dynamic modeling procedure can be written as

$$\widehat{\overline{Z\overline{Z}}} - \widehat{\overline{Z}}\widehat{\overline{Z}} = C\widehat{\Delta}^2(\nabla\widehat{\overline{Z}})^2 - C\Delta^2(\nabla\overline{Z})^2, \quad (2)$$

where $\widehat{\cdot}$ denotes test filtering. This equation is solved by making the assumption that $\widehat{C} = C$, and using a least square estimation technique.

The above methodology suffers from two principal drawbacks. First, the assumption of local equilibrium is not strictly valid in transient inhomogeneous flows and the physical transport of sub-filter variance can usually not be neglected. It has further been found that solving a transport equation for a sub-filter scalar variance leads to large errors in the case of implicit filtering and second order numerical schemes. In order to account for spatial transport as well as to avoid numerical inaccuracies, a new method has been developed. The second moment of the mixture-fraction ($\overline{Z^2}$) is solved using a transport equation. This transport equation does not contain any production terms but only the scalar dissipation rate, which is then modeled using

$$\overline{\chi} = \frac{C_z}{\tau} (\overline{Z^2} - \overline{Z}^2), \quad (3)$$

where C_z is a dynamically determined coefficient and τ is a suitable turbulent time scale. Clearly, the sub-filter variance can then be obtained using $\overline{Z''^2} = \overline{Z^2} - \overline{Z}^2$.

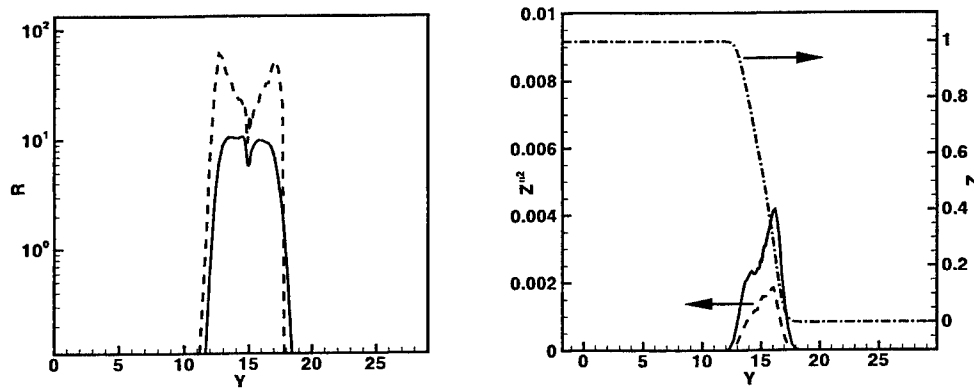


Figure 1: (Left) Comparison of scalar-to-mechanical time-scale ratios computed using DM (dashed) and DL (solid) procedures. (Right) Comparison of variance computed using DM (dashed) and DM(solid) models.

A second difficulty with using Eq. 2 is that typical dynamic modeling procedures assume azimuthal homogeneity and scale independence of the modeled coefficient (C_z in Eq. 3). To overcome this issue, the dynamic localization (DL) procedure is used to formulate an

integral equation that is then solved using an iterative technique to obtain C_z as a three-dimensional field. As a first step, the dynamic modeling procedure has been developed assuming local equilibrium and tested using DNS as well as LES simulations. Results from shear-flow calculations, shown in Fig. 1, indicate that the dynamic model overpredicts the scalar-to-mechanical time-scale ratio compared to the DL model by a factor of 10. The DL model consequently predicts a higher variance across the shear-layer. To account for non-equilibrium effects, the DL procedure is being extended to modeling the $\overline{Z^2}$ equation. Results of this extended model as well as the local-equilibrium assumption based DL model will be compared against the experimental results of Wang and Tong.

CO Predictions in Complex Flows Using LES

A combined model that can account for premixed combustion within a diffusion flame is currently being developed and validated. This combined approach is based on a steady flamelet model. The G -equation, which accounts for the movement of premixed flame fronts, is introduced on top of the steady diffusion flamelet model to distinguish between the burned gas on one side of the flame front and the unburned gas on the other. In the unburned gas region, pure mixing without chemical reactions is used to calculate the value of the reactive scalars, while in the burned gas region the steady diffusion flamelet model is used. Previous simulations of the Bowman/Edwards experiment have shown that in regions close to the nozzle, the premixed flame is rather rich, and the evaluation of the relevant parameters reveal that combustion in these areas takes place in the thin reaction zones regime. It has also been observed that the way the local heat release is determined from the G -field strongly impacts the velocity field. In a new regime diagram for premixed turbulent combustion, we have shown that in the thin reaction zones regime, the flame thickness is larger than the filter size, if the local sub-filter Damköhler number is smaller than unity. In the solution of the filtered Navier-Stokes equations, the heat release appears through the density field. The flame broadening of the reaction zone cannot be described by evaluating the density from the flamelet library. A new method to compute the filtered density has been devised to account

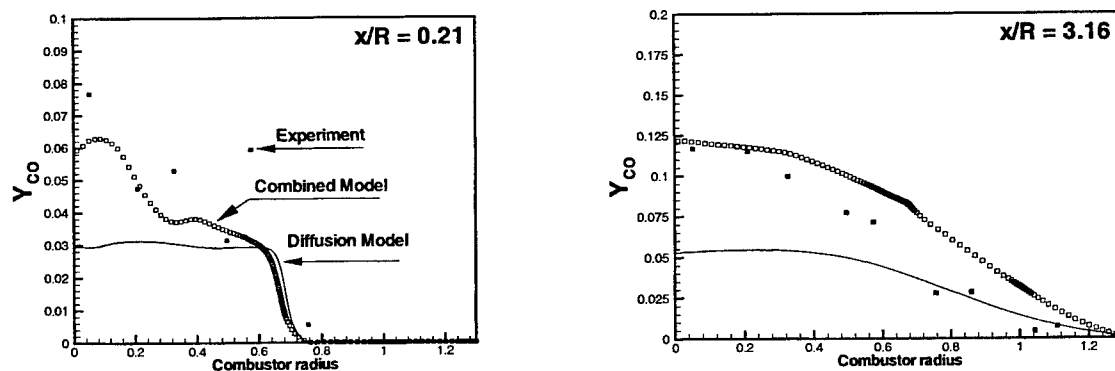


Figure 2: CO mass fractions predicted by the diffusion and combined models at several axial locations in the combustor.

for the turbulent flame broadening in the thin reaction zones regime. The filtered density is determined from the temperature, which is computed through the solution of a transport equation. This temperature equation is to be solved only in the unburned region. The burned

gas temperature, determined from the steady flamelet library, is enforced through a source term as a boundary condition at the flame front. It has to be noted that the flame position is still determined from the G -equation and then imposed on the temperature equation. It would be incorrect to solve a temperature equation in numerical computations of premixed turbulent combustion.

This model has been evaluated through the simulation of a well documented gas-phase combustor experiment. The experiment by Spadacchini et al. has been used. The flow configuration resembles a simplified aircraft engine combustor and is essentially non-premixed. The flame is lifted off the nozzle and stabilized through multiple recirculation regions. Initial simulations indicate that the combined model has a substantial influence on the predictions as compared with a steady flamelet model without the G -equation. Fig. 2 shows predicted CO mass fractions at two different cross-sections in the combustor compared with experimental data. Although for overall lean combustion, the CO mass fractions are very sensitive to the flow conditions, the data is well predicted.

Development of Reduced Mechanisms for JP-8 Surrogate Fuels

It is presently impossible to model the true chemistry of realistic fuels. Hence, numerical simulations have to use surrogate fuels, which consist of one or more chemical components and reproduce the behavior of the real fuel. In this project, we are developing a component library for surrogate fuels of different complexity, matching various requirements depending on the physical problem considered. Key parameters include heat release, volatility, sooting tendency, boiling point distribution and cost.

We have acquired a semi-detailed mechanism for multiple component surrogate fuels, which has recently been developed by Violi et al. This mechanism has been extensively tested and validated against experimental data for each single surrogate component as well as mixtures of these. We have evaluated the performance of the individual components including dodecane, iso-octane, benzene, toluene, methyl-cyclohexane and alpha-methylnaphthalene. Ignition delay times, reactivity, and component mass fractions have been computed under a wide variety of physical conditions and compared with experimental data. The two distinct goals of that preliminary step were first to assess the validity of the mechanism, then to create a large library of experimental cases relevant to the present simulations. Those cases will serve as reference data throughout the reduction process.

The present mechanism is semi-detailed in the sense that only the evolution of small species is described by mean of detailed elementary reactions. Larger hydrocarbon decomposition and oxidation mechanisms are represented in terms of lumped reactions, in which similar intermediate species are replaced by an equivalent or lumped pseudo-species. First attempts to reduce this mechanism have shown that this approach is not suitable for systematic reduction, as part of the detailed mechanism is already lumped into global reactions.

A newer multi-component mechanism developed by Sarofim et al. will soon be acquired. It will first be validated against the wide collection of experimental data, including new experimental data for homogeneous auto-ignition delay times from Hanson and extinction and counterflow ignition data by Seshadri. Future work includes exploitation of this new mechanism toward a suited form for systematic reduction, establishment of a surrogate library to match main practical applications and the development of an automatic reduction procedure leading to skeletal mechanisms.

PDF MODELING OF TURBULENT COMBUSTION

AFOSR Grant F-49620-03-1-0015

Principal Investigator: Stephen B. Pope

Mechanical & Aerospace Engineering
Cornell University
Ithaca, NY 14853

SUMMARY

The overall goal of the research is to develop and demonstrate improved computational approaches for turbulent combustion. In both space and aircraft applications, the design of combustors in propulsion systems remains a significant technical challenge. Computational modeling is used extensively in the design process: our work is aimed at increasing the accuracy and efficiency of such models. In the last year the focus of the research has been on performing PDF model calculations of lifted hydrogen flames in a vitiated co-flow, and comparing the results to experimental measurements from Sandia and Sydney. These calculations have been made both with the velocity-frequency-composition PDF method using the research code HYB2D, and also with the composition PDF method using Fluent. In both cases, parallel processing based on domain decomposition is used, and research is ongoing on effective strategies for using *in situ* adaptive tabulation (ISAT) in such parallel environments. Collaboration with the University of Pittsburgh continues and has resulted in the first LES/PDF calculations of a turbulent flame (Sheikhi et al. 2004). Some basic issues concerning LES have been explored (Pope 2004), and the PI has contributed to the plenary lecture on turbulent combustion to be presented at the Thirtieth International Symposium on Combustion (Bilger et al. 2004).

PDF CALCULATIONS OF LIFTED TURBULENT FLAMES

Masri et al. (2004) describe composition PDF calculations of the lifted hydrogen jet flames in a vitiated co-flow studied experimentally by Cabra et al. (2002). Research continues on these flames, as there are several fundamental issues yet to be resolved. This flame is significantly different from lifted flames in cold co-flows, in that the basic stabilization mechanism is the autoignition of hot lean mixtures formed in the mixing of jet and co-flow fluid.

Figure 1 shows the lift-off height as a function of the co-flow temperature. As may be seen, the experimental measurements (from the University of Sydney) show significant sensitivity to the co-flow temperature. The PDF calculations are performed with two recent hydrogen mechanisms: that of Mueller et al. (1999) and the update to this mechanism provided by Li et al. (2003). The main conclusions are that the PDF calculations agree well with the experimental data, and that there is some sensitivity to the details of the chemical mechanism. (The uncertainties in the measured co-flow temperature and ambiguities in the definitions of lift-off height necessitate caution in drawing stronger conclusions.)

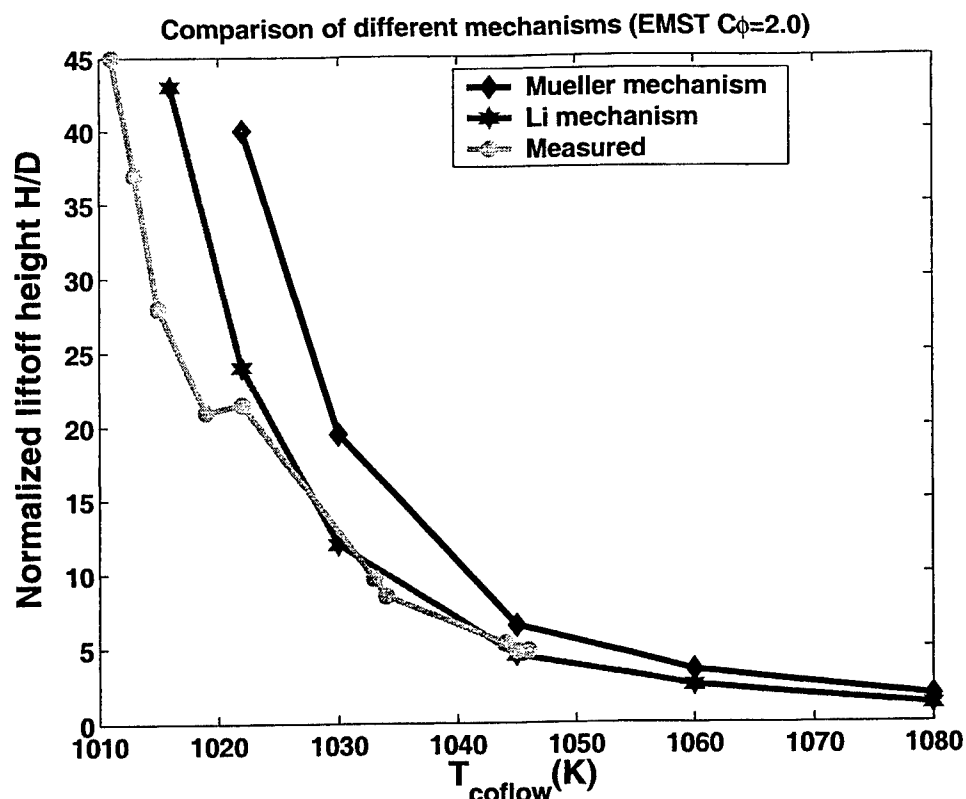


Figure 1. Lift-off height (in jet diameters) against co-flow temperature for the hydrogen jet flame in a vitiated co-flow: comparison of experimental measurements and joint PDF calculations using the Mueller and Li chemical mechanisms.

An important outstanding question is the accuracy of the mixing sub-models used in PDF methods. The three most widely used models are named IEM, MC and EMST. It has been found previously that, in some circumstances, these three models yields significantly different results (Subramaniam & Pope 1999, Ren & Pope 2004). For the lifted hydrogen flame in a vitiated co-flow, Fig. 2 shows the lift-off height as a function of the co-flow temperature for the three mixing models. As may be seen, the sensitivity to the choice of model is not great. It remains to delineate the circumstances in which the different models provide an adequate description of mixing.

EFFICIENT PARALLEL IMPLEMENTATION OF IN SITU ADAPTIVE TABULATION

In the last year, a significant advance has been in our extensive use of parallel clusters to speed up the turn around time of PDF computations. Both our research code HYB2D and Fluent run effectively in parallel using domain decomposition.

If there are P processors, then the load associated with solving the finite-volume equations is well balanced if the solution domain is partitioned into P subdomains, each containing approximately the same number of cells. Further, with such a decomposition, the computational particles used in the PDF algorithm are approximately equally distributed between the processors.

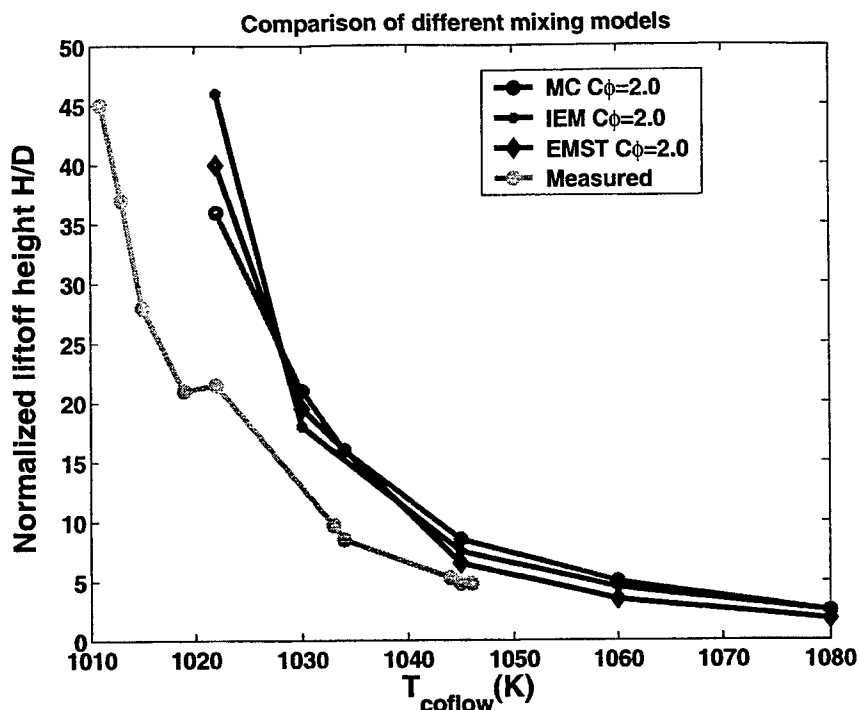


Figure 2. Lift-off height (in jet diameters) against co-flow temperature for the hydrogen jet flame in a vitiated co-flow: comparison of experimental measurements and joint PDF calculations with three different mixing models.

Hence there is good load balancing of particle tracking and of mixing. However, the load associated with reaction (i.e., incrementing the particle compositions due to reaction over the time step) which can dominate the CPU time can be poorly balanced. For example, the particles on one processor may be inert (e.g., cold air) and hence require negligible time to evaluate their reaction; whereas the particles on another processor may be highly reactive. Even using ISAT, reactive particles take much longer to treat, especially during the early phase of the computation when the ISAT table is being built.

We are developing general software to address this problem. The abstraction of the particular problem is as follows: there is a function $f(x)$ which is computationally expensive to compute, and the evaluation cost depends on x (and indeed on all previous x considered). In an MPI environment, on each processor there is an ensemble of values of x for which $f(x)$ is to be evaluated. The task is to use message passing so that $f(x)$ is evaluated for all given values of x in the shortest possible time. (That is, the value of x on one processor may be passed to another processor which evaluates $f(x)$ and passes back the value of f .) (In the present context x represents the particle composition at the beginning of the reaction fractional step, and f represents the composition after reaction.) Various strategies have been devised and are in the process of being evaluated.

PUBLICATIONS

The following papers based on AFOSR sponsored research have been published or written in 2003-2004.

R.W. Bilger, S.B. Pope, K.N.C. Bray and J.F. Driscoll (2004) "Paradigms in Turbulent Combustion Research," Proceedings of the Combustion Institute, **30**, (to be published).

R. Cao and S.B. Pope (2003) "Numerical integration of stochastic differential equations: weak second-order mid-point scheme for applications in the composition PDF method," J. Comput. Phys. **185**, 194-212.

A.Y. Klimenko and S.B. Pope (2003) "A model for turbulent reactive flows based on multiple mapping conditioning", Physics of Fluids **15**, 1907-1925.

A.R. Masri, R. Cao, S.B. Pope and G.M. Goldin (2004) "PDF Calculations of Turbulent Lifted Flames of H_2/N_2 issuing into a vitiated co-flow," Combustion Theory and Modelling, **8**, 1-22.

S.B. Pope (2004) "Ten questions concerning the large-eddy simulation of turbulent flows," New Journal of Physics **6**, 35.

M.R.H. Sheikhi, T.G. Drozda, P. Givi and S.B. Pope (2003) "Velocity-scalar filtered density function for large eddy simulation of turbulent flows," Physics of Fluids **15**, 2321-2337.

M.R.H. Sheikhi, T.G. Drozda, P. Givi, F.A. Jaber and S.B. Pope (2004) "Large eddy simulation of a turbulent nonpremixed piloted methane jet flame (Sandia Flame D)," Proceedings of the Combustion Institute, **30**, (to be published).

Q. Tang and S.B. Pope (2004) "A more accurate projection in the rate-controlled constrained-equilibrium method for dimension reduction of combustion chemistry," Combustion Theory and Modelling **8**, 255-279.

Other references:

R. Cabra, T. Myrvold, J.Y. Chen, R.W. Dibble, A.N. Karpetis and R.S. Barlow, (2002) "Simultaneous Laser Raman-Rayleigh-LIF measurements and numerical modeling results of a lifted turbulent H_2/N_2 jet flame in a vitiated coflow," *Proc. Combust. Inst.*, **29**, 1881-1888.

Li, J., Zhao, Z., Kazakov, A., and Dryer, F.L. "An Updated Comprehensive Kinetic Model for H_2 Combustion", Fall Technical Meeting of the Eastern States Section of the Combustion Institute, Penn State University, University Park, PA, October 26-29, 2003.

M.A. Mueller, T.J. Kim, R.A. Yetter, and F.L. Dryer, (1999) "Flow Reactor Studies and Kinetic Modeling of the H_2/O_2 Reaction," *International Journal of Chemical Kinetics*, **31**:113-125.

Z. Ren and S.B. Pope, (2004) "An investigation of the performance of turbulent mixing models," *Combust. Flame*, **136**, 208-216.

S. Subramaniam and S.B. Pope, (1999) "Comparison of mixing model performance for nonpremixed turbulent reactive flow," *Combust. Flame*, **117**, 732-754.

MODEL DEVELOPMENT FOR IC ENGINES

(DAAD19-00-1-0487)

Principal Investigator(s): R.D. Reitz and C.R. Rutland

Engine Research Center
University of Wisconsin-Madison
1500 Engineering Drive
Madison, WI 53706

SUMMARY/OVERVIEW

Sophisticated 3-D, multiphase CFD models are available for predicting combustion in IC engines. These models rely on a range of sub-models for multiphase flow predictions, turbulence models, heat transfer, and chemical reactions, among others. Efforts at the ERC include developing better sub-models, more suited to an engine operating environment, and developing methods to apply these detailed models for design. This abstract briefly describes two projects, one involving development of a sub-grid scale spray model to use with LES turbulence models, and the second a method for using system simulations enhanced by neural networks to optimize the operation of a heavy duty engine.

TECHNICAL DESCRIPTION

LES Turbulent Combustion Modeling

A Sub-Grid Droplet Source (SGDS) Spray model, which takes into account the effect of droplet existence on the sub-grid scales of a two-phase turbulent flow, was developed and implemented into the KIVA-3V engine simulation code. This approach simulates the particles in a Lagrangian manner and the continuous phase in an Eulerian manner with two-way coupling of interactions between spray droplets and the carrier gas. The SGDS spray model is used in conjunction with a Dynamic Structure Large Eddy Simulation (LES) turbulence model (Pomraning and Rutland, 2002) for the momentum transport. The dynamic structure model is a dynamic, one equation, non-viscosity model, which uses a transport equation for the sub-grid kinetic energy of the flow field. This dynamic structure model can capture the flow field more accurately than conventional viscosity-based models and gives better estimates of the quantities such as the sub-grid kinetic energy that are needed for spray modeling.

In the SGDS model, the production term in the sub-grid kinetic energy equation due to spray droplets is modeled to include the interaction of droplets with the continuous phase via the drag force. The model also considers the effect of both the sub-grid and resolved scales on the spray droplets. A method is adopted for the determination of sub-grid continuous phase velocities at the droplet locations. This approach assumes a Gaussian distribution for the sub-grid turbulent velocities and that each droplet interacts with these fluctuations for its 'eddy residence time'.

Direct Numerical Simulation (DNS) data of high Reynolds number ($Re_p = 102$) two-phase turbulent flow with high-speed spray droplets from the S3D code simulation is used for *a priori* testing of the model. Comparison between the exact and modeled spray droplet source terms in the sub-grid kinetic equation shows very good results as indicated by the example in Figure 1. The simulated results for liquid penetration length and spray dispersion are also presented in comparison to the diesel spray experiments conducted by Siebers, 1998 and Kim and Ghandhi, 2001.

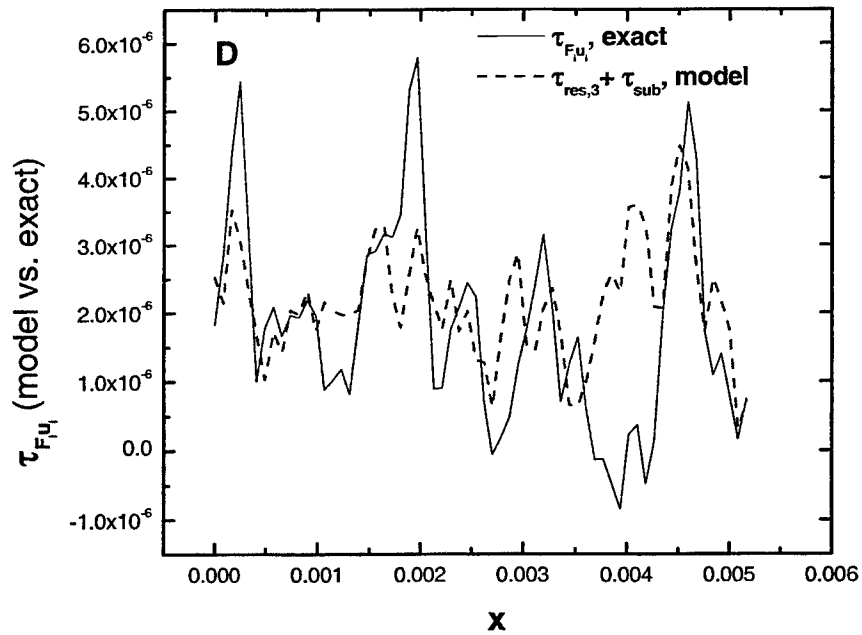


Figure 1: Comparison of DNS results (solid line) and LES model for spray source term in sub-grid kinetic energy equation.

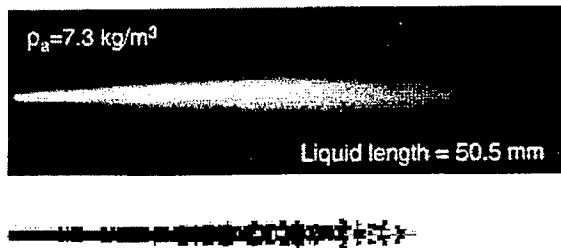


Figure 2: Experimental (top, Siebers 1998) and predicted spray images (bottom) for DF2. The chamber temperature, density, injection pressure and orifice diameter are 1000K, 7.3 kg/m³, 135 MPa and 246 μm respectively

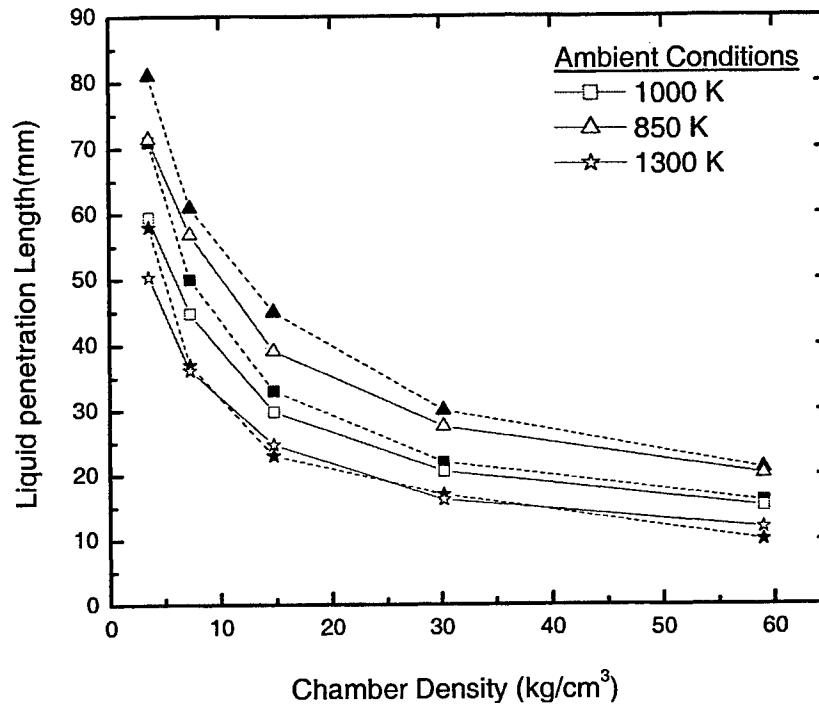


Figure 3: Liquid penetration length as a function of chamber density for DF2. The values in the legend are ambient temperature. The orifice diameter and injection pressure were 0.246 mm and 135 MPa respectively. Solid lines represent the simulation results and dotted lines represent the experimental results from Siebers.

Engine Optimization using Engine System Models

This project expands on the use of neural networks for engine computations. One reason for using neural networks is to capture the accuracy of multi-dimensional CFD calculations or experimental data while saving computational time, so that system simulations can be performed within a reasonable time frame. Three methods to improve upon neural network predictions were recently developed. Improvement is demonstrated for in-cylinder pressure predictions in particular.

The first method incorporates a physical combustion model within the transfer function of the neural network, so that the network predictions incorporate physical relationships as well as mathematical models to fit the data. The second method shows how partitioning the data into different regimes based on different physical processes, and training different networks for different regimes, improves the accuracy of predictions. The third method shows how using an ensemble of different networks based on engine operating parameters can provide greater accuracy than each of the individual networks. Although these methods have been implemented for engine computations, they might hold promise for other applications too.

Neural networks are useful tools for optimization studies since they are very fast, so that while capturing the accuracy of multi-dimensional CFD calculations or experimental data, they can be run numerous times as required by many optimization techniques. A set of neural networks trained on a multi-dimensional CFD code to predict pressure, temperature, heat flux, torque and emissions, have been used by a genetic algorithm in combination with a hill-climbing type algorithm to optimize operating parameters of a diesel engine over the entire speed-torque map of the engine.

The optimized parameters are mass of fuel injected per cycle, shape of the injection profile for dual split injection, start of injection, EGR level and boost pressure. These have been optimized for minimum emissions. These optimized parameters were used as inputs to another set of neural networks that were then trained to predict the optimized operating conditions for each speed-torque point of the engine (see Fig. 4). These networks can be thought of as 'engine maps' and have been used to simulate the emissions of the engine over the FTP heavy duty diesel cycle. Improvements resulting from the optimization were observed. The entire process of getting optimized parameters for an engine, starting from raw engine data or CFD results is capable of being automated and has been shown to take a reasonably small amount of computational time.

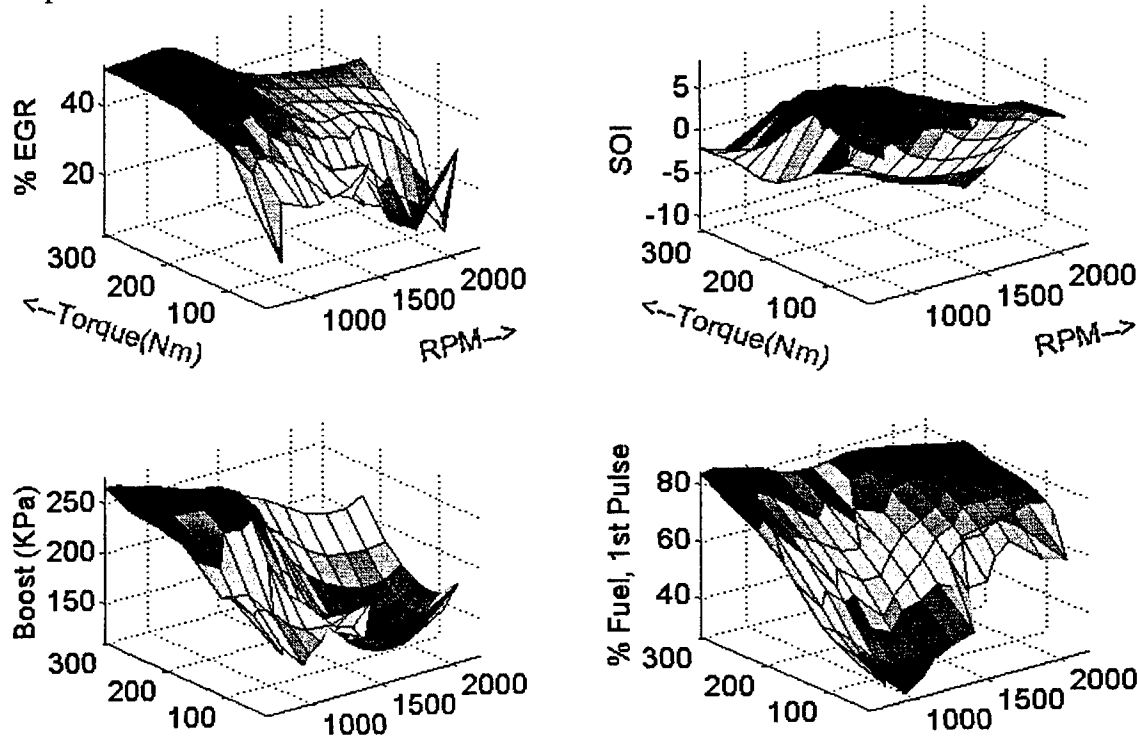


Figure 4: Optimized engine operating maps developed using neural network based simulations.

References

Kim T., and Ghandhi J. B., *Quantitative 2-D fuel vapor concentration measurements in an evaporating diesel spray using exciplex fluorescence method*, SAE Technical paper 2001-01-3495, 2001.

Pomraning E. and Rutland C. J., "Dynamic one-equation nonviscosity large eddy simulation model," *AIAA Journal*, 40, 4, April 2002

Siebers D. L., *Liquid phase fuel penetration in diesel sprays*, SAE technical paper 980809, 1998.

STUDY OF IN-CYLINDER REACTIONS OF HIGH POWER-DENSITY DIRECT INJECTION DIESEL ENGINES

(DAAD19-01-1-0766)

Principal Investigator(s):

K. T. Rhee

Department of Mechanical and Aerospace Engineering
Rutgers, The State University of New Jersey
Piscataway, New Jersey 08855-0909

SUMMARY/OVERVIEW:

Work tasks were carried out in four main areas during the reporting period: (1) high-speed five-camera spectral IR imaging system (Super Imaging System, SIS); (2) a spectrometer; (3) spectrometric methods; and (4) data analysis methods.

The entire electronic package of the SIS has been newly designed/fabricated/tested. An Ebert-Fastie spectrometer was designed/built to incorporate with the SIS. A new four-color artificial intelligence spectrometric method has been developed/improved in order to achieve "quantitative imaging," namely determination of distributions of temperature, soot and water vapor in the cylinder by processing raw data from the SIS. In addition, development of a new vector-weighted digital image analysis method has been initiated in order to quantitatively evaluate the stability and variation of flame propagations within the combustion chamber.

TECHNICAL DISCUSSION

SUPER IMAGING SYSTEM (SIS). This system, as schematically shown in Fig. 1, includes five (5) units of high-speed infrared (IR) camera (cryogenically cooled focal plane array, FPA of PtSi, 128x64): Four units (FPA, 1-4) are lined up with a single optical train (the upper portion in Fig. 1), and another unit (FPA, 5) is a part of newly designed-fabricated spectrometer, which is discussed later.

The arrangement is to *simultaneously capture* (1) four geometrically identical images in respective spectral bands and (2) a spectrally-resolved radiation, in a varied sub-range within the entire imaging range, over FPA-5. These spectral digital images and the said spectra distribution are obtained at high rates from *many consecutive* cycles. Goals of this system include determination of *when, where and what species* are formed during the reaction period.

In order to improve high-speed data handling, entirely new modular control units (with individual A/D units) were introduced replacing a single control approach employed in the earlier system. At this time, electronic boards in the modules were newly designed-fabricated by outside specialist that replace all in-house-laboratory-built electronic boards.

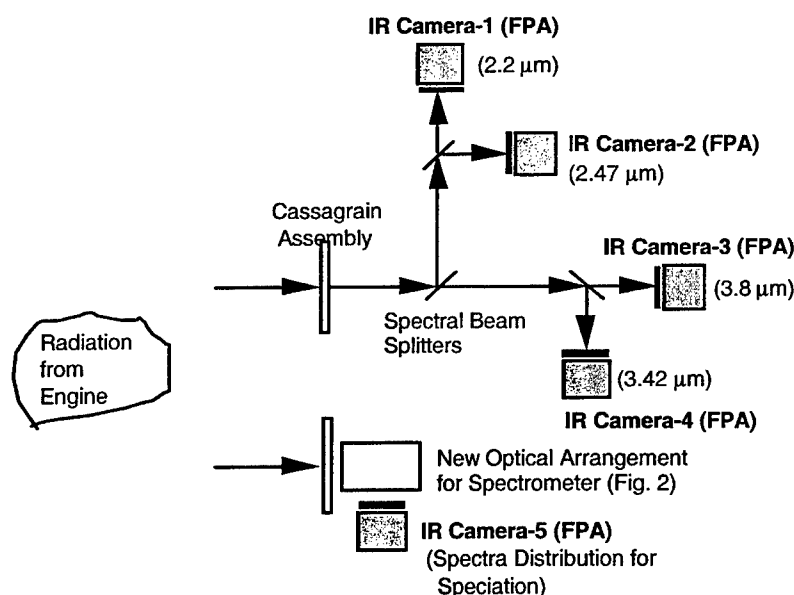


Fig. 1. Multispectral IR Digital Imaging System with Five (5) Units of Identical Cameras (Focal Plane Arrays, FPA) for Achieving Speciation and Quantitative Imaging.

SPECTROMETER. Since the present one-of-a-kind SIS (with a tight space limitation) would not readily accommodate spectrometers available on the shelf, it was decided to newly design and fabricate the optical portion of the system. The basic idea of the mutual incorporation of the two is that a new spectrometer package is placed directly above the present SIS (without employing a separate beam splitter).

In determining the optical arrangement for the present spectrometer, out of two layouts, e.g., two-mirror Czerny-Turner vs. single-mirror Ebert-Fastie spectrometers, the latter was employed in the present design. Without elaborating development processes, it is noted that the optical layout has been fabricated third time to date in order to achieve the most desirable performance under given space-system limitations (a new learning process). The new layout is expected to offer greater flexibility and adjustment capability in capturing spectra distributions over a choice of spectral range, which is facilitated by incremental-multi-dimensional-relocation (adjustment) features of individual optical elements.

This laboratory designed/fabricated spectrometer will be a stand-alone instrumentation capable of in-depth analytical investigation of thermochemical reaction phenomena. For example, alteration of a flame when some additives are introduced into its fuel or air would be more closely studied by using this new SIS-spectrometer system.

SAMPLE RESULTS. A set of sample results (propane fueled SI engine) is shown in Fig. 2. It is a copy of computer screen exhibiting *in each column*: (1) four respective spectral images; (2) a spectra distribution; (3) pressure-time date of the cycle by marking there in the crank angle (CA) when the imaging and those data were gathered. Each column included results from individual cycles, i.e., at CA of 15 aTDC (in 11 consecutive cycles).

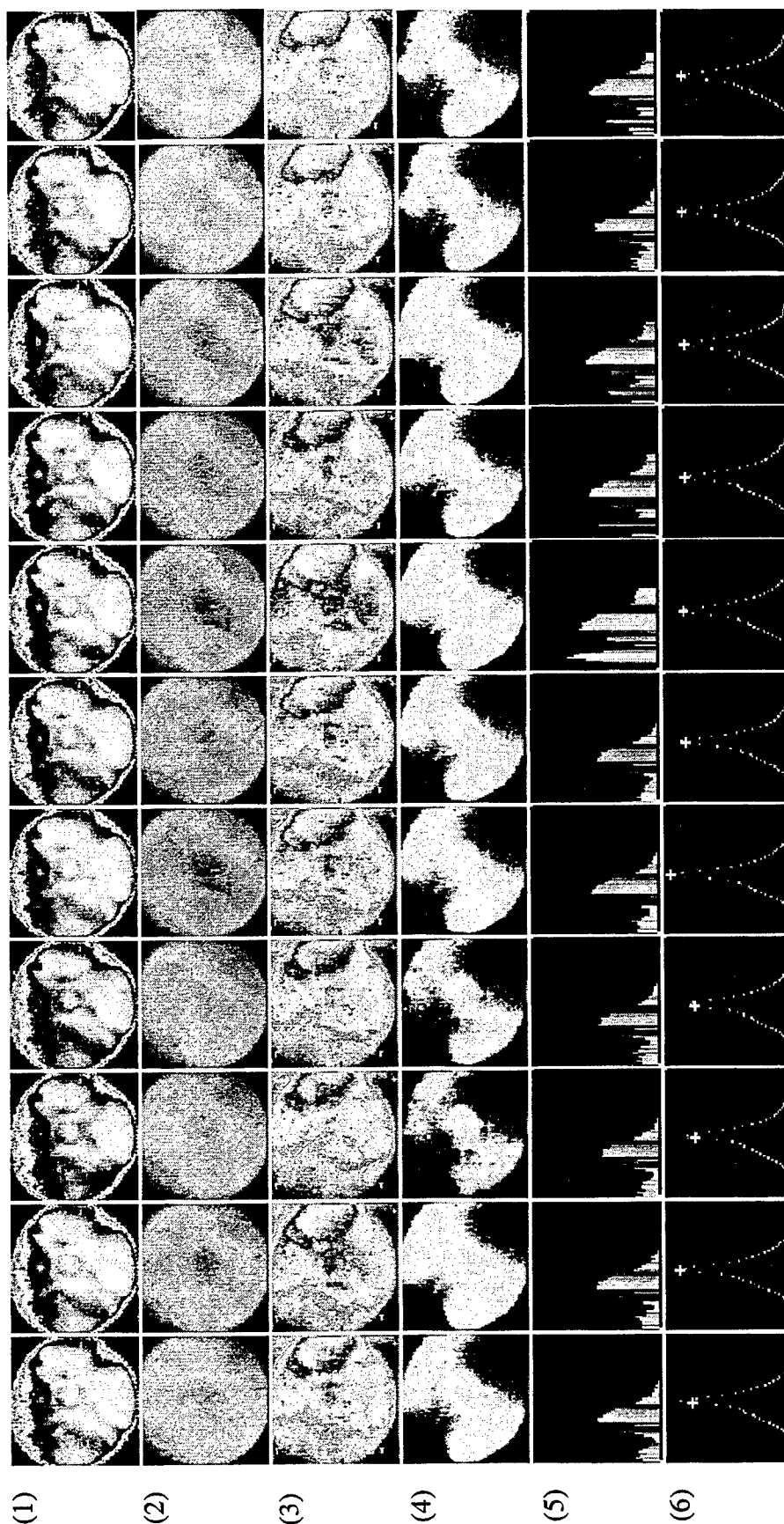


Fig. 2. Results from Propane-operated SI Engine. (1) - (4) Spectral Images in 3.8 μm , 2.2 μm , 3.45 μm and 2.47 μm , respectively; (5) Spectra Distribution; and (6) Pressure-time History.

FOUR-COLOR ARTIFICIAL INTELLIGENCE METHOD. When respective spectral intensities estimated for a controlled case (using the NASA IR Handbook, 1973) were introduced to our governing equations of spectrometric methods to see if our four-color method could reproduce the designated specifications, it was not the case to generate the same. There were multiple sets of solutions (hereafter called "*results*") for the same set of intensities. In turn, the same set of spectral intensities is estimated *for many* combinations of combustion objects in respective physical conditions. The main reasons for our inability of mathematically finding a converged set of solutions from our governing equations turned out to be due to the existence of such multiple solutions.

Consequently, an entirely new solution strategy was introduced in search of results as briefly explained next. It is to employ a vast-volume data-base in search of the result. The method would be therefore regarded as *an artificial intelligence method*.

First of all, a new data base is generated for discrete numerical variations of parameters (i.e., results) within the ranges expected in typical combustion systems (for example, wall temperature varying from 300 to 900K, and water concentration ranging from 1 to 18%, etc.), which is to generate many sets of matching spectral intensities to be stored in the data-base.

In finding the solution for set of intensities within a given combustion environment, which is the reverse of the above, another unique methodology was introduced. For a set of spectral intensities (from experiment), in addition to all possible results, those matching to intensities encompassing a $\pm 2.5\%$ error are extracted from the data-base. The next task is to determine which set of those results is the exact and final *out of multiple solutions*. The large amount of results extracted from our new data-base for a given set of intensities (plus a error range) is clustered with each of its nearest neighbors. Those groups are examined then to eliminate the unlikely ones by reflecting the combustion characteristics being considered. For example, it would be unlikely to have a high mixture temperature when water (product) concentration is very low.

Without further elaborating the details, after the elimination process, the solution is implemented for the measurement (with a very small error at this time) by limiting the range of results according to those identified within the final group, which then leads the iteration to rapidly converge to the final results.

VECTOR-WEIGHTED DIGITAL IMAGE ANALYSIS (VWIA). When cyclic variation is evaluated of IC engines, pressure-time data has been almost exclusively employed. Since this approach is neglecting space-resolved nature of variations, a new VWIA is introduced. The basic idea of this method is to quantitatively describe strong reaction zones in terms of both location (with respective a reference point, e.g. {0,0} and intensity. At present, variations of location and intensity of reaction zones at respective CA are determined to graphically display for facilitating space-resolved cyclic analysis of in-cylinder reactions. Note this is incorporated with Rutgers Animation Program whose example is shown in Fig. 2.

PULSE DETONATION PHYSIOCHEMICAL AND EXHAUST RELAXATION PROCESSES

LRIR 01PR02COR

Principal Investigator: Dr. Fred Schauer (AFRL/PRTC)

AFRL/PRTS

1790 Loop Road North, Building 490
Wright-Patterson AFB OH 45433-7103

SUMMARY/OVERVIEW:

The objective of this program is to establish the scientific knowledge of detonation initiation, propagation, and blow-down needed to develop a pulse detonation engine (PDE) that will function on hydrocarbon fuels. The complex interaction of chemistry, gas dynamics, turbulent mixing, and geometry are responsible for the success or failure of the detonation phenomena required to operate a PDE. Detonation tube exhaust blow-down conditions, which are predicted to have a significant impact upon performance, will be explored in order to achieve basic understanding of the relationships between detonations, nozzles, and multiple detonation tube interactions.

TECHNICAL DISCUSSION

The technological motivation for this program is the need to develop low-cost high-performance PDE's that can operate on hydrocarbon fuels. PDE's rely upon detonation combustion to produce a pressure rise in the combustion chamber instead of the expensive rotating machinery used in gas turbine engines. Consequently, the most expensive and maintenance-intensive components of a conventional turbine engine, namely the compressor and turbine stages, will not be necessary in PDE's. PDE's operates on a near-constant-volume heat addition cycle as opposed to the constant-pressure cycle employed in nearly all conventional aero-propulsion systems. The constant volume cycle offers improvements to specific thrust, specific fuel consumption, and specific impulse at a greatly reduced cost. In theory, the PDE can efficiently operate at Mach numbers from zero to above four without using a combined cycle/rocket approach. However, there are some major technical problems that must be resolved before the full potential of PDE's can be realized.

Foremost among the hurdles for a practical PDE system are the requirements for initiation and successful propagation of a detonation with hydrocarbon fuels in air. Although this has not been achieved in 60 years of PDE research, modern computational fluid mechanics (CFD), laser diagnostics, and high-speed instrumentation have not been applied to this challenge until recently. CFD and experimental studies of deflagration-to-detonation transition (DDT) and propagation are being carried out in order to explore the parameters controlling detonation

initiation including: geometry effects, plasma ignition, hybrid fueled pre-detonators, and endothermic fuels.

Previously, techniques for developing hydrocarbon/air deflagration to detonation transition (DDT) were demonstrated without the use of excess oxygen. This work has continued and scaling mechanisms have become better understood to enable DDT in a wide range of detonator tube sizes. This work has culminated in a demonstration of this initiation technology shown in Figure 1. Now flight certified after undergoing endurance trials, these scaling techniques, developed last summer through CFD and experimental work, enabled detonation initiation of a practical liquid hydrocarbon/air mixture in large tubes under practical conditions.

However, one of the limitations of DDT techniques with practical fuels is the induction time required for successful detonation initiation in air. Preliminary work on supercritical fuel injection has been completed, with results shown in Figure 2. Utilizing premixed supercritical fuel injection to produce flash vaporized or superheated fuel significantly reduced both ignition time and ignition to DDT time. Already, this technology could eliminate 20% of the propulsion system weight and improve thrust at least 15% in the system shown in Fig 1. Work on this promising fuel injection system will continue, and may extend to endothermic fuel cooling in order to further improve DDT performance.

Despite the above successes, the relatively long chemical induction time required for the preliminary deflagration ignition still dominate the DDT process. As discussed previously, split detonation initiation had been demonstrated as a possible advanced detonation initiation method... Previously, we demonstrated an 85% reduction in DDT time by employing this technique with hydrogen/air mixtures. The technique was recently extended to hydrocarbon/air

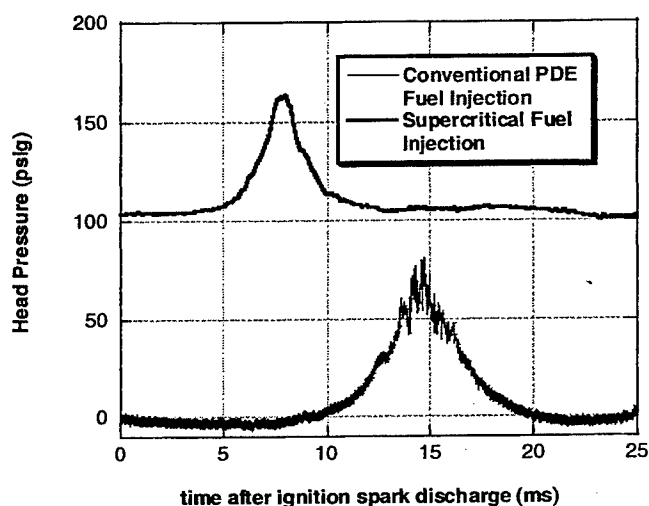


Figure 2. Head pressure versus time after ignition for conventional fuel injected PDE and supercritical fuel injection. Both data sets are for HC/air operation.

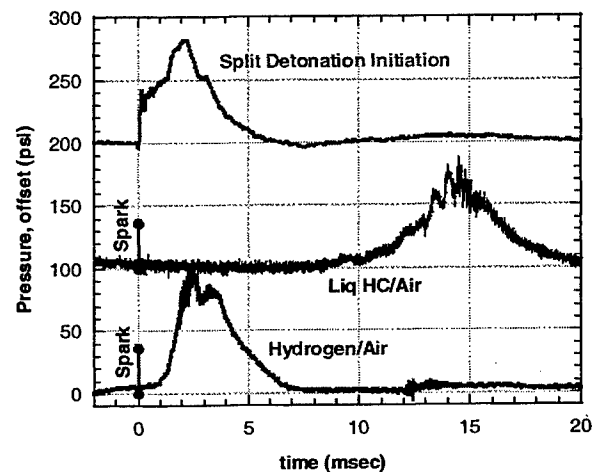


Figure 3. Head pressure versus time for spark ignition for hydrogen and HC fuel (with deflagration to detonation transition) versus split detonation initiation (near direct initiation). Each detonation is offset in 100 psi increments for clarity. Split detonation initiation resulted in similar results for both fuels.

mixtures, which are two orders of magnitude more difficult to detonate. As shown in the comparison of spark ignition with DDT versus split detonation ignition in Figure 3, a dramatic shortening of the initiation time is accomplished along with greatly increased thrust pressures. In fact, the ignition time is completely eliminated and

the DDT time is greatly reduced. As with hydrogen, split detonation ignition is much more robust and also simpler without the need for individual igniters for each detonator tube.

In our last annual report, we described the sensitivity of DDT to proper mixture and demonstrated an in-situ measurement of equivalence ratio based upon OH emission. However, the technique was limited to measurement only in the detonation front, lacking resolution in time and space. Utilizing the broad 3.39 micron hydrocarbon absorption feature, a diagnostic technique was developed which enabled in-situ measurement of vapor-phase fuel equivalence ratio in both detonating and cold-flow experiments. This allowed the charge mixing and stratification to be assessed as shown in Figure 3.

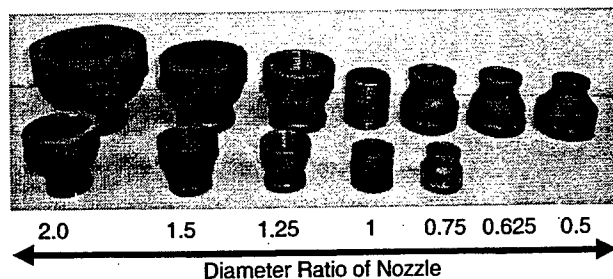


Figure 4. Nozzles used for 2" dia (upper) and 1" (lower) detonation tubes.

When compared to the actual equivalence ratio which was regulated by choked nozzles, the results demonstrated that the technique can produce quantitative data even in the unsteady and harsh PDE environment. In fact, the results shown above were obtained using published absorption coefficients for propane with no 'fitting' required. Other hydrocarbon fuels (without validated absorption coefficients) required a simple calibration procedure in a fuel cell. This technique proved so robust, it is currently being used to quantify and calibrate fuel injector performance in a PDE demonstration at Mach 3 flight conditions.

The influence of nozzles upon PDE performance has been found to be highly sensitive to initial detonation conditions, which are strongly influenced by the unsteady nozzle behavior. Previously, we showed the impact of unsteady flow interactions with nozzle performance. Recently, a wide variety of nozzle expansion ratios were examined with two different detonation tube sizes as shown in Figure 4. The impact of nozzle expansion ratio upon thrust is summarized in Figure 5 below for various fill fractions (ff). For each detonation tube diameter, thrust has been normalized by the reference values at the fill fraction of and diameter ratios of unity. As discussed previously, initial conditions tend to drive nozzle performance. Consequently, the converging nozzles, which tend to backpressure the detonation tube, result in higher thrust levels. As the fill fraction is reduced, the 'tamping' effect becomes more pronounced and the initial conditions become less dependent upon nozzle geometry at these conditions.

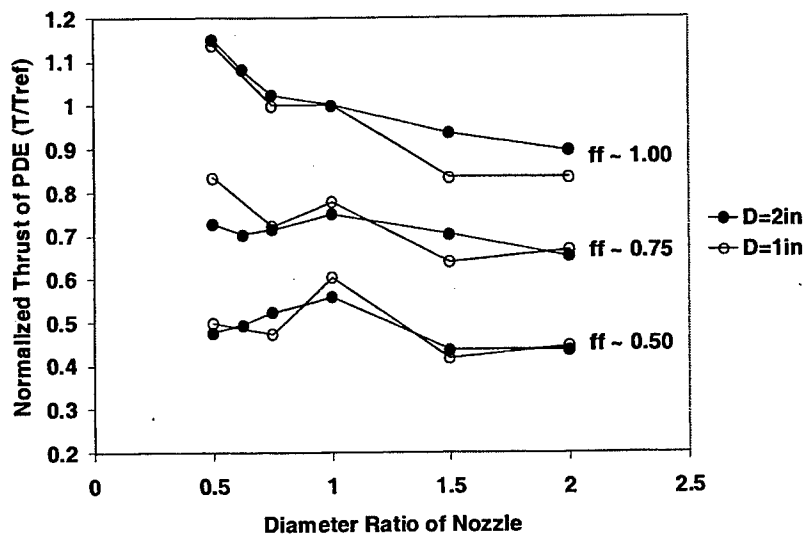


Figure 5. Normalized thrust versus nozzle ratio for two different tube diameters and various fill fractions.

Recent studies of common nozzles indicated potential benefits through back pressurization and multi-tube coupling in addition to enabling the use of a conventional common nozzle. An alternative approach to solving unsteady nozzle performance is to couple detonator tubes with an ejector in an effort to augment detonation blow down performance. This approach remains popular due to the promising performance of unsteady ejectors. Thrust augmentation of up to 100% has been claimed previously.

However, with straight walled ejector configurations, thrust augmentation of ~10% (primarily due to impacts upon detonation blow down as opposed to mass flow entrainment) was the highest obtained with our test rig. Utilizing an improved ejector design shown in Figure 6, with adjustment of ejector length and location, significant thrust augmentation was obtained. Results are shown in Figure 7 for a variety of fill fractions (ff) and ejector locations. Although these performance improvements do not quite make the 100% thrust augmentation claimed with proprietary rigs, they are quite significant and merit further investigation.



Figure 6. Ejector augmentation versus ejector position for various fill fractions.

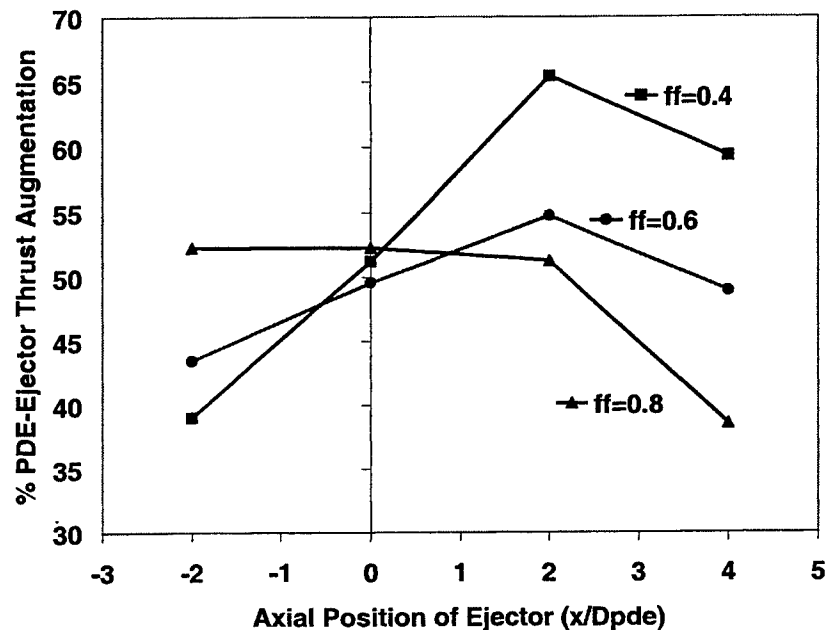


Figure 6. Ejector augmentation versus ejector position for various fill fractions.

EXPERIMENTAL STUDY OF VELOCITY, SCALAR, AND SCALAR-DISSIPATION FILTERED JOINT DENSITY FUNCTION

(AFOSR Grant F-49620-02-1-0130)

Principal Investigator: Chenning Tong

Department of Mechanical Engineering
Clemson University
Clemson, SC 29634-0921

SUMMARY

The velocity, scalar, and scalar-dissipation filtered joint density function (FJDF) and its transport equation for PDF-based large eddy simulation (LES) of turbulent combustion are studied experimentally in an axisymmetric turbulent jet. This approach is consistent with the flamelet limit and is important for developing mixing models that include intermittency effects. The FJDF and the unclosed terms in its transport equation are analyzed using their conditional averages. The FJDF is found to have qualitatively different characteristics depending on the instantaneous subgrid-scale (SGS) scalar variance and kinetic energy. When both are large compared to their mean values, the scalar dissipation shows a strong dependence on the SGS velocity and scalar. The scalar dissipation also shows a dependence on the energy dissipation. The dynamics of the FJDF is also different under different SGS conditions. The results show that mixing models that include intermittency should be consistent with the SGS scalar and scalar dissipation structure and have the correct dependence on the velocity and energy dissipation.

TECHNICAL DISCUSSION

PDF-based LES approaches for turbulent combustion have shown great promise. A method recently established by Givi and Pope (Skeikhi et al. 2003) solves the velocity-scalar FJDF transport equation, in which the SGS scalar transport term is in closed form while mixing of SGS scalars is modeled. The velocity-scalar FJDF approach has been studied experimentally (Wang et al. 2004). Here we study the velocity, scalar, and scalar-dissipation FJDF and its transport equation, which are important for developing mixing models that include intermittency effects. The FJDF approach is also consistent with the flamelet limit. In addition, because scalar dissipation fluctuations play an important role in local extinction and reignition in turbulent nonpremixed flames, inclusion of the scalar dissipation in FJDF models is essential to accurate predictions of these phenomena.

The velocity, scalar, and scalar-dissipation FJDF is defined as

$$f(\mathbf{v}, \hat{\phi}, \hat{\chi}; \mathbf{x}, t) = \int \prod_{i=1}^3 \delta[u_i(\mathbf{x}', t) - v_i] \delta[\phi(\mathbf{x}', t) - \hat{\phi}] \delta[\chi(\mathbf{x}', t) - \hat{\chi}] G(\mathbf{x}' - \mathbf{x}) d\mathbf{x}', \quad (1)$$

where \mathbf{v} , $\hat{\phi}$, $\hat{\chi}$, δ , and G are the sample-space variables for \mathbf{u} , ϕ , and χ ($= D \frac{\partial \phi}{\partial x_j} \frac{\partial \phi}{\partial x_j}$), the Dirac delta function, and the filter function, respectively. The integration is over all physical space. The FJDF represents the weighted joint distribution of the velocity, the scalar, and the scalar scalar in a grid cell. The transport equation of the FJDF is

$$\frac{\partial f}{\partial t} + v_j \frac{\partial f}{\partial x_j} = \frac{\partial \langle p \rangle_L}{\partial x_j} \frac{\partial f}{\partial v_j} + \frac{\partial}{\partial v_j} \left\{ \left\langle \frac{\partial p'}{\partial x_j} \right| \mathbf{v}, \hat{\phi}, \hat{\chi} \right\rangle_L f \right\}$$

$$\begin{aligned}
& -\frac{\partial}{\partial v_i} \left\{ \left\langle \nu \frac{\partial^2 u_i}{\partial x_j \partial x_j} \right| \mathbf{v}, \hat{\phi}, \hat{\chi} \right\rangle_L f \right\} - \frac{\partial}{\partial \hat{\phi}} \left\{ \left\langle D \frac{\partial^2 \phi}{\partial x_j \partial x_j} \right| \mathbf{v}, \hat{\phi}, \hat{\chi} \right\rangle_L f \right\} - \frac{\partial}{\partial \hat{\chi}} \left\{ \left\langle D \frac{\partial^2 \chi}{\partial x_j \partial x_j} \right| \mathbf{v}, \hat{\phi}, \hat{\chi} \right\rangle_L f \right\} \\
& + 2 \frac{\partial}{\partial \hat{\chi}} \left\{ \left\langle D g_{kj} \frac{\partial \phi}{\partial x_j} \frac{\partial \phi}{\partial x_j} \right| \mathbf{v}, \hat{\phi}, \hat{\chi} \right\rangle_L f \right\} + 2 \frac{\partial}{\partial \hat{\chi}} \left\{ \left\langle D^2 \frac{\partial^2 \phi}{\partial x_k \partial x_j} \frac{\partial^2 \phi}{\partial x_k \partial x_j} \right| \mathbf{v}, \hat{\phi}, \hat{\chi} \right\rangle_L f \right\}. \quad (2)
\end{aligned}$$

where $\langle \cdot | \mathbf{v}, \hat{\phi}, \hat{\chi} \rangle_L$ denotes a conditionally filtered variable conditional on \mathbf{u} , ϕ , and χ . The left hand side represents the time rate of change of the FJDF and transport of FJDF in physical space. The first three terms on the right hand side are transport in velocity space by resolvable-scale pressure gradient, SGS pressure gradient, and viscous acceleration. The next two terms are transport in scalar and scalar-dissipation spaces by molecular diffusion. The last two terms are transport in scalar-dissipation space due to production and destruction of χ .

The FJDF is a random process and requires statistical descriptions. Here we employ conditional sampling and averaging techniques. Our previous studies of conserved scalar FDF, scalar-scalar-dissipation FJDF, the velocity FJDF, and the velocity-scalar FJDF using these techniques (Tong 2001, Wang and Tong 2002 and 2004, Rajagopalan and Tong 2003, Wang et al. 2004) have shown that the SGS velocity and scalar are in spectral equilibrium and nonequilibrium for small and large *instantaneous* SGS energy and scalar variance, respectively. The nonequilibrium SGS scalar contains diffusion layers and the FDF is bimodal. The scalar dissipation shows a strong dependence on the SGS scalar and velocity. For nonequilibrium SGS velocity, the velocity FJDF is approximately uniform, suggesting that the SGS velocity is under local rapid distortion, which may be modeled using the velocity-wavevector model (Slooten and Pope 1997). The results suggest that mixing models that can better predict the nonequilibrium regime are needed. In this work we investigate the statistical dependence among \mathbf{u} , ϕ , and χ . The FJDF and the SGS terms in its transport equation are analyzed using their conditional means with the SGS scalar variance $\langle \phi''^2 \rangle_L$ and the SGS kinetic energy, $k_L = (\langle u_1''^2 \rangle_L + \langle u_2''^2 \rangle_L)/2$ as conditioning variables.

Our measurements were made in an axisymmetric turbulent jet at 80 jet nozzle diameters ($D = 15$ mm) downstream. The jet Reynolds number UD/ν is 40000. A sensor array consisting of three hot- and cold-wire probes is used to obtain data for performing filtering operations in both the streamwise (x) and transverse (y) directions. The filter size is varied from 63 to 250 Kolmogorov scales. This technique enables us to acquire a large amount of data (2×10^8 samples) necessary to achieve sufficient statistical convergence.

A. Velocity, scalar, and scalar-dissipation FJDF

The mean FJDF conditional on the SGS energy, the resolvable-scale velocity, the SGS scalar variance, and the resolvable-scale scalar has qualitatively different forms depending on the conditioning variables. For small k_L ($< \langle k_L \rangle$) and $\langle \phi''^2 \rangle_L$ ($< \langle \phi''^2 \rangle$), the conditional FJDF is close to joint-Gaussian [Fig. 1(a)], similar to the JPJDF in a fully developed turbulent jet, which is in quasi-equilibrium. The dependence of χ on u_1'' and ϕ'' is weak.

For large $\langle \phi''^2 \rangle_L$, the FJDF has a horse-shoe shape with the two branches beginning to appear at approximately $\ln(\chi/\langle \chi_L | \langle \phi''^2 \rangle_L, k_L \rangle) = 2$ regardless of the values of k_L , indicating a bimodal FJDF (in the ϕ and u_1 spaces). The FJDF is consistent with a scalar diffusion-layer structure. The highest FJDF values are near $\ln \chi = -2$, similar to the scalar-scalar-dissipation FJDF (Rajagopalan and Tong 2003). For small k_L (not shown) the two branches of the FJDF are located near $\phi''/\langle \phi''^2 \rangle_L \approx \pm 1$ and $u_1'' = 0$. The correlation between the SGS scalar and the velocity component u_1 is low, indicating small conditional SGS flux. For large k_L [Fig. 1(b)] the branches are located approximately at $\phi''/\langle \phi''^2 \rangle_L \approx \pm 1$ and $u_1'' = \pm 0.5$. Very large χ values tend to occur at $\phi'' = 0$ and $u_1'' = 0$, indicating that they occur almost exclusively near the center of the diffusion layer. The correlation among ϕ'' ,

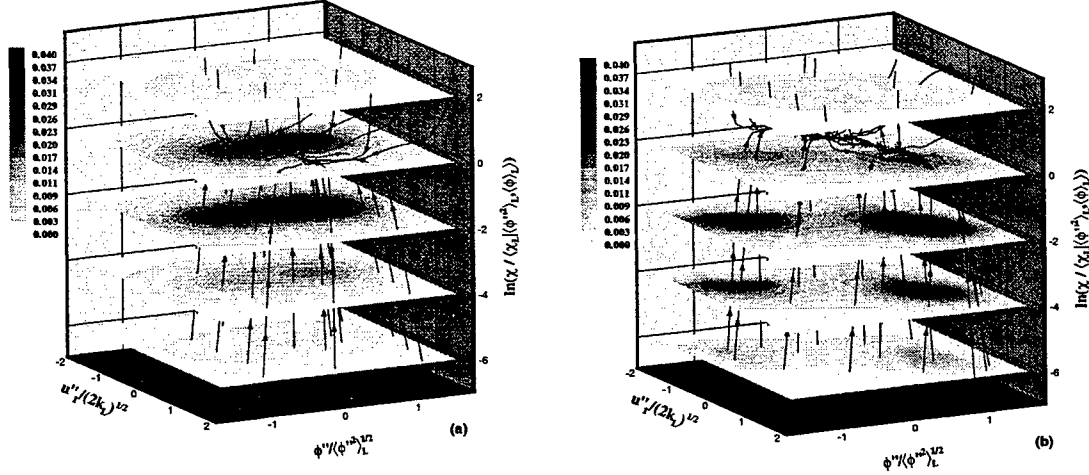


Figure 1: Mean FJDF conditional on k_L , $\langle \mathbf{u} \rangle_L$, $\langle \phi'' \rangle_L$, and $\langle \phi \rangle_L$ on the jet centerline for $\langle u_1 \rangle_L = \langle u_1 \rangle$ (3.07 m/s) and $\langle u_2 \rangle_L = 0$: (a) $k_L / \langle k_L \rangle = 3.04$ and $\langle \phi'' \rangle_L / \langle \phi'' \rangle = 6.09$; (b) $k_L / \langle k_L \rangle = 0.64$ and $\langle \phi'' \rangle_L / \langle \phi'' \rangle = 6.09$. The streamlines are the conditionally filtered scalar diffusion, scalar-dissipation diffusion, and viscous acceleration:

u''_1 , and χ is strong, indicating large SGS scalar flux and a strong dependence of mixing on the SGS scalar and velocity. Intense mixing is expected in the region between the two branches, further demonstrating the need for mixing models to depend on the velocity. This FJDF shape is consistent with a scalar diffusion layer associated with a local plane strain (converging-diverging) velocity field. In such a structure the scalar gradient is the largest in the diffusion layer where the SGS velocity is the smallest. The structure is similar to the counter-flow model for laminar flamelets. Therefore, mixing models should be consistent with their structures. In particular, when modeling intermittency effects, the scalar dissipation should exhibit a similar dependence on the SGS scalar and velocity to that observed here.

B. Conditionally filtered scalar diffusion, scalar-dissipation diffusion, and viscous acceleration

In the present study the conditionally filtered scalar diffusion, dissipation, and the viscous acceleration are obtained using the streamwise derivatives. These variables transport the FJDF in scalar, scalar-dissipation, and velocity spaces, respectively, and are represented in Fig. 1 as “streamlines”. In general, the streamlines approach an attracting manifold before converging to a “stagnation point”. For small $\langle \phi'' \rangle_L$ and k_L the manifold is located approximately on the plane of $\chi = \langle \chi_L | \langle \phi'' \rangle_L, k_L \rangle$, on which the peak of the FJDF is also located. The manifold is approximately parallel to the u_1 axis. The conditional diffusion of χ appears to have the same time scale as that of ϕ whereas the viscous acceleration have a larger time scale.

For large $\langle \phi'' \rangle_L$ and k_L the streamlines quickly approach the plane $\ln(\chi / \langle \chi_L | \langle \phi'' \rangle_L, k_L \rangle) = -1$, indicating that the conditional diffusion of χ is faster than that of ϕ and the conditional viscous acceleration. The manifold is still close to a straight line, but has an angle with respect to the u_1 axis, due to the correlation between the SGS velocity and scalar caused by the combination of diffusion layer and plane strain structures. Therefore, the FJDF equation has different characteristics under different SGS conditions. The results further demonstrate that mixing models need to be consistent with these structures.

C. FJDF of scalar, scalar dissipation, and energy dissipation

In models for the scalar dissipation, the energy dissipation can be used to include the

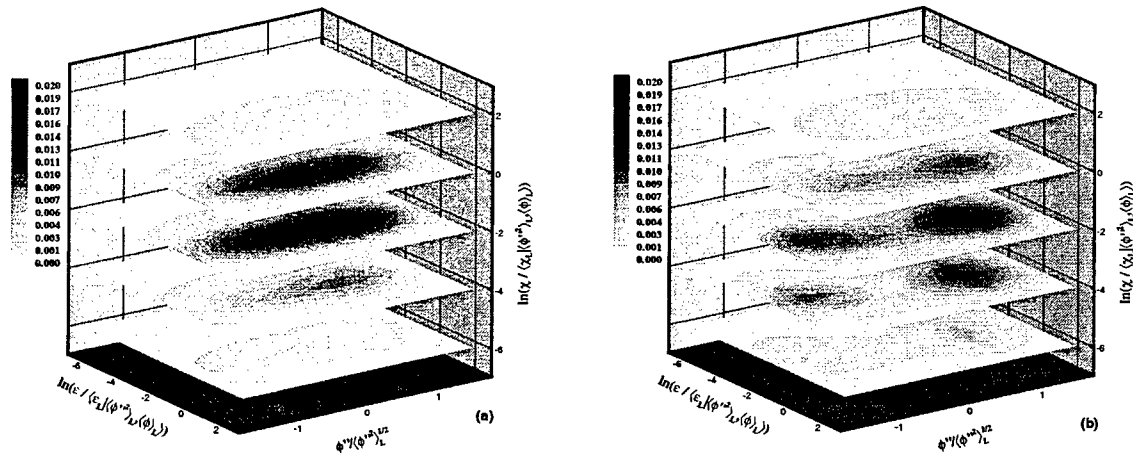


Figure 2: The FJDF of scalar, scalar-dissipation, and energy dissipation.

influence of the dissipation-scale velocity field. Therefore, we also study the FJDF of scalar, scalar dissipation, and energy dissipation. For small $\langle \phi''^2 \rangle_L$ and k_L the FJDF is unimodal, similar to a joint Gaussian [Fig. 2(a)]. For large $\langle \phi''^2 \rangle_L$ and k_L the FJDF has a horseshoe shape [Fig. 2(b)]. Very large χ values tend to occur at moderate ϵ values (and small ϕ''). The marginal FJDF (not shown) is bimodal even at these χ values. Plotting the isocontours in the $\epsilon - \chi$ plane also show some correlation between them. Therefore, the energy dissipation provides additional information as well as imposes additional constraints on the scalar dissipation and it may be beneficial to include it in models for χ .

The present study show that for nonequilibrium SGS scalar and velocity there is a strong statistical dependence among the SGS scalar, the scalar dissipation, and the SGS velocity field. Mixing models that include intermittency effects need to be consistent with the dependence. The energy dissipation can also be used in modeling intermittency effects.

REFERENCES

- Rajagopalan, A.G. and Tong, C. (2003) Experimental investigation of scalar-scalar-dissipation filtered joint density function and its transport equation. *Phys. Fluids*, **15**, 227–244.
- Sheikhi, M. R. H., Drozda, T. G., Givi, P., and Pope, S. B. (2003) Velocity-scalar filtered density function for large eddy simulation of turbulent flows. *Phys. Fluids*, **15**, 2321–2337.
- Tong, C. (2001) Measurements of conserved scalar filtered density function in a turbulent jet. *Phys. Fluids* **13**, 2923–2937.
- Van Slooten, P. R. and Pope, S. B. (1997) PDF modeling for inhomogeneous turbulence with exact representation of rapid distortions. *Phys. Fluids* **9**, 1085–1105.
- Wang, D. and Tong, C. (2002) Conditionally filtered scalar dissipation, scalar diffusion, and velocity in a turbulent jet. *Phys. Fluids* **14**, 2170–2185.
- Wang, D. and Tong, C. (2004) Experimental investigation of velocity-scalar filtered density function for LES of turbulent combustion. To appear in *Proc. Combust. Inst.*
- Wang, D., Tong, C., and Pope, S.B. (2004) Experimental investigation of velocity filtered density function for large eddy simulation. Submitted to *Physics of Fluids*.

EXPERIMENTAL INVESTIGATION OF THE INTERACTION OF ELECTROTHERMAL PLASMAS WITH SOLID PROPELLANTS

(Grant No. DAAD19-00-1-0420)

Principal Investigators: Philip L. Varghese and Noel T. Clemens

Center for Aeromechanics Research
The University of Texas at Austin
1 University Station, C0604
Austin, TX 78712-0235

SUMMARY / OVERVIEW

The primary focus of the proposed work is a detailed experimental study of the plasma and its interaction with representative solid propellants. The objective of the work is to develop an experimental database of certain species concentrations both during the plasma-propellant interaction and immediately thereafter. Such a database is vital to develop a correct thermochemical model of mechanisms that lead to rapid, repeatable ignition and which permit temperature compensation of the gun charge. This knowledge is essential if the Army is to field plasma initiators.

TECHNICAL DISCUSSION

ARL studies of propellant charges ignited by plasma discharges have shown that this technique has significant advantages over conventional (primer) ignition. Ignition delay and jitter were substantially reduced, and temperature compensation achieved with a plasma energy input that was substantially smaller than the energy required to heat the propellant bed to the reference condition. However, the mechanism of the interaction is unknown. The plasma could function merely as an improved thermal source since it has a very high temperature compared to conventional combustion products. It could function as a radiant source that distributes the energy into the propellant bed more uniformly and rapidly than simple flame spread. Alternatively, the plasma could provide a source of highly reactive species, or plasma jets issuing into the propellant beds may penetrate more effectively than combustion products from a primer, and thus give a more distributed ignition. It is also possible that the blast wave accompanying the plasma discharge causes microfractures in the propellant grains that increase the burning surface area sufficiently to provide temperature compensation, though it seems hard to reconcile the observed repeatability of the process with known mechanisms of microfracture.

A combination of several of these mechanisms might also contribute to the observed performance improvement. An improved fundamental understanding of the interaction will help the Army design better initiators that tailor the plasma to the propellant thus reducing energy required or enhancing gun performance. For example, it may be possible to achieve the observed temperature compensation with a much smaller energy input than is currently needed, which would reduce the size of the power source required. A fundamental understanding is also needed to reduce risk. Because of the current lack of understanding, one cannot rule out the possibility that the plasma is interacting with only a minor component of the propellant charge, and thus plasma igniters could fail because of minor changes in propellant composition.

Owing to the complexity of the physical processes involved in plasma-induced ignition, achieving an understanding of the fundamental physics will likely be achieved only through computational/theoretical approaches aided by experimental data. To date, however, there is insufficient experimental data on the plasma-propellant interaction to properly develop and validate chemical models. Therefore, the primary goal of this project is to aid in this effort by experimentally studying the interaction of an electrothermal capillary plasma with solid propellants. This involves both the characterization of the electrothermal plasma source itself, as well as the plasma-ignition of a solid propellant in a confined reactor.

The major objective of this work is to generate as complete a picture as possible of the plasma-propellant interaction and subsequent ignition. This is being accomplished by the application of a range of diagnostics including emission spectroscopy, heat flux sensors, high-framing rate visible luminosity imaging and planar laser-induced fluorescence (PLIF). The PLIF is directed at obtaining the spatial distributions of species that either mark the plasma (e.g. atomic copper), or provide important information about the state of combustion (e.g. OH and NO).

The plasma-propellant flow field is a very challenging environment in which to make measurements because of the high temperatures and densities, complex chemistry, transient nature of the interaction, and high electrical noise caused by the pulse forming network. This progress report describes results obtained over the past year and some of the problems that have been encountered while working in this difficult environment.

PLIF imaging of atomic copper is being developed to provide a marker of the plasma when ignition takes place in the combustion chamber. As a first step toward this end Cu PLIF is being applied in the freely expanding plasma jet as well. For Cu PLIF we pump the $^2P_{3/2} \leftarrow ^2S_{1/2}$ line at 327 nm and detect the fluorescence from the $^2P_{3/2} \rightarrow ^2D_{5/2}$ line at 578 nm. The laser source is a Nd:YAG-pumped dye laser tuned to 654 nm, which was then frequency doubled to 327 nm. The laser was operated at 10 Hz, with energy per pulse of about 10 mJ. The laser triggers a custom-designed electronic circuit, which provides for the synchronization of the laser and transient plasma. The fluorescence was imaged with either one or two intensified CCD cameras (Princeton Instruments) gated to about 30 ns to help reject the high background luminosity. The cameras were fitted with 50 mm focal length, f/1.4 camera lenses and interference filters (3 nm bandwidth) to help reject background luminosity. For the two-camera experiments one camera captured the fluorescence and the other was gated just after the fluorescence terminated to provide a background image so that single-shot background subtractions could be used. The reason for this is that the fluorescence signals are very low compared to the background luminosity and so single-shot background corrections can help to improve the signal-to-background ratio of the measurements.

The propellant is supplied in flexible-sheet form with a thickness of 2.5 mm (nominally 0.1 in) and has a composition shown in Table 1. Preliminary ignition experiments with the plasma issuing into room air and impinging normally on the propellant surface did not lead to ignition, and hence the closed combustion chamber shown in Fig. 2 was constructed to confine the plasma. Sample disks of diameter 12 mm were cut from this sheet and attached to a support rod mounted inside the combustion chamber. The plasma-jet issues normal to the propellant disk. The chamber includes three windows to provide optical access for the laser sheet and imaging. Furthermore, a measurement port has been machined to enable pressure measurements in the chamber during the discharge by using a fast-response pressure transducer (Kistler, 10,000 psi). Interactions of the plasma with the propellant sample led to propellant ignition for initial capacitor voltages of 3.6 kV or greater. The corresponding discharge energy is 1.6 kJ.

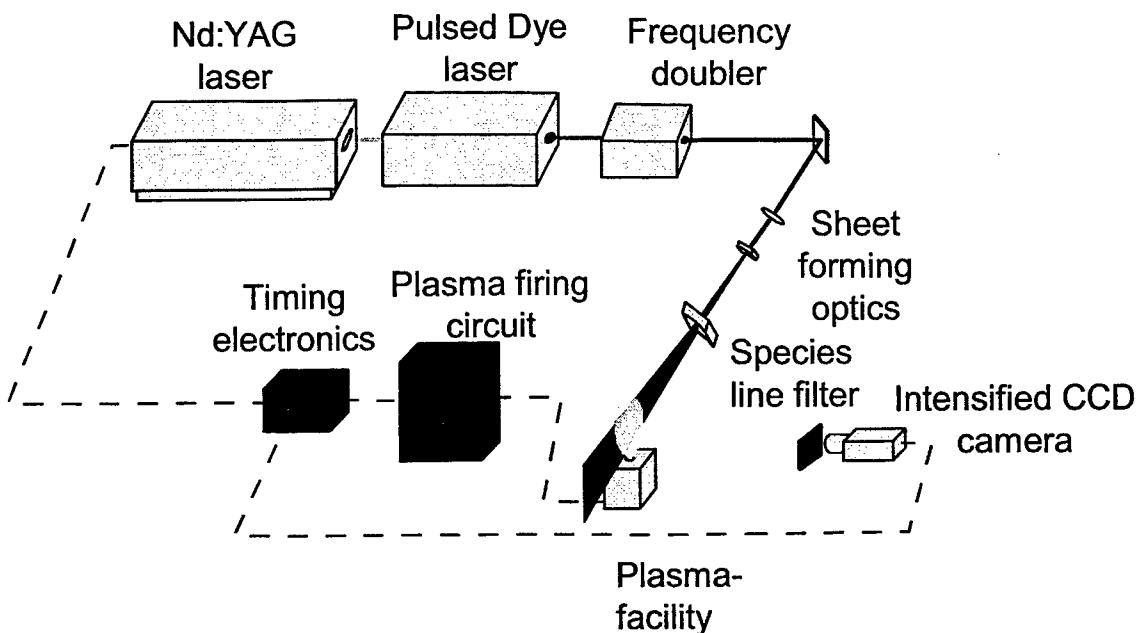


Figure 1. Experimental set-up for the PLIF imaging of the plasma-jet. The jet is shown issuing into air but a similar arrangement will be used for closed chamber experiments.

Table 1 Composition of JA-2 Propellant

Constituent	% by mass
Nitrocellulose	58.14
Nitroglycerine	15.82
Diethylene glycol dinitrate	25.23
Akardit II	0.71
Magnesium oxide	0.05
Graphite	0.05
Total	100.0

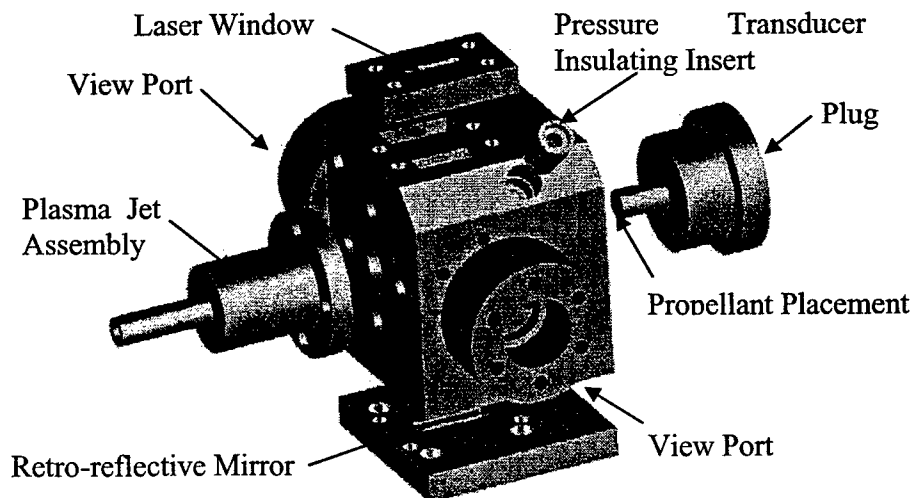


Figure 2. Closed combustion chamber with windows for viewing and laser passage

Figure 3 shows a sequence of images of the visible luminosity for the case of plasma-ignition of JA-2 in the combustion chamber. The initial discharge voltage and energy were 4 kV and 2 kJ, respectively. These images were taken with a Kodak Ektapro HS4540 at a framing rate of 13,500 frames per second. The distance between the exit of the plasma jet and the JA-2 disk was about 20 mm. The sequence is actually a composite assembled from different runs, because a single camera/lens setting does not have sufficient dynamic range to capture the range of intensities that occur over the duration of a run. In these images the plasma axis is horizontal and it travels left to right. The propellant disk (12 mm diameter) is vertical and is labeled in the second image.

The first image, captured at 0.222 ms from the start of the plasma discharge, shows the structure of the impinging plasma jet. The luminous bore exit can be seen at left and the very luminous Mach disk is seen as the triangular shaped region at right. At this instant the propellant is enveloped in the plasma. At 1.48 ms the high plasma luminosity has largely dissipated, although swirling lower-luminosity gas can still be seen in the videos. It should also be noted that the side of the propellant mounting rod can be seen in the image. Interestingly, at 10 ms the rod is no longer visible. At between 30-50 ms the videos show bright luminous specks are ejected from the surface of the propellant, which presumably marks the beginning of ignition. Such specks can be seen at 50, 100 and 150 ms in Fig. 3.

Current work is directed at making PLIF measurements on OH in the closed chamber to study the ignition of the propellant after interaction with the plasma. Scattering from nanoparticles, presumably generated by condensation of electrode material vaporized during the plasma discharge, complicate the measurement. Work is in progress to address these problems. In the future we plan to conduct laser absorption measurements in addition to LIF measurements in order to improve the characterization of the interaction and ignition processes.

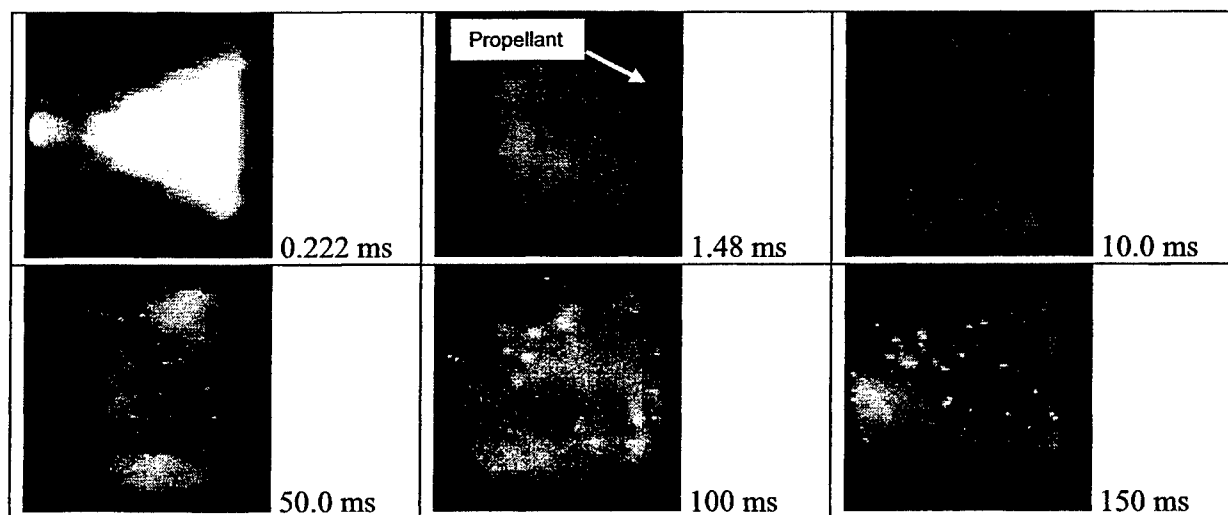


Figure 3. Visible-luminosity images of plasma-ignition of JA-2. The images were acquired at a framing rate of 13,500 frames per second.

CONCURRENT RESEARCH ON HIGH GRAVITY (g) COMBUSTION WITH ENABLING MATERIALS

(LRIR: 99PR12COR)

Principal Investigator: Dr. Joseph Zelina

Air Force Research Laboratory
AFRL/PRTC
WPAFB, OH 45433

SUMMARY/OVERVIEW

A gas turbine combustor concept that uses high g-loading in the circumferential cavity is being tested at AFRL to provide the foundation for development of a low-emissions, ultra-compact, high performance combustion system for future military and commercial aircraft. This work comprises experimental testing and modeling and simulation of different high g-loaded combustion cavities. Initial tests indicate that, by using highly swirling flows, the combustor performance can be enhanced in the form of improved combustor efficiencies at reduced combustor length. Understanding the impact of high g-loading on the pollutant emissions, operability limits, and combustor durability are three major areas where the AFOSR program will progress the scientific understanding of the physical processes involved in this novel combustion system.

TECHNICAL DISCUSSION

This AFOSR-sponsored work addresses fundamental combustion issues that will lead to the development of a revolutionary propulsion system that operates on a highly efficient, near constant temperature (NCT) cycle instead of the constant pressure cycle of today's engines. Such a propulsion system could provide increased power extraction, thrust augmentation, and specific thrust (ST) enhancements. A key technology essential for the development of a propulsion system that operates on a NCT cycle is an ultra-compact combustion (UCC) system that will efficiently add heat between the turbine stages and is constructed of advanced, light-weight ceramic-matrix composites (CMC) materials. This combustor has been referred to in the literature as an inter-turbine burner (ITB).

The first objective of this program is to establish the scientific base needed to develop an ultra-compact, high-energy-density turbine combustor that would enable aero propulsion systems to operate on a near-constant temperature cycle. The high-g loading is a new parameter space for combustion. Rotating, swirling flows are used to enhance mixing and increases reaction rates. However, the centrifugal acceleration in typical combustion systems is less than 80 g. No one has yet addressed what happens to a diffusion flame at loading above 800 g¹.

The AFRL team has been working on the premise that high g loading can provide benefits compared to conventional gas turbine combustion systems. A concept design for a high-g combustion system that can serve as a main combustor or as an ITB has been completed however, understanding of the combustion process at high g-loading conditions is necessary. A photograph of the combustor, showing the between-vane volume and the radial vane cavity is shown in Fig. 1. Notice that the combustion

¹ Yonezawa, Y., Toh, H., Goto, S., and Obata, M., "Development of the Jet-Swirl High Loading Combustor," 26th AIAA/SAE/ASME/ASEE Joint Propulsion Conference, Orlando, FL, AIAA-90-2451, 1990.

process is complete at or before the trailing edge of the vane at atmospheric pressure conditions. The axial flame length is approximately 3 inches; significantly less length than conventional systems.

The AFRL team is focused on what we believe are the key combustion issues. (1) What are the fundamental processes that control combustion in a highly accelerated (high-g) flows? (2) How does swirling flow from the main air supply impact the cavity combustion process? and (3) Can we integrate CMC vanes into flow path while turning the flow? Related to Issues 1-3 that is overarching is using the modeling and simulation and advanced diagnostics tools to help understand the physical processes related to the UCC/ITB concept.

Approach

Flame-Vortex Interaction to Investigate Flame Speed Enhancements: The AFRL team would like to validate Lewis² finding with diffusion flames using a flame-vortex interaction experiment. Fundamental flame-vortex interaction experiments will be conducted to determine the physical processes that cause the increased burning rates as a result of g-loads for diffusion flames. In an attempt to increase the flame speed to a value beyond that of a turbulent flame, Lewis² has investigated the role of centrifugal forces on flame spreading. He argued that flames propagate in combustible mixtures in three modes; 1) laminar burning in which flame speed depends on the heat conduction and radical diffusion into fresh mixture, 2) turbulent burning in which turbulent transport of small elements of flame into the unburned mixture act as new ignition sources, and 3) bubble burning in which small packets of burnt gases rise through fresh mixture due to buoyancy and spread the flames surrounding them.

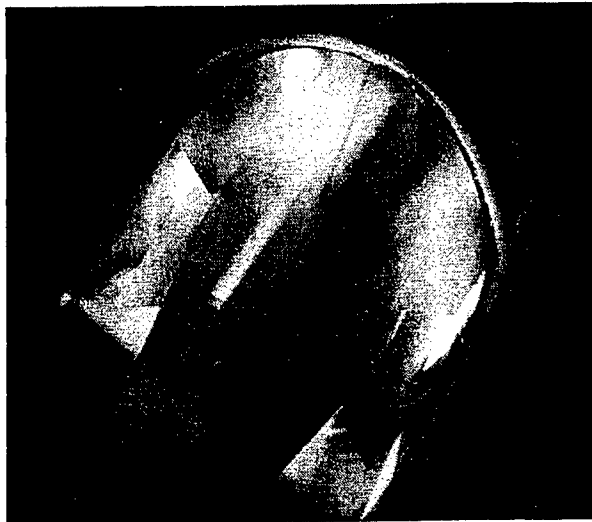


Figure 1: UCC/ITB Experimental Apparatus.

Lewis² found that for propane-air mixtures, the flame propagation rate remained nearly constant at 5 m/sec up to about 200 g's. For values of 500-3500g's, the flame speed increases as the square root of the g-loading up to nearly 18 m/sec. His data shows that the observed flame speed is 3-4 times higher than documented turbulent flame speeds. Lewis² attributed the increased flame speed to the turbulent enhancement due to "bubbles" or eddies that move ahead of the flame front due to the centripetal acceleration. Lewis² describes this process in Fig. 2. In the picture on the left, the bubble or eddy velocity exceeds the turbulent flame speed and the flame propagates at the eddy velocity. On the right, is a visualization of the case where the eddy velocity is lower than the turbulent flame speed and the mixture propagates at the turbulent flame speed.

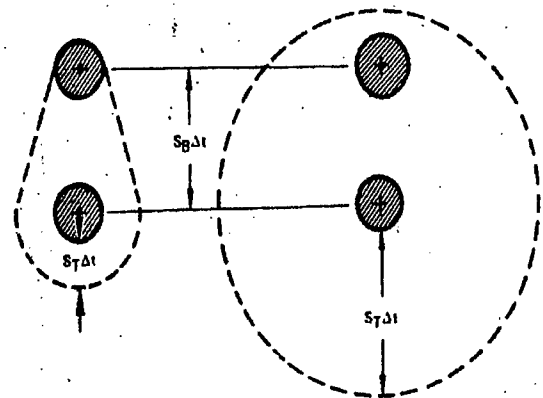


Figure 2: Bubble or Eddy Burning Velocity for High g Combustion.

² Lewis, G.D., "Centrifugal-Force Effects on Combustion," 14th Symposium (International) on Combustion, The Combustion Institute, pp.413-419, 1973.

To confirm the “bubble-transport” hypothesis in increasing the flame speed, first-order numerical experiments are conducted using UNICORN (Unsteady Ignition and Combustion with Reactions) code. Flame propagation in a tube that is 50-mm wide and 1000-mm long is simulated by performing laminar, two-dimensional, time-dependent calculations. A hydrogen-air mixture, with a stoichiometric value of 0.8, is considered in this study. The tube is vertically mounted in space and uniform gravitational force is imposed along the length. Flame is initiated at the bottom of the tube by providing three ignition sources. Calculations are repeated by changing the applied gravitational force between $0g_0$ and $500g_0$.

Results obtained for $10g_0$ and $500g_0$ cases are shown in Figs. 3a and 3b, respectively. For each case two-dimensional flame structures in the tube at three instants are shown. When the applied gravitational force is small (less than $\sim 10g_0$) the individual flamelets initiated from the three ignition sources merged quickly and resulted in a uniform flat flame across the tube. The propagation velocity of this flat flame is ~ 1.86 m/s, which is close to the laminar burning velocity in the 0.8-equivalence-ratio H_2 /air mixture. Even though the propagation velocity of the individual flamelet is increasing with the gravitational force, the velocity of the flat flame (formed after mixing of flamelets) is independent of the applied gravitational force. When gravitational force is increased to $500g_0$, as seen in Fig. 3b, a mushroom vortex is formed due to small differences in the initial flamelets. The buoyancy acting on the light combustion products contained in the vortex propelled the vortex and the flame around it at a significantly higher speed. The propagation velocity of the flame in this case reached 9.2 m/s that is ~ 5 times that of the laminar burning velocity. The simulation in Fig. 3b confirms the bubble-transport

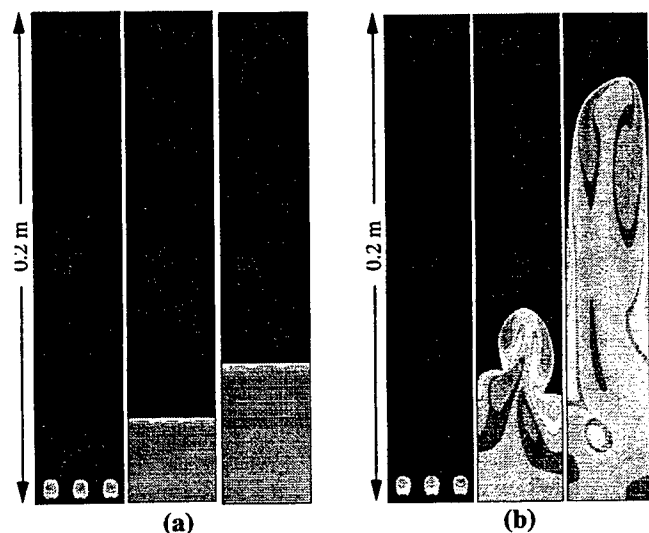


Figure 3: Spreading of a Flame Under (a) $10g$ and (b) $500g$ Force.

hypothesis, however, in a laminar flow situation. It may be argued that turbulence is a small-scale phenomenon and modifies (increases) the local burning velocity along the flame front. Consequently, in a turbulent-flow environment the flat flame in Fig. 3a propagates at the turbulent flame speed and the flame around the vortex in Fig. 3b propagates at turbulent burning velocity plus the bubble velocity.

We propose to study flame-vortex interaction using a simple experimental setup, a jet-in-crossflow burner (Rolon³). In this device, repeatable vortex rings of premixed methane and air are formed at the exit of a central nozzle using a solenoid-driven piston at the bottom of the fuel tube. Ignition is initiated at various

phases with respect to vortex formation and propagation using a pair of electrodes located near the nozzle periphery. A co-flow of air surrounded the fuel-air jet, and a shroud flow of nitrogen is used to reduce external disturbances. A steady background flow rate of 0.14 m/s is maintained for all flows when the piston is not being actuated. When acetone planar laser-induced fluorescence (PLIF) measurements are performed, the nozzle air supply is diverted into an acetone-seeding system prior to premixing with methane.

In the experiment proposed for this work, a premixed fuel-air mixture will be ignited and stabilized to form a flame front instead of co-flowing air. The vortex will be forced through the flame front, and the flame speed as a result of the vortex burst will be measured and compared to turbulent burning velocity. Studies will be conducted at various fuel-air ratios, vortex velocities, and vortex composition (fuel-air or exhaust products).

³ Rolon, J. C., Aguerre, F. and Candel, S. (1995), *Combustion and Flame*, 100:422-429.

Impact of Main Air Swirling Flow on Cavity Aerodynamics: In an actual gas turbine engine, the air exiting the compressor is de-swirled and decelerated before entering the combustion system plenum. The air is then locally re-swirled in the combustion chamber to promote mixing and flame stabilization, and then the flow is turned once again and accelerated before entering the turbine. All of this also takes axial length, and results in pressure losses to the system that impact fuel burn. In the UCC concept, it is hypothesized that the cavity can be “driven” by the swirled flow exiting the compressor rotor. By doing this, the compressor exit guide vane and diffuser can be eliminated, greatly reducing engine pressure loss, axial length and engine weight. Experiments are planned that will investigate the effects of main air swirl on combustion performance parameters. These experiments will be conducted at atmospheric and high-pressure conditions.

High Temperature Materials Studies:

A key technology essential for the development of a propulsion system that operates on a NCT cycle is an ITB that will efficiently add heat between the turbine stages and is constructed of advanced, lightweight CMC materials. AFRL/PRTC will continue to work with AFRL/ML in developing the materials technology to enable the use of a UCC and an ITB in future weapons systems. The AFRL/ML team has been studying the oxide-oxide materials in a combustion device, and has a preliminary design of a CMC turbine which is shown in Fig. 4. This CMC material can be used as the vane material in the originally proposed UCC/ITB design, or as the transport strut arrangement in the proposed vaneless ITB design.

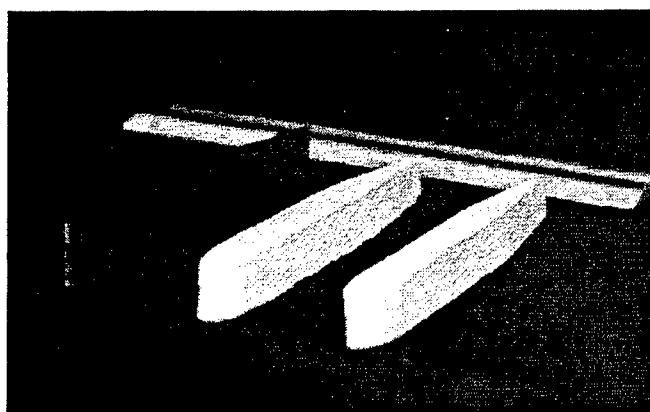


Figure 4: Oxide-Oxide Ceramic Matrix Composite (CMC) Materials Vane Prototype.

Advanced Diagnostics: AFRL/PRTC in conjunction with the Air Force Institute of Technology (AFIT), have used laser Doppler velocimetry (LDV) techniques to measure velocity fields in the combustor cavity and have found that the turbulence intensity within the cavity is quite high, leading to enhanced mixing due to the high g-loaded system⁴. AFRL/PRTC will continue leveraging additional AFOSR support/programs with AFIT that will provide advanced diagnostics capabilities to measure species concentration in the combustion cavity⁵. In a recently completed experiment, fiber optic sensors are staggered both radially and circumferentially to map out the fuel-air ratio in the entire combustor cavity. This information will be used to identify entrainment effects of the main flow into the cavity, and to assess and understand the complex flowfield in the cavity as a result of air injection, fuel injection, and main airflow aerodynamics.

External Collaboration: AFRL/PRTC has ITB and high-g combustion collaborative efforts with AADC, ISSI, CFD Research Corporation, and Williams International. We started start a 6.2 program with AADC and Williams International, utilizing our 6.1 results to demonstrate an UCC/ITB. This collaborative approach provides a clear transition path for the 6.1 research and would provide additional funds needed to demonstrate a turbine burner concept.

⁴ Quaale, R. J., Anthenien, R. A., Zelina, J., Ehret, J., “Flow Measurements Within a High Swirl Ultra Compact Combustor for Gas Turbine Engines,” ISABE 2003-1141.

⁵ Brown, M. S., Meyer, T. R., Sturgess, G. J., Zelina, J., and Gord, J. R., “Chemiluminescence as a Measurement of Local Equivalence Ratio,” AIAA 2002-3865.

Invitees

Dr. Waldo Acosta
Army Research Laboratory
Vehicle Technology Directorate
NASA Glenn Research Center
21000 Brookpark Road
Cleveland, OH 44135-3191
(216) 433-3393
waldo.acosta@us.army.mil

Dr. Ajay Agrawal
University of Oklahoma
Department of Aerospace and Mechanical Engineering
865 Asp Avenue, Room 212
Norman, OK 73019
(405) 325-1754
FAX: 325-1088
aagrawal@ou.edu

Dr. M.S. Anand
Rolls-Royce Corporation
P.O. Box 420
Speed Code T14
Indianapolis, IN 46206-0420
(317) 230-2828
FAX: 230-3691
m.s.anand@rolls-royce.com

Dr. William Anderson
AMSRL-WT-PC
US Army Research Laboratory
Aberdeen Proving Ground, MD 21005-5066
(410) 306-0731
DSN 298-9992
FAX: 306-1909
willie@arl.army.mil

Dr. Kurt Annen
Aerodyne Research, Inc.
45 Manning Road
Manning Park Research Center
Billerica, MA 01821-3976
(978) 663-9500, Ext. 234
FAX: 663-4918
kannen@aerodyne.com

Dr. Chris Atkinson
West Virginia University
Dept. of Mechanical & Aerospace Engineering
P.O. Box 6106
Morgantown, WV 26506-6106
(304) 293-4111
FAX: 293-2582

Mr. Steve Beckel
Pratt and Whitney
M/S 715-83
P.O. Box 109600
West Palm Beach, FL 33410-9600

Dr. Josette Bellan
Jet Propulsion Laboratory
MS 125-109
4800 Oak Grove Drive
Pasadena, CA 91109
(818) 354-6959
FAX: 393-5011
josette.bellan@jpl.nasa.gov

Dr. Michael Berman
AFOSR/NL
4015 Wilson Boulevard, Room 713
Arlington, VA 22203-1954
(703) 696-7781
DSN 426-7781
FAX: 696-8449
michael.berman@afosr.af.mil

Dr. William Berry
Director for Research
Defense Research & Engineering
3040 Defense Pentagon
Washington, DC 20301-3040

Dr. Thomas Beutner
AFOSR/NA
4015 Wilson Boulevard, Room 713
Arlington, VA 22203-1954
(703) 696-6961
DSN 426-6961
FAX: 696-8451
thomas.beutner@afosr.af.mil

Dr. Robert Bill
Army Research Laboratory
Vehicle Technology Directorate
NASA Glenn Research Center, MS 77-12
21000 Brookpark Road
Cleveland, OH 44135-3191
(216) 433-3703
FAX: 433-3000
bob.bill@us.army.mil

Dr. Mitat Birkan
AFOSR/NA
4015 Wilson Boulevard, Room 713
Arlington, VA 22203-1954
(703) 696-7234
DSN 426-7234
FAX: 696-8451
mitat.birkan@afosr.af.mil

Dr. Kevin Bowcutt
Rockwell International Corp.
North American Aircraft Division
P.O. Box 3644
Seal Beach, CA 90740-7644

Mr. Andreja Brankovic
Flow Parametrics, LLC
15 Debra Drive
Bear, DE 19701
(302) 838-7368
FAX: 838-7369
brankov@flowparametrics.com

Dr. R.C. Brown
Aerodyne Research, Inc.
45 Manning Road
Manning Park Research Center
Billerica, MA 01821-3976
(978) 663-9500
FAX: 663-4918

Dr. Walter Bryzik
Propulsion Systems Division
ATTN: AMSTA-TR-R, MS 121
USA Tank-Automotive Command
Warren, MI 48397-5000
(810) 574-6461
FAX: 574-5054
bryzik@cc.tacom.army.mil

Dr. T.D. Butler
MS B-210 T-DO: THEORETICAL DIVISION
Los Alamos National Laboratory
Los Alamos, NM 87545
(505) 667-4401
FAX: 665-4055
tdbutler@lanl.gov

Dr. George Caledonia
Physical Sciences, Inc
20 New England Business Center
Andover, MA 01810
(508) 689-0003
FAX: 689-3232

Mr. Donald Campbell
NASA Glenn Research Center
21000 Brookpark Road
Mail Stop 3-2
Cleveland, OH 44135
(216) 433-2929
(216) 433-5266

Dr. Herb Carlson
AFOSR/CA
4015 Wilson Boulevard, Room 713
Arlington, VA 22203-1954
(703) 696-7550
DSN 426-7550
FAX: 696-9556
herb.carlson@afosr.af.mil

Dr. Campbell Carter
AFRL/PRA
1950 Fifth Street
Building 18, Room D224
Wright-Patterson AFB, OH 45433-7251
(937) 255-7203
DSN 785-7203
Campbell.Carter@wpafb.af.mil

Dr. Len Caveny
13715 Piscataway Drive
Ft. Washington, MD 20744
(301) 292-5319
FAX: 292-3724
Lcaveny@compuserve.com

Dr. Nicholas Cernansky
Drexel University
Department of Mechanical Engineering
32nd and Chestnut Streets
Philadelphia, PA 19104-2884

Dr. Chine I. Chang
Director
US Army Research Office
P.O. Box 12211
Research Triangle Park, NC 27709-2211
(919) 549-4203
DSN 832-4203
FAX: 549-4348
jchang@aro-emh1.army.mil

Dr. Harsha Chelliah
University of Virginia
Dept. of Mechanical, Aero and Nuclear Engineering
Charlottesville, VA 22903-2442
(804) 924-6037
FAX: 982-2037
harsha@virginia.edu

Dr. Jacqueline Chen
Sandia National Laboratories
MS 9051
P.O. Box 969
Livermore, CA 94551-0969
(510) 294-2586
FAX: 294-1012
jhchen@sandia.gov

Dr. S.Y. Cho
Princeton University
Department of Mechanical and Aerospace Engineering
Princeton, NJ 08544-5263

Dr. M.B. Colket
United Technologies Research Center
411 Silver Lane, MS 129-29
East Hartford, CT 06108
(860) 610-7481
(860) 658-9502
FAX: 610-7593
colketmb@utrc.utc.com

Dr. S.M. Correa
GE Corp. Research & Development
P.O. Box 8, K1ES112
Schenectady, NY 12301
(518) 387-5853
FAX: 387-7258
correa@crd.ge.com

Dr. Werner Dahm
The University of Michigan
Department of Aerospace Engineering
3056 FXB 2140
Ann Arbor, MI 48109-2140
(734) 764-4318
(734) 761-2026
FAX: 763-0578
wdahm@umich.edu

Mr. Eugene Danielson
US Army Tank-Automotive and Armaments
Command
ATTN: AMSTA-TR-R - MS 121
Warren, MI 48397-5000

Dr. Ron Davis
National Institute of Standards & Technology
Chemical Science and Technology Lab
Building 221, Room B312
Gaithersburg, MD 20899

Dr. Peter A. DeBarber
MetroLaser
2572 White Road
Irvine, CA 92614
(949) 553-0688
FAX: 553-0495
debarber@deltanet.com

Dr. Paul Dimotakis
California Institute of Technology
1201 East California Boulevard
MC 301-46
Pasadena, CA 91125
(626) 395-4456
(626) 794-2594
(626) 395-4447
dimotakis@caltech.edu

Dr. Glenn Diskin
NASA Langley Research Center
MS 197
Hypersonic Airbreathing Prop. Branch
Hampton, VA 23681-2199
(757) 864-6268
FAX: 864-7923
g.s.diskin@larc.nasa.gov

Dr. Gregory Dobbs
United Technologies Research Center
Mail Stop 90
Silver Lane
East Hartford, CT 06108
(860) 610-7145

Dr. James F. Driscoll
University of Michigan
Department of Aerospace Engineering
3004 FXB Building
Ann Arbor, MI 49109-2118
(734) 936-0101
FAX: 763-0578
jamesfd@umich.edu

Dr. J. Philip Drummond
NASA Langley Research Center
Mail Stop 197
Hampton, VA 23681-0001
(757) 864-2298
FAX: 864-7923
j.p.drummond@larc.nasa.gov

Dr. C. Dutton
University of Illinois
Department of Mechanical and Industrial Engineering
Urbana, IL 61801

Dr. Tarek Echehki
North Carolina State University
Department of Mechanical & Aerospace Engineering
2601 Stinson Drive, Campus Box 7910
Raleigh, NC 27695-7910
(919) 515-5238
FAX: 515-7968
techehki@eos.ncsu.edu

Dr. J.T. Edwards
AFRL/PRTG
Building 490, Room 111
1790 Loop Road, N
Wright-Patterson AFB, OH 45433-7251
(937) 255-3524
DSN 785-3524
FAX: 255-1125
james.edwards@wpafb.af.mil

Dr. Fokion N. Egolfopoulos
University of Southern California
Department of Mechanical Engineering
Olin Hall 400B
Los Angeles, CA 90089-1453
(213) 740-0480
FAX: 740-8071
egolfopo@almaak.usc.edu

Col. Donald Erbschloe
AFOSR/CD
4015 Wilson Boulevard, Room 713
Arlington, VA 22203-1954
(703) 696-7555
DSN 426-7555
FAX: 696-9556
steven.reznick@afosr.af.mil

Dr. G.M. Faeth
University of Michigan
Department of Aerospace Engineering
3000 FXB Building
Ann Arbor, MI 48109-2140
(734) 764-7202
FAX: 936-0106
gmfaeth@umich.edu

Dr. Parviz Famouri
West Virginia University
Department of Computer Science and Electrical
Engineering
P.O. Box 6109
Morgantown, WV 26506
(304) 293-0405 x 2530
pfamouri@wvu.edu

Dr. Gregory W. Faris
SRI International
Molecular Physics Laboratory
333 Ravenswood Avenue
Menlo Park, CA 94025-3493
(650) 859-4131
FAX: 859-6196
gregory.faris@sri.com

Dr. Patrick Farrell
University of Wisconsin
Engine Research Center
1500 Engineering Drive
Madison, WI 53706
(608) 263-1686
farrell@engr.wisc.edu

Dr. David E. Foster
University of Wisconsin
Engine Research Center
1500 Engineering Drive
Madison, WI 53706
(608) 263-1617
foster@engr.wisc.edu

Dr. Bish Ganguly
AFRL/PRPE
2645 Fifth Street, Suite 13
Wright-Patterson AFB, OH 45433-7919
(937) 255-2923
DSN 785-2923
FAX: 656-4095
biswa.ganguly@pr.wpafb.af.mil

Dr. Richard G. Gann
National Institute of Standards & Technology
Building and Fire Research Laboratory
100 Bureau Drive, Stop 8650
Gaithersburg, MD 20899-8650
(301) 975-6866
FAX: 975-4052
rggann@nist.gov

Dr. Alan Garscadden
AFRL/PR
1950 Fifth Street, Building 18A
Wright-Patterson AFB, OH 45433-7251
(937) 255-2246
DSN 785-2246
FAX: 986-4657
alan.garscadden@pr.wpafb.af.mil

Dr. Kresimir Gebert
BKM, Inc.
5141 Santa Fe Street
San Diego, CA 92109
(858) 270-6760
bkm-inc@worldnet.att.net

Mr. R. Giffen
General Electric Company
Aircraft Engine Group
Neumann Way
Cincinnati, OH 45215

Dr. Sharath Girimaji
Texas A&M University
Department of Aerospace Engineering
College Station, TX 77843-3141
(979) 845-1674
FAX: 845-6051
girimaji@aero.tamu.edu

Dr. Peyman Givi
University of Pittsburgh
Department of Mechanical Engineering
644 Benedum Hall
Pittsburgh, PA 15261
(412) 624-9605
FAX: 624-4846
givi@engr.pitt.edu

Dr. Irvin Glassman
Princeton University
Department of Mechanical and Aerospace Engineering
Princeton, NJ 08544-5263
(609) 258-5199
(813) 442-1118
FAX: 258-5963
glassman@princeton.edu

Dr. George Gogos
University of Nebraska-Lincoln
Department of Mechanical Engineering
Lincoln, NE 68588-0656
(402) 472-3006
ggogos1@unl.edu

Dr. Judah Goldwasser
Office of Naval Research
Mechanics Division, Code 333
800 North Quincy Street
Arlington, VA 22217-5660
(703) 696-2164
DSN 426-2164
FAX: 696-2558
goldwaj@onr.navy.mil

Dr. James Gord
AFRL/PRTS
Building 5, Room 5P23
1790 Loop Road N
Wright-Patterson AFB, OH 45433-7251
(937) 255-7431
DSN 785-7431
FAX: 656-4570
james.gord@pr.wpafb.af.mil

Dr. Jay P. Gore
Purdue University
School of Mechanical Engineering
1003 Chaffee Hall
West Lafayette, IN 47907-1003
(317) 494-1500
FAX: 494-0530

Dr. Larry Goss
Systems Research Labs, Inc.
Research Applications Division
2800 Indian Ripple Road
Dayton, OH 45440-3696
(513) 252-2706

Dr. Richard Gould
North Carolina State University
Department of Mechanical and Aerospace Engineering
Box 7910
Raleigh, NC 27695-7910
(919) 515-5236
FAX: 515-7968
gould@eos.ncsu.edu

Dr. Frederick Gouldin
Cornell University
Department of Mechanical and Aerospace Engineering
Ithaca, NY 14853-5692
(607) 255-5280
fcg2@cornell.edu

Dr. Mark Gruber
AFRL/PRA
1790 Loop Road North
Wright-Patterson AFB, OH 45433-7251
(937) 255-2175
DSN 785-2175
FAX: 656-4659
Mark.Gruber@afrl.af.mil

Dr. Brian K. Gullett
U.S. Environmental Protection Agency
National Risk Management Research Laboratory
Air Pollution Technology Branch (MD-65)
Research Triangle Park, NC 27711
(919) 541-1534
FAX: 541-0290
gullett.brian@epa.gov

Dr. Rajendra Gupta
University of Arkansas
Department of Physics
226 Physics Building
Fayetteville, AK 72701
(501) 575-5933
rgupta@comp.uark.edu

Dr. Mark A. Hagenmaier
AFRL/PRA
Building 18
1950 Fifth Street, Suite 10
Wright-Patterson AFB, OH 45433-7251
(937) 255-5210
DSN 785-5210
FAX: 476-4659
hagenma@possum.appl.wpafb.af.mil

Dr. Nabil S. Hakim
Director, Advanced Engineering
Detroit Diesel Corporation
13400 W. Outer Drive, R03-B
Detroit, MI 48239-4001
(313) 592-7455
FAX: 592-5906

Dr. Robert D. Hancock
AFRL/PRTS
Building 490
1790 Loop Road, N
Wright-Patterson AFB, OH 45433-7103
(937) 255-6814
DSN 785-6814
FAX: 255-1125
hancockr@ward.appl.wpafb.af.mil

Dr. Ronald Hanson
Stanford University
Department of Mechanical Engineering
Building 530, Room 112
Stanford, CA 94305-3030
(650) 723-4023
FAX: 725-4862
hanson@me.stanford.edu

Dr. Naeim Henein
Wayne State University
Department of Mechanical Engineering
2121 Engineering Building
Detroit, MI 48201
(313) 577-3887
FAX: 577-8789
henein@me1.eng.wayne.edu

Dr. Cecil F. Hess
MetroLaser
2572 White Road
Irvine, CA 92614
(949) 553-0688
FAX: 553-0495
chess@metrolaserinc.com

Mr. Robert Holland
United Technologies Chemical
Systems Division
P.O. Box 49028
San Jose, CA 95161-9028
(408) 224-7656

Dr. Tian-Sen Huang
Prairie View A&M University
P.O. Box 307
Prairie View, TX 77446-0307
(936) 857-2859
FAX: 857-2850
ts_huang@pvamu.edu

Dr. Lawrence Hunter
Johns Hopkins University
Applied Physics Laboratory
Johns Hopkins Road
Laurel, MD 20707-6099
(301) 953-5000
Ext. 7406

Dr. Frank Hurley
U.S. Army Research Office
P.O. Box 12211
Research Triangle Park, NC 27709-2211
(919) 549-4432
DSN 832-4432
FAX: 549-4310
hurley@aro-emh1.army.mil

Dr. Farhad Jaber
Kansas State University
Department of Mechanical and Nuclear Engineering
Manhattan, KS 66506
(785) 532-5619
FAX: 532-7057
jaberi@mne.ksu.edu

Dr. Thomas Jackson
AFRL/PRSC
Building 18
1950 Fifth Street
Wright-Patterson AFB, OH 45433-7251
(937) 255-2175
DSN 785-2175
FAX: 656-4659
thomas.jackson@afrl.af.mil

Dr. Jeff Jagoda
Georgia Institute of Technology
School of Aerospace Engineering
Atlanta, GA 30332-0150
(404) 894-3060
jeff.jagoda@aerospace.gatech.edu

Dr. Jay Jeffries
Stanford University
Department of Mechanical Engineering
Thermophysics Division, Building 520
Stanford, CA 94305-3032
(650) 736-0007
FAX: 723-1748
Jeffries@Navier.Stanford.edu

Mr. Gordon Jensen
United Technologies Chemical
Systems Division
P.O. Box 49028
San Jose, CA 95161-9028
(408) 365-5552

Mr. Jeff Jensen
Kaiser-Marquardt
16555 Staycoy Street
Van Nuys, CA 91406

Mr. Craig Johnston
Lockheed Advanced Dev. Company
Lockheed-Martin Corporation
1011 Lockheed Way
Palmdale, CA 93599-7212

Dr. Walter Jones
AFOSR/NA
4015 Wilson Boulevard, Room 713
Arlington, VA 22203-1954
(703) 696-8457
DSN 426-8457
FAX: 696-8451
walter.jones@afosr.af.mil

Dr. John Kelly
Altex Technologies Corporation
650 Nuttman Road, Suite 114
Santa Clara, CA 95054
(408) 980-8610

Dr. Barry Kiel
AFRL/PRTC
Building 490, Room 109
1950 Fifth Street
Wright-Patterson AFB, OH 45433-7251
(937) 255-7272
DSN 785-7272
Barry.Kiel@wpafb.af.mil

Dr. G.B. King
Purdue University
Department of Mechanical Engineering
West Lafayette, IN 47907-1288
(765) 494-6518
kinggb@ecn.purdue.edu

Dr. Merrill K. King
NASA Headquarters
Code UG
300 E Street, SW
Washington, DC 20546-0001
(202) 358-0817
FAX: 358-3091
mking1@mail.hq.nasa.gov

Dr. David E. Klett
North Carolina Agricultural and Technical
State University
Department of Mechanical Engineering
Greensboro, NC 27401-3209

Dr. Charles Kolb
Aerodyne Research, Inc.
45 Manning Road
Manning Park Research Center
Billerica, MA 01821-3976
(978) 663-9500
FAX: 663-4918

Mr. John Koshoffer
General Electric Aircraft Engines
1 Neuman Way
M.D. G52
Cincinnati, OH 45215
(513) 243-2995
FAX: 243-1022
john.koshoffer@ae.ge.com

Dr. Kenneth Kuo
Pennsylvania State University
Department of Mechanical Engineering
University Park, PA 16802
(814) 865-6741
FAX: 863-3203

Dr. Ming-Chia Lai
Wayne State University
Department of Mechanical Engineering
Detroit, MI 48202

Dr. John Larue
University of California
Department of Mechanical Engineering
Irvine, CA 92717

Dr. Allan Laufer
U.S. Department of Energy
Office of Energy Research
19901 Germantown Road
Germantown, MD 20874
(202) 903-5820
Allan.Laufer@oer.doe.gov

Dr. Normand Laurendeau
Purdue University
School of Mechanical Engineering
West Lafayette, IN 47907-1288
(765) 494-2713
FAX: 494-0539
Laurende@ecn.purdue.edu

Dr. C.K. Law
Princeton University
Department of Mechanical and Aerospace Engineering
Princeton, NJ 08544-5263
(609) 258-5271
FAX: 258-6233
cklaw@princeton.edu

Dr. C.C. Lee
Environmental Protection Agency
Cincinnati, OH 45268
(513) 569-7520

Dr. Calvin Lee
Natick Research, Development & Engineering Center
Applied Research Division
Kansas Street
Natick, MA 01760-5017
(508) 233-4267
FAX: 233-5000
calvin.k.lee@us.army.mil

Dr. Anthony Leonard
California Institute of Technology
Graduate Aeronautical Labs
Pasadena, CA 91125
(626) 395-4465

Dr. Arthur Lewis
University of Dayton Research Institute
Aerospace Mechanics Division
300 College Park
Dayton, OH 45469-0110
(937) 229-4235
FAX: 229-4251

Mr. Randy L. Lewis
General Electric Aircraft Engines
1 Neuman Way
M.D. G52
Cincinnati, OH 45215
(513) 243-0517
FAX: 243-1022
Randy.Lewis@ae.ge.com

Dr. Goang Liaw
Alabama A&M University
Department of Civil Engineering
P.O. Box 367
Normal, AL 35762
(205) 851-5565

Dr. Timothy Lieuwen
Georgia Institute of Technology
School of Aerospace Engineering
Atlanta, GA 30332-0150
(404) 894-3041
FAX: 894-2760
tim.lieuwen@aerospace.gatech.edu

Dr. Mark A. Linne
Lund Institute of Technology
Department of Combustion Physics
P.O. Box 118
S-221 00 Lund, Sweden
+46 (0) 46-2224756
mark.linne@forbrf.lth.se

Dr. Charles L. Liotta
Georgia Institute of Technology
Department of Chemical Engineering
Atlanta, GA 30332-0100
(404) 853-9344
FAX: 894-6956

Dr. Thomas A. Litzinger
Pennsylvania State University
Department of Mechanical Engineering
0201 Hammond Building
University Park, PA 16802
(814) 865-4015
tal2@psu.edu

Dr. Lyle N. Long
Pennsylvania State University
Department of Aerospace Engineering
233 Hammond Building
University Park, PA 16802
(814) 865-1172
FAX: 865-7092
lnl@psu.edu

Dr. Jeffery Lovett
Pratt and Whitney
400 Main Street
MS 163-03
East Hartford, CT 06108
(860) 557-0559
jeffery.lovett@pw.utc.com

Dr. Kevin Lyons
North Carolina State University
Department of Mechanical and Aerospace Engineering
P.O. Box 7910
Raleigh, NC 27695
(919) 515-5293
FAX: 7968
lyons@eos.ncsu.edu

Dr. Bruce MacDonald
Systems Research Labs, Inc.
Research Applications Division
2800 Indian Ripple Road
Dayton, OH 45440-3696
(513) 252-2706

Mr. Nick Makris
SA-ALC/SFT
Kelly AFB, TX 78241-5000
AV945-8212
FAX: 945-9964

Dr. David Mann
U.S. Army Research Office
P.O. Box 12211
4300 South Miami Boulevard
Research Triangle Park, NC 27709-2211
(919) 549-4249
DSN 832-4249
FAX: 549-4310
david.mann1@us.army.mil

Dr. Nagi Mansour
Computational Fluid Mechanics
Branch, RFT 202A-1
NASA Ames Research Center
Moffett Field, CA 94035
(415) 604-6420

Dr. John Marek
NASA Glenn Research Center
Mail Stop 5-11
21000 Brookpark Road
Cleveland, OH 44135-3127
(216) 433-3584
FAX: 433-3000
cecil.j.marek@lerc.nasa.gov

Dr. Jay Martin
University of Wisconsin-Madison
Engine Research Center
1500 Engineering Drive
Madison, WI 53706
(608) 263-9460
FAX: 262-6707
martin@engr.wisc.edu

Dr. James McDonald
Naval Research Laboratory
Code 6110
Chemistry Division
Washington, DC 20375-5342
(202) 767-3340
DSN 297-3340

Dr. A.M. Mellor
Vanderbilt University
Department of Mechanical & Materials Engineering
512 Kirkland Hall
Nashville, TN 37240
(615) 343-6214
FAX: 343-6687

Dr. Lynn Melton
University of Texas, Dallas
Programs in Chemistry
P.O. Box 830688
Richardson, TX 75083-0688
(972) 883-2913
(972) 680-2163
FAX: 883-2925
melton@utdallas.edu

Dr. Suresh Menon
Georgia Institute of Technology
School of Aerospace Engineering
270 Ferst Drive
Atlanta, GA 30332-0150
(404) 894-9126
FAX: 894-2760
suresh.menon@aerospace.gatech.edu

Dr. Hameed Metghalchi
Northeastern University
Mechanical, Industrial and Manufacturing Dept. 334SN
360 Huntington Avenue
Boston, MA 2115
(617) -373-2973
FAX: 373-2921
metghal@coe.neu.edu

Dr. Michael M. Micci
Pennsylvania State University
Department of Aerospace Engineering
233 Hammond Building
University Park, PA 16802
(814) 863-0043
(814) 692-8751
FAX: 865-7092
micci@henry2.aero.psu.edu

Dr. Andrzej Miziolek
AMSRL-WT-PC
Army Research Laboratory
Aberdeen Proving Gnd, MD 21005-5066
(410) 278-6157
FAX: 278-6094
miziolek@arl.army.mil

Dr. H.C. Mongia
Manager, Combustion Technology
GE Aircraft Engines
One Neumann Way, M/D A404
Cincinnati, OH 45215-6301
(513) 243-2552
FAX: 243-2538
Hukam.Mongia@ae.ge.com

Dr. Arje Nachman
AFOSR/NM
4015 Wilson Boulevard, Room 713
Arlington, VA 22203-1954
(703) 696-8427
DSN 426-8427
FAX: 696-8450
arje.nachman@afosr.af.mil

Dr. Herbert Nelson
Naval Research Laboratory
Code 6110, Chemistry Division
4555 Overlook Avenue, SW
Washington, DC 20375-5342
(202) 767-3686

Dr. Elaine Oran
US Naval Research Laboratory
LCP&FD, Code 6404
4555 Overlook Avenue, SW
Washington, DC 20375-5344
(202) 767-2960
FAX: 767-4798
ORAN@lcp.nrl.navy.mil

Dr. Michelle Pantoya
Texas Tech University
Dept. of Mechanical Engineering, MS 1021
Lubbock, TX 79409
(806) 742-3563
FAX: 742-3540
michelle.pantoya@coe.ttu.edu

Dr. T.E. Parker
Colorado School of Mines
Engineering Division
Golden, CO 80401-1887
(303) 273-3657
FAX: 273-3602
tparker@mines.colorado.edu

Dr. Phillip H. Paul
Sandia National Laboratories
MS 9051
P.O. Box 969
Livermore, CA 94551-9051
(510) 294-1465
FAX: 294-1012
phpaul@sandia.gov

Dr. Lisa Pfefferle
Yale University
Department of Chemical Engineering
New Haven, CT 06520-8286
(203) 432-2222
FAX: 432-7232
pfefferle@htcre.eng.yale.edu

Dr. Emil Pfender
The University of Minnesota
Department of Mechanical Engineering
125 Mechanical Engineering
Minneapolis, MN 55455

Dr. Heinz G. Pitsch
Stanford University
Department of Mechanical Engineering
Building 500, Room 500M
Stanford, CA 94305-3035
(650) 725-6635
FAX: 725-7834
h.pitsch@stanford.edu

Dr. Robert Pitz
Vanderbilt University
Dept. of Mechanical and Materials Engineering
Nashville, TN 37235
(615) 322-0209
FAX: 343-8730
pitzrw@ctrvan.vanderbilt.edu

Dr. S.B. Pope
Cornell University
Dept. of Mechanical and Aerospace Engineering
Ithaca, NY 14853-7501
(607) 255-4314
FAX: 255-1222
pope@mae.cornell.edu

Dr. David Pratt
AFRL/VAS
Building 45 Annex
2130 Eighth Street, Suite 1
Wright-Patterson AFB, OH 45433-7542
(937) 255-5042
DSN 785-5042
FAX: 656-7915
David.Pratt@va.af.mil

Dr. Ala Qubbaj
University of Texas-Pan American
Dept. of Mechanical Engineering, ENB 3230
1201 West University Drive
Edinburg, TX 78539-2999
(956) 318-5220
qubbaj@panam.edu

Dr. Martin J. Rabinowitz
Mail Stop 5/10
NASA Glenn Research Center
21000 Brookpark Road
Cleveland, OH 44135-3191
(216) 433-5847
FAX: 433-5588
marty@lerc.nasa.gov

Dr. Larry Rahn
Sandia National Laboratories
7011 East Avenue
Mail Stop 9056
Livermore, CA 94551-0969
(510) 294-2091
FAX: 294-2276
rahn@sandia.gov

Dr. Mohan K. Razdan
Rolls-Royce Company
P.O. Box 420
Speed Code T10B
Indianapolis, IN 46206-0420
(317) 230-6404
FAX: 230-3691
mohan.razdan@rolls-royce.com

Mr. Robert Reed
Sverdrup Technology, Inc.
AEDC
1099 Avenue C
Arnold AFB, TN 37389-9013
(615) 454-4648
DSN 340-4648
(615) 454-6317

Dr. Rolf D. Reitz
University of Wisconsin
Department of Mechanical Engineering
1500 Johnson Drive
Madison, WI 53706
(608) 262-0145
FAX: 262-6717

Dr. Kyung T. Rhee
Rutgers, The State University of NJ
Dept. of Mechanical and Aerospace Engineering
Piscataway, NJ 08854-0909
(732) 445-3651
KTRhee@jove.rutgers.edu

Dr. James Riley
University of Washington
Department of Mechanical Engineering
Seattle, WA 98195
(206) 543-5347
73671.737@Compuserve.com

Dr. William Roberts
Dept. of Mechanical and Aerospace Engineering
Box 7910
North Carolina State University
Raleigh, NC 27695-7910
(919) 515-5294
FAX: 515-7968
wrobert@eos.ncsu.edu

Mr. Gerald A. Roffe
GASL
77 Raynor Avenue
Ronkonkoma, NY 11779

Dr. W.M. Roquemore
AFRL/PRTS
Building 5
Wright-Patterson AFB, OH 45433-7251
(937) 255-6813
DSN 785-6813
FAX: 656-4570
melvyn.roquemore@wpafb.af.mil

Dr. Daniel Rosner
Yale University
Department of Chemical Engineering
New Haven, CT 06520-8286
(203) 432-4391
FAX: 432-7232
daniel.rosner@yale.edu

Dr. John Ross
Stanford University
Department of Chemistry
Stanford, CA 94305-3032
(650) 723-9203

Dr. Gabriel Roy
Office of Naval Research
Mechanics Division, Code 1132
800 North Quincy Street
Arlington, VA 22217-5660
(703) 696-4406
DSN 426-4406
FAX: 696-0934
roy@ocnr-hq.navy.mil

Dr. Robert C. Ryder
Flow Parametrics, LLC
15 Debra Drive
Bear, DE 19701
(302) 838-7368
FAX: 838-7369
rryder@flowparametrics.com

Mr. Kurt Sacksteder
NASA Glenn Research Center
MS 500-217
21000 Brookpark Road
Cleveland, OH 44135
(216) 433-2857

Dr. Mohammad Samimy
Ohio State University
Department of Mechanical Engineering
206 West 18th Street
Columbus, OH 43210-1107
(614) 422-6988
(614) 848-9439
FAX: 292-3163
msamimy@magnus.acs.ohio-state.edu

Dr. G.S. Samuelsen
University of California
Dept. of Mechanical and Aerospace Engineering
Irvine, CA 92697-3975
(949) 824-5468

Dr. Lakshmi Sankar
Georgia Institute of Technology
School of Aerospace Engineering
Atlanta, GA 30332
(404) 894-3014

Dr. Domenic Santavica
Pennsylvania State University
Propulsion Engineering Research Center
106 Research Building East - Bigler Road
University Park, PA 16802-2320
(814) 863-1863

Dr. R.J. Santoro
Pennsylvania State University
Department of Mechanical Engineering
University Park, PA 16802-2320
(814) 863-1285
FAX: 865-3389
rjs2@email.psu.edu

Dr. Sutanu Sarkar
University of California
Dept. of Applied Mechanics & Engineering Science
MC 0411
La Jolla, CA 92093-0411
(858) 534-8243
FAX: 534-7599
ssarkar@ucsd.edu

Dr. John Schaefer
Acurex Corporation
Energy and Environmental Division
555 Clyde Ave., P. O. Box 7555
Mountain View, CA 94039

Dr. Frederick Schauer
AFRL/PRTS
Building 490, Room 112
1790 Loop Road, N
Wright-Patterson AFB, OH 45433-7251
(937) 255-6462
DSN 785-6462
FAX: 255-1125
frederick.schauer@wpafb.af.mil

Dr. Peter Schihl
Propulsion Systems Division
ATTN: AMSTA-TR-R, MS 121
USA Tank Automotive Command
Warren, MI 48397-5000
FAX: 574-5054
schihlp@tacom.army.mil

Dr. Lyle Schwartz
AFOSR/CC
4015 Wilson Boulevard, Room 713
Arlington, VA 22203-1954
(703) 696-8457
DSN 426-7551
lyle.schwartz@afosr.af.mil

Dr. Ernest Schwarz
Propulsion Systems Division
ATTN: DRSTA-RGD
USA Tank-Automotive Command
Warren, MI 48397-5000
(810) 574-5656
FAX: 574-5054
schwarze@cc.tacom.army.mil

Mr. Lee Scuderi
McDonnell Douglas Aerospace
P.O. Box 516
St. Louis, MO 63166-0516

Dr. Jerry Seitzman
Georgia Institute of Technology
School of Aerospace Engineering
Atlanta, GA 30332-0150
(404) 894-0013
FAX: 894-2760
jerry.seitzman@ae.gatech.edu

Dr. Kalyanasundaram Seshadri
University of California
Center for Energy and Combustion Research, 0407
La Jolla, CA 92093-0407
(619) 534-4876
seshadri@ames.ucsd.edu

Dr. Robert Shaw
U.S. Army Research Office
Division of Chemical and Biological Sciences
Research Triangle Park, NC 27709-2211
(919) 549-0641

Dr. Adam Siebenhaar
Aerojet Propulsion Division
P.O. Box 13222
Sacramento, CA 95813-6000

Dr. Gupreet Singh
U.S. Department of Energy
1000 Independence Avenue, S.W.
Washington, DC 20585
(202) 586-2333
FAX: 586-4166
GUPREET.SINGH@hq.doe.gov

Dr. William Sirignano
University of California
Dept. of Mechanical and Aerospace Engineering
Irvine, CA 92697-3975
(949) 824-3700
FAX: 824-3773
sirignan@uci.edu

Mr. Davey Smith
Northrop Grumman Corporation
B-2 Division Dayton Office
2850 Presidential Dr., Ste 100
Fairborn, OH 45324

Dr. Gregory Smith
SRI International
Department of Chemical Kinetics
333 Ravenswood Avenue
Menlo Park, CA 94025-3493
(415) 859-3496

Dr. James Smith
University of Alabama in Huntsville
Department of Chemical Engineering
Huntsville, AL 35899
(256) 824-3594
smithje1@uah.edu

Dr. Kenneth A. Smith
Massachusetts Institute of Technology
Department of Chemical Engineering
Room 66-540
Cambridge, MA 02139
(617) 253-1973
FAX: 253-2701
kas@mit.edu

Dr. Judi Steciak
University of Idaho-Boise
800 Park Boulevard
Boise, ID 83712-7742
(208) 364-4080
FAX: 387-1246
jsteciak@uidaho.edu

Dr. David Stewart
University of Illinois
Dept. of Theoretical and Applied Mechanics
Urbana, IL 61801

Dr. Geoffrey J Sturgess
Dayton, OH
gsturgess@aol.com

Dr. B. Sturtevant
California Institute of Technology
Dept. of Engineering and Applied Science
Pasadena, CA 91125

Dr. G. Sullins
Johns Hopkins University
Applied Physics Laboratory
Johns Hopkins Road
Laurel, MD 20707-6099
(301) 953-5000

Dr. Rodney Tabaczynski
Director, Power Train Research Lab
Ford Motor Research Laboratory
3623 Scientific Research Lab
P.O. Box 2053
Dearborn, MI 48121-2053
(313) 322-8930

Dr. Douglas Talley
AFRL/PRSA
10 East Saturn Boulevard
Edwards AFB, CA 93524-7660
(661) 275-6174
DSN 525-6174
FAX: 275-6245
Douglas.Talley@ple.af.mil

Dr. Jefferson W. Tester
Massachusetts Institute of Technology
M.I.T. Energy Laboratory
Room E40-455
Cambridge, MA 02139
(617) 253-3401
FAX: 253-8013
testerel@mit.edu

Dr. Stefan Thynell
Pennsylvania State University
Department of Mechanical Engineering
0309 Reber Building
University Park, PA 16802
(814) 863-0977
FAX: 863-8682
umt@psu.edu

Dr. Julian Tishkoff
AFOSR/NA
4015 Wilson Boulevard, Room 713
Arlington, VA 22203-1954
(703) 696-8478
DSN 426-8478
FAX: 696-8451
julian.tishkoff@afosr.af.mil

Dr. Chenning Tong
Clemson University
Mechanical Engineering Department
248 Fluor Daniel EIB
Clemson, SC 29634-0921
(864) 656-7225
FAX: 656-4435
ctong@ces.clemson.edu

Dr. Michael Trenary
The University of Illinois
Department of Chemistry
Chicago, IL 60680

Dr. James Trolinger
MetroLaser
2572 White Road
Irvine, CA 92614
(949) 553-0688
FAX: 553-0495
jtrolinger@vmsa.oac.uci.edu

Dr. Timothy Troutt
Washington State University
Department of Mechanical Engineering
Pullman, WA 99164-2920

Dr. Gretar Tryggvason
The University of Michigan
Dept. of Mechanical Engrg. & Applied Mechanics
2350 Hayward, Room 2250
Ann Arbor, MI 48109-2125
(734) 763-1049
FAX: 764-4256
gretar@umich.edu

Dr. Frank Tully
U.S. Department of Energy
SC-141
19901 Germantown Road
Germantown, MD 20874
(301) 903-5998
Frank.Tully@science.doe.gov

Dr. A.D. Vakili
University of Tennessee
Space Institute
Tullahoma, TN 37388

Dr. Mark Valco
Army Research Laboratory
Propulsion Directorate
NASA Glenn Research Center, MS 49-1
Cleveland, OH 44135-3127
(216) 433-3717
FAX: 433-2182
aamark@lims01.lerc.nasa.gov

Dr. David Van Wie
The Johns Hopkins University
Applied Physics Laboratory
11100 Johns Hopkins Road
Laurel, MD 20723-6099
(240) 228-5194
FAX: 228-5850
David.VanWie@jhuapl.edu

Dr. Ian Waitz
Massachusetts Institute of Technology
Department of Aeronautics and Astronautics
Bldg. 33-207
77 Massachusetts Avenue
Cambridge, MA 02139-4307
(617) 253-0218
FAX: 258-7566
iaw@mit.edu

Dr. Joe Wander
AFRL/MLQL
139 Barnes Drive, Suite 2
Tyndall AFB, FL 32403-5323
(904) 283-6240
DSN 523-6240
FAX: 283-6064
Jwander@mlq.af.mil

Dr. Hai Wang
University of Delaware
Department of Mechanical Engineering
Newark, DE 19716
(302) 831-2421
FAX: 831-3619
hwang@me.udel.edu

Dr. Zhicheng Wang
Clark Atlanta University
223 James P. Brawley Drive, SW
Atlanta, GA 30314
(404) 880-6125
FAX: 880-6615
zhicheng_wang@hotmail.com

Dr. Charles Westbrook
Lawrence Livermore National Laboratories
P.O. Box 808
Livermore, CA 94551
(925) 422-4108
FAX: 422-2644
westbrook1@llnl.gov

Dr. Phillip R. Westmoreland
University of Massachusetts
Department of Chemical Engineering
Amherst, MA 01003
(413) 545-1750
(413) 545-2507
(413) 545-1647
westm@ecs.umass.edu

Dr. James Whitelaw
Imperial College of Science and Technology
Department of Mechanical Engineering
London SW7 2BX, UK

Dr. Forman Williams
University of California
Center for Energy and Combustion Research, 0310
La Jolla, CA 92093-0310
(858) 534-5492
(858) 534-4285
FAX: 534-7720
fwilliams@ucsd.edu

Dr. Skip Williams
AFRL/VSBXT
29 Randolph Street
Hanscom AFB, MA 01731
(781) 377-2076
FAX: 377-7091
skipw@plh.af.mil

Dr. Bernard T. Wolfson
Wolfson Associates International
4797 Lake Valencia Boulevard, West
Palm Harbor, FL 33563
(813) 786-3007

Dr. Mary J. Wornat
Louisiana State University
Department of Chemical Engineering
South Stadium Drive
Baton Rouge, LA 70803
(225) 578-7509
FAX: 578-1476
mjwornat@lsu.edu

Dr. J.M. Wu
University of Tennessee
Space Institute
Tullahoma, TN 37388

Dr. Vigor Yang
The Pennsylvania State University
Propulsion Engineering Research Center
111 Research Building East
University Park, PA 16802-2320
(814) 863-1502
FAX: 865-4784
vigor@arthur.psu.edu

Dr. Richard Yetter
Pennsylvania State University
Dept. of Mechanical and Nuclear Engineering
State College, PA 16802
(814) 863-6375
rayetter@psu.edu

Dr. Joseph Zelina
AFRL/PRTC
Building 490, Room 109
1790 Loop Road, N
Wright-Patterson AFB, OH 45433-7251
(937) 255-7487
DSN 785-7487
joseph.zelina@wpafb.af.mil

Dr. Ben Zinn
Georgia Institute of Technology
School of Aerospace Engineering
Atlanta, GA 30332-0150
(404) 894-3033
FAX: 894-2760
ben.zinn@aerospace.gatech.edu